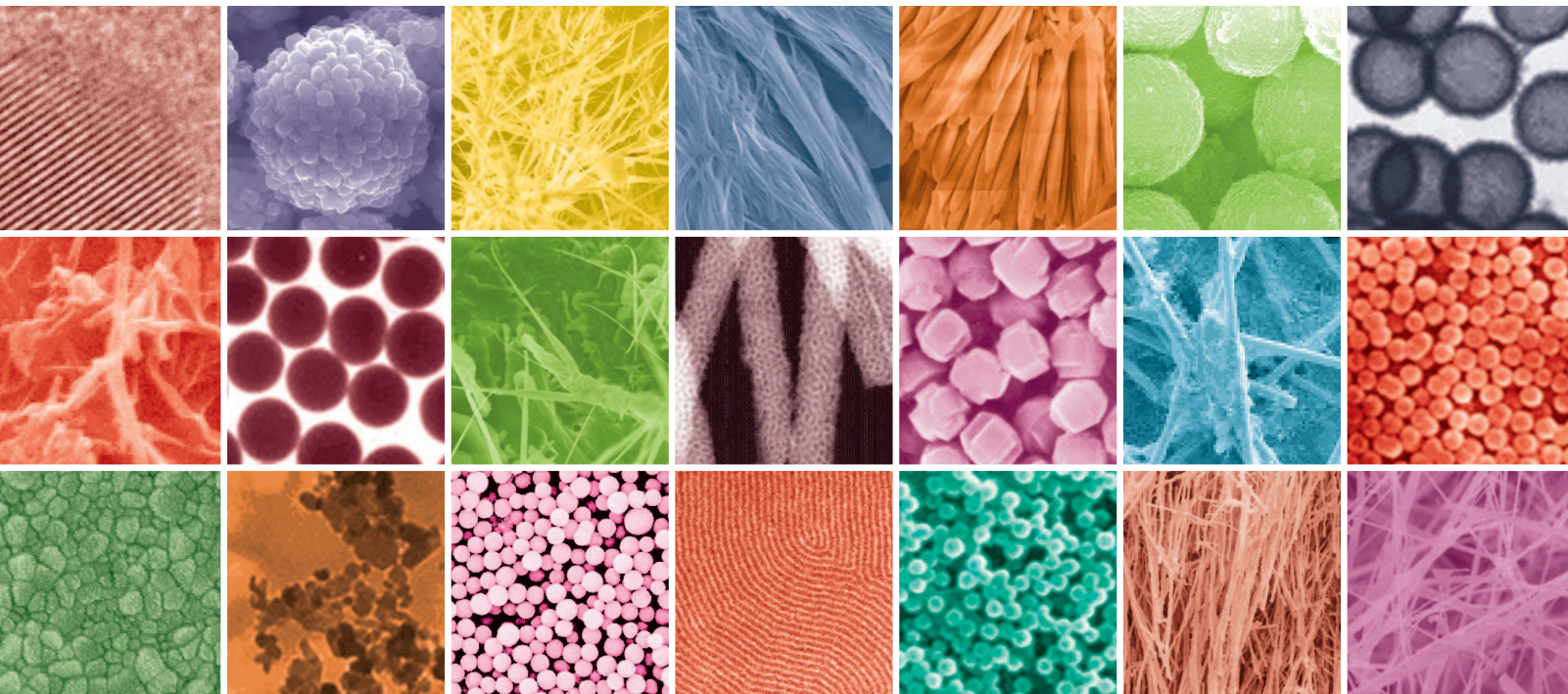


Nanoporous and Nanostructured Materials for Catalysis, Sensor, and Gas Separation Applications

Guest Editor: Songwei Lu





Nanoporous and Nanostructured Materials for Catalysis, Sensor, and Gas Separation Applications

Journal of Nanomaterials

**Nanoporous and Nanostructured Materials
for Catalysis, Sensor, and Gas Separation
Applications**

Guest Editor: Songwei Lu



Copyright © 2006 Hindawi Publishing Corporation. All rights reserved.

This is a special issue published in volume 2006 of "Journal of Nanomaterials." All articles are open access articles distributed under the Creative Commons Attribution License, which permits unrestricted use, distribution, and reproduction in any medium, provided the original work is properly cited.

Editor-in-Chief

Michael Z. Hu, Oak Ridge National Laboratory, USA

Advisory Board

James Adair, USA
Jeff Brinker, USA
Taeghwan Hyeon, South Korea

Nathan Lewis, USA
Alon McCormick, USA
Gary Messing, USA

Z. L. Wang, USA
Alan Weimer, USA
Jackie Ying, USA

Associate Editors

John Bartlett, Australia
Michael Harris, USA
Do Kyung Kim, South Korea

S. J. Liao, China
Jun Liu, USA
Sanjay Mathur, Germany

Michael S. Wong, USA
M. Yoshimura, Japan

Editorial Board

Donald A. Bansleben, USA
Siu Wai Chan, USA
Gang Chen, USA
Sang-Hee Cho, South Korea
Chunxiang Cui, China
Ali Eftekhari, Iran
Claude Estournes, France
Alan Fuchs, USA
Lian Gao, China
Hongchen Gu, China
Justin Holmes, Ireland

David Hui, USA
Alan Lau, Hong Kong
Butrand I., Lee USA
J. Li, Singapore
J. -Y. Liu, USA
Songwei Lu, USA
Ed Ma, USA
Pierre Panine, France
Donglu Shi, USA
Bohua Sun, South Africa
Xiaogong Wang, China

Y. Wang, USA
E. G. Wang, China
C. P. Wong, USA
Zhili Xiao, USA
Ping Xiao, UK
Nanping Xu, China
Doron Yadlovker, Israel
Zhenzhong Yang, China
Peidong Yang, USA
Kui Yu, Canada

Contents

Nanoporous and Nanostructured Materials for Catalysis, Sensor, and Gas Separation Applications,

Songwei Lu

Volume 2006, Article ID 48548, 2 pages

Ni Hollow Nanospheres: Preparation and Catalytic Activity, Kaifu Zhong, Pu Jin, and Qianwang Chen

Volume 2006, Article ID 37375, 7 pages

Visible Light Photocatalysis via CdS/TiO₂ Nanocomposite Materials, Sessa S. Srinivasan, Jeremy Wade, and Elias K. Stefanakos

Volume 2006, Article ID 87326, 7 pages

Fractal Dimension of Active-Site Models of Zeolite Catalysts, Francisco Torrens and Gloria Castellano

Volume 2006, Article ID 17052, 9 pages

Synthesis and Characterization of Photocatalytic TiO₂-ZnFe₂O₄ Nanoparticles, Sessa S. Srinivasan, Jeremy Wade, and Elias K. Stefanakos

Volume 2006, Article ID 45712, 4 pages

Photocatalytic Oxidation of a Volatile Organic Component of Acetaldehyde Using Titanium Oxide Nanotubes, Huifang Xu, Ganesh Vanamu, Ziming Nie, Hiromi Konishi, Rakesh Yeredla, Jonathan Phillips, and Yifeng Wang

Volume 2006, Article ID 78902, 8 pages

Porous and Nanoporous Semiconductors and Emerging Applications, Helmut Föll, Jürgen Carstensen, and Stefan Frey

Volume 2006, Article ID 91635, 10 pages

Atomic Layer Deposition for the Conformal Coating of Nanoporous Materials, Jeffrey W. Elam,

Guang Xiong, Catherine Y. Han, H. Hau Wang, James P. Birrell, Ulrich Welp, John N. Hryn, Michael J. Pellin, Theodore F. Baumann, John F. Poco, and Joe H. Satcher Jr.

Volume 2006, Article ID 64501, 5 pages

Size-Dependent Specific Surface Area of Nanoporous Film Assembled by Core-Shell Iron Nanoclusters,

Jiji Antony, Joseph Nutting, Donald R. Baer, Daniel Meyer, Amit Sharma, and You Qiang

Volume 2006, Article ID 54961, 4 pages

New Development in Nanoporous Composites: Novel Functional Materials for Capturing Nitrosamines in Airstreams, Ting Ting Zhuang, Jia Hui Xu, Jia Rong Xia, Yi Cao, Shi Lu Zhou, Ying Wang, Yuan Chun, and Jian Hua Zhu

Volume 2006, Article ID 54909, 9 pages

Synthesis and Characterization of Strontium Titanate Nanoparticles as Potential High Temperature Oxygen Sensor Material, Florian Voigts, Tanja Damjanović, Günter Borchardt, Christos Argirusis, and Wolfgang Maus-Friedrichs

Volume 2006, Article ID 63154, 6 pages

Ferromagnetic Nanostructures Incorporated in Quasi-One-Dimensional Porous Silicon Channels Suitable for Magnetic Sensor Applications, P. Granitzer, K. Rumpf, and H. Krenn

Volume 2006, Article ID 18125, 7 pages

Gas Sensors Based on Tin Oxide Nanoparticles Synthesized from a Mini-Arc Plasma Source, Ganhua Lu, Kyle L. Huebner, Leonidas E. Ocola, Marija Gajdardziska-Josifovska, and Junhong Chen

Volume 2006, Article ID 60828, 7 pages

Effect of Pressure on Synthesis of Pr-Doped Zirconia Powders Produced by Microwave-Driven Hydrothermal Reaction, A. Opalinska, C. Leonelli, W. Lojkowski, R. Pielaszek, E. Grzanka, T. Chudoba, H. Matysiak, T. Wejrzanowski, and K. J. Kurzydowski

Volume 2006, Article ID 98769, 8 pages

Epoxy-Carbazole Polymeric Network Nanolayers for Organic Light-Emitting Devices, Jin-Woo Park, Eung-Kyoo Lee, Myon Cheon Choi, Hwajeong Kim, Jihwan Keum, Chang-Sik Ha, and Youngkyoo Kim

Volume 2006, Article ID 46787, 8 pages

Incorporation of Vanadium Oxide in Silica Nanofiber Mats via Electrospinning and Sol-Gel Synthesis, Jeanne E. Panels and Yong Lak Joo

Volume 2006, Article ID 41327, 10 pages

Editorial

Nanoporous and Nanostructured Materials for Catalysis, Sensor, and Gas Separation Applications

Songwei Lu

Glass Technology Center, PPG Industries, Inc., Pittsburgh, PA 15238-0472, USA

Received 31 December 2006; Accepted 31 December 2006

Copyright © 2006 Songwei Lu. This is an open access article distributed under the Creative Commons Attribution License, which permits unrestricted use, distribution, and reproduction in any medium, provided the original work is properly cited.

Nanostructures in the form of thin films, nanoparticles, nanoporous materials, nanocomposites, and bulk nanocrystalline materials are of interest both for basic scientific research and technological applications as their properties are dominated by the extremely large specific surface areas. Such surfaces have generally unique properties which greatly differ from those of bulk materials, and which may even acquire characteristic size dependence at the nanometer scale. Because of the high surface-to-volume ratio, local phenomena, such as adsorption or changes in the surface electronic state, may contribute significantly to the overall properties of the materials. The detailed understanding of nanoporous materials and nanostructured materials defines challenges in basic science, not only in synthesis but also with respect to characterization and modeling, for instance, of surface-related properties. In addition, these nanomaterials have an immense potential for technological applications in chemical production, environmental control, photovoltaic and energy systems.

This special issue of Journal of Nanomaterials titled “Nanoporous and nanostructured materials for catalysis, sensor, and gas separation applications” is based in part on papers submitted to the Materials Research Society (MRS) 2005 Spring Meeting, Symposium R “Nanoporous and nanostructured materials for catalysis, sensor, and gas separation applications,” organized by Songwei Lu of PPG Industries, Inc., Horst Hahn of Technical University of Darmstadt, James Gole of Georgia Institute of Technology, and Jörg Weissmüller of Research Center Karlsruhe. The symposium was financially supported by the donors of the American Chemical Society Petroleum Research Fund and PPG Industries, Inc.

This special issue with a total of fifteen papers covers a wide range of topics related to nanoporous and nanostructured materials for catalysis and sensor applications, ranging

from basic to applied materials research and focusing on synthesis, functionalization, processing, characterization, and applications. Among fifteen papers, nine papers were presented in the Symposium R during the MRS 2005 Spring Meeting, and six papers are from open call for papers for the special issue. It divides into four sessions: nanostructured materials for catalysis and photocatalysis applications; nanoporous materials; nanostructured materials for sensor applications; and nanomaterials synthesis and other applications.

The first session includes five papers focusing on nanostructured materials for catalysis and photocatalysis applications. The first paper “Ni hollow nanospheres: preparation and catalytic activity” by Kaifu Zhong et al. demonstrates a method to prepare monodispersed silica nanospheres as templates for fabrication of nickel-silica composite hollow spheres, which display relative high activity and selectivity in acetone hydrogenation, showing potential applications as nanocatalysts. In “Fractal dimension of active-site models of zeolite catalysts,” F. Torrens and G. Castellano. calculated the active-site of zeolite catalysts and compared other calculation methods. While most of research focused on photocatalysis in UV region, Sesha S. Srinivasan et al. in their two papers explored the visible-light photocatalytic activities of $\text{TiO}_2\text{-ZnFe}_2\text{O}_4$ nanoparticles and CdS-TiO_2 nanocomposite materials. Huifang Xu et al. described synthesis and photocatalytic property of titania nanotubes in their paper “Photocatalytic oxidation of acetaldehyde using titanium oxide nanotubes.”

The second session with a topic of “nanoporous materials” includes four papers. Helmut Föll et al. in their paper “Porous and nanoporous semiconductors and emerging applications” briefly review pore formation, properties of porous semiconductors and emerging applications. The paper “Atomic layer deposition for the conformal coating of

nanoporous materials” by Jeffrey W. Elam et al. used atomic layer deposition (ALD) to apply precise, conformal coatings over nanoporous anodic aluminum oxide (AAO) membranes and silica aerogels, which may have a great promise as hydrogen sensors. In “Size-dependent specific surface area of nanoporous film assembled by core-shell iron nanoclusters,” Jiji Antony et al. presented synthesis and characterization of stable monodispersed iron-iron oxide core-shell nanoporous films, which may have applications in remediation and environmental treatments using their large surface area. In addition, T. T. Zhuang et al. described the capability of capturing volatile nitrosamines in airstreams using various modified zeolite in their paper titled “New development in nanoporous composites: novel functional materials for capturing nitrosamines in airstreams.”

The third session including three papers is “nanostructured materials for sensor applications.” Florian Voigts et al. reported a potential high-temperature oxygen sensor material using undoped and 1 at % Nb-doped strontium titanate nanoparticle films in their paper titled “Synthesis and characterization of strontium titanate nanoparticles as potential high-temperature oxygen sensor material.” The paper titled “Ferromagnetic nanostructures incorporated in quasi-one-dimensional porous silicon channels suitable for magnetic sensor applications” by Petra Granitzer et al. describes a novel fabrication method for porous silicon/Ni-nanocomposite system which exhibits a twofold switching behavior of the magnetization curve at two different field ranges, indicating a possible application as a high magnetic field sensor based on a silicon technology. In “Gas sensors based on tin oxide nanoparticles synthesized from a mini-arc plasma source,” Ganhua Lu et al. reported on the fabrication and characterization of a functional tin oxide nanoparticle gas sensor, exhibiting a fast response and a good sensitivity.

The last session “nanomaterials synthesis and other applications” includes three papers: “Effect of pressure on synthesis of Pr-doped zirconia powders produced by microwave-driven hydrothermal reaction” by Agnieszka Opalinska et al. describing a microwave hydrothermal synthesis of Pr-doped zirconia nanocrystals; “Epoxy-carbazole polymeric network nanolayers for organic light-emitting devices” by Jin-Woo Park et al. regarding organic light-emitting devices; and “Incorporation of vanadium oxide in silica nanofiber mats via electrospinning and sol-gel synthesis” by J. E. Panels and Y. L. Joo outlining a unique synthesis method for vanadium oxide-silica nanofibers.

Songwei Lu

Ni Hollow Nanospheres: Preparation and Catalytic Activity

Kaifu Zhong, Pu Jin, and Qianwang Chen

Hefei National Laboratory for Physical Science at Microscale, Department of Materials Science & Engineering, School of Chemistry and Materials, University of Science and Technology of China, Hefei 230026, China

Received 1 November 2005; Revised 18 April 2006; Accepted 4 May 2006

A method to prepare monodispersed silica nanospheres as templates for fabrication of nickel-silica composite hollow spheres is presented. The structures for both silica nanospheres and nickel-silica composite hollow spheres were characterized by X-ray diffraction (XRD), transmission electron microscopy (TEM), and scanning electron microscopy (SEM). The catalytic activity for acetone hydrogenation on nickel-silica composite hollow spheres was evaluated, and high conversion efficiency of 70% with good selectivity of 82.7% to 2-propanol was observed. The mechanism of high catalytic activity and good selectivity in acetone hydrogenation reaction was discussed.

Copyright © 2006 Kaifu Zhong et al. This is an open access article distributed under the Creative Commons Attribution License, which permits unrestricted use, distribution, and reproduction in any medium, provided the original work is properly cited.

1. INTRODUCTION

It is well known that properties of materials inherently associate with their morphologies and sizes. Shape and size of tunable materials are desirable for many applications, such as catalysis, medicine, electronics, ceramics, pigments, and cosmetics [1–6].

Recently, monodispersed nanospheres with the unique chemical and physical properties have attracted much attention. Specifically, silica nanospheres have been extensively studied, as they can be easily prepared and simply modified to dope selectively or attach functional groups. Recent researches on monodispersed silica nanospheres are expanding rapidly to assemble nanospheres in two-dimensional (2D) and three-dimensional (3D) ordered superstructures, such as preparation of photonic crystals [7]. A key requirement to successfully produce such spatially ordered structure is the preparation of highly monodispersed silica nanospheres. In addition, silica nanospheres have wide practical applications in labeling technology, [8] separation technologies [9], and biomedicine. For the purpose of achieving specific physical, chemical, or biological performance, monodispersed nanospheres are often used as templates to prepare core-shell nanostructures or hollow nanospheres. The common way to prepare hollow spheres is to encapsulate nanospheres such as silica or polystyrene spheres with nanocrystals, followed by removal of the templates by utilizing acid or base etching [10, 11].

In the previous work, we have reported a coating process to prepare nickel-silica composite hollow nanospheres

(650 nm in outer diameter) with controllable shell thickness in large-scale. The shell with porous structure consists of needle-like nickel nanoparticles with an average size of 15 nm [12]. It has been reported that particle dimension of metal catalyst strongly influences catalytic activity and selectivity [13]. In order to investigate the activity and selectivity of nickel-silica composite hollow nanospheres in heterogeneous catalysis reaction, we have performed acetone hydrogenation reaction using the as-prepared catalyst at temperatures ranging from 180 to 220°C, which exhibits good catalysis and high selectivity. In this paper, we further discuss the improvement of preparing monodispersed silica nanospheres and silica-nickel nanocomposite hollow spheres, the results of acetone hydrogenation, and its reaction and our explanation of the reaction mechanism.

2. EXPERIMENTAL

2.1. Preparation of monodispersed silica nanospheres

We have synthesized monodispersed silica nanospheres by tetraethyl orthosilicate (TEOS) hydrolysis as reported elsewhere [12]. The method to prepare silica nanospheres is not exactly the same as reported by Stobber et al. [14]. They used the gaseous ammonia saturated ethanol as solvent to control concentration of ammonia, while H₂O was added later. In our experiment, we chose aqueous ammonia solution as the source for ammonia and added TEOS solution dropwise into the aqueous ammonia. The main advantage of this method is to simplify the preparation of base reagent

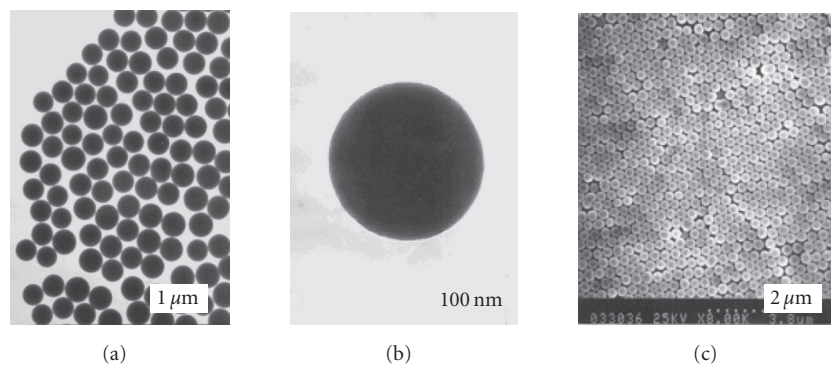


FIGURE 1: (a), (b) TEM images of bare silica nanospheres with a diameter of approximately 500 nm, (c) SEM image of monodispersed silica nanospheres, which is in good agreement with the observation of TEM.

(ammonia solution) and keep the same concentration of aqueous ammonia. The adverse factor is the extra addition of water, which has a great influence on the nucleation and growth of silica nanospheres. During the experiment, we also have investigated the influence of main reagents on preparation of monodispersed silica nanospheres by changing concentrations of ammonia and TEOS.

2.2. Preparation of $\text{SiO}_2/\text{Ni}_3\text{Si}_2\text{O}_5(\text{OH})_4$ core-shell structures and nickel-silica hollow spheres

The simple description of preparation of nickel-silica hollow spheres, the characterization of samples such as X-ray fluorescence analysis, dimethyl glyoxime gravimetric analysis, X-ray diffraction (XRD), transmission electron microscopy (TEM), scan electron microscopy (SEM), N_2 adsorption/desorption isotherm data, and pressure composition measurement (PCT) have been reported elsewhere [12]. Samples were analyzed by Shimadzu XRF-1800 (40 kv 95 mA) X-ray fluorescence spectrometer. XRD patterns were recorded using a Rigaku (Japan) D/max- γ A X-ray diffractometer equipped with graphite monochromatized Cu K-alpha radiation ($\lambda = 1.54178 \text{ \AA}$). SEM, TEM images, and electron diffraction (ED) were taken on Hitachi X-650 SEM and Hitachi H-800 TEM. Nitrogen adsorption isotherms of samples were measured by an ASAP 2010 volumetric sorption analyzer with an additional option for micropore analysis.

In this section, in order to find out the optimal way to prepare nickel-silica hollow spheres, we have investigated the influences of reaction order, morphology, and performance of samples through a series of controlled experiments. The process of coating nickel shells on silica templates was achieved by using homogeneous precipitation of slowly decomposing urea in nickel nitrate solution [12]. In order to better understand the reaction, we carried out the same reaction in the solution system without any silica nanosphere, at the same time we kept concentration of reagents, time, and temperature of reaction unchanged. The composition and phase of samples were analyzed by XRD. In addition,

we used commercial silica nanospheres on micron scale as templates to prepare core-shell nanostructures, characterized morphology, and relevant properties of final samples compared to that of using the as-prepared silica nanospheres.

2.3. Acetone hydrogenation on nickel-silica hollow nanospheres

Acetone hydrogenation at 100, 150, and 200°C with silica-supported Pd, nickel-silica composite hollow spheres, and Pd-precipitated composite hollow spheres was carried out [12]. Emphasis has been placed on selectivity of catalysts at 200°C and mechanism of acetone hydrogenation using nickel-silica hollow spheres.

3. RESULTS AND DISCUSSION

3.1. Synthesis of monodispersed silica nanospheres

As shown in Figures 1(a) and 1(b), silica nanospheres having uniform size and spherical morphology have been synthesized. Preferably monodispersed nanospheres with diameter of approximately 500 nm can be obtained through hydrolysis and polycondensation of TEOS. The direct SEM observation of the surface of silica nanosphere samples is shown in Figure 1(c), which is in good agreement with TEM images in Figures 1(a) and 1(b).

It has been suggested that ammonia as catalyst has an ability of controlling the morphology of silica nanospheres [14]. It is very important to keep constant concentration of ammonia in the overall process in order to synthesize monodispersed silica nanospheres. We studied the different sequences of adding reagents: adding ammonia dropwise into TEOS system or adding TEOS dropwise into ammonia system. Figure 2 shows SEM images of silica nanospheres obtained from choosing different sequences of adding reagents. The results showed that the first method was not as good as the second method to prepare monodispersed silica nanospheres. Two possible reasons might explain the phenomenon: one is that the first step of synthesizing silica

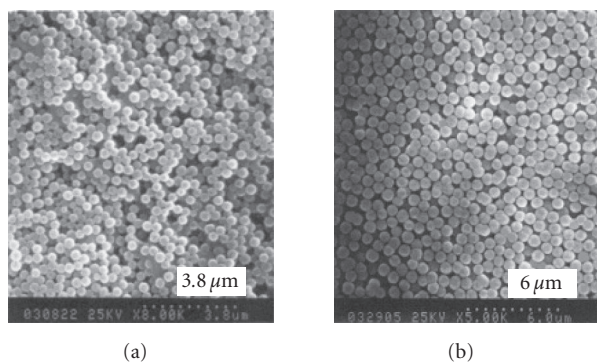


FIGURE 2: SEM images of silica nanospheres obtained from different sequences of adding reagents: (a) from adding ammonia dropwise into TEOS system; (b) from adding TEOS dropwise into ammonia system.

spheres is hydrolysis of TEOS. Adding ammonia into TEOS system inevitably brings some amount of water, which greatly affects the rate of TEOS hydrolysis, and finally results in the multidispersion of final particles. The other possible interpretation is ammonia's ability of controlling morphology of nanoparticles. In the first method, concentration of ammonia in the system ranges greatly at different stages of the reaction, resulting in different abilities of controlling the shape of silica nanoparticles. This leads to the appearance of the elliptical and other irregular shapes of silica nanoparticles. We also found that it is not easy to control the ratio of reagents, adjust the parameters to the optimal condition, and control the size and uniformity of particles when we choose the first method. At the same time, it is easy to gelate by forming silica network structure, and finally unable to obtain the regular shape of nanoparticles. In the second method, the variation of ammonia concentration is relatively low when adding TEOS into the system. Therefore, the second method is more preferable for synthesizing the monodispersed silica nanospheres.

In order to investigate the influence of reagent ratio, we used different concentrations of ammonia and TEOS. First, ammonia with a concentration of 1 mol/L was introduced to the TEOS system, which resulted in a very slow hydrolysis of TEOS. The solution system finally became an azury silica sol with irregular particles. When using high ammonia concentration of 25% and 28%, spherical silica particles were obtained. This indicated the critical catalytic effect of ammonia on hydrolysis of TEOS and controlling morphology of silica nanospheres. Second, we altered the concentration of TEOS while remaining other conditions unchanged. Figure 3 shows SEM images of silica nanospheres obtained from using different concentrations of TEOS in the reaction system of 20 ml. We observed that the size of silica nanospheres increase with increasing TEOS concentration. In addition, nonspherical particles became more and more with increasing TEOS concentration. The appearance of irregular silica particles could be explained by different growth rates of particles during the reaction.

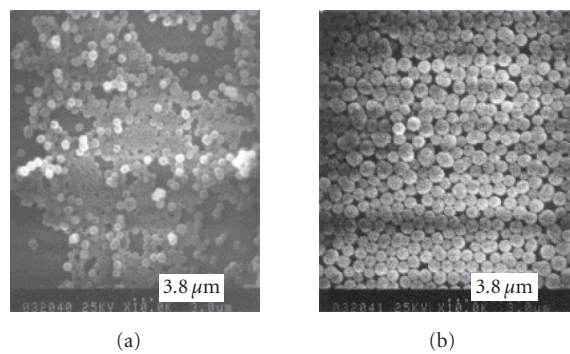


FIGURE 3: SEM images of silica nanospheres obtained from using different concentrations of TEOS, (a) 1.5 mL TEOS, (b) 3.0 mL TEOS.

3.2. Preparation of $\text{SiO}_2/\text{Ni}_3\text{Si}_2\text{O}_5(\text{OH})_4$ core-shell structures and nickel-silica hollow nanospheres

In the control experiment, XRD profile of samples obtained from decomposing urea in nickel nitrate solution without any silica nanosphere at a constant temperature of 95°C is given in Figure 4(a). XRD analysis indicates that the precipitate is poor crystalline hexagonal $\alpha\text{-3Ni}(\text{OH})_2 \cdot x\text{H}_2\text{O}$ (JCPDS no. 22-0444), with a growth orientation at (001). Figure 4(b) shows thermal decomposition result of the precipitates from 0 to 1000°C under ambient atmosphere. The weight loss (4%) at about 66°C may be attributed to the evaporation of adsorbed water. There is a weight loss of 24% at approximately 344°C which may be connected with decomposition of nickel hydroxide. XRD pattern of the heat-treated sample is given in Figure 5(a). All of detectable peaks are consisted with those of NiO phase. TEM results in Figure 5(b) indicated NiO nanocrystals with a length of 50 nm and a width of 10–25 nm. The appearance of partial diffraction spots in selected electron diffraction image (Figure 5(c)) indicated the improvement of NiO crystallinity. In order to further compare our experiment, we performed the reduction of NiO powders in H_2 atmosphere at high temperature. XRD analysis of the final samples confirmed cubic nickel particles, whose sharp peaks indicated further growth of NiO after high temperature treatment.

When we choose monodispersed silica nanospheres or commercial silica nanospheres as templates to synthesize nickel-silica hollow spheres, the process of reaction and properties of samples will alter greatly, which probably attributes to the mutual interaction between catalyst and silica templates [15]. Prokes et al. [16] pointed out that the concentration of SiOH groups on surface of silica particles can influence bonding of metal complexes to the surface, and the subsequent morphology of a created, decorated metal ion surface. Hereon, we mainly discuss the as-prepared silica templates' function in surface deposition and prosperities of final samples.

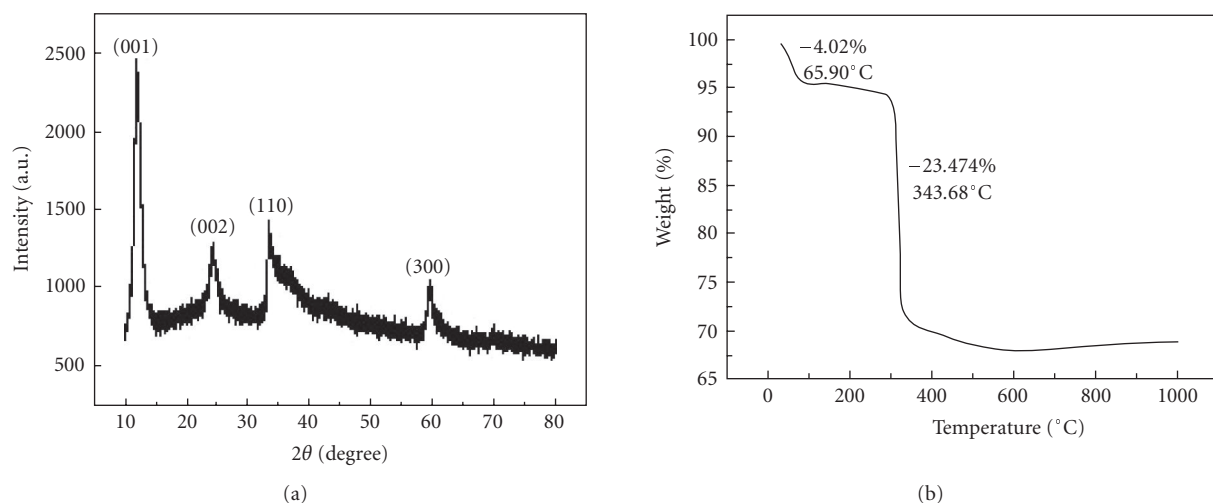


FIGURE 4: XRD profile (a) and thermogravimetric curve (b) of precipitates obtained from decomposing urea in nickel nitrate solution without any silica nanospheres.

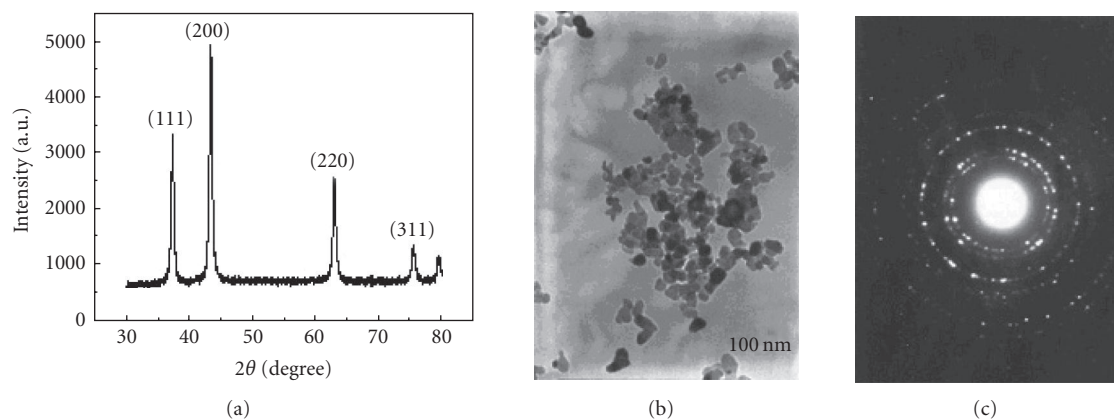


FIGURE 5: XRD pattern (a), TEM image (b), and selected electron diffraction pattern (c) of heat-treated samples prepared from $\text{Ni}(\text{OH})_2$.

We used the homogeneous precipitation [15] of slowly decomposing urea at above 70°C in nickel nitrate solution to coat sediments on the surface of silica. With the presence of silica spheres in the solution system, hydrosilicate will form through reaction between $\text{Ni}(\text{OH})_2$ and SiO_2 . The merit of selecting homogeneous precipitation is that nickel particles have an excellent colloidal dispersion which may influence the activity and selectivity of acetone hydrogenation. This preparation method also considerably affects the thermal stability of crystal particles, because sintering growth of crystal particles mainly depends on the initial-dimensional dispersion of crystals.

The as-prepared silica nanospheres in our experiment on nano-scale can easily react with nickel ion or $\text{Ni}(\text{OH})_2$ by precipitating on the surface of silica particles compared to commercial silica nanospheres on micron scale, due to the better solubility and higher concentration of hydroxyl groups on the surface of silica nanospheres. In the experiment, nucleation and deposition only occur on the surface

of silica nanospheres rather than in solution system based on the actual reaction phenomenon. First, if deposition takes place in solution system, final samples inevitably consist of the separate $\text{Ni}(\text{OH})_2$ sediments and the shells of $\text{Ni}(\text{OH})_2$ on surface of silica. However, under observation of electronic microscope, except the abundant core-shell particles, it does not contain any separate $\text{Ni}(\text{OH})_2$ particle with size of 25–50 nm, which appeared in the control experiment, the solo preparation of $\text{Ni}(\text{OH})_2$ without any silica nanosphere as discussed above. The possible explanation is that the continuous dissolved silica or hydroxyl groups on surface of nanospheres react with nickel ion eventually form indissoluble nickel hydrosilicate to adhere to the spherical particles. From TEM image (Figure 6), we can obviously observe the shell structure, which is accumulated by nanoparticles, totally different from the smooth surface of silica before coating. We also found that the shell with some thickness gradually separates from the sphere as a result of fuzz on the shell. The thickness of shell and the length of fuzz increase correspondingly with

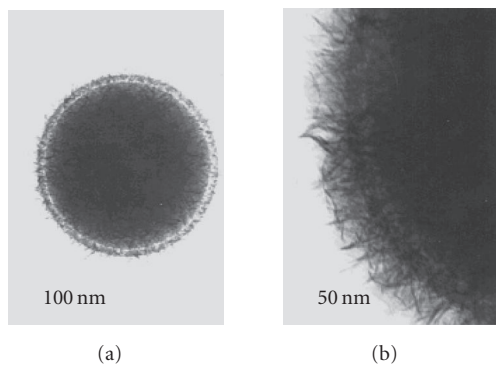


FIGURE 6: TEM photograph of silica/nickel hydrosilicate core-shell structure.

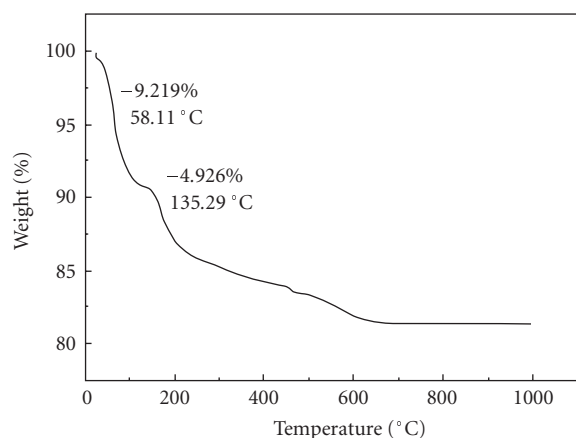


FIGURE 7: Thermogravimetric curve of silica/hydrosilicate core-shell particles.

the times of coating. In addition, the chemical composition of the shell structure is not a simple $\text{Ni}(\text{OH})_2$ but nickel hydrosilicate, XRD analysis of the heated composite core-shell spheres indicates no obvious physical structure alteration of the shell.

Figure 7 shows the thermal decomposition result of silica/hydrosilicate core-shell particles under ambient atmosphere. The weight loss of 9% at about 58°C and 5% at approximately 135°C may be associated to water desorption on silica. However, the decomposition of nickel hydroxide at 343°C is not obvious in Figure 8, probably because of the thermal stability of nickel hydrosilicate at this temperature.

Besides, the more important influence is that core-shell nanostructures using, the as-prepared silica nanospheres are less reducible, compared with simplex nickel hydroxide or commercial silica supported samples. We have carried out the deoxidization of silica/nickel hydrosilicate composite spheres through pure H_2 , which could not be completely reduced even at 550°C. However, after removing silica cores, the shells are easier to be reduced even at 450°C. The expla-

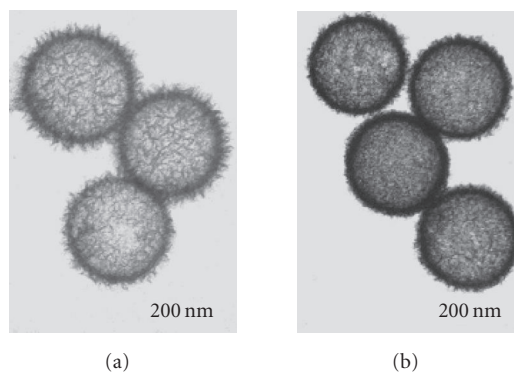


FIGURE 8: TEM images of nickel-silica hollow nanospheres (a) reduction after removing silica cores, (b) removing silica cores after reduction [12].

nation is that the low interaction between silica and nickel or nickel ion [12]. In order to weaken the interaction between shell and silica sphere, reduce the shell more completely and keep the porous surface, we prepared nickel-silica hollow spheres by removing cores before the process of deoxidization.

Our previous work [12] showed the distinctive morphology of nickel-silica hollow nanospheres through different sequences of reduction and etching (Figure 8). From Figure 8(a), we observe that preparing nickel-silica hollow nanospheres by reduction after removing silica cores reserves the fuzz structure of the shell and produces large specific surface area, which implies the potential application in gas heterogeneous catalysis. Compared to the former samples, the fuzz structure (Figure 8(b)) on the surface of nickel-silica hollow nanospheres prepared by removing silica cores after reduction has been destroyed, the shell also becomes denser. No matter the sequence of etching and reduction, both involved the process of etching silica cores. In order to keep the morphology of hollow spheres, we should control the concentration of base solution as shown in Figure 9(b), otherwise the shape of hollow sphere is distorted or broken up, even collapse as shown in Figure 9(a).

Consequently, considering the efficiency of reduction, the morphology, and property of samples, we should choose the way of preparing nickel-silica composite hollow spheres by removing silica cores before reduction.

3.3. Acetone hydrogenation using nickel-silica hollow nanospheres as catalyst

Recent works have been carried out on activity and selectivity of nickel-silica hollow nanospheres in acetone hydrogenation reaction with resultant samples typically 2-propanol, methyl isobutyl ketone (MIBK), methyl isobutyl carbinol (MIBC), and diisopropyl ether (DIPE). Unnikrishnan and Narayanan [17] have reported superior $\text{Ni}/\text{Al}_2\text{O}_3$, $\text{Co}/\text{Al}_2\text{O}_3$, and layered double hydroxides or hydrotalcite-like compounds such as NiMgAl , CoMgAl to prepare 2-propanol, and MIBK with high selectivity and conversion at a relatively

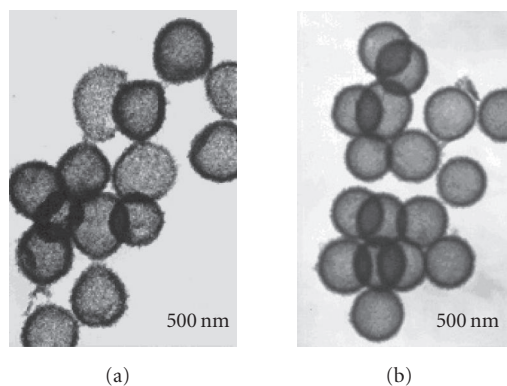


FIGURE 9: TEM images of samples from choosing different concentrations of NaOH to remove silica cores: (a) NaOH 5 mol/L; (b) NaOH 0.5 mol/L.

low temperature of 100°C. Even though Ir(0)_n nanoclusters plus HCl from Saim Özkar's recent work [18] can achieve selectivity of 95% to 2-propanol with nearly 100% acetone conversion at low temperature of 22°C, the main drawback is the limited catalytic lifetime due to nanocluster precipitation. While in our work, nickel-silica hollow nanospheres show relative high conversion of 70% and selectivity of 82.7% to 2-propanol and 13.8% to MBIK. Compared to the Gandia et al. [13] work using silica-supported nickel as catalyst at 200°C and atmosphere pressure, the major difference is higher acetone conversion, less selectivity to 2-propanol, and with some amount of MBIK samples in our catalyst system. The nickel-silica hollow nanospheres show lower selectivity to 2-propanol, mainly due to relatively high activity of this catalyst for the formation of MBIK associated with the special structure of catalyst.

4. EXPLANATION OF THE MECHANISM OF ACETONE HYDROGENATION REACTION IN OUR CATALYST SYSTEM

It has been reported that using pure nickel particles or bare silica spheres as catalyst to perform acetone hydrogenation cannot produce MBIK. Consequently, the synthesis of MBIK in nickel-silica hollow sphere catalyst system is likely performed on the layer between nickel and silica. Narayanan and Unnikrishnan [19] have pointed out that acetone conversion takes place both on metal sites and on acidic or basic sites of catalyst, but hydrogenation of acetone to 2-propanol over a metal site is more favorable than condensation of acetone over an acid-base site. In their researches on metal containing layered double hydroxides efficient catalyst, Unnikrishnan and Narayanan [17] indicated that the formation of MIBK or MIBC is attributed to the cooperative effect of both hydrogenating and acid-base properties of catalyst. Through detailed examination of Unnikrishnan's research, we found out that nickel-silica hollow sphere catalytic mechanism is very similar to what Unnikrishnan has pointed out. On the one hand, the relative high activity and conversion of hollow nanospheres in acetone hydrogenation can be explained by

the following factors. (1) Nickel-silica hollow nanospheres with high BET surface areas (288 m²/g) can absorb larger amount of H₂ than normal nickel particles [12]. In addition, the porous structure would be favorable for transportation of H₂ and make it likely stay in the inner part of hollow spheres to prolong the reaction time. (2) The shells are composed of acicular nanoparticles with an average size of 15 nm. For the structure-sensitive reaction, size of particles can greatly influence the selectivity and activity. Furthermore much larger amount of acetone can be absorbed on surface of nickel particles. There are two mechanisms to describe acetone absorption which both involve charge transfer, one is that π electrons are transferred from carbonyl group to free d orbital of the metal, and the other involves d electrons of nickel filling in the antibonding orbital of carbonyl group. As Rao et al. [20] pointed out, either way of charge transfer can weaken or break the bond of carbonyl group and make the reaction easier. Consequently, the unique porous structure with high capacities of H₂ and acetone absorption and low energy for acetone hydrogenation contributes to the high activation and conversion. On the other hand, nickel-silica hollow spheres contain a nickel-silica interface where electron deficient sites such as nickel ion resulting from the unreduced Ni(OH)₂ or nickel hydrosilicate [12]. At meantime, silica can act as base site to attract a methyl proton and Niⁿ⁺ can activate carbonyl group of acetone when O-atom of carbonyl coordinates to the Niⁿ⁺ site. As a result, absorbed methyl reacts with the neighboring coordinated carbonyl and neighboring H atoms absorbed on the metal sites to form MIBK and water.

Based on the fact that the main composition of nickel-silica hollow spheres is nickel metal, and hydrogenation of acetone to 2-propanol over a metal site is more favorable than condensation of acetone over an acid-base site as we discussed above, the acetone hydrogenation reaction shows the higher selectivity to 2-propanol and lower selectivity to MBIK and MBIC.

5. CONCLUSIONS

The above researches illustrate that monodispersed silica nanospheres can be used as templates for large-scale preparation of nickel-silica composite hollow spheres with an outer diameter of 650 nm and a thickness of 40 nm through encapsulating and etching. The nickel-silica hollow spheres display relative high activity and selectivity in acetone hydrogenation, showing potential applications as nanocatalysts. It is suggested that the unique porous structures with high capacities of H₂ and acetone absorption and lower energy for acetone hydrogenation contribute to the high activity and conversion. The synthesis process might be extended to prepare hollow nanospheres of other materials for catalytic application.

ACKNOWLEDGMENT

This work was supported by the Natural Science Foundation of China (20321101, 20125103, and 90206034).

REFERENCES

- [1] K. J. Klabunde, "Introduction to the nanoworld," in *Nanoscale Materials in Chemistry*, K. J. Klabunde, Ed., pp. 6–7, John Wiley & Sons, New York, NY, USA, 2001.
- [2] J. Parker, "Applications of nanocrystals," in *Nanoscale Materials in Chemistry*, K. J. Klabunde, Ed., pp. 280–285, John Wiley & Sons, New York, NY, USA, 2001.
- [3] W. E. Buhro and V. L. Colvin, "Semiconductor nanocrystals: shape matters," *Nat Mater*, vol. 2, no. 3, pp. 138–139, 2003.
- [4] E. Matijevic, "Controlled colloid formation," *Current Opinion in Colloid & Interface Science*, vol. 1, p. 176, 1996.
- [5] A. Polman and P. Wiltzius, "Materials science aspects of photonic crystals," *MRS Bulletin*, vol. 26, no. 8, pp. 608–610, 2001.
- [6] P. Jiang, J. Cizeron, J. F. Bertone, and V. L. Colvin, "Preparation of macroporous metal films from colloidal crystals," *Journal of the American Chemical Society*, vol. 121, no. 34, pp. 7957–7958, 1999.
- [7] W. Wang, B. Gu, L. Liang, and W. Hamilton, "Fabrication of two- and three-dimensional silica nanocolloidal particle arrays," *Journal of Physical Chemistry B*, vol. 107, no. 15, pp. 3400–3404, 2003.
- [8] K. R. Peters, G. Rutter, H. H. Gschwendner, and W. Haller, "Derivatized silica spheres as immunospecific markers for high resolution labeling in electron microscopy," *Journal of Cell Biology*, vol. 78, no. 2, pp. 309–318, 1978.
- [9] X. Q. Liu, J. M. Xing, Y. P. Guan, G. B. Shan, and H. Z. Liu, "Synthesis of amino-silane modified superparamagnetic silica supports and their use for protein immobilization," *Colloids and Surfaces A: Physicochemical and Engineering Aspects*, vol. 238, no. 1–3, pp. 127–131, 2004.
- [10] D. Wang, R. A. Caruso, and F. Caruso, "Synthesis of macroporous titania and inorganic composite materials from coated colloidal spheres—a novel route to tune pore morphology," *Chemistry of Materials*, vol. 13, no. 2, pp. 364–371, 2001.
- [11] K. M. Kulinowski, P. Jiang, H. Vaswani, and V. L. Colvin, "Porous metals from colloidal templates," *Advanced Materials*, vol. 12, no. 11, pp. 833–838, 2000.
- [12] P. Jin, Q. Chen, L. Q. Hao, R. F. Tian, L. X. Zhang, and L. Wang, "Synthesis and catalytic properties of nickel-silica composite hollow nanospheres," *Journal of Physical Chemistry B*, vol. 108, no. 20, pp. 6311–6314, 2004.
- [13] L. M. Gandia, A. Diaz, and M. Montes, "Selectivity in the high-temperature hydrogenation of acetone with silica-supported nickel and cobalt catalysts," *Journal of Catalysis*, vol. 157, no. 2, pp. 461–471, 1995.
- [14] W. Stobber, A. Fink, and E. Bohn, "Controlled growth of monodisperse silica spheres in the micron size range," *Journal of Colloid and Interface Science*, vol. 26, pp. 62–69, 1968.
- [15] J. T. Richardson and R. J. Dubus, "Preparation variables in nickel catalysts," *Journal of Catalysis*, vol. 54, no. 2, pp. 207–218, 1978.
- [16] S. M. Prokes, W. E. Carlos, L. Seals, S. Lewis, and J. L. Gole, "Formation of ferromagnetic Ni/SiO₂ nanospheres," *Materials Letters*, vol. 54, no. 1, pp. 85–88, 2002.
- [17] R. Unnikrishnan and S. Narayanan, "Metal containing layered double hydroxides as efficient catalyst precursors for the selective conversion of acetone," *Journal of Molecular Catalysis A: Chemical*, vol. 144, no. 1, pp. 173–179, 1999.
- [18] S. Özkar and R. G. Finke, "Iridium(0) nanocluster, acid-assisted catalysis of neat acetone hydrogenation at room temperature: exceptional activity, catalyst lifetime, and selectivity at complete conversion," *Journal of the American Chemical Society*, vol. 127, no. 13, pp. 4800–4808, 2005.
- [19] S. Narayanan and R. Unnikrishnan, "Selective hydrogenation of acetone to methyl isobutyl ketone (MIBK) over coprecipitated Ni/Al₂O₃ catalysts," *Applied Catalysis A: General*, vol. 145, no. 1–2, pp. 231–236, 1996.
- [20] R. S. Rao, A. B. Walters, and M. A. Vannice, "Influence of crystallite size on acetone hydrogenation over copper catalysts," *Journal of Physical Chemistry B*, vol. 109, no. 6, pp. 2086–2092, 2005.

Visible Light Photocatalysis via CdS/TiO₂ Nanocomposite Materials

Sesha S. Srinivasan, Jeremy Wade, and Elias K. Stefanakos

Clean Energy Research Center, College of Engineering, University of South Florida, Tampa, FL 33620, USA

Received 17 January 2006; Revised 8 August 2006; Accepted 9 August 2006

Nanostructured colloidal semiconductors with heterogeneous photocatalytic behavior have drawn considerable attention over the past few years. This is due to their large surface area, high redox potential of the photogenerated charge carriers, and selective reduction/oxidation of different classes of organic compounds. In the present paper, we have carried out a systematic synthesis of nanostructured CdS-TiO₂ via reverse micelle process. The structural and microstructural characterizations of the as-prepared CdS-TiO₂ nanocomposites are determined using XRD and SEM-EDS techniques. The visible light assisted photocatalytic performance is monitored by means of degradation of phenol in water suspension.

Copyright © 2006 Sesha S. Srinivasan et al. This is an open access article distributed under the Creative Commons Attribution License, which permits unrestricted use, distribution, and reproduction in any medium, provided the original work is properly cited.

1. INTRODUCTION

Anatase TiO₂ is the most widely used semiconductor photocatalyst for an effective decomposition of organic compounds in air and water under UV light irradiation, with wavelength shorter than 387 nm [1, 2]. The major problem is that only about 4% of the solar spectrum falls in this UV range. The efficient use of sunlight becomes an appealing challenge for developing photocatalysts [3–5]. One approach for achieving this objective is to sensitize TiO₂ by using a narrow band gap semiconductor with a higher conduction band than that of TiO₂. CdS with band gap energy of 2.5 eV is considered to be one of the many sensitizers used for large band gap semiconductors because of the ideal position of its conduction and valence band edges. CdS alone, however, shows negligible photocatalytic activity because of its instability and rapid electron-hole pair (EHP) recombination rates. Studies have proven that with the appropriate particle interaction, CdS-TiO₂ nanocomposites can efficiently decompose organics such as phenol and methylene blue under visible light irradiation less than 495 nm [6–8].

The reaction as shown in Figure 1 occurs when a CdS particle is excited by a photon with a wavelength less than 495 nm. An EHP is formed, and subsequently the photogenerated electron is quickly transferred to the conduction band of a coupled TiO₂ particle that has a conduction band edge more positive than the CdS particle (~ 0.5 eV). The photogenerated hole in the quantum-sized CdS particle can theoretically migrate to the surface and participate in the

oxidation of adsorbed organics. The electrons that are transferred to the conduction band of TiO₂ have no holes to recombine with and therefore participate in reduction reactions according to the conduction band energy level of TiO₂. In order to establish a quantum size effect, one must have to synthesize extremely small particles of the order of the excitonic diameter and to stabilize them against further growth. Reverse micelle process provides a controlled environment to achieve this goal.

Reverse micelles are thermodynamically stable structures which consist of a nanometer-sized spherical water core that is encapsulated by surfactant molecules in a nonpolar medium. They have been used to synthesize semiconductors, metals, and other inorganic crystallites [9–11]. Interparticle electron transfer between size quantized CdS and TiO₂ semiconductor nanoclusters for the photocatalysis and hydrogen production applications is reported in recent years [12–19].

In the present study, we have carried out the successful formulation of CdS-TiO₂ nanocomposite via reverse micelle process and studied their structural, microstructural, UV-Vis spectral characteristics and visible light photocatalytic behavior.

2. EXPERIMENTAL DETAILS

2.1. Materials and method

The chemicals used for the synthesis of CdS-TiO₂ nanocomposite are of the purest quality and are used as received:

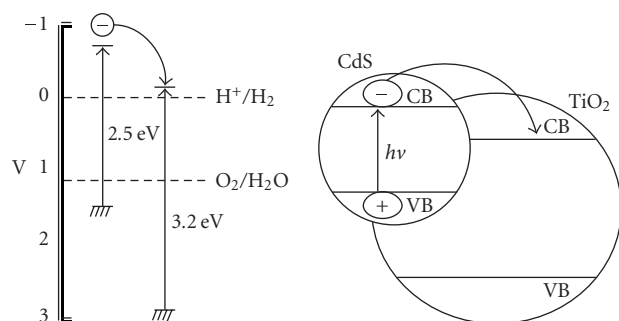


FIGURE 1: CdS-TiO₂ nanocomposite with band edge energy levels.

cadmium perchlorate hydrate ($\text{Cd}(\text{ClO}_4)_2 \cdot x\text{H}_2\text{O}$), titanium (IV) isopropoxide ($\text{Ti}(\text{OCH}_2\text{CH}_2\text{CH}_3)_4$), sodium sulfide (Na_2S), Aerosol-OT, solvents such as isooctane, 2-propanol, *n*-heptane are obtained from Sigma-Aldrich. Initially the reverse micelles are prepared by optimizing the surfactant to water mole ratio (w_0) in nonpolar medium (say, isooctane);

$$w_0 = [\text{AOT}]/[\text{H}_2\text{O}]. \quad (1)$$

In the next step, adding 1 M $\text{Cd}(\text{ClO}_4)_2 \cdot x\text{H}_2\text{O}$ to this reverse micelle to form microemulsion “A.” Similarly, the microemulsion “B” is formed by adding 0.1 M Na_2S to a separate reverse micelle solution. Mixing the microemulsions A and B with vigorous stirring at room temperature thus produces CdS yellowish microemulsion “C.” Another microemulsion “D” is formed by adding 1 M $\text{Ti}(\text{OPr})_4/2$ -propanol in separate reverse micelle and stirred continuously for 1 hour. The water to alkoxide ratio (h) have been varied and optimized for the TiO_2 precipitation,

$$h = [\text{H}_2\text{O}]/[\text{Ti}(\text{OPr})_4]. \quad (2)$$

The microemulsions of “C” and “D” are finally mixed and vigorously stirred to form CdS- x wt.% TiO_2 ($x = 5, 10, 50$). The CdS- TiO_2 precipitate obtained is then washed couple of times with DI water, ethanol, and acetone to remove the surfactant. The amorphous nanocomposite of CdS- TiO_2 is calcined at 500°C under the flow of N_2 for 3 hours.

2.2. Structural and microstructural characterization

The structural characterization for the phase identification and particle size analysis has been carried out using Philips X’pert pro powder X-ray diffractometer with $\text{CuK}\alpha$ radiation ($\lambda = 1.54060 \text{ \AA}$). The incident and diffraction slit width used for all the experiments are 1° and 2°, respectively, and the incident beam mask used corresponds to 10 mm. The XRD profile analysis and particle sizes have been calculated using PANalytical X’pert Highscore software version 1.0 e.

The microstructural characterizations such as surface morphology and chemical composition were performed using scanning electron microscope SEM (Hitachi S-800) both in imaging and EDS modes. Genesis software has been used to analyze the microstructures and elemental composition of the CdS- TiO_2 nanocomposites.

2.3. BET surface area measurements

Catalysts and photocatalysts are often characterized by their interaction with gases. At low temperatures, nonreactive gases (nitrogen, argon, krypton, etc.) are *physisorbed* by the surface. Through gas physisorption the total surface area of the sample can be calculated by the BET method. The Chem-BET 3000 from Quantachrome Instruments has been employed to determine the surface area and a pore size distribution of the pure TiO_2 , pure CdS, and CdS- TiO_2 nanocomposites. A known amount of sample ($\sim 100 \text{ mg}$) was placed in a glass tube and the sample was outgassed at 300°C for 5 hours. Multipoint BET method using nitrogen as the adsorbate gas, the isotherm has been measured at 77 K.

2.4. UV-Vis transmittance spectroscopy

The transmittance measurement is performed by UV-Vis spectrometer. The powder samples of pure TiO_2 and CdS- TiO_2 nanocomposite are made into slurry by dissolving it in (Acetylacetone + H_2O + Triton X-100) solution. Thus obtained slurry was spin coated at 4000 rpm on to the glass slide for UV-Vis spectrum studies. The homogeneous films obtained from spin coating samples were then subjected to UV-Vis spectroscopy measurements in transmittance and absorption modes using an Ocean Optics USB2000 fiber optic spectrometer.

2.5. Photocatalytic reactor testing

Photocatalytic experiments using visible light and a combination of UV-A and visible light were performed using a single lamp and an annular reflector to provide irradiation to all sides of the reaction vessel as shown in Figure 2. The immersion well was used as a means of concentrating the aqueous solution to the perimeter of the reaction vessel to optically optimize the system. A 1000 W metal halide lamp was experimentally chosen, since it adequately replicated both the pattern and intensity peaks of the solar spectrum more accurately than other visible sources such as high-pressure sodium and fluorescent lamps.

The metal halide spectrum, as shown in Figures 3(a) and 3(b), was found to contain sufficient UV-A radiation in the range of 350 nm–400 nm to serve as both a UV-A and visible light source. For photocatalytic experiments using visible light region, a longpass UV filter provided by Edmund Optics was used to cut off the wavelengths shorter than 400 nm, at a cost of approximately 8% attenuation at wavelengths greater than 400 nm. The system was cooled from 110°C to 70°C using ventilation provided by three fans inputting and removing air from the surface of the lamp and inside the reactor.

2.6. Phenol degradation by UV-Vis spectroscopy measurement

Photocatalytic phenol degradation experiments were conducted using the following procedure. A solution of deionized water, phenol, and the catalyst under test were mixed

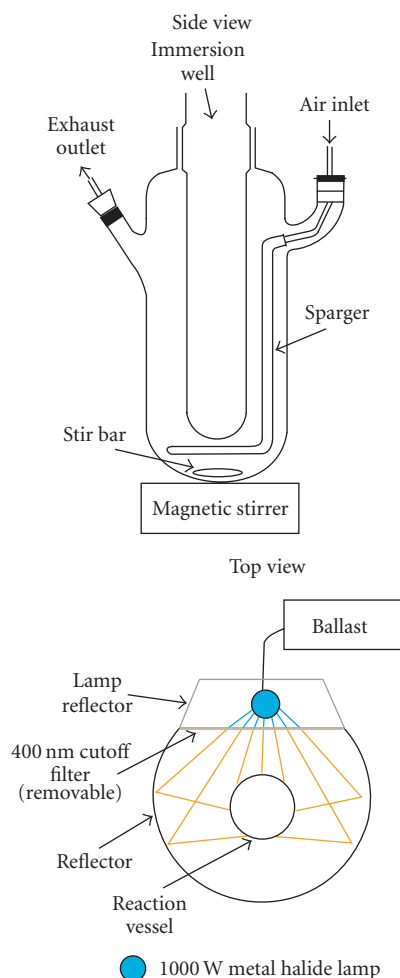


FIGURE 2: UV-Vis/visible light photocatalytic reactor used for phenol degradation studies.

using magnetic stirring, and air was injected to scavenge photogenerated electrons and also to help suspend the catalyst. The phenol concentration in all experiments was 40 ppm which was selected as a value large enough to accurately measure using absorption measurements and small enough to degrade within hours when exposed to an efficient photocatalyst. Air was dispersed in the aqueous solution through a 12-inch rod sparger and was used in place of pure O_2 to simulate real-world experimental conditions. Periodic 1.5 mL samples were retrieved from the reaction vessel in desired time increments and placed in Eppendorf microcentrifuge tubes for analysis of the photocatalytic degradation of phenol. The nanoparticle catalysts were separated from the phenol and water mixtures by centrifuging the Eppendorf tubes for 10 minutes at 4000 rpm and 3220 rcf using an Eppendorf 5810 R centrifuge. UV-Vis spectroscopy using an Ocean Optics USB2000 fiber optic spectrometer was used to analyze the degradation of phenol with respect to time by monitoring the intensity of the absorption peak of phenol located at 268.63 nm. Phenol degradation was determined with respect to its initial concentration, and therefore all degradation

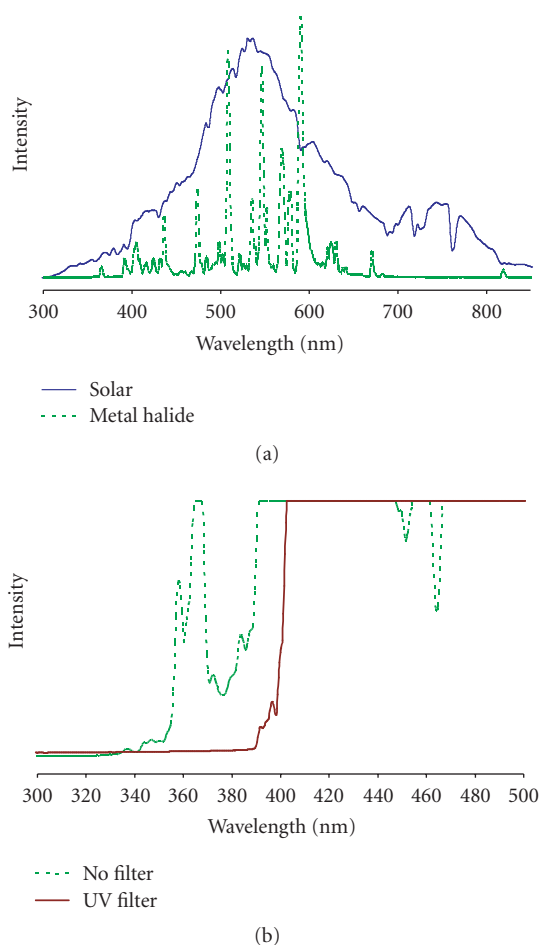


FIGURE 3: (a) UV-Vis metal halide spectrum compared to solar irradiation and (b) effects of UV-cutoff filter on metal halide irradiation pattern.

plots are normalized based on C/C_0 values which are interpreted as the concentration at the measured time divided by the initial concentration.

3. RESULTS AND DISCUSSION

3.1. Structural characterization

Figure 4 represents the X-ray diffraction patterns of (a) pure CdS nanoparticle (b) pure TiO_2 anatase and (c) CdS-50 wt.% TiO_2 nanocomposite prepared via reverse micelle process. No impurity peaks from the precursor ingredients such as cadmium perchlorate hydrate and sodium sulfide are observed for the pure TiO_2 and CdS as shown in Figures 4(a) and 4(b). However, for the CdS-50 wt.% TiO_2 nanocomposite, impurity peaks due to sodium perchlorate ($NaClO_4$) (see Figure 4(c)) are observed at the angle of orientations 22.4098° and 30.21111° . This may be due to the starting precursor reactions, which needs further filtration and purification. Also from these X-ray patterns, it is easily discernable that there exist two different grain sizes of the nanocomposite

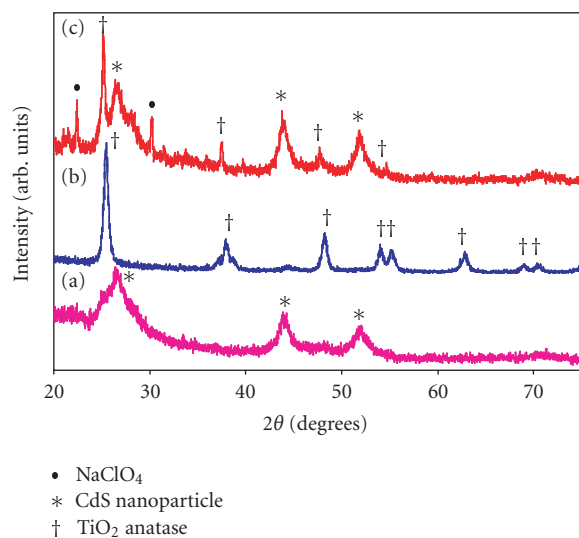


FIGURE 4: X-ray diffraction patterns of pure CdS, pure TiO₂ anatase, and CdS-50 wt.% TiO₂ nanocomposite prepared via reverse micelle process.

mixture due to CdS nanoparticle and TiO₂ anatase. We have calculated the average crystallite sizes from the X-ray diffraction patterns (Figure 4) according to Scherrer's equation and given in Table 1. The nanocomposite CdS-50 wt.% TiO₂ exhibits the larger crystallites when compared to either pure TiO₂ or pure CdS. This is due to high temperature (500°C) calcination involved after the composite formation in reverse micelle process.

3.2. Microstructural and chemical characterization

The microstructural characterization of the CdS-50 wt.% TiO₂ nanocomposite is carried out via scanning electron microscopy. Figures 5(a) and 5(b) show the SEM image and EDS spectrum of the CdS coupled TiO₂ nanocomposite structure. Reverse micelle process of preparing semiconductor nanocomposite yields homogeneous particles, thus improves the interparticle electron transfer from high-lying conduction band semiconductor with a small band gap (e.g., CdS ~ 2.5 eV) to low-lying conduction band semiconductor with a large band gap (e.g., TiO₂ ~ 3.2 eV). The EDS profile shows correct stoichiometry of CdS to TiO₂ in the nanocomposite structure. The atomic ratio of Cd and Ti in the nanocomposite structure was 3 at.% : 9 at.%, obtained from the SEM-EDS spectrum as shown in Figure 5(b).

The growth of intergrain boundaries between the CdS and TiO₂ nanostructures and the particle size varies with the experimental parameters such as water-to-surfactant ratio (w_0), water-to-alkoxide ratio (h), pH concentration of obtained solution, ratio of CdS to TiO₂ precursors, and calcination temperatures. The optimized parameters for the reverse micelle nanocomposite CdS-50 wt.% TiO₂ structure are given in Table 2. The standards for determining the optimizing conditions given in Table 2 are explained below.

The molar ratio of H₂O to surfactant AOT (w_0) was varied as 2, 4, 6, 8, and 10. The reverse micelle and gelation formation rates are highly controlled by varying this ratio. Rapid gelation with larger crystallites occurred during the higher molar ratio of water to surfactant, (e.g., $w_0 = 8, 10$) whereas slow gelations are due to the lower value of w_0 (e.g., 2, 4). An optimum value of [AOT]/[H₂O] = 6 was found and used for the further experiments. Similarly, the ratio of [H₂O]/[Ti-alkoxide] was optimized to obtain appropriate concentration of TiO₂. The acidic/basic nature of the reverse micelle CdS-TiO₂ is easily controlled by decreasing or increasing the pH value. The rapid precipitation effect was monitored and controlled by suitably adjusting the pH to 9. Thus obtained CdS-TiO₂ nanocomposite was then calcined at different temperatures under flowing N₂ atmosphere. Increasing the calcination temperature above 500°C, the appearance of rutile TiO₂ structure is inevitable and thus lowers the photocatalytic effect of CdS-TiO₂ nanocomposites. Calcination temperature below 500°C yields poor crystalline structure of CdS and TiO₂. Hence the optimum calcination temperature was found to be 500°C for rest of the experiments.

3.3. UV-Vis spectral response

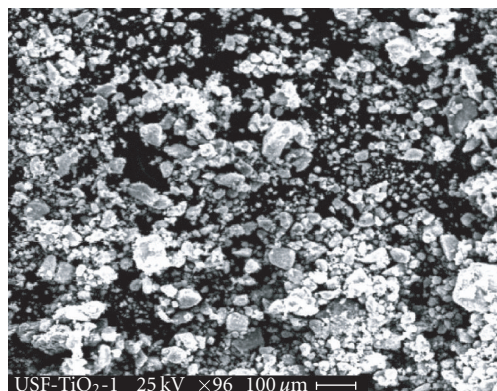
The UV-Vis transmittance spectral response for the pure TiO₂ and CdS-50 wt.% TiO₂ nanocomposite is shown in Figure 6. The onset of transmittance starts below 350 nm and a sharp transition occurred at around 380 nm for the pure TiO₂ anatase structure. Whereas for the case of CdS-50 wt.% TiO₂ nanocomposite prepared by reverse micelle process, the spectral curve extends to the visible light region with the onset value corresponding to 490 nm. The absorption edge of TiO₂ in CdS-TiO₂ nanocomposites observed above 400 nm indicates a significant "blue shift" of the bandgap energy compared to pristine TiO₂. The quantum-sized effect of CdS in the nanocomposite structure seems plausible explanation for this "blue shift" effect [20]. However, in the present study, the quantum CdS is not observed due to the coalescent or agglomeration of nanoparticles in the reverse micelle process. This may suggest that the nanocomposite coupled semiconductor (CdS-50 wt.% TiO₂) is expected to increase photogenerated charge carriers under the irradiation of visible light. It is noteworthy to mention that the absorption spectrum due to TiO₂ is not present in the CdS-TiO₂ nanocomposite films due to the different film thickness between TiO₂ and CdS nanoparticles. Besides, the concentration of TiO₂ also affects the optical absorption of CdS-TiO₂ nanocomposites in the UV range.

3.4. Photodegradation of phenol in water suspension

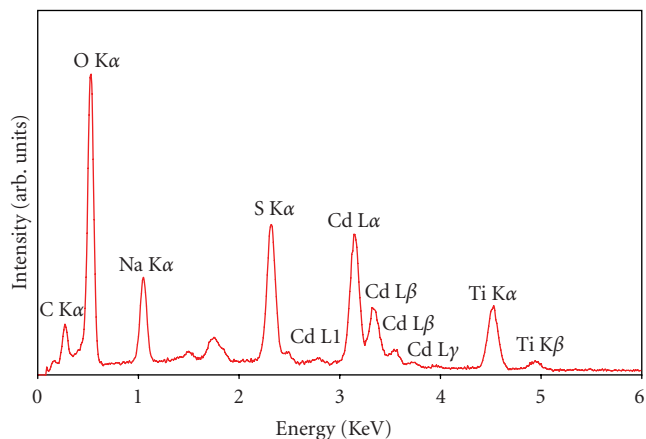
Photoactivity of the as-prepared CdS-Xwt.% TiO₂ nanocomposite materials is determined by the degradation of phenol in water suspension under visible light irradiation. Photocatalytic experiments using purely visible light, a long-pass UV filter provided by Edmund Optics was used to cut off the wavelengths below 400 nm. Phenol is chosen as a

TABLE 1: Average crystallite sizes of CdS, TiO₂ anatase, and CdS-50 wt.% TiO₂ nanocomposite.

No.	Photocatalyst material	Average crystallite size	Surface area, BET
(1)	Pure CdS (Figure 4(a))	11.9 nm	36 m ² /g
(2)	Pure TiO ₂ anatase (Figure 4(b))	37.9 nm	50 m ² /g
(3)	CdS-TiO ₂ nanocomposite (Figure 4(c))	CdS ~ 18.1 nm TiO ₂ ~ 59.9 nm	24 m ² /g



(a)



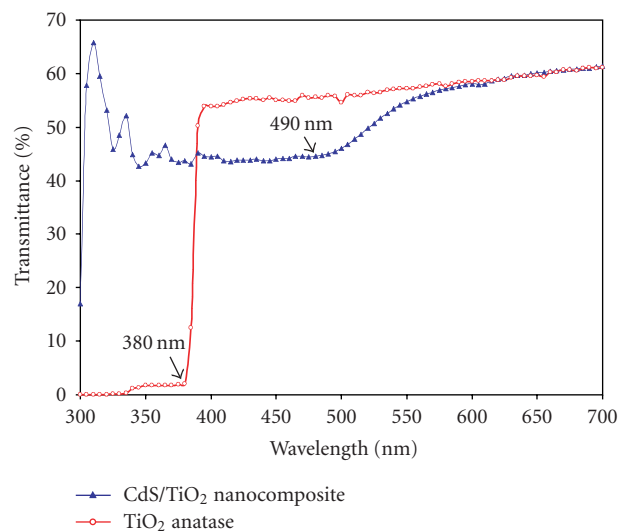
(b)

FIGURE 5: (a) SEM microstructure image of CdS-50 wt.% TiO₂ nanocomposite prepared via reverse micelle and (b) SEM-EDS spectrum of CdS-50 wt.% TiO₂ nanocomposite prepared via reverse micelle.TABLE 2: Experimental parameters for the optimized CdS-50 wt.% TiO₂ nanocomposite material.

No.	Experimental parameter	Optimized value
(1)	Water-to-surfactant ratio, w_0	6
(2)	Water-to-alkoxide precursor ratio, h	4
(3)	pH	9
(4)	Calcination temperature (N ₂ atmosphere)	500°C

test degradant for its photoactivity behavior. The primary reason is that phenol is an ideal degradant for visible light photocatalysis measurements because it absorbs only UV-C radiation with an absorption peak between 265 nm and 270 nm. This implies that it will not be susceptible to photolysis when irradiated by UV-A and visible light. Phenol is also a test degradant that exhibits application, since it is a common contaminant of industrial effluents. Photocatalytic oxidation of phenolic compounds in industry has been suggested to replace other processes such as activated carbon adsorption, chemical oxidation, biological treatment, wet oxidation, and ozonolysis [21]. A third reason phenol is used is that the photooxidation of phenolic compounds illuminated TiO₂ surfaces has been widely studied and the reaction kinetics are found to be first order following the well established Langmuir-Hinshelwood equation [22, 23].

The normalized phenolic concentrations (C/C_0) at regular intervals for the CdS-Xwt.% TiO₂ nanocomposite have been plotted in Figure 7.

FIGURE 6: UV-Vis spectral responses for pure TiO₂ and CdS-TiO₂ nanocomposite.

There is no direct correlation of rate of degradation and the CdS content was observed in the CdS-TiO₂ nanocomposite structure. However, the photodegradation of phenol concentration up to 40% is achieved in the CdS-50 wt.% TiO₂ nanocomposite material. Great efforts are presently being carried out to tailor the nanocomposite system by optimizing

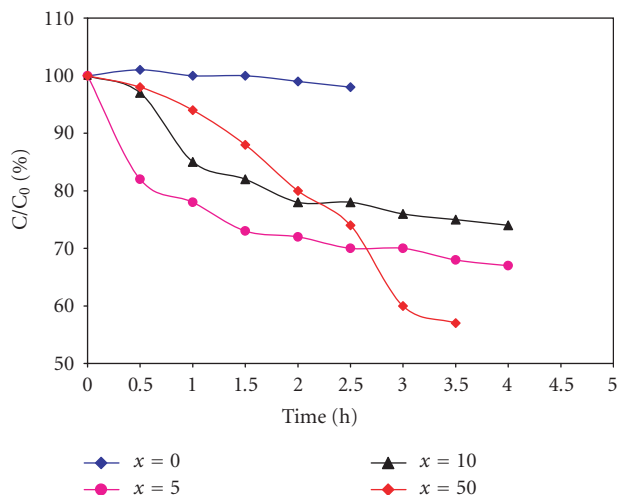


FIGURE 7: Phenol degradation of CdS-Xwt.% TiO₂.

the experimental conditions and solve the corrosion behavior of CdS for the effective photoactivity under visible light irradiations. We will also attempt to synthesize these systems by mechanochemical process employing high energy planetary milling and the results will be forthcoming.

4. CONCLUSIONS

We have systematically carried out the synthesis of pure TiO₂, pure CdS and CdS coupled TiO₂ nanocomposite by employing reverse micelle process. The X-ray phase analysis of these systems shows evidence for the formation of heterojunction CdS-Xwt.% TiO₂ nanocomposite structure with average crystallite sizes ranging from 18 nm to 60 nm. The microstructural investigation of the nanocomposite envisages the correct stoichiometry of CdS to TiO₂ and homogeneous surface morphology. The surface-coated CdS and TiO₂ anatase nanocomposite extends the absorption band edge in the visible region as observed from the UV-Vis measurements. The as-synthesized nanocomposite materials exhibit better photoactivity under visible light irradiation than that of pure TiO₂.

ACKNOWLEDGMENTS

Authors wish to thank the Nanomaterials and Nanomanufacturing Research Center at University of South Florida for extensive use of X-ray diffraction and SEM facilities. Financial support from DOE and Center for Biological Defense are gratefully acknowledged.

REFERENCES

- [1] N. Serpone and E. Pelizzetti, *Photocatalysis: Fundamentals and Applications*, John Wiley & Sons, New York, NY, USA, 1989.
- [2] M. A. Fox and M. T. Dulay, "Heterogeneous photocatalysis," *Chemical Reviews*, vol. 93, no. 1, pp. 341–357, 1993.
- [3] R. Asahi, T. Morikawa, T. Ohwaki, K. Aoki, and Y. Taga, "Visible-light photocatalysis in nitrogen-doped titanium oxides," *Science*, vol. 293, no. 5528, pp. 269–271, 2001.
- [4] M. R. Hoffmann, S. T. Martin, W. Choi, and D. W. Bahnemann, "Environmental applications of semiconductor photocatalysis," *Chemical Reviews*, vol. 95, no. 1, pp. 69–96, 1995.
- [5] S. Yin and T. Sato, "Synthesis and photocatalytic properties of fibrous titania prepared from protonic layered tetratitanate precursor in supercritical alcohols," *Industrial and Engineering Chemistry Research*, vol. 39, no. 12, pp. 4526–4530, 2000.
- [6] W. Chengyu, S. Huamei, T. Ying, Y. Tongsoo, and Z. Guowu, "Properties and morphology of CdS compounded TiO₂ visible-light photocatalytic nanofilms coated on glass surface," *Separation and Purification Technology*, vol. 32, no. 1–3, pp. 357–362, 2003.
- [7] A. Kumar and A. K. Jain, "Photophysics and photochemistry of colloidal CdS-TiO₂ coupled semiconductors—photocatalytic oxidation of indole," *Journal of Molecular Catalysis A: Chemical*, vol. 165, no. 1–2, pp. 265–273, 2001.
- [8] K. R. Gopidas, M. Bohorquez, and P. V. Kamat, "Photophysical and photochemical aspects of coupled semiconductors: charge-transfer processes in colloidal cadmium sulfide-titania and cadmium sulfide-silver(I) iodide systems," *The Journal of Physical Chemistry*, vol. 94, no. 16, pp. 6435–6440, 1990.
- [9] P. Lianos and J. K. Thomas, "Cadmium sulfide of small dimensions produced in inverted micelles," *Chemical Physics Letters*, vol. 125, no. 3, pp. 299–302, 1986.
- [10] M. L. Steigerwald, A. P. Alivisatos, J. M. Gibson, et al., "Surface derivatization and isolation of semiconductor cluster molecules," *Journal of the American Chemical Society*, vol. 110, no. 10, pp. 3046–3050, 1988.
- [11] V. Arcoletto and V. Turco Liveri, "AFM investigation of gold nanoparticles synthesized in water/AOT/n-heptane microemulsions," *Chemical Physics Letters*, vol. 258, no. 1–2, pp. 223–227, 1996.
- [12] P. A. Sant and P. V. Kamat, "Interparticle electron transfer between size-quantized CdS and TiO₂ semiconductor nanoclusters," *Physical Chemistry Chemical Physics*, vol. 4, no. 2, pp. 198–203, 2002.
- [13] J. C. Yu, L. Wu, J. Lin, P. Li, and Q. Li, "Microemulsion-mediated solvothermal synthesis of nanosized CdS-sensitized TiO₂ crystalline photocatalyst," *Chemical Communications*, vol. 9, no. 13, pp. 1552–1553, 2003.
- [14] Y. Bessekhouad, D. Robert, and J. V. Weber, "Bi₂S₃/TiO₂ and CdS/TiO₂ heterojunctions as an available configuration for photocatalytic degradation of organic pollutant," *Journal of Photochemistry and Photobiology A: Chemistry*, vol. 163, no. 3, pp. 569–580, 2004.
- [15] E. Hao, B. Yang, J. Zhang, X. Zhang, J. Sun, and J. Shen, "Assembly of alternating TiO₂/CdS nanoparticle composite films," *Journal of Materials Chemistry*, vol. 8, no. 6, pp. 1327–1328, 1998.
- [16] M. G. Kang, H.-E. Han, and K.-J. Kim, "Enhanced photodecomposition of 4-chlorophenol in aqueous solution by deposition of CdS on TiO₂," *Journal of Photochemistry and Photobiology A: Chemistry*, vol. 125, no. 1–3, pp. 119–125, 1999.
- [17] J.-S. Hu, Y.-G. Qu, H.-P. Liang, L.-J. Wan, C.-L. Bai, and Y.-G. Wang, "Interface assembly synthesis of inorganic composite hollow spheres," *Journal of Physical Chemistry B*, vol. 108, no. 28, pp. 9734–9738, 2004.
- [18] S. V. Tambwekar, D. Venugopal, and M. Subrahmanyam, "H₂ production of (CdS-ZnS)-TiO₂ supported photocatalytic system," *International Journal of Hydrogen Energy*, vol. 24, no. 10, pp. 957–963, 1999.

- [19] W.-W. So, K.-J. Kim, and S.-J. Moon, "Photo-production of hydrogen over the CdS-TiO₂ nano-composite particulate films treated with TiCl₄," *International Journal of Hydrogen Energy*, vol. 29, no. 3, pp. 229–234, 2004.
- [20] H. Fujii, K. Inata, M. Ohtaki, K. Eguchi, and H. Arai, "Synthesis of TiO₂/CdS nanocomposite via TiO₂ coating on CdS nanoparticles by compartmentalized hydrolysis of Ti alkoxide," *Journal of Materials Science*, vol. 36, no. 2, pp. 527–532, 2001.
- [21] Ö. E. Kartal, M. Erol, and H. Oğuz, "Photocatalytic destruction of phenol by TiO₂ powders," *Chemical Engineering and Technology*, vol. 24, no. 6, pp. 645–649, 2001.
- [22] G. W. Robertson and C. N. Satterfield, "Effectiveness factor for porous catalysts. Langmuir-hinshelwood kinetic expressions," *Industrial & Engineering Chemistry Fundamentals*, vol. 4, no. 3, pp. 288–293, 1965.
- [23] G. W. Robertson and C. N. Satterfield, "Effectiveness factor for porous catalysts. Langmuir-hinshelwood kinetic expressions for bimolecular surface reactions," *Industrial & Engineering Chemistry Fundamentals*, vol. 5, no. 3, pp. 317–325, 1966.

Fractal Dimension of Active-Site Models of Zeolite Catalysts

Francisco Torrens¹ and Gloria Castellano^{2,3}

¹*Institut Universitari de Ciència Molecular, Universitat de València, Edifici d'Instituts de Paterna, P.O. Box 22085, 46071 València, Spain*

²*Departamento de Química, Universidad Politécnica de Valencia, Camino de Vera s/n, 46022 València, Spain*

³*Departamento de Ciencias Experimentales, Facultad de Ciencias Experimentales, Universidad Católica de Valencia San Vicente Mártir, Guillem de Castro 94, 46003 València, Spain*

Received 20 March 2006; Revised 31 May 2006; Accepted 9 June 2006

A method for the calculation of *fractal* surfaces of crystals is presented. The *fractal dimension* D of fragments of zeolites is calculated. Results compare well with reference calculations (GEPOL). The active site of Brønsted acid zeolites is modeled by a set of Al–OH–Si units. These units form 2–12-membered rings. Topological indices for the different active-site models are calculated. The comparison between GEPOL and SURMO2 allows calculating the active-site indices. Most cavities show no fractal character, while for the 6–8-unit rings, D lies in the range 4.0–4.3. The 6-ring shows the greatest D and is expected to be the most reactive.

Copyright © 2006 F. Torrens and G. Castellano. This is an open access article distributed under the Creative Commons Attribution License, which permits unrestricted use, distribution, and reproduction in any medium, provided the original work is properly cited.

1. INTRODUCTION

Zeolites provided an example of the fruitful symbiosis between mineralogists, structural crystallographers, inorganic chemists, and materials scientists. Joint professorships of chemistry and mineralogy were typical in the US during the early 19th century, and mineralogists were listed as one of the six subcategories of chemists in 1870. Many zeolites were first described as minerals, as well as the chemical substitutions in the frameworks of synthetic zeolites, and the new related microporous aluminophosphate-based materials were known earlier in the feldspar and feldspathoid groups of minerals. The mathematical concepts used to describe the topology of frameworks in zeolites developed from ones known to Greek philosophers, as well as ones used to such stunning effect in Romanesque and Islamic decorations. In the 20th century, development of crystallographic and spectroscopic techniques led to spectacular discoveries about the topochemistry of zeolites. Deliberate control of crystallization processes produced many materials not known in nature. Controlled chemical and physical treatments were used to tailor valuable new products for industry, for example, shape-selective molecular-sieve catalysts. Aluminosilicate zeolites play an increasingly important technological role in the petroleum and petrochemical industries. The properties of zeolites that are exploited in their use as catalysts, sorbents, or ionexchangers reflect particular structural char-

acteristics. A detailed knowledge of structure is a prerequisite for understanding zeolite performance. Zeolite structural characterization is hampered by the complexity of zeolite structures, their relatively unfavourable X-ray scattering characteristics, and general unavailability as suitably large single crystals. Problems of phase purity, homogeneity, intergrowths, or stacking disorder are relatively common, preventing the application of traditional methods for structure elucidation; for example, zeolite beta is a near extreme of such stacking disorder.

The catalytic properties of zeolites were determined by the framework composition of the zeolite [1]. Alteration of the Si/Al ratio led to dramatic variations in the catalytic activity and stability of the zeolite framework [2]. It was possible to isomorphously substitute certain elements into the framework tetrahedral positions of zeolites [3]. Isomorphously substituted zeolites showed large variations in the polarity and acidity of the framework, and they became also important means by which to tailor zeolites to suit particular catalytic needs. *Ab initio* molecular-orbital calculations were used to predict structural and acidic properties of zeolites [4, 5]. By using model-cluster units to represent a portion of the framework surrounding a particular active site, the fundamental difference in acidity between a bridged Al hydroxyl (–OH) and a free or terminal –OH was predicted. B [6], Ga, and Ge isomorphously substituted forms were included, with the B and Ga forms corresponding to

isomorphous substitution of Al, as well as the Ge form representing substitution of Si [7]. The calculated acidic characteristics were in good agreement with experiment. The use of zeolites as acidic catalysts raised interest in the structure and properties of their active sites [8, 9]. The sources of Brønsted acidity in zeolites are bridged $-\text{OH}$ s, which arise from the presence of Al or T^{III} atoms replacing Si in their structure [10]. The use of nanomaterials with defined structure and properties allows building solid architectures with a precise control at several scales. Zeolites are ideal precursors for building multifunctional hierarchical solids, due to their (1) crystal structure, (2) chemical and thermal stabilities, (3) acidic, interchange, and molecular-sieve properties, (4) low cost, as well as (5) structural and chemical varieties. Some applications are the preparations of (1) advanced zeolites and zeotypes from conventional zeolites via hydrothermal treatment, (2) mesoporous crystal structures of zeolitic walls and their molecular sieve and catalytic properties in the cracking of voluminous hydrocarbons, as well as (3) hierarchical mesoporous silicas from cell-membrane phospholipids and resolutions of these new nanostructures.

In earlier publications, the fractal dimension of different structural-type zeolites was calculated [11]. Correlation models were obtained between the fractal dimension and some topological indices. Some Brønsted-acid models were proposed [12]. The smallest unit $\text{SiH}_3-\text{OH}-\text{AlH}_3$ represented a bridged $-\text{OH}$, and the remaining models closed rings consisting of $\text{SiH}_2-\text{OH}-\text{AlH}_2-$ units. An analysis of the geometric and topological indices for the active-site models was performed [13]. The aim of the present report is to perform a comparative study of the properties of a set of Brønsted-acid models representative of Si–Al zeolites and to distinguish a particular ring that suggests the greatest reactivity. The smallest investigated unit $\text{SiH}_3-\text{OH}-\text{AlH}_3$ is taken to represent a bridged $-\text{OH}$. The remaining active-site models are built by closing rings consisting of 2–12 $-\text{SiH}_2-\text{OH}-\text{AlH}_2-$ units. In the next section, the geometric descriptors and topological indices are described. Following that, the results for the descriptors and indices of different active-site models of zeolites are presented and discussed. The last section summarizes the conclusions.

2. GEOMETRIC DESCRIPTORS AND TOPOLOGICAL INDICES

In our program TOPO for the theoretical simulation of the shape of crystal fragments [14], their surface is represented by the external surface of a set of overlapping spheres with appropriate radii, centred on the atomic nuclei [15]. The fragment is treated as a solid in space, defined by tracing spheres around the atomic nuclei. It is computationally enclosed in a graduated rectangular box, and the geometric descriptors evaluated by counting points within the solid or close to chosen surfaces. The fragment volume V , surface area S , and two topological indices of fragment shape can be calculated. Consider S_e as the surface area of a sphere whose volume is equal to the fragment volume V [16]. The ratio $G = S_e/S$ is interpreted as a descriptor of fragment

globularity. The ratio $G' = S/V$ is interpreted as a descriptor of fragment rugosity.

The properties of the systems solvated in water are strongly related to the contact surface between solute and water molecules. Starting from this fact, another molecular geometric descriptor was proposed: the *solvent-accessible surface area* AS [17]. The AS is defined by means of a probe sphere, which is allowed to roll on the outside while maintaining contact with the *bare* molecular surface [18]. The AS can be calculated in the same way as the bare molecular surface area by means of pseudoatoms, whose van der Waals radii [19] have been increased by the probe radius R [20]. The *accessibility* is a dimensionless quantity varying between 0 and 1, and it also represents the ratio of the solvent-accessible surface area in a particular structure to the solvent-accessible surface area of the same atom when isolated from the molecule. The *fractal dimension* D of the molecules may be obtained as $D = 2 - d(\log \text{AS})/d(\log R)$ [21]. The fractal dimension D provides a quantitative indication of the degree-of-surface accessibility towards different solvents [22]. TOPO allows an atom-to-atom analysis of D on each atom i , to obtain an atomic dimension index D_i from the atomic contributions to the accessible surface area AS_i . The D_i can be weight-averaged to obtain a new molecular dimension index $D' = (\sum_i \text{AS}_i D_i)/\text{AS}$, where the AS_i are used as weights for the D_i . Note that if an $\text{AS}_i = 0$ for any probe, D_i cannot be calculated for atom i , and so, this atom does not contribute to D' . Thus, D' represents a D averaged for atoms *nonburied* (accessible) to any of the solvent-accessible surfaces in the range of probe spheres. In particular, $D' = D$ for systems without buried atoms, for example, inert gases, C_{60} , and so forth.

A version of TOPO has been implemented in our versions of programs AMYR [23], GEPOL [24], and SURMO2 [25]. AMYR carries out the theoretical simulation of molecular associations and chemical reactions. GEPOL performs an accurate triangular tessellation of the molecular surface and is used for reference calculations. Both TOPO and GEPOL recognize the cavities in inclusion molecules and are adequate to study intercalation compounds. On the other hand, SURMO2 does not recognize cavities. Furthermore, the combination of SURMO2 and GEPOL results allows the characterization of the molecular surface of internal cavities. Our version of SURMO2 has been corrected for the deviation from the spherical shape, by dividing each point contribution by the cosine of the angle formed by the semiaxis and the corresponding normal vector to the surface at this point. The volume and surfaces of crystal fragments with cavities have been corrected by maximizing, in each angular orientation, the distance of the most distant atom in each semiaxis.

3. CALCULATION RESULTS AND DISCUSSION

The following zeolites of different structural types have been studied, namely faujasite, ZSM-11, ZSM-5, mordenite, sodalite, and beta-A. The topological indices calculated for the zeolite crystals are reported (cf. Table 1), including two fragments of faujasite (I and II) with different number of atoms. The faujasite, ZSM-11, ZSM-5, and beta-A structures

TABLE 1: Topological indices for zeolites.

Zeolite	D^a	D'^b	Framework density F_d^c	Type of rings: R_{\max}	Type of access	G^d	G'^e
Faujasite-I	1.866	2.317	12.7	12	3	0.326	0.838
Faujasite-II	1.912	2.193	12.7	12	3	0.295	0.864
ZSM-11	1.962	2.315	17.7	10	3	0.300	0.851
ZSM-5	2.026	2.174	17.9	10	3	0.295	0.867
Mordenite	1.961	2.058	17.2	12	2	0.317	0.882
Sodalite	2.149	2.311	17.2	6	3	0.225	0.934
Beta-A	1.981	2.215	15.1	12	3	0.276	0.825

^aFractal dimension of the solvent-accessible surface.

^bFractal dimension of the solvent-accessible surface averaged for nonburied atoms.

^cThe framework density is expressed as the number of T sites per 1000 \AA^3 .

^dFragment globularity.

^eFragment rugosity (\AA^{-1}).

TABLE 2: Geometric descriptors and topological indices for zeolite fragments.

Zeolite	V^a	S^b	AS^c	HBAS ^d	HLAS ^e	AS'^f	G^g	G'^h
Faujasite-I	5536	4639	4163	1258	2905	4742	0.326	0.838
Faujasite-II	6844	5910	5954	3986	1968	6513	0.295	0.864
ZSM-11	6781	5773	4433	2631	1802	4660	0.300	0.851
ZSM-5	6729	5835	4789	2988	1801	4752	0.295	0.867
Mordenite	5186	4576	3759	2343	1416	3943	0.317	0.882
Sodalite	12157	11355	7874	5429	2445	6805	0.225	0.934
Beta-A	9022	7602	6295	4314	1981	6389	0.276	0.825

^aFragment volume (\AA^3).

^bFragment surface area (\AA^2).

^cWater-accessible surface area (\AA^2).

^dHydrophobic-accessible surface area (\AA^2).

^eHydrophilic-accessible surface area (\AA^2).

^fSide-chain-accessible surface area (\AA^2).

^gFragment globularity.

^hFragment rugosity (\AA^{-1}).

show three-dimensional channels, while mordenite shows two-dimensional channels. Each type of zeolite possesses a well-defined crystalline structure, with pores of certain distinct sizes. The studied zeolites cover different pore sizes: faujasite, mordenite, and beta-A are large-pore zeolites (showing channels with access limited by 12-ring windows), while ZSM-11 and ZSM-5 (10-ring) as well as sodalite (6-ring) show smaller windows.

The geometric descriptors and topological indices for the zeolite fragments (cf. Table 2) show a relative error for the fragment volumes V of 0.8%. However, for the fragment surface areas, the errors are larger, for example, 6% for the bare fragment surface area S . Furthermore, the error drops for the water-surface-accessible surface area AS (3%) and even for the side-chain-accessible surface area AS' (2%) due to the internal cavities. The atom-to-atom analysis of the water-accessible surface area AS shows that in general, its hydrophobic term $HBAS$ is almost double than its hydrophilic component part $HLAS$. In particular, on going from mordenite to sodalite, the geometric descriptors are doubled. On

going from sodalite to mordenite, the fragment globularity G increases by 42%. The fragment rugosity G' shows the opposite trend. On going from beta-A to sodalite, G' increases by 13%. The structural class of sodalite is quantitatively distinguished from other classes with respect to all the indices.

Table 3 lists the accessibility of the solvent-accessible surface for different solvents, as well as fractal dimensions D and D' for some zeolite fragments. The accessibility of the solvent-accessible surface is calculated for solvents with different molecular sizes. The radius of the solvent molecule varies from $R_s = 1.250 \text{ \AA}$ (representing a water molecule) to $R_s = 3.500 \text{ \AA}$ (protein side chain). On going from water to the side chain, the accessibility of the solvent-accessible surface monotonically decreases by 66% on average. In particular, for faujasite, the relative decrease in accessibility is the lowest and, for ZSM-5, the diminution in this property is the greatest. The fractal dimension D of the solvent-accessible surface lies in the range 1.9–2.1, and its relative error is 1%. On going from faujasite to sodalite (Table 1), D increases by 14%. In particular, for faujasite, ZSM-11, mordenite, and

TABLE 3: Topological indices for zeolite fragments: accessibility and fractal dimension.

Zeolite	Acc. ₁ ^a	Acc. ₂	Acc. ₃	Acc. ₄	Acc. ₅	Rel. decline Acc ₅₋₁ (%)	D^b	D'^c
Faujasite-I	7.42	5.93	4.66	3.63	2.67	64.0	1.866	2.317
Faujasite-II	9.64	7.74	6.07	4.58	3.37	65.0	1.912	2.193
ZSM-11	7.18	5.67	4.33	3.20	2.41	66.4	1.962	2.315
ZSM-5	7.75	6.07	4.56	3.26	2.46	68.3	2.026	2.174
Mordenite	8.11	6.35	4.80	3.61	2.72	66.5	1.961	2.058
Beta-A	7.64	6.16	4.83	3.55	2.48	67.5	1.981	2.215

^aAccessibility (%) of the solvent-accessible surface for different solvents with radii R_s : (1) water, $R_s = 1.250 \text{ \AA}$; (2) $R_s = 1.617 \text{ \AA}$; (3) $R_s = 2.092 \text{ \AA}$; (4) $R_s = 2.706 \text{ \AA}$; and (5) side chain, $R_s = 3.500 \text{ \AA}$.

^bFractal dimension of the solvent-accessible surface.

^cFractal dimension of the solvent-accessible surface averaged for nonburied atoms.

beta-A, the D are intermediate between that for a completely smooth line ($D = 1$) and that for a completely smooth surface ($D = 2$). However, for ZSM-5 and sodalite, the D are intermediate between that for a completely smooth surface and that for a completely porous material ($D = 3$). D increases, in general, with the relative decline of the accessibility (column 7 of Table 3). On the other hand, the atomic analysis of TOPO allows averaging D only for nonburied atoms. The D' fractal dimension increases by 11% and lies in the range 2.1–2.3. Thus, for all the zeolite fragments, the D' are intermediate between that for a completely smooth surface and that for a completely porous material. In particular, the pictures of faujasite, ZSM-11, mordenite, and beta-A change from a channelled to a porous material. For mordenite, the $D' - D$ increment is the smallest (5%), and for ZSM-11, is the greatest (18%). Thus, the structural class of mordenite is quantitatively distinguished from the other classes with respect to the $D' - D$ increment.

Linear and quadratic correlation models of the fractal dimension D have been carried out versus the structural properties of the zeolite crystals, as well as the geometric descriptors and topological indices of the fragments, via least-squares regression. Faujasite-I is omitted in all the fits in order not to overweight this particular structure. The best linear regression for D results are as follows:

$$\begin{aligned}
 D &= 1.69 + 0.0216F_d + 0.00958R_{\max} - 2.30G + 0.590G', \\
 \text{PESS} &= 0.0248, \quad \text{MAPE} = 0.42\%, \\
 \text{AEV} &= 0.0237, \quad r^2 = 0.9763,
 \end{aligned} \tag{1}$$

where the prediction error sum of squares (PESS), mean absolute percentage error (MAPE), approximation error variance (AEV), and coefficient of determination (r^2) are reported. The zeolites (Table 1) are arbitrarily sorted. The linear model (cf. Figure 1(a)) incorrectly predicts the fractal dimensions of ZSM-11 and ZSM-5. Furthermore, the best quadratic model for D results are as follows:

$$\begin{aligned}
 D &= 2.00 - 0.00337z_{31} + 0.0776z_{32} + 0.000519z_{31}z_{32}, \\
 z_{31} &= 6.15 - 10.1G - 0.317R_{\max}, \\
 z_{32} &= 0.898z_{22} - 0.135z_{21}^2 + 0.158z_{21}z_{22} + 0.0341z_{22}^2,
 \end{aligned}$$

$$\begin{aligned}
 z_{21} &= -8.81 + 0.541F_d, \\
 z_{22} &= 3.62z_{11} + 1.56z_{12} + 30.2z_{11}^2 - 69.7z_{11}z_{12} + 37.5z_{12}^2, \\
 z_{11} &= -11.2 + 1.48F_d + 81.7G^2 - 4.21G \cdot F_d, \\
 z_{12} &= 6.15 - 10.1G - 0.317R_{\max}, \\
 \text{PESS} &< 0.00005, \quad \text{MAPE} = 0.01\%, \\
 \text{AEV} &< 0.00005, \quad r^2 > 0.99995,
 \end{aligned} \tag{2}$$

and AEV decreases virtually by 100%. The model results are superposed to the original data (Figure 1(b)), and the agreement is faultless.

A set of Brønsted-acid model units representative of Si–Al zeolites is studied. The smallest unit investigated SiH₃–OH–AlH₃ is taken to represent a bridged hydroxyl group; the remaining active-site models are built by closing rings consisting of 2–12 –SiH₂–OH–AlH₂– units (cf. Figure 2).

The internal cavities of these rings contribute to both total volume and fragment surface area. On the one hand, the total volume V_t of the zeolite active-site models is the sum of both fragment V_f and cavity V_c volumes: $V_t = V_f + V_c$. On the other, the fragment surface area S_f is the sum of both external S_e and cavity S_c surface areas: $S_f = S_e + S_c$. Table 4 lists the geometric descriptors for the active-site models. The calculations labelled fragment + cavity have been carried out with SURMO2. SURMO2 is unable to recognize the internal cavities of the active-site models. Hence, the calculated volume V is a measure of the total volume V_t ; for example, for the 6-membered ring, V_t equals 567.3 \AA^3 . Furthermore, GEPOL does recognize the cavities, and the value of the fragment volume V_f is available; for example, $V_f(6\text{-ring}) = 490.9 \text{ \AA}^3$. The external surface area $S_e(6\text{-ring}) = 360.7 \text{ \AA}^2$ is estimated by SURMO2. Besides, the actual (external plus internal) fragment surface area $S_f(6\text{-ring}) = 656.6 \text{ \AA}^2$ (GEPOL).

Table 5 reports the topological indices for the zeolite active-site models. The fragment globularity G is the topological index that better differentiates the active-site models. Not surprisingly, G is rather greater as calculated by SURMO2 (closer to unity for the largest ring in the

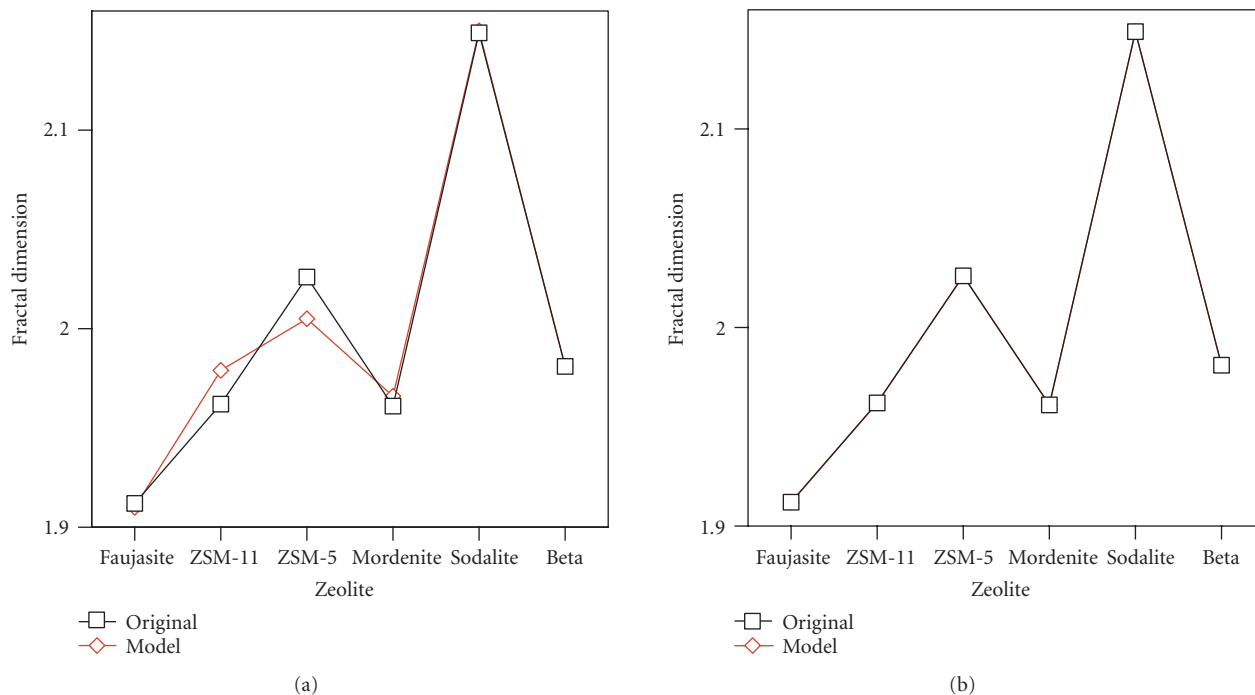


FIGURE 1: Comparison of data with models (fractal dimension): (a) linear and (b) quadratic models.

TABLE 4: Geometric descriptors for zeolite active-site models.

Type of ring	V^a fragment + cavity	V^b fragment	S^c fragment + cavity	S^b fragment	AS^d fragment + cavity	AS^b fragment	$AS'^{b,e}$ fragment
2	176.3	160.0	186.7	210.2	422.6	371.6	746.1
4	433.5	328.8	346.0	439.6	652.4	659.7	1106.0
6	567.3	490.9	360.7	656.6	854.9	992.2	1509.2
8	813.4	660.9	414.6	907.9	959.4	1363.3	2052.6
10	742.4	825.3	447.2	1135.5	910.9	1731.9	2631.2
12	888.2	989.2	460.7	1360.7	1062.9	2091.8	3203.6

^aFragment volume (\AA^3).^bCalculations carried out with the GEPOL program.^cFragment surface area (\AA^2).^dWater-accessible surface area (\AA^2).^eSide-chain-accessible surface area (\AA^2).

$G_{\text{fragment+cavity}}$ column) compared with GEPOL (G_{fragment}). Moreover, the fragment rugosity G' is smaller. Note that the internal cavity effect is difficult to appreciate in the context of the fragment volume, globularity, and rugosity (10–12-ring), water-accessible surface (2-ring), and side-chain-accessible surface area (2–6-ring), because of their small or null calculated cavity contributions.

From the calculation results referring to the total (SURMO2) and cavity-sensitive (GEPOL) fragment shape, the geometric descriptors and topological indices for the cavities of the zeolite active-site models have been estimated. The results (cf. Table 6) show that the cavity volume and sur-

face areas are smaller for the 6-ring than for the 8-ring. However, for the 6-ring, the globularity, rugosity, and fractal dimension are greater. Note that for the 2–8-ring cavities, $S > AS \geq AS'$, because a water molecule with an effective radius of 1.41\AA and a volume ca. 12\AA^3 can hardly be contained inside the smallest cavities. Moreover, a probe sphere representing a protein side chain, with a radius of 3.5\AA and a volume ca. 180\AA^3 , cannot be contained inside any of the cavities. For the 2–4- and 10–12-ring cavities, the fractal dimension D is ca. 2, indicating that the solvent-accessible surface of these rings is hardly sensitive to solvent size. Notwithstanding, for the 6–8-ring cavities, D lies in the range 4.0–4.3.

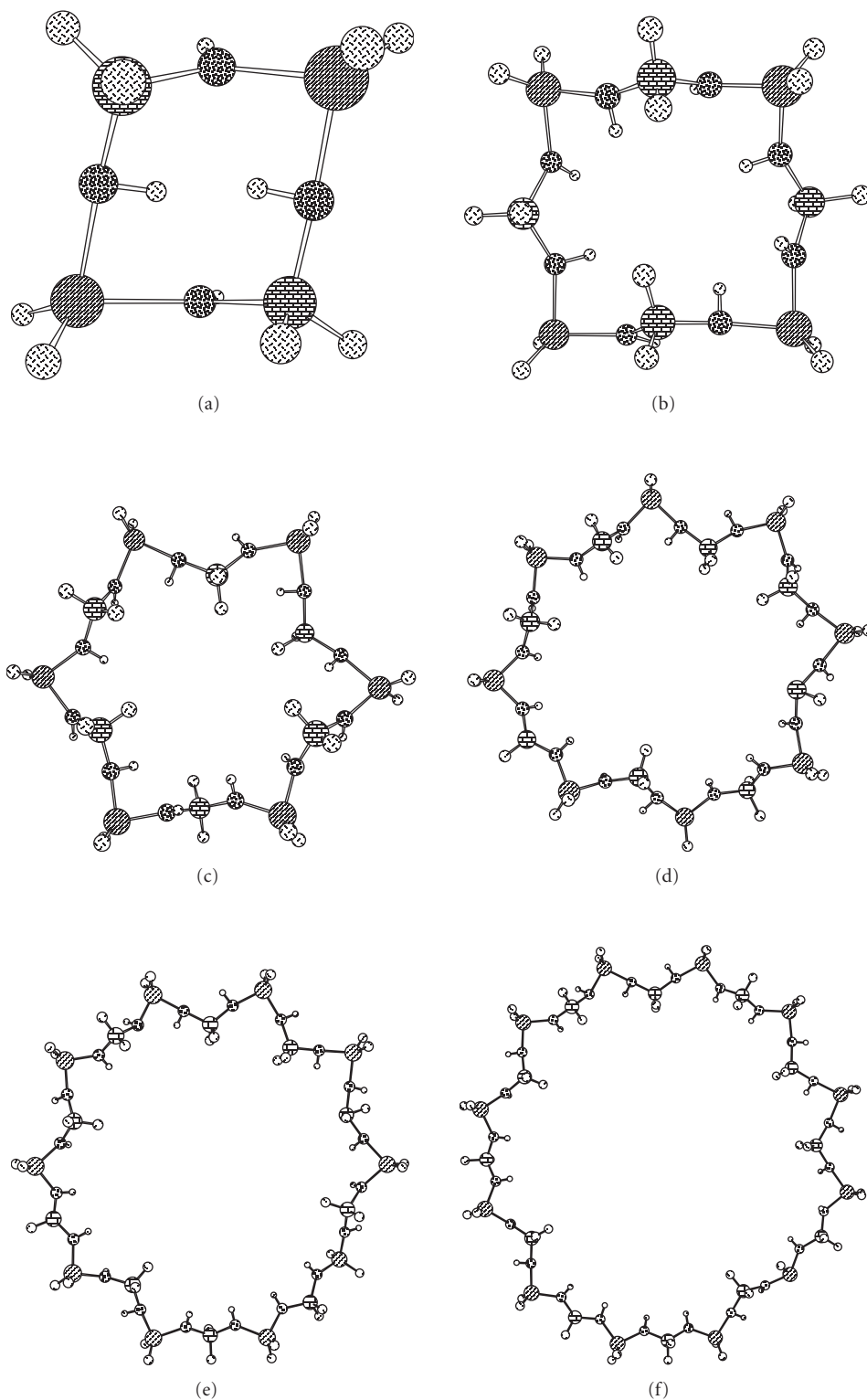


FIGURE 2: Molecular images of $-(\text{SiH}_2-\text{OH}-\text{AlH}_2-\text{OH}-)_n$ rings: (a)–(f) $n = 2, 4, 6, 8, 10,$ and 12 .

In particular, the 6-ring cavity shows the greatest value of D , indicating the greatest sensitivity of the cavity accessible surface to solvent size. Therefore, it is suggested that the 6-ring cavity can have the greatest Brønsted-acid catalytic activity.

Figure 3 shows the variation of the side-chain-accessible surface area (AS') with the water-accessible surface area (AS) of the zeolite active-site models for the 1–12-ring. Three points (1-, 2-, and 4-ring) appear superposed.

TABLE 5: Topological indices for active-site models of zeolites.

Type of ring	G^a fragment + cavity	G^b fragment	G^c fragment + cavity	G^b fragment	D^d fragment + cavity	D^b fragment
2	0.814	0.678	1.059	1.313	1.262	1.324
4	0.800	0.524	0.798	1.337	1.372	1.501
6	0.919	0.458	0.636	1.337	1.372	1.598
8	1.016	0.404	0.510	1.374	1.261	1.603
10	0.887	0.375	0.602	1.376	1.305	1.595
12	0.970	0.353	0.519	1.376	1.268	1.587

^aFragment globularity.

^bCalculations carried out with the GEPOL program.

^cFragment rugosity (\AA^{-1}).

^dFractal dimension of the solvent-accessible surface.

TABLE 6: Descriptors/indices for active-site model cavities.

Type of ring	V^a	S^b	AS^c	AS^d	G^e	G^f	D^g
2	16.3	23.46	0.0	0.0	1.325	1.439	2.000
4	104.7	93.56	7.3	0.0	1.148	0.894	2.000
6	76.4	295.92	137.3	0.0	0.294	3.873	4.271
8	152.5	493.34	403.9	45.3	0.280	3.235	3.951
10	0.0	688.28	821.0	819.7	0.000	∞	1.985
12	0.0	899.99	1028.9	1103.3	0.000	∞	1.943

^aCavity volume (\AA^3).

^bCavity surface area (\AA^2).

^cWater-accessible surface area (\AA^2).

^dSide-chain-accessible surface area (\AA^2).

^eCavity globularity.

^fCavity rugosity (\AA^{-1}).

^gFractal dimension of the solvent-accessible surface.

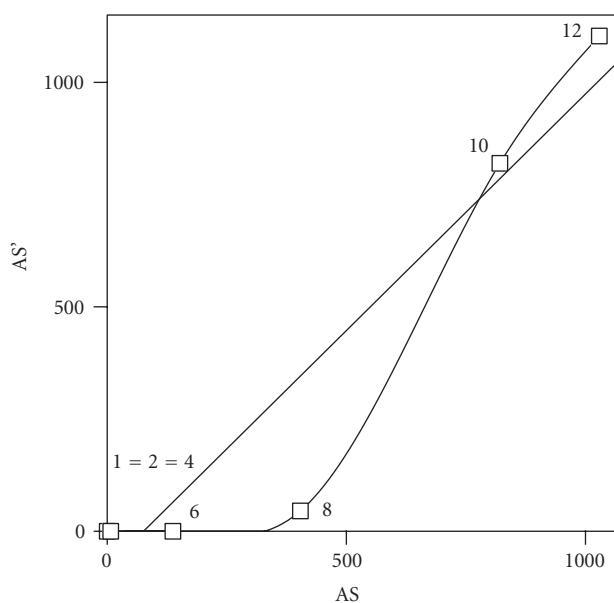


FIGURE 3: Side-chain versus water-accessible surface areas of active-site models of zeolites.

TABLE 7: Geometric and topological indices for zeolite 6-ring active-site model: atomic analysis.

Atom	V^a	S^b	G^c	G'^d	AS^e	Accessibility ^f	AS'^g	D^h
Si	26.1	26.59	1.602	1.017	29.0	20.3	10.3	3.022
O	6.5	6.49	2.591	1.001	3.2	3.6	0.1	5.749
H(O)	7.7	9.09	2.076	1.179	3.2	3.5	8.9	2.963
Al	9.8	11.41	1.941	1.164	2.9	3.2	0.1	5.594
Cavity	76.4	295.92	0.294	3.873	137.3	—	0.0	4.271
All rings	487.9	624.64	0.480	1.280	965.7	18.4	1490.6	1.584

^aRing volume (\AA^3).

^bRing surface area (\AA^2).

^cRing globularity.

^dRing rugosity (\AA^{-1}).

^eWater-accessible surface area (\AA^2).

^fAccessibility (%) of the water-accessible surface.

^gSide-chain-accessible surface area (\AA^2).

^hFractal dimension of the solvent-accessible surface area.

The linear fit corresponds to

$$AS' = -80.0 + 1.05 AS, \quad r = 0.953. \quad (3)$$

The slope indicates that an increase of 1.00\AA^2 in AS corresponds to an increase of 1.05\AA^2 in AS' . The abscissa (or the intersection with the interpolation line) at $AS = 76.2 \text{\AA}^2$ is closer to the 6-ring, indicating the greatest sensitivity of its solvent-accessible surface to solvent size.

The atom-to-atom analysis of the geometric descriptors and topological indices for the zeolite 6-ring active-site model, carried out with TOPO, considers (Table 7) four atoms, namely Si, O, H(O), and Al in each $-\text{SiH}_2-\text{OH}-\text{AlH}_2-$ unit. The greatest contribution to the ring volume V comes from each Si atom (52% of that for Si/O/H/Al). The same trend has been observed for the surface area S_{Si} (50%), as well as solvent-accessible surface areas AS_{Si} (76%) and AS'_{Si} (53%), due to the greatest accessibility of each Si atom ($\text{Acc}_{\text{Si}} = 20.3\%$). The Si-atom term in the ring globularity G_{Si} is the lowest. Moreover, each Si-atom component part in the ring rugosity G'_{Si} is small. Each Si-atom input to the ring fractal dimension D_{Si} is low; however, for the O atoms, D_{O} is the greatest, and for the Al atoms, D_{Al} is large. The ring cavity contributes to the total volume and surface area, as explained above (Table 5). Again, $S_{\text{cavity}} > AS_{\text{cavity}} \geq AS'_{\text{cavity}}$, as expected for a small cavity. The fractal dimension D_{cavity} is large, indicating the sensibility of the solvent-accessible surface of the cavity to solvent size and suggesting that this cavity can have large Brønsted-acid catalytic activity. The ring rugosity G' and accessibility are small. The ring fractal dimension D is large.

Our results, indicating the maximal sensibility of the solvent-accessible surface of the 6-ring cavity to solvent size, are in agreement with Hammonds et al.'s rigid-unit crystal vibrational mode (RUM) model for the binding site of cations [26]. In faujasite, the 6-ring was calculated to be opening and closing under the influence of a local RUM, in agreement with experiments.

4. CONCLUSIONS

From the present results, the following conclusions can be drawn.

- (1) The fragment globularity G is the topological descriptor that better differentiates the zeolite active-site models.
- (2) The 6-membered-ring cavity model of the zeolite active site shows the greatest fractal dimension, indicating the greatest sensitivity of its solvent-accessible surface to solvent size. Therefore, it is suggested that the 6-ring can have the greatest activity as acidic catalyst. Work is in progress to check the validity of this result.

ACKNOWLEDGMENTS

We wish to thank Dr. C. M. Zicovich-Wilson for providing us with calculation results before publication on the optimized geometry of zeolites. The authors acknowledge financial support from the Spanish MEC-DGI (Project no. CTQ2004-07768-C02-01/BQU), Generalitat Valenciana (DGEUI INF01-051 and INFRA03-047, and OCYT GRUPOS03-173), and Universitat de València–Mediscovery.

REFERENCES

- [1] J. A. Rabo, Ed., *Zeolite Chemistry and Catalysis*, American Chemical Society, Washington, DC, USA, 1976.
- [2] G. T. Kerr, "Hydrogen zeolite Y, ultrastable zeolite Y, and aluminum-deficient zeolites," *Advances in Chemistry Series*, vol. 121, pp. 219–229, 1973.
- [3] R. M. Barrer, *Hydrothermal Chemistry of Zeolites*, Academic Press, New York, NY, USA, 1982.
- [4] W. J. Mortier, J. Sauer, J. A. Lercher, and H. Noller, "Bridging and terminal hydroxyls. A structural chemical and quantum chemical discussion," *Journal of Physical Chemistry*, vol. 88, no. 5, pp. 905–912, 1984.

- [5] J. G. Fripiat, F. Berger-André, J.-M. André, and E. G. Derouane, "Non-empirical quantum mechanical calculations on pentasil-type zeolites," *Zeolites*, vol. 3, no. 4, pp. 306–310, 1983.
- [6] P. J. O'Malley and J. Dwyer, "Ab initio molecular orbital calculations on the acidic properties of boralite," *Journal of the Chemical Society, Chemical Communications*, no. 2, pp. 72–73, 1987.
- [7] P. J. O'Malley and J. Dwyer, "Ab initio molecular orbital calculations on the acidic characteristics of isomorphously substituted zeolites," *Chemical Physics Letters*, vol. 143, no. 1, pp. 97–100, 1988.
- [8] H. W. Haynes Jr., "Chemical, physical, and catalytic properties of large pore acidic zeolites," *Catalysis Reviews*, vol. 17, pp. 273–336, 1978.
- [9] P. A. Jacobs, "Acid zeolites: an attempt to develop unifying concepts (P. H. Emmett award address, 1981)," *Catalysis Reviews*, vol. 24, no. 3, pp. 415–440, 1982.
- [10] P. Viruela-Martín, C. M. Zicovich-Wilson, and A. Corma, "Ab initio molecular orbital calculations of the protonation reaction of propylene and isobutene by acidic OH groups of isomorphously substituted zeolites," *Journal of physical chemistry*, vol. 97, no. 51, pp. 13713–13719, 1993.
- [11] F. Torrens, "Fractal dimension of different structural-type zeolites and of the active sites," *Topics in Catalysis*, vol. 18, no. 3-4, pp. 291–297, 2002.
- [12] F. Torrens, "Characterizing cavity-like spaces in active-site models of zeolites," *Computational Materials Science*, vol. 27, no. 1-2, pp. 96–101, 2003.
- [13] F. Torrens, "Fractal dimension of zeolite catalysts," *Molecular Physics*, vol. 100, no. 19, pp. 3105–3109, 2002.
- [14] F. Torrens, E. Ortí, and J. Sánchez-Marín, "Vectorized TOPO program for the theoretical simulation of molecular shape," *Journal de Chimie Physique et de Physico-Chimie Biologique*, vol. 88, pp. 2435–2441, 1991.
- [15] A. Y. Meyer, "Molecular mechanics and molecular shape. Part 1. van der Waals descriptors of simple molecules," *Journal of the Chemical Society, Perkin Transactions 2*, pp. 1161–1169, 1985.
- [16] A. Y. Meyer, "Molecular mechanics and molecular shape. V. On the computation of the bare surface area of molecules," *Journal of Computational Chemistry*, vol. 9, pp. 18–24, 1988.
- [17] B. Lee and F. M. Richards, "The interpretation of protein structures: estimation of static accessibility," *Journal of Molecular Biology*, vol. 55, no. 3, pp. 379–400, 1971.
- [18] R. B. Hermann, "Theory of hydrophobic bonding. II. Correlation of hydrocarbon solubility in water with solvent cavity surface area," *Journal of Physical Chemistry*, vol. 76, no. 19, pp. 2754–2759, 1972.
- [19] A. Bondi, "Van der Waals volumes and radii," *Journal of Physical Chemistry*, vol. 68, no. 3, pp. 441–451, 1964.
- [20] S. J. Wodak and J. Janin, "Analytical approximation to the accessible surface area of proteins," *Proceedings of the National Academy of Sciences of the United States of America*, vol. 77, no. 4, pp. 1736–1740, 1980.
- [21] M. Lewis and D. C. Rees, "Fractal surfaces of proteins," *Science*, vol. 230, no. 4730, pp. 1163–1165, 1985.
- [22] F. Torrens, J. Sánchez-Marín, and I. Nebot-Gil, "New dimension indices for the characterization of the solvent-accessible surface," *Journal of Computational Chemistry*, vol. 22, no. 5, pp. 477–487, 2001.
- [23] F. Torrens, M. Rubio, and J. Sánchez-Marín, "AMYR 2: a new version of a computer program for pair potential calculation of molecular associations," *Computer Physics Communications*, vol. 115, no. 1, pp. 87–89, 1998.
- [24] J. L. Pascual-Ahuir, E. Silla, J. Tomasi, and R. Bonaccorsi, "Electrostatic interaction of a solute with a continuum. Improved description of the cavity and of the surface cavity bound charge distribution," *Journal of Computational Chemistry*, vol. 8, no. 6, pp. 778–787, 1987.
- [25] B. Terry and J. Barriol, "On the evaluation of the usual quantities or coefficients related to the shape of a molecule approximated on the basis of the van der Waals radii," *Journal de Chimie Physique et de Physico-Chimie Biologique*, vol. 78, pp. 207–212, 1981.
- [26] K. D. Hammonds, V. Heine, and M. T. Dove, "Rigid-unit modes and the quantitative determination of the flexibility possessed by zeolite frameworks," *Journal of Physical Chemistry B*, vol. 102, no. 10, pp. 1759–1767, 1998.

Synthesis and Characterization of Photocatalytic TiO₂-ZnFe₂O₄ Nanoparticles

Sesha S. Srinivasan, Jeremy Wade, and Elias K. Stefanakos

Clean Energy Research Center, College of Engineering, University of South Florida, Tampa, FL 33620, USA

Received 20 January 2006; Revised 29 June 2006; Accepted 13 July 2006

A new coprecipitation/hydrolysis synthesis route is used to create a TiO₂-ZnFe₂O₄ nanocomposite that is directed towards extending the photoresponse of TiO₂ from UV to visible wavelengths (> 400 nm). The effect of TiO₂'s accelerated anatase-rutile phase transformation due to the presence of the coupled ZnFe₂O₄ narrow-bandgap semiconductor is evaluated. The transformation's dependence on pH, calcinations temperature, particle size, and ZnFe₂O₄ concentration has been analyzed using XRD, SEM, and UV-visible spectrometry. The requirements for retaining the highly photoactive anatase phase present in a ZnFe₂O₄ nanocomposite are outlined. The visible-light-activated photocatalytic activity of the TiO₂-ZnFe₂O₄ nanocomposites has been compared to an Aldrich TiO₂ reference catalyst, using a solar-simulated photoreactor for the degradation of phenol.

Copyright © 2006 Sesha S. Srinivasan et al. This is an open access article distributed under the Creative Commons Attribution License, which permits unrestricted use, distribution, and reproduction in any medium, provided the original work is properly cited.

1. INTRODUCTION

The wide-bandgap semiconductor TiO₂ has become the dominant UV-activated photocatalyst in the field of air and water detoxification because of its high stability, low cost, high oxidation potential, and chemically favorable properties. The demand for visible-light-activated photocatalytic systems is increasing rapidly; however, currently, the efficiency and availability of photocatalysts that can be activated effectively by the solar spectrum and particularly indoor lighting are severely limited. Environmental pollution on a global scale is proposed to be the greatest problem that chemical scientists will face in the 21st century, and an increasing number of these scientists are looking for new photocatalytic systems for the solution. The vast majorities of current photocatalytic system use pure or modified TiO₂ with a metastable anatase crystal structure (3.2 eV bandgap), although two key shortcomings exist. The first shortcoming is low photocatalytic efficiencies that plague current photocatalysts due to undesired electron-hole pair (EHP) recombination, and the second is that TiO₂ utilizes only 3–5% of the solar spectrum and virtually none of the light commonly used for indoor illumination. Both of these spectral regions have applications needing active photocatalysts [1]. The push towards extending the photoresponse of TiO₂ to visible wavelengths is increasing exponentially every year, for both solar ($\lambda > \text{UV-A}$, 320 nm) and visible light applications

(> 400 nm). The most successful techniques used thus far for the development of modified TiO₂ for visible-light photocatalysts are ion implantation methods using Cr or V ions [2], various synthesis techniques [3], and substitutional doping of nonmetals such as N (TiO_{2-x}N_x) [4, 5].

Recent efforts have also been sought to extend the photoresponse of TiO₂ through charge-transfer interactions with narrow-bandgap metal oxides such as the *n*-type ZnFe₂O₄ with a 1.9 eV bandgap. ZnFe₂O₄, most prominently known for its magnetic properties, is a photocatalyst active for irradiation wavelengths shorter than 652 nm, although its photoactive lifetime is short due to the tendency of absorbing intermediate oxidation byproducts, thereby inhibiting it from oxidizing target organics [6]. Numerous publications in the past year have used sol-gel techniques [7, 8] to dope TiO₂ with ZnFe₂O₄ or Zn²⁺ and Fe³⁺ ions [9] for solar-light-irradiated photocatalytic studies. TiO₂-ZnFe₂O₄ alloys, on the other hand, are difficult to prepare because of the differences in preparation procedures (ZnFe₂O₄ is typically prepared through coprecipitation in alkaline solutions) and also the enhancement of TiO₂'s anatase to rutile transformation by the substitutional presence of Fe³⁺ ions. However, a complex colloidal chemistry method using surfactant capping has been reported for creating photoactive TiO₂-ZnFe₂O₄ nanocomposites that exhibit increased photocatalytic response to solar irradiation [10]. In this report, a simple coprecipitation/hydrolysis synthesis method is

used to create $\text{TiO}_2\text{--ZnFe}_2\text{O}_4$ alloys for the purpose of creating an inexpensive and nontoxic photocatalyst that is photoactive in response to wavelengths greater than 400 nm.

2. EXPERIMENTAL METHOD

A coprecipitation/hydrolysis synthesis method was used for the formation of $\text{TiO}_2\text{--}(X)\text{ZnFe}_2\text{O}_4$ nanocomposites with X (mole fraction) values of 0.01, 0.05, 0.1, 0.15, and 0.2. All chemicals used were purchased from Sigma Aldrich and were of 99.9% purity or higher. ZnFe_2O_4 was first precipitated using the respective quantity of $\text{Fe}(\text{NO}_3)_3 \cdot 9\text{H}_2\text{O}$ and $\text{Zn}(\text{NO}_3)_2 \cdot 6\text{H}_2\text{O}$ precursors in a solution of $\text{C}_3\text{H}_7\text{OH}$ (isopropyl alcohol) heated at 65°C and stirred for 30 minutes. To coprecipitate the nitrate precursor, the pH of the aqueous solution was raised to 6.5 by slowly adding a 3.5 M NH_4OH solution using $\text{C}_3\text{H}_7\text{OH}$ as the solvent. Approximately 10 g of deionized H_2O was next added dropwise to the solution in addition to the H_2O already existing from the added NH_4OH and the solution was left stirring for 45 minutes. A separately prepared solution of $\text{Ti}(\text{O}i\text{Bu})_4$ and $\text{C}_3\text{H}_7\text{OH}$ was mixed in a ratio of 1 : 2 by weight and added dropwise to the coprecipitated ZnFe_2O_4 solution for a controlled hydrolysis with $\text{H}_2\text{O} : \text{Ti}(\text{O}i\text{Bu})_4$ ratios of 50, 25, 15, 5 : 1. The final solution was kept stirring at 65°C for 90 minutes, filtered, dried at 100°C and 220°C , respectively. Thus prepared $\text{TiO}_2\text{--ZnFe}_2\text{O}_4$ nanoparticles have been calcined in a flowing air atmosphere at various temperatures for 3 hours.

The UV-Vis and visible-light photoactivity of the nanocomposites were determined using photoreactor consisting of a 1000 W ($340 < \lambda < 680$ nm) metal halide lamp, reflector, and borosilicate reaction vessel. For visible-light photoactivity experiments, a thin-film UV cutoff filter provided by Edmund Optics was inserted on the glass lens of the metal halide lamp to completely remove irradiation with wavelengths shorter than 400 nm. Phenol was used as the organic test degradant since it absorbs wavelengths around 265 nm and therefore will not be susceptible to photolysis. Experimental reaction conditions for all studies consisted of 40 ppm phenol, 1100 g of deionized H_2O , 1 g/L catalyst loading, magnetic stirring, and 1.5 L/min of air injected through a sparger to perform the role of electron scavenging. The degradation of phenol was evaluated by centrifuging the retrieved samples and measuring the intensity of phenol's absorption peak (268 nm) relative to its initial intensity (C/C_0) by UV-Vis spectroscopy with an Ocean Optics fiber optic spectrometer.

3. RESULTS AND DISCUSSION

3.1. X-ray diffraction

To confirm the multiphase synthesis of $\text{TiO}_2\text{--}(X)\text{ZnFe}_2\text{O}_4$ nanocomposites, alloys were formed using a high concentration ($X = 0.2$) of ZnFe_2O_4 . XRD measurements revealed the formations of anatase and rutile TiO_2 , as well as ZnFe_2O_4 and traces of ZnTiO_3 and ZnO . Although a low calcination

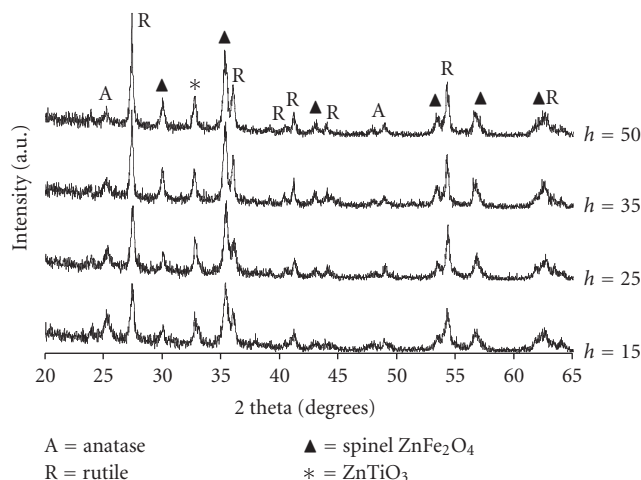


FIGURE 1: XRD spectra of $\text{TiO}_2\text{--}(0.2)\text{ZnFe}_2\text{O}_4$ calcined at 400°C for various h values.

temperature of 400°C was used, the anatase-to-rutile transformation was nearly complete due to the inherent substitution of Fe^{3+} for Ti^{4+} ions, thereby creating oxygen vacancies that promote the formation of rutile throughout the bulk of the nanoparticles [11]. The considerable amount of Fe^{3+} ions needed to realize such a low temperature anatase-rutile transformation may also explain the formation of ZnTiO_3 and ZnO as an incomplete formation of ZnFe_2O_4 due to the absence of available Fe. Figure 1 shows the XRD spectra of the $\text{TiO}_2\text{--}(0.2)\text{ZnFe}_2\text{O}_4$ nanocomposites using various h values ($h = \text{H}_2\text{O}/\text{Ti}[\text{O}i\text{Bu}]_4$), since this ratio effects the hydrolysis of TiO_2 and therefore the photoactivity of the nanocomposite.

Based on the previous experiment, as well as others conducted on pure hydrolyzed TiO_2 [12], it was decided to use h values of 25 for the remainder of the nanocomposites. This ratio provides the optimal tradeoff between hydrolysis homogeneity, anatase content, and photocatalytic activity. $\text{TiO}_2\text{--}(X)\text{ZnFe}_2\text{O}_4$ nanocomposites were next synthesized using X values of 0.01, 0.05, 0.1, and 0.15 to determine the maximum concentration of ZnFe_2O_4 that can be coupled with TiO_2 while still maintaining an anatase crystal structure which is predicted to be needed for the redox reactions derived from a charge-transfer phenomenon. The XRD spectra of the $\text{TiO}_2\text{--}X\%\text{ZnFe}_2\text{O}_4$ nanocomposites are shown in Figure 2.

Figure 2 shows the effect of ZnFe_2O_4 alloying concentration on the anatase-to-rutile transformation. For a calcination temperature of 450°C , X values of 0.01, 0.05, 0.1, 0.15, and 0.2 correspond to respective anatase mass fractions of 100, 100, 72.7, 54.1, and 47.2%, as calculated by the equation

$$X_A = \frac{1}{1 + 1.26 \cdot (I_A/I_R)} \cdot 100, \quad (1)$$

X_A is the mass fraction of anatase, I_A and I_R are the X-ray integrated intensities of the (101) reflection of anatase and rutile phases, respectively. It should be noted that this equation only takes into consideration the percent of anatase and

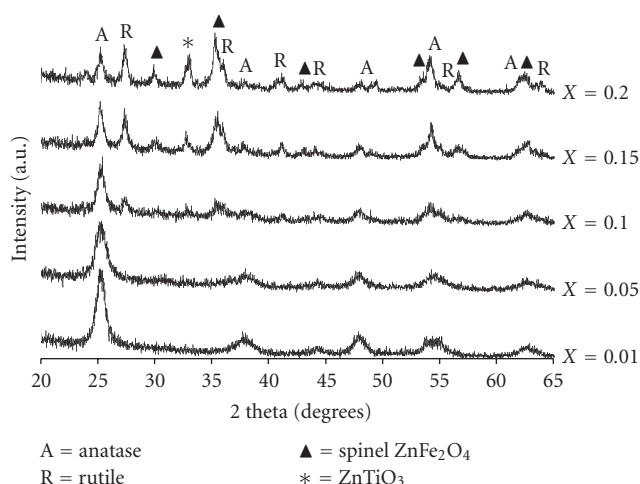


FIGURE 2: XRD spectra of TiO₂-(X) ZnFe₂O₄ calcined at 450°C.

rutile in the formed TiO₂ and not of the entire nanocomposite.

3.2. UV-visible spectroscopy

An Oriel Instruments spectrometer with an integrating sphere has been used for UV-Vis spectrometry measurements used to analyze the redshifts in the absorption regions as a function of ZnFe₂O₄ alloying concentration. The nanoparticles have been deposited on the glass slides by spin-coating technique at 3000 rpm. The UV-Vis transmittance measurements were taken and converted into absorption readings. Figure 3 represents the UV-Vis absorption spectra for TiO₂-(X) ZnFe₂O₄ nanocomposites with X = 0.01, 0.05, 0.1, 0.15, and 0.2. It can be seen that the redshift of the absorption edge is roughly proportional to the ZnFe₂O₄ alloying concentration. The absorption bands were smooth for low alloying concentrations (X < 0.15), however small shoulders appeared for higher ZnFe₂O₄ concentrations as often seen in the absorption bands of doped photocatalysts.

3.3. Photocatalytic studies

The photocatalytic activity of the samples in response to UV-Vis and visible-light irradiation was determined using phenol degradation over a 105-minute time period, with samples withdrawn every 15 minutes. The UV photoactivity of the TiO₂-(X) ZnFe₂O₄ nanocomposites was found to decrease in rough proportion to the increasing concentration of ZnFe₂O₄. The visible-light photoactivity (shown in Figure 4), however, was characterized by a bell curve, with the maximum degradation being achieved with X equal to 0.10. For comparison with the nanocomposite materials, pure ZnFe₂O₄ prepared by the hydrolysis and coprecipitation method has been plotted in this figure. Figure 5 shows a breakdown of the photocatalytic activity of TiO₂-(X) ZnFe₂O₄ nanoparticles from various degradation experiments.

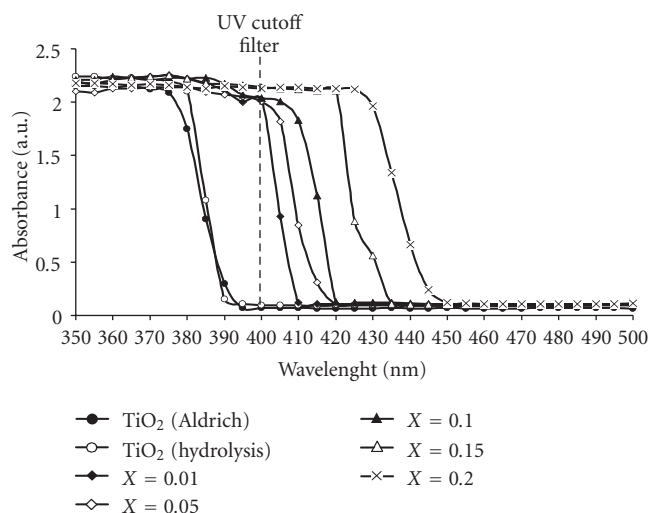


FIGURE 3: UV-Vis absorbance spectra of TiO₂-(X) ZnFe₂O₄ nanocomposites.

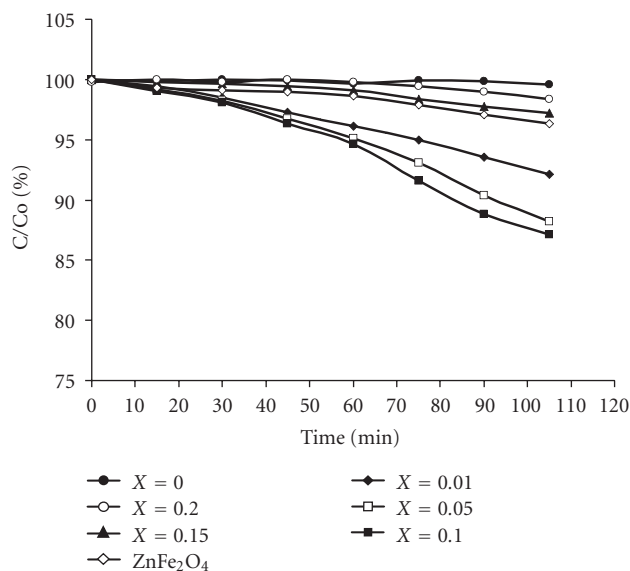


FIGURE 4: Visible-light-activated photocatalytic degradation rates for TiO₂(X) ZnFe₂O₄ nanocomposites.

The decreasing photoactivity for the catalysts for X values more than 0.1 when irradiated by UV light is attributed to the increasing formation of the rutile phase with ZnFe₂O₄ concentrations as well as possible defects in the TiO₂ lattice, in addition to enhanced electron-hole pair (EHP) recombination. The increased photoactivity for X values of 0.01 to 0.10 may be associated with the role ZnFe₂O₄ substituted or surface-stabilized anatase TiO₂ serves in extending the photoresponse of the catalyst to short-wavelength visible irradiation and effectively transferring charge carriers to particles capable of the appropriate redox reactions.

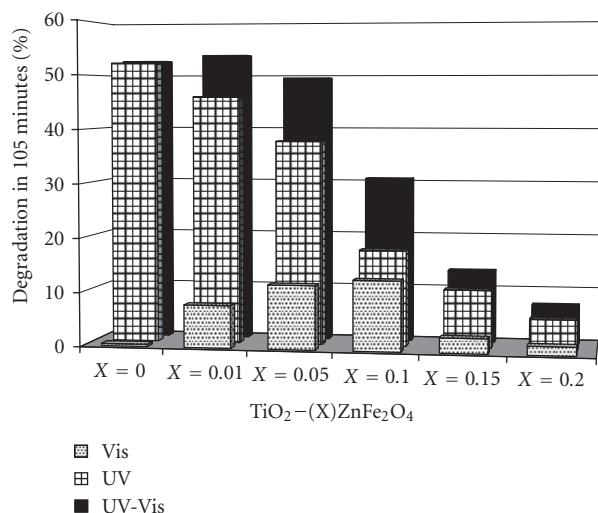


FIGURE 5: Breakdown of the degradation characteristics for $\text{TiO}_2-(X)\text{ZnFe}_2\text{O}_4$ nanocomposites irradiated by UV, and UV-Vis, and visible light.

The photoactivity that characterizes the nanocomposite photocatalysts using visible-light irradiation is not directly (or at least completely) linked to ZnFe_2O_4 . The reason for this conclusion is that the consistent degradation rates characteristic of the $\text{TiO}_2-(X)\text{ZnFe}_2\text{O}_4$ nanocomposites are dissimilar to the degradation rates for ZnFe_2O_4 which were found in prior experiments to cease after short durations using both UV and visible-light irradiations. It can also be concluded from the poor visible-light photocatalytic activity of nanocomposites with X equal to 0.15 and 0.20 that anatase TiO_2 plays a critical role in the visible-light photocatalysis of $\text{TiO}_2-\text{ZnFe}_2\text{O}_4$ alloys. Although the ZnFe_2O_4 concentration increases, thereby allowing more charge carriers in response to enhanced visible-light absorption, it is thought that the high rutile concentrations impede the overall reaction.

4. CONCLUSION

$\text{TiO}_2\text{ZnFe}_2\text{O}_4$ nanocomposites were synthesized, and their photocatalytic activity in response to UV, UV-Vis (solar), and visible light was determined. It was concluded that the narrow-bandgap semiconductor ZnFe_2O_4 can be effectively coupled with TiO_2 for visible-light (> 400 nm)-activated photocatalysis. This study shows the potential of inexpensive and nontoxic photocatalysts for indoor visible-light applications.

ACKNOWLEDGMENTS

The authors wish to thank the Nanomaterials and Nanomanufacturing Research Center at University of South Florida for extensive use of X-ray diffraction facilities. Financial support from USF, DOE, and Center for Biological Defense are gratefully acknowledged.

REFERENCES

- [1] M. Anpo, "Applications of titanium oxide photocatalysts and unique second-generation TiO_2 photocatalysts able to operate under visible light irradiation for the reduction of environmental toxins on a global scale," *Studies in Surface Science and Catalysis*, vol. 130 A, pp. 157–166, 2000.
- [2] M. Anpo, "Applications of TiO_2 photocatalyst to better our environment," *Protecting the Environment*, pp. 75–88, 1998.
- [3] W. Chengyu, S. Huamei, T. Ying, Y. Tongsoo, and Z. Guowub, "Properties and morphology of CdS compounded TiO_2 visible-light photocatalytic nanofilms coated on glass surface," *Separation and Purification Technology*, vol. 32, no. 1–3, pp. 357–362, 2003.
- [4] J. Premkumar, "Development of super-hydrophilicity on nitrogen-doped TiO_2 thin film surface by photoelectrochemical method under visible light," *Chemistry of Materials*, vol. 16, no. 21, pp. 3980–3981, 2004.
- [5] S. Mozia, M. Toaszewska, B. Kosowska, B. Brzmił, A. W. Morawski, and K. Kalucki, "Decomposition of nonionic surfactant on a nitrogen-doped photocatalyst under visible-light irradiation," *Applied Catalysis B: Environmental*, vol. 55, no. 3, pp. 195–200, 2005.
- [6] W. Meng, F. Li, D. G. Evans, and X. Duan, "Photocatalytic activity of highly porous zinc ferrite prepared from a zinc-iron(III)-sulfate layered double hydroxide precursor," *Journal of Porous Materials*, vol. 11, no. 2, pp. 97–105, 2004.
- [7] G.-G. Liu, X.-Z. Zhang, Y.-J. Xu, X.-S. Niu, L.-Q. Zheng, and X.-J. Ding, "Effect of ZnFe_2O_4 doping on the photocatalytic activity of TiO_2 ," *Chemosphere*, vol. 55, no. 9, pp. 1287–1291, 2004.
- [8] P. Cheng, W. Li, T. Zhou, Y. Jin, and M. Gu, "Physical and photocatalytic properties of zinc ferrite doped titania under visible light irradiation," *Journal of Photochemistry and Photobiology A: Chemistry*, vol. 168, no. 1-2, pp. 97–101, 2004.
- [9] Z.-H. Yuan, J.-H. Jia, and L.-D. Zhang, "Influence of co-doping of Zn(II) + Fe(III) on the photocatalytic activity of TiO_2 for phenol degradation," *Materials Chemistry and Physics*, vol. 73, no. 2-3, pp. 323–326, 2002.
- [10] Z.-H. Yuan and L.-D. Zhang, "Synthesis, characterization and photocatalytic activity of $\text{ZnFe}_2\text{O}_4/\text{TiO}_2$ nanocomposite," *Journal of Materials Chemistry*, vol. 11, no. 4, pp. 1265–1268, 2001.
- [11] F. C. Gennari and D. M. Pasquevich, "Kinetics of the anatase-rutile transformation in TiO_2 in the presence of Fe_2O_3 ," *Journal of Materials Science*, vol. 33, no. 6, pp. 1571–1578, 1998.
- [12] N. V. Golubko, M. I. Yanovskaya, I. P. Romm, and A. N. Ozerin, "Hydrolysis of titanium alkoxides: thermochemical, electron microscopy, saxs studies," *Journal of Sol-Gel Science and Technology*, vol. 20, no. 3, pp. 245–262, 2001.

Photocatalytic Oxidation of a Volatile Organic Component of Acetaldehyde Using Titanium Oxide Nanotubes

Huifang Xu,¹ Ganesh Vanamu,² Ziming Nie,¹ Hiromi Konishi,¹ Rakesh Yeredla,¹ Jonathan Phillips,³ and Yifeng Wang⁴

¹ Department of Geology and Geophysics and Material Science Program, University of Wisconsin, 1215 West Dayton Street, Madison, WI 53706, USA

² Department of Chemical and Nuclear Engineering, University of New Mexico, Albuquerque, NM 87131, USA

³ Los Alamos National Laboratory, Engineering Science and Applications Division, MS C390, Los Alamos, NM 87545, USA

⁴ Sandia National Laboratories, P.O. Box 5800, Albuquerque, NM 87185, USA

Received 14 February 2006; Revised 9 November 2006; Accepted 22 December 2006

Titanium oxide nanotubes are prepared and treated with Au (Au/nanotube sample) and Pt (Pt/nanotube sample), and the photoactivity of these catalysts compared to a standard Degussa P25 photocatalyst is investigated. The samples were analyzed using X-ray diffraction, field emission gun scanning transmission electron microscopy (STEM). Both high-resolution TEM images and high-angle annular dark-field (HAADF) images were recorded for the specimens. Oxidation of acetaldehyde was used to test the efficiency of the catalysts. Nanotube samples showed better photoactivity than the standard P25, because the P25 titania deactivates quickly. Enhanced reactivity of the nanotube is related to surface charge polarity developed on outer and inner surfaces due to the difference in overlap of oxygen anions that resulted from curving of octahedral sheets. A tentative and qualitative surface polarity model is proposed for enhancing electron-hole pair separation. The inner surface benefits reduction; whereas, the outer surface benefits oxidation reactions. Both the metal identity and the size of the metal particles in the nanotubes affected the photocatalytic activity. Specifically, the addition of platinum increased the activity significantly, and increased the total yield. The addition of gold had lesser impact compared to the platinum. Formation of Pt large nanoparticles on the nanotube surfaces reduces the oxidation reactivity.

Copyright © 2006 Huifang Xu et al. This is an open access article distributed under the Creative Commons Attribution License, which permits unrestricted use, distribution, and reproduction in any medium, provided the original work is properly cited.

1. INTRODUCTION

Interest in photocatalysis continues to grow [1–4], reflecting the demonstrated success of these catalysts for decontamination and purification of water and air polluted by volatile organic compounds [5–7]. In particular, illuminated semiconductors have been used to oxidize compounds typically found in low concentrations in industrial effluent streams including alkanes, alkenes, phenols, aromatic acids, and surfactants [8–13]. Heterogeneous photocatalytic systems have also been used to recover metals, for example, from reductive deposition of heavy metals from wastewater streams, and to produce novel well-dispersed metal-loaded semiconductor catalysts by photodeposition of metallic ions [14].

Among photocatalytic materials, titanium oxide is believed to be the most promising, due to its great capacity for oxidation, wide band gap, nontoxicity, low cost, widespread availability, and long term stability [15]. Photocatalytic reactions involving titanium dioxide have been studied since

the 1920s when Kiedel studied the roles of titania (called “titanium white pigment” for fading in paints [16]). Interest in titania photocatalysis increased dramatically after Fujishima and Honda [1], in 1972, discovered that a rutile titanium dioxide electrode could split water illuminated by near UV light.

For the present work, we tested the photocatalytic efficiency of a new form of titanium oxide, metal-doped and metal-coated Ti-oxide nanotubes, for the oxidation of acetaldehyde [17–19] and demonstrated that these novel catalysts are better than the industrial standard P25 in long-term run. Also, following the positive results of recent literature [20–22], we tested the impact of metal addition by standard wet impregnation and found that platinum increased the maximum activity significantly, whereas gold had lesser impact. Earlier studies that showed a benefit with metal addition required the use of ion implantation or plasma processes. The present process for metal addition is clearly simpler and less costly.

2. SAMPLES AND EXPERIMENTAL METHODS

To test the impact of various treatments on the photoreactive performance of titanium oxides, we studied batches of four samples: (1) P25 (Degussa), (2) Titanium oxide nanotube, (3) Au nanoparticle-coated nanotube (Au/nanotube), and (4) Pt-treated nanotube (Pt/nanotube). Titanium oxide nanotubes are prepared by adding 1 g of P25 powder to 60 ml 10 M NaOH solution and annealing at 150°C in digestion bomb for 20 hours [23]. The products were washed using distilled water until water became neutral. Au/nanotube samples were prepared by mixing 0.5 g of wet nanotube sample and 20 ml H₂AuCl₄ solution (10 wt% Au), stirring for 30 minutes at ambient temperature. The mixture was then centrifuged to separate liquid and powder components. The powder product was washed using distilled water 5 times, dried at 110°C for 10 hours and finally, ground into fine powder. Pt/nanotube samples were prepared in a similar fashion only substituting H₂PtCl₆ solution (10 wt% Pt), for the gold compound.

The specific surface area and pore size characterization are done using a NOVA 2200 surface area and pore size analyzer (quantachrome instruments) using nitrogen gas as the adsorbate. The samples were degassed at 230°C for 20 hours before analysis. X-ray powder diffraction analyses were carried out by using a powder X-ray diffraction unit (Scintag Pad V with a Ge solid-state detector; Cu K_α radiation) with the solid specimens mounted on a low background quartz holder.

Both TEM and STEM analyses were carried out by using a Tecnai F30 field emission gun scanning transmission electron microscope equipped with an X-ray energy-dispersive spectroscopy (EDS) system (EM Vision 4.0), and a JEOL FEG-2010F field emission gun scanning transmission electron microscope (STEM) with attached Oxford instruments' X-ray energy-dispersive spectroscopy (EDS) system and Gatan imaging filtering (GIF) system. Both high-resolution TEM images and high-angle annular dark-field (HAAD) images were recorded for the specimens. HAAD imaging is a chemical sensitive technique. The local intensity of a HAAD image is approximately proportional to the square of local average atomic number (Z) [24, 25]. Therefore, it is very sensitive to detect "bright" clusters and nanoparticles of heavy metals (like Au and Pt).

The photocatalytic oxidation of acetaldehyde was done using a continuous flow reactor [26] with same flow rates for all the experiments. As shown in Figure 1, helium is passed through a sparger that was kept at 0 degree using ice and water mixture in order to carry the saturated acetaldehyde to the annular photoreactor. Oxygen was set to 20% of the total flow for all the experiments. In all cases, 25 mg of catalyst was evenly dispersed on the inner surface of the outer tube of the 12 cm long, 3 cm outer diameter, annular reactor. We placed suspensions of the photocatalysts and acetone on inner surfaces of the reactor tubes and rolled the tubes until the suspensions dry. The reactor (see Figure 2) has a total volume of nearly 13.3 cm³. The inner tube is the source of the light, a TL 8 W "black light" (Philips, Made in Holland). The space

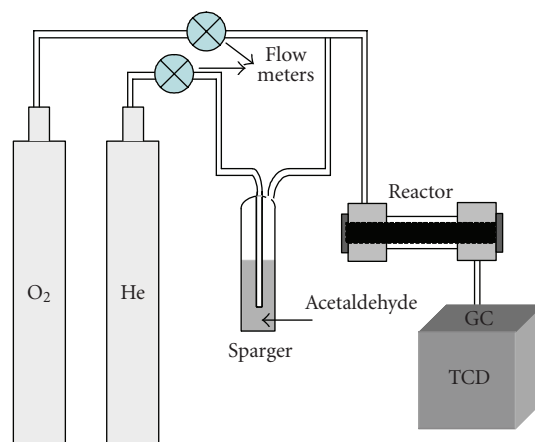


FIGURE 1: Experimental setup for the continuous photocatalysis of oxidation of acetaldehyde.

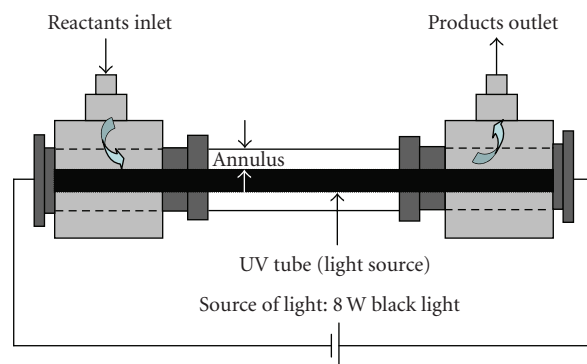


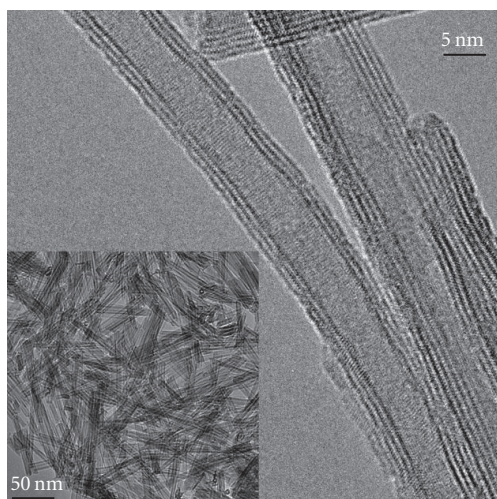
FIGURE 2: Schematic of the annular reactor.

from the lamp to the catalyst film is approximately 1 mm, which will ensure that gas phase mass transfer effects are minimized. Temperature measurement with a thermocouple showed that during operation the catalyst was at about 50°C.

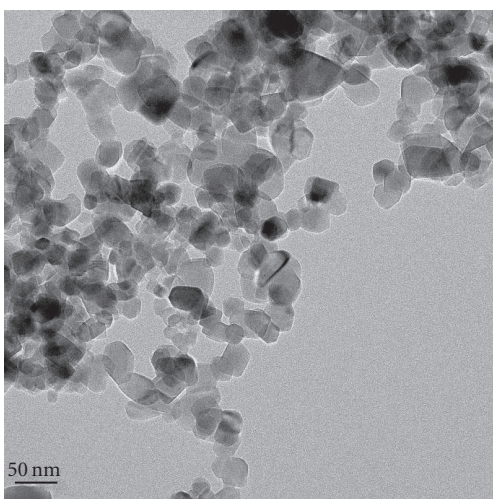
Both product and reactant (sequentially in all cases) analysis was performed using the thermal conductivity detector function of an HP 5890 series II gas chromatography (GC) equipped with a 10-port valve. A Haysep D column (8 feet × 1/8 inch SS) was employed to separate acetaldehyde, acetic acid, carbon dioxide, carbon monoxide, and water at ambient temperature. All the experiments were carried at similar conditions. The purpose of the experiments is to obtain relative reactivity of the nanotube-based photocatalysts with respect to P25 titania.

3. RESULTS

Figure 3 shows the TEM image of the pure titanium oxide nanotubes (top) and a reference photocatalyst of Degussa P25 titania (bottom). It can be seen that the nanotube sample consists of low-defect density nanotubes virtually all of which have an inner diameter of ~4–6 nm. This nanotube is basically Na-titanate nanotube with chemical formula of



(a)



(b)

FIGURE 3: (a) High-resolution TEM image and bright-field TEM image (insert at the low-left corner) of the pure titanium oxide nanotube; (b) bright-field TEM image of the P25 titania with size range of about 20–60 nm.

(Na, H)₂Ti₃O₇ [27, 28]. P25 titania is a mixture of anatase (84%) and rutile (16%) nanocrystals based on our quantitative X-ray analysis using Rietveld method with a software GSAS (see Figure 4). X-ray diffraction pattern from the nanotube sample displays very broad peaks due to curved (001) lattice planes and thin tube walls (see Figure 5). The measured surface areas using multipoint BET method for the P25 titania and nanotube samples are 61 m²/g, and 149 m²/g, respectively.

Figure 6(a) shows the HAAD image of Au/nanotube sample. It clearly shows Au nanoparticles (bright spots) with diameter of ~1 nm attached to the nanotube surfaces. Figure 6(b) shows the HAAD image of Pt/nanotube sample. The HAAD image does not show visible Pt clusters on the nanotube surfaces. However, X-ray EDS spectra clearly show

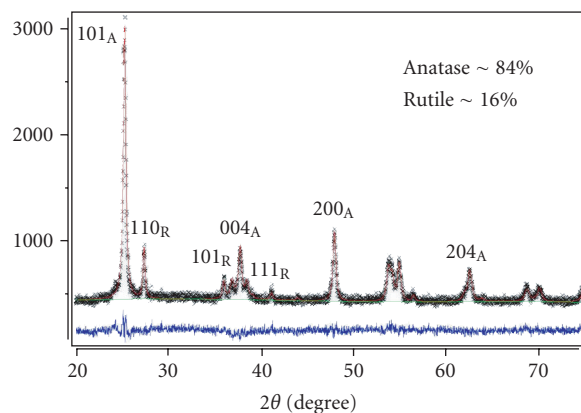


FIGURE 4: X-ray powder diffraction pattern from the P25 titania photocatalyst. Quantitative analysis using Rietveld method shows that photocatalyst contains 84% of anatase and 16% of rutile.

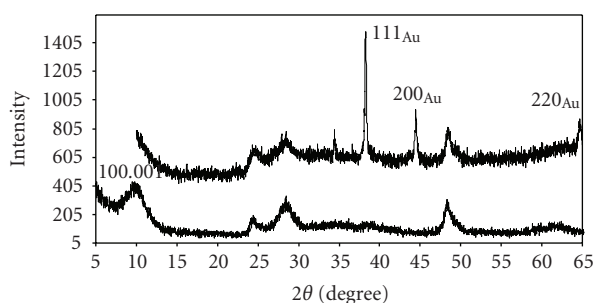


FIGURE 5: X-ray powder diffraction pattern of the Ti-oxide nanotube (bottom), and Au-treated nanotube sample with large gold nanocrystals (upper) showing broad diffraction peaks due to curving of (001) lattice planes and thin crystal sheets from the nanotubes and relatively sharp peaks from gold.

the Pt in the nanotubes. It is suggested that Pt (that may be sorbed on nanotube surface in forms of cation and/or metal complex) are distributed evenly on both outer and inner surfaces of the nanotubes. In order to test the effect of nanoparticle size on the photo reactivity, we prepared the nanotubes coated with large Au and Pt particles by heating the Au and Pt treated nanotubes at 150°C for over night). HAAD images show relatively large Au and Pt nanocrystals (see Figure 7). An XRD pattern from the Au-coated nanotube sample clearly displays strong peaks from gold nanocrystals (see Figure 5).

Reactivity testing showed that all the novel catalysts studied are better (per gram) than the standard titania catalysts, P25 from Degussa, for the oxidation reaction studied. Acetaldehyde was readily oxidized to carbon dioxide at room temperature on all titania samples when the UV lights were turned on, as shown in Figure 8. In all the cases, the rate of photocatalytic oxidation (per gram) was plotted as a function of time. Except for the pure nanotube sample, all other photocatalysts decrease in their reactivity. Indeed, deactivation during hydrocarbon oxidation processes has been noted and studied repeatedly for high concentration experiments in

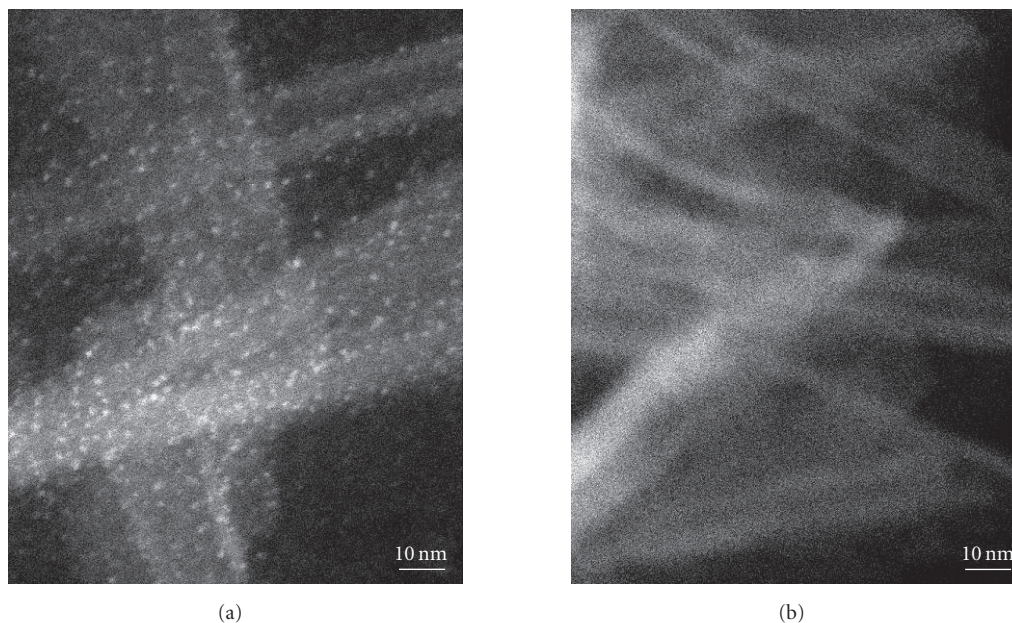


FIGURE 6: HAAD images of the Au-treated nanotube sample (a) and Pt-treated nanotube sample (b).

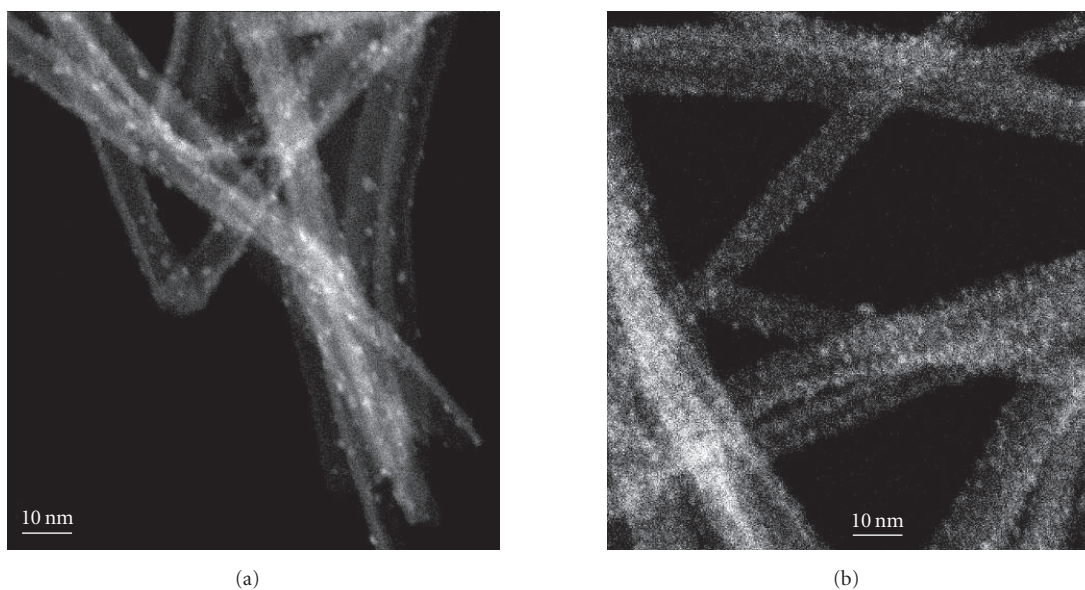


FIGURE 7: HAAD scanning transmission electron microscopic (STEM) images of the nanotube samples with large Au particles (a) and the sample with large Pt particles (b).

recent years [29, 30] and there are several proposals for the mechanism of this deactivation [31].

As noted above, all the catalysts were more active than the standard material, P25. In the case of nanotube without metal addition, the activity is similar based on same weight and less reactive based on per unit surface area, initially. However, P25 rapidly deactivates and the nanotube photocatalytic activity actually increases slightly. Pt containing nanotube is a dramatically better catalyst than P25. The

highest activity of this catalyst is more than 10 times the maximum rate of P25, and more than 6 times maximum rate of the pure nanotube sample. It must be noted that the reported relative rates closely reflect relative intrinsic rates with respect to P25 titania. After the reaction, the white Pt/nanotube specimen became grayish. Our TEM results show some Pt nanodots (<1 nm) formed on the nanotube surfaces (see Figure 9). It is suggested that the nanotubes with uniformly distributed Pt (ions and metal complex) are

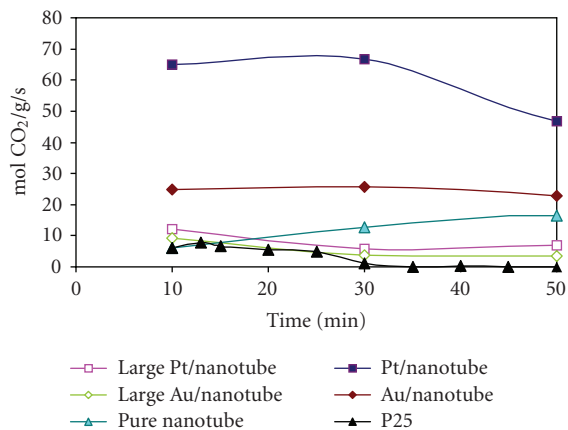


FIGURE 8: Photocatalytic oxidation rates of various titanium-oxide-based catalysts.

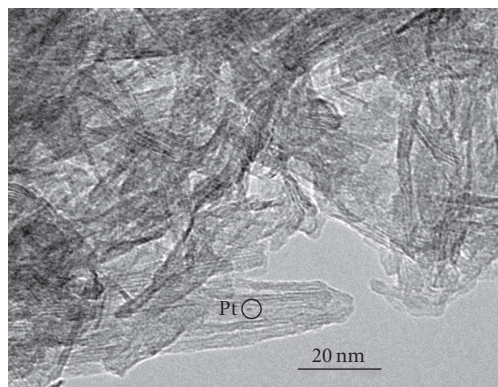


FIGURE 9: TEM image showing Pt dots without crystalline feature on the nanotube after photocatalytic reaction of the Pt/nanotube sample. The nanotubes become less regular in shape after treatment in acidic solutions.

more photo reactive than those with large Pt nanoparticles. The maximum activity of Au containing nanotube was not as high as that of the platinum-bearing sample, but still it reached an activity more than twice the maximum rate of the pure nanotube sample. It is also found that the reactivity decreased with larger particles. The nanotube samples coated with about 2 ~ 4 nm Au and Pt nanoparticles (see Figure 7) showed lower photo-reactive rates compared to the Au/nanotube and Pt/nanotube samples (see Figure 8).

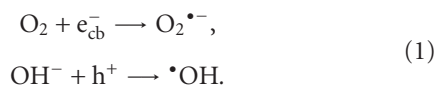
4. DISCUSSIONS

Initial activity studies of the photocatalytic activity of titanium oxide nanotubes showed that these materials have the potential for widespread application. Indeed, the measured activity for “neat” nanotubes for photocatalytic oxidation (PCO) of low concentrations of acetaldehyde at room temperature showed them to be more active than the standard material, P25. Metal addition, by a standard wet impregnation process, particularly platinum addition, increased the

activity to the point that it is more than an order of magnitude better than the standard. Many more studies are required to understand the characteristic of these materials that increases the activity so dramatically.

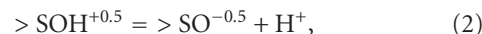
It is generally believed that the photocatalytic process occurs because light of sufficient energy (e.g., greater than the optical band gap of Ti-oxides, 3–3.2 eV, i.e., 388–413 nm) excites electrons in semiconductors from the valence band to the conduction band that can either recombine and release great amounts of energy, or migrate to the surface where they are available for reduction and oxidation reactions by charge transfer to species adsorbed onto the semiconductor surface.

The mechanism of TiO₂ photocatalyzed reactions is that superoxide, O₂⁻, and specifically, hydroxyl radicals, •OH, act as active reagents for the mineralization of the organic compounds [15, 17]. The radicals are formed by the scavenging of the electron-hole pair by molecular oxygen and water following equation (1):



Insertion of •OH radicals into C–H bonds leads ultimately to the complete oxidation of the organic substrate. Indeed, complete mineralization of a variety of organic compounds, such as phenols, hydrocarbons, carboxylic acids, and chlorinated aliphatic and olefinic compounds, has been realized. Thus, as mentioned above, one feature of photocatalysts that impacts activity is the structure of the absorption band edge and separation of the electron-hole pairs. Small modifications in the impurity concentration or structure of titania are known to effect the structure of the absorption band edge. As the nanotubes are neither rutile nor anatase [27, 28], the two phases of pure titania and the structures are generally believed to be the best photocatalysts, the adsorption band edge of the nanotubes could be different, and that could account for its high observed reactivity. Our recent study shows that the band gap of the nanotube (3.1 eV) is very close to that of anatase (3.2 eV). It is also proposed that the surface of curved octahedral sheets of the nanotubes may be more reactive than normal titania crystal surface due to electrical polarity developed between the inner and outer surfaces.

The deprotonation/prototation reaction on oxide surface in aqueous solution can be simplified as



where $> \text{SOH}^{+0.5}$ is protonated (positively charged) surface site, and $> \text{SO}^{-0.5}$ is deprotonated (negatively charged) surface site [32–35]. Its equilibrium constant K will be expressed as

$$K = \frac{[> \text{SO}^{-0.5}][\text{H}^+]}{[> \text{SOH}^{+0.5}]}, \quad (3)$$

where K can be related to pK by a relationship of

$$pK = -\log K. \quad (4)$$

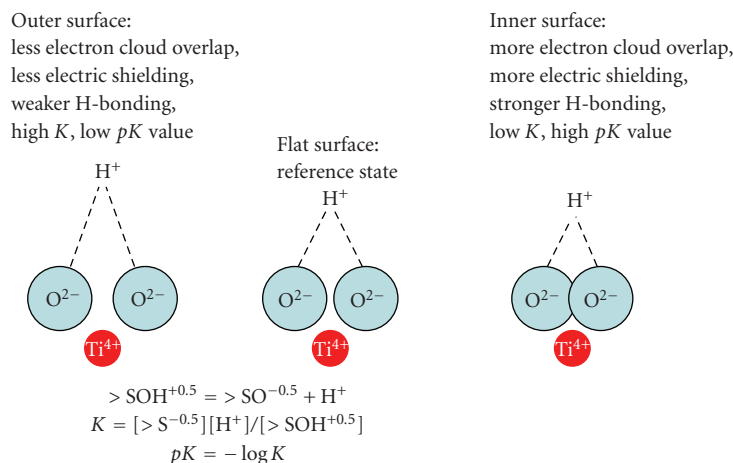


FIGURE 10: Models illustrate oxygen ions on inner surface (right) and outer surface (left) of the nanotube. The degree of electron clouds overlap between neighboring oxygen directly affect electric charge shielding from Ti^{4+} , and therefore determines the bonding strength between H^+ and surface oxygen. “> S” represents surface of the nanotube.

When the octahedral sheets (or nanoplates) are rolled into nanotubes, the inner surface oxygen atoms will be closer than those on flat surface, which will result in more electron clouds overlaps, and shielding from Ti^{4+} in the center of octahedra. This will result in strong bonding between H^+ and surface oxygen, or more protonated surface sites (see Figure 10). The effect will be opposite on the outer surface (with positive curvature). This will result in difference in surface protonation or surface acidity, that is, pK value of the inner surface will be higher than that of flat surface; and the pK value of outer surface will be lower than that of flat surfaces. Based on the proposed mechanism in Figure 10, it can be inferred that the inner surface of the nanotube has high acidity, and the outer surface has lower acidity.

The different surface acidities will result in different charges on inner and outer surfaces, or electrical polarity. In a solution at certain pH conditions, outer surface will display net negative charge and inner surface will display net positive charge (see Figure 11). The electrical polarity will enhance electron-hole separation, and therefore leading positive holes in the valence band to the outer surface for photo-catalytic oxidation, and electrons in the conduction band to the inner surface for photo-catalytic reduction and even reduction of water to hydrogen (see Figure 11).

Our data from photo-catalytic oxidation of acetaldehyde (a VOC) shows that reactivity of the nanotube and Degussa P25 titania is very similar at the beginning (relatively dry) based on same weight (see Figure 8). After 30 minutes of reaction, the reactivity of P25 decreases dramatically. However, the reactivity of nanotube increases (see Figure 8). We propose that the development of electrical polarity on the nanotube surface in aqueous system enhances the charge separation and photocatalytic oxidation (see Figures 10 and 11). The oxidation of acetaldehyde will produce water and carbon dioxide through the net reaction of

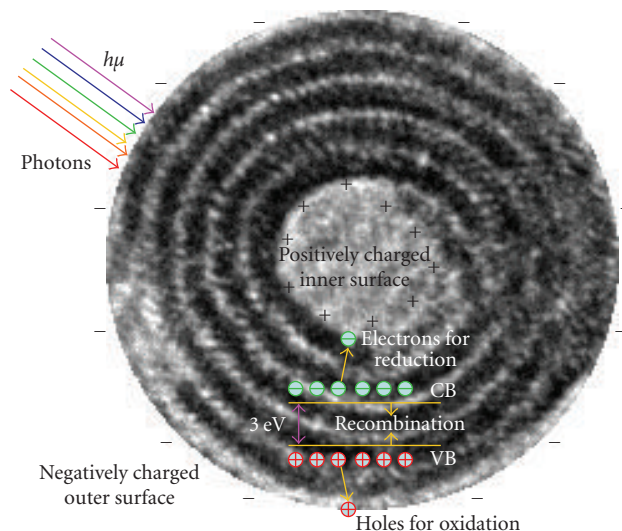


FIGURE 11: A diagram showing Ti-oxide nanotube with positive charges on inner surface and negative charges on outer surface in aqueous solution, which will enhance charge separation of electron-hole pairs (i.e., migration of negatively charged electrons to the inner surface and positively charged holes to the outer surface). See reactions (1) for generation of radicals by incorporating electrons and holes, CB = conduction band, VB = valence band.

Water and CO_2 will result in weak acidic solution sorbed on the nanotube surfaces, which enhances surface polarity and drives the oxidation further.

The testing of the impact of metal additives in the present work reflects recent findings by others. For example, Anpo et al. [17] showed that metal ion implantation can dramatically change the photo-activity of titania for NO reduction. Other works [20, 21] indicate that “plasma treated” doped titania shows improved performance for some photo-activated processes. Yet, more recent works [21, 22] suggest

that N-doped titania is a more effective catalyst for some frequency ranges than undoped titania. Notably, all earlier studies used high-energy processes to add metal “dopants” to the lattice in order to modify the photoadsorption edge, per the theory discussed above. In several of these earlier studies, it was found that the high energy doping processes modified other characteristics of the material, notably the phase. Thus, simple correlations of changed activity with band-gap and surface reactivity are suspect. The results of the present paper show that simple, standard methods of metal addition (such as the Pt/nanotube sample), without the need for “ion implantation” or other complex and expensive processes, can dramatically improve the performance of titanium oxide for some (i.e., hydrocarbon oxidation) photocatalytic reactions, although the influence of “band edge” changes on photocatalytic activity is not clear.

5. CONCLUSIONS

The titanium oxide nanotube is a potential catalyst for photocatalytic oxidation of low concentrations of acetaldehyde at room temperature. The commercial P25 deactivates quickly in the photo-oxidation of acetaldehyde. The pure nanotube is more reactive than P25 titania in long run. The bending and curving of the Ti–O octahedral sheets results in electrical polarity being developed on outer and inner surfaces, which enhances the electron-hole separation and the observed photo oxidation by the nanotubes. Both Au- and Pt-treated nanotube samples increase the photo reactivity. However, size of the Au and Pt nanoparticles on the nanotube surfaces likely affected the photo reactivity. Large size of the Au and Pt particles will decrease the photo reactivity. Specifically, the addition of platinum without formation of obvious nanoparticles on the nanotube surfaces increased the maximum activity significantly, and increased the total yield. The thin films of the titanium oxide nanotube could be further tested in a scaled-up photocatalytic reactor.

ACKNOWLEDGMENTS

This work was supported by NSF (EAR02-10820), the University of New Mexico, and the Graduate School of the University of Wisconsin-Madison. Authors thank three reviewers for critical comments and suggestions.

REFERENCES

- [1] O. Legrini, E. Oliveros, and A. M. Braun, “Photochemical processes for water treatment,” *Chemical Reviews*, vol. 93, no. 2, pp. 671–698, 1993.
- [2] M. A. Fox and M. T. Dulay, “Heterogeneous photocatalysis,” *Chemical Reviews*, vol. 93, no. 1, pp. 341–357, 1993.
- [3] A. Hagfeldt and M. Graetzel, “Light-induced redox reactions in nanocrystalline systems,” *Chemical Reviews*, vol. 95, no. 1, pp. 49–68, 1995.
- [4] P. V. Kamat, “Photochemistry on nonreactive and reactive (semiconductor) surfaces,” *Chemical Reviews*, vol. 93, no. 1, pp. 267–300, 1993.
- [5] H. Gerischer and A. Heller, “Photocatalytic oxidation of organic molecules at TiO₂ particles by sunlight in aerated water,” *Journal of the Electrochemical Society*, vol. 139, no. 1, pp. 113–118, 1992.
- [6] N. B. Jackson, C. M. Wang, Z. Luo, et al., “Attachment of TiO₂ powders to hollow glass microbeads. Activity of the TiO₂-coated beads in the photoassisted oxidation of ethanol to acetaldehyde,” *Journal of the Electrochemical Society*, vol. 138, no. 12, pp. 3660–3664, 1991.
- [7] M. Nair, Z. Luo, and A. Heller, “Rates of photocatalytic oxidation of crude oil on salt water on buoyant, cenosphere-attached titanium dioxide,” *Industrial and Engineering Chemistry Research*, vol. 32, no. 10, pp. 2318–2323, 1993.
- [8] R. Cai, K. Hashimoto, K. Itoh, Y. Kubota, and A. Fujishima, “Photokilling of malignant cells with ultrafine TiO₂ powder,” *Bulletin of the Chemical Society of Japan*, vol. 64, no. 4, pp. 1268–1273, 1991.
- [9] G. Mills and M. R. Hoffmann, “Photocatalytic degradation of pentachlorophenol on titanium dioxide particles: identification of intermediates and mechanism of reaction,” *Environmental Science and Technology*, vol. 27, no. 8, pp. 1681–1689, 1993.
- [10] C. Kormann, D. W. Bahnemann, and M. R. Hoffmann, “Photolysis of chloroform and other organic molecules in aqueous titanium dioxide suspensions,” *Environmental Science and Technology*, vol. 25, no. 3, pp. 494–500, 1991.
- [11] A. Chemseddine and H. P. Boehm, “A study of the primary step in the photochemical degradation of acetic acid and chloroacetic acids on a TiO₂ photocatalyst,” *Journal of Molecular Catalysis*, vol. 60, no. 3, pp. 295–311, 1990.
- [12] H. Hidaka, J. Zhao, E. Pelizzetti, and N. Serpone, “Photodegradation of surfactants. 8. Comparison of photocatalytic processes between anionic DBS and cationic BDDAC on the titania surface,” *Journal of Physical Chemistry*, vol. 96, no. 5, pp. 2226–2230, 1992.
- [13] E. Pelizzetti, C. Minero, P. Piccinini, and M. Vincenti, “Phototransformations of nitrogen containing organic compounds over irradiated semiconductor metal oxides. Nitrobenzene and atrazine over TiO₂ and ZnO,” *Coordination Chemistry Reviews*, vol. 125, no. 1-2, pp. 183–193, 1993.
- [14] M. R. Prairie, L. R. Evans, B. M. Stange, and S. L. Martinez, “An investigation of titanium dioxide photocatalysis for the treatment of water contaminated with metals and organic chemicals,” *Environmental Science and Technology*, vol. 27, no. 9, pp. 1776–1782, 1993.
- [15] A. J. Bard, “Photoelectrochemistry,” *Science*, vol. 207, no. 4427, pp. 139–144, 1980.
- [16] E. Keidel, “Die Beeinflussung der Lichtechtheit von Teerfarblacken durch Titanweiss [Influence of titanium white on the fastness to light of coal-tar dyes],” *Farben-Zeitung*, vol. 34, pp. 1242–1243, 1929.
- [17] M. Anpo, “Use of visible light. Second-generation titanium oxide photocatalysts prepared by the application of an advanced metal ion-implantation method,” *Pure and Applied Chemistry*, vol. 72, no. 9, pp. 1787–1792, 2000.
- [18] S. Luo and J. L. Falconer, “Aldol condensation of acetaldehyde to form high molecular weight compounds on TiO₂,” *Catalysis Letters*, vol. 57, no. 3, pp. 89–93, 1999.
- [19] S. Luo and J. L. Falconer, “Acetone and acetaldehyde oligomerization on TiO₂ surfaces,” *Journal of Catalysis*, vol. 185, no. 2, pp. 393–407, 1999.
- [20] H. Yamashita, M. Harada, J. Misaka, M. Takeuchi, K. Ikeue, and M. Anpo, “Degradation of propanol diluted in water under visible light irradiation using metal ion-implanted

- titanium dioxide photocatalysts," *Journal of Photochemistry and Photobiology A: Chemistry*, vol. 148, no. 1–3, pp. 257–261, 2002.
- [21] I. Nakamura, N. Negishi, S. Kutsuna, T. Ihara, S. Sugihara, and K. Takeuchi, "Role of oxygen vacancy in the plasma-treated TiO₂ photocatalyst with visible light activity for NO removal," *Journal of Molecular Catalysis A: Chemical*, vol. 161, no. 1–2, pp. 205–212, 2000.
- [22] K. Takeuchi, I. Nakamura, O. Matsumoto, S. Sugihara, M. Ando, and T. Ihara, "Preparation of visible-light-responsive titanium oxide photocatalysts by plasma treatment," *Chemistry Letters*, vol. 29, no. 12, pp. 1354–1355, 2000.
- [23] T. Kasuga, M. Hiramatsu, A. Hoson, T. Sekino, and K. Niihara, "Formation of titanium oxide nanotube," *Langmuir*, vol. 14, no. 12, pp. 3160–3163, 1998.
- [24] P. D. Nellist and S. J. Pennycook, "Accurate structure determination from image reconstruction in ADF STEM," *Journal of Microscopy*, vol. 190, no. 1–2, pp. 159–170, 1998.
- [25] E. J. Kirkland, R. F. Loane, and J. Silcox, "Simulation of annular dark field stem images using a modified multislice method," *Ultramicroscopy*, vol. 23, no. 1, pp. 77–96, 1987.
- [26] G. Vanamu, "Study of modification of irregular titania powder passed as an aerosol through a low power microwave plasma torch and its application as a photocatalyst," M.S. thesis, University of New Mexico, Albuquerque, NM, USA, 2002.
- [27] G. H. Du, Q. Chen, R. C. Che, Z. Y. Yuan, and L.-M. Peng, "Preparation and structure analysis of titanium oxide nanotubes," *Applied Physics Letters*, vol. 79, no. 22, pp. 3702–3704, 2001.
- [28] Q. Chen, G. H. Du, S. Zhang, and L.-M. Peng, "The structure of trititanate nanotubes," *Acta Crystallographica Section B: Structural Science*, vol. 58, part 4, pp. 587–593, 2002.
- [29] M. Anpo, "Use of visible light. Second-generation titanium oxide photocatalysts prepared by the application of an advanced metal ion-implantation method," *Pure and Applied Chemistry*, vol. 72, no. 9, pp. 1787–1792, 2000.
- [30] S. Luo and J. L. Falconer, "Aldol condensation of acetaldehyde to form high molecular weight compounds on TiO₂," *Catalysis Letters*, vol. 57, no. 3, pp. 89–93, 1999.
- [31] J. L. Falconer and K. A. Magrini-Bair, "Photocatalytic and thermal catalytic oxidation of acetaldehyde on Pt/TiO₂," *Journal of Catalysis*, vol. 179, no. 1, pp. 171–178, 1998.
- [32] W. H. Van Riemsdijk, G. H. Bolt, L. K. Koopal, and J. Blaakmeer, "Electrolyte adsorption on heterogeneous surfaces: adsorption models," *Journal of Colloid and Interface Science*, vol. 109, no. 1, pp. 219–228, 1986.
- [33] W. H. Van Riemsdijk, J. C. M. De Wit, L. K. Koopal, and G. H. Bolt, "Metal ion adsorption on heterogeneous surfaces: adsorption models," *Journal of Colloid and Interface Science*, vol. 116, no. 2, pp. 511–522, 1987.
- [34] L. K. Koopal and W. H. Van Riemsdijk, "Electrosorption on random and patchwise heterogeneous surfaces: electrical double-layer effects," *Journal of Colloid and Interface Science*, vol. 128, no. 1, pp. 188–200, 1989.
- [35] C. Contescu, J. Jagiello, and J. A. Schwarz, "Chemistry of surface tungsten species on tungsten trioxide/alumina composite oxides under aqueous conditions," *Journal of Physical Chemistry*, vol. 97, no. 39, pp. 10152–10157, 1993.

Porous and Nanoporous Semiconductors and Emerging Applications

Helmut Föll, Jürgen Carstensen, and Stefan Frey

Chair for General Materials Science, Faculty of Engineering, Christian-Albrechts-University of Kiel, 24143 Kiel, Germany

Received 15 March 2006; Revised 14 September 2006; Accepted 3 October 2006

Pores in single-crystalline semiconductors can be produced in a wide range of geometries and morphologies, including the “nanometer” regime. Porous semiconductors may have properties completely different from the bulk, and metamaterials with, for example, optical properties not encountered in natural materials are emerging. Possible applications of porous semiconductors include various novel sensors, but also more “exotic” uses as, for example, high explosives or electrodes for micro-fuel cells. The paper briefly reviews pore formation (including more applied aspects of large area etching), properties of porous semiconductors, and emerging applications.

Copyright © 2006 Helmut Föll et al. This is an open access article distributed under the Creative Commons Attribution License, which permits unrestricted use, distribution, and reproduction in any medium, provided the original work is properly cited.

1. INTRODUCTION

The dominant role of silicon in microelectronics along with the discovery of light-emitting nanoporous Si [1, 2] has focused electrochemical investigations on this semiconductor even before 1991, and a large range of possible applications has emerged (for a recent review see [3]). While porous silicon was already discovered in 1957 by Uhlir [4] (but not recognized for what it was), it took until 2000 to find conditions for pore production in Ge [5–7]. Investigations of porous III–V semiconductors (mainly GaP, GaAs, InP) were also done more recently; see [8]. Pores in GaN [9], SiC [10, 11], and ZnSe [12] have also been reported in the meantime, and the exploration of the available parameter space is an ongoing activity in many laboratories (cf. [13]).

2. POROSIFICATION OF SEMICONDUCTORS

It is helpful to first define a few terms to classify the tremendous variety of pores (cf. Figure 1). Pore *geometry* refers to (average) diameters of pores and distances between pores, that is, to the pore dimensions, while pore *morphology* addresses the pore shape (e.g., cylindrical, branched, faceted, fractal, ...).

According to IUPAC standards, micro-, meso-, or macropores refer to pores with typical dimensions of < 2 nm, 2 nm–50 nm, or > 50 nm, respectively. The term “nanopores” thus is open to interpretation; here we use it somewhat loosely for pore dimensions well below 1 μm .

Generally, porosification can be obtained by anodizing the semiconductor in a suitable electrolyte, under suitable conditions. The necessary chemical reaction at the semiconductor-electrolyte interface is generally a mixture of direct dissolution, oxide formation, and oxide dissolution, with details sensitive to many parameters, for example, electrolyte chemistry, applied potential or current density, temperature, flow conditions of the electrolyte, doping type and level of the semiconductor, illumination state of the semiconductor (front or backside), and surface conditions (polished, rough, masked). The overall reaction may occur uniformly as electropolishing (often observed at high current densities) nonuniformly but everywhere on the surface, or highly localized including some self-organization—this is then the pore-producing mode.

While many details of the pore formation mechanism are still unclear, a few general statements can be made here. During pore formation, direct dissolution of the semiconductor almost always competes with oxidation plus subsequent dissolution of the oxide. The electrolyte therefore has to be able to dissolve the oxide. In the case of silicon, fluoride-containing electrolytes are thus mandatory, while for other semiconductors the choice is more relaxed (GeO₂, e.g., even dissolves in water). A second prerequisite for the dissolution reaction and thereby pore formation in a semiconductor is electronic holes. In general, at least one hole is needed to initiate the reaction chain at the interface that ultimately leads to the “loss” of one atom (or molecule in the case of compound semiconductors). One of the major “tricks” for

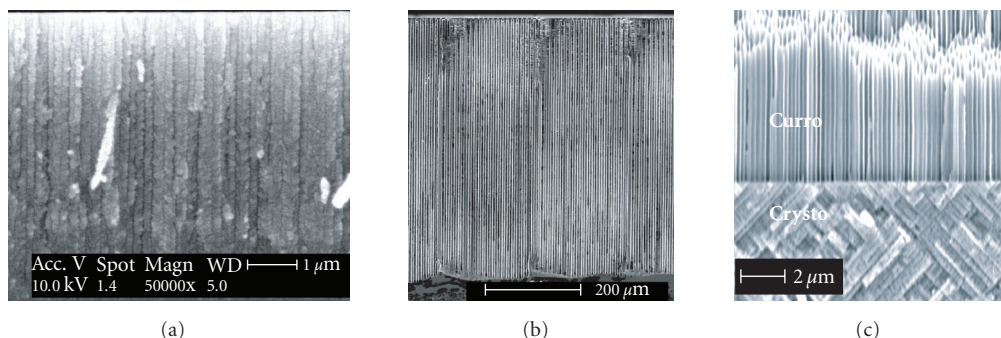


FIGURE 1: Variety of pores in semiconductors: (a) mesopores in Si, (b) macropores in Si with lithographic prestructuring, (c) “Curro”-“Crysto” transition in InP.

successful porosification experiments is to supply holes only locally. This trick obviously works only in n -doped material, where holes are the minority carriers. Holes then may be supplied by illumination [14], or via electrical tunneling or avalanche breakdown of the material due to high field strengths, as it is the case for the pores in III–V compounds [8]. However, while so far no pores could be obtained in most p -doped semiconductors, Si, SiC [15], and very recently Ge [7, 16] provide the exceptions.

In the case of p -type materials it is necessary to drive the system in a state where holes can only be consumed at certain places. Generally, one operates in a regime with insufficient oxidation, either by a low current density (p -type macropores in aqueous electrolytes [17]) or by using electrolytes that inherently produce worse and less oxide [3]. Alternatively, the use of a highly doped semiconductor, where most of the voltage is dropped on the electrolyte side of the junction, leads to a “fast” chemistry favoring direct dissolution in comparison to anodic oxidation (p -type mesopores), again enhancing passivation relative to oxidation aspects during dissolution. Micropores in p -type Si are yet a different case; at least parts of their formation are due to quantum wire effects [2]. However, while a “quantum-wire model” can account for micropores in Si, it is not specific to Si and thus fails to account for the absence of micropores in most other semiconductors up to now.

Pore formation in semiconductors is a highly interdisciplinary enterprise. There are even reasons to believe that the dissolution of the semiconductor electrode and all aspects of pore formation can only be sufficiently described by invoking in addition to all that was mentioned before, a stochastic component including self-organization in time and space, as championed in the “current burst” model [18].

3. ETCHING AND ETCHING EQUIPMENT

In order to obtain reproducible results, it is almost inevitable to use a potentiostat or a galvanostat with one or two reference electrodes instead of a simple power supply. While early experiments with illumination employed halogen lamps (with cold filters), high-intensity IR-LED arrays offer more flexibility and higher intensity for this kind of

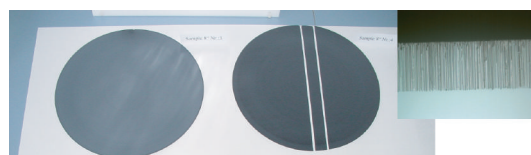


FIGURE 2: First electrochemically etched 200 mm p -type wafers (inset: macropores in organic electrolyte; the most demanding etching process).

experiments (for detailed information on all used hardware, see [19]). All chemical processes are strongly influenced by temperature, making it unavoidable to use computer-controlled cooling/heating systems with temperature stability in the 0.1°C region. To ensure constant electrolyte conditions at the interface, a rapid movement of the electrolyte is also unavoidable. Simple magneto-stirrers (or no stirring at all) will quickly lead to an insufficient uniformity in space and time. Considering that many electrolytes are highly dangerous and/or corrosive, these are demanding conditions even for small samples with areas in the 1 cm^2 region, while the uniform etching of whole wafers becomes rather complex from a technical point of view.

To produce homogeneous porous layers over whole wafers a few setups have been proposed [3, 20], which, however, address only parts of the parameter space. Our group has developed and commercialized [19] a large-area etcher meeting all requirements (including safety issues). The wafer is put on a vacuum chuck and hung head-over into the electrolyte. The electrolyte convection is ensured via a rocking table, on which the whole setup is mounted. Because the wafer and etching cell form an almost seamless surface, the rocking motion is enough to ensure sufficient and—on time average—a uniform electrolyte flow. This avoids potentially dangerous pumping equipment and allows an all-Teflon design, which can accommodate even ultra-aggressive electrolytes, for example, HF/organic solvent mixtures which dissolve practically everything except Teflon. Wafers up to 200 mm diameter have been processed with superb uniformity (cf. Figure 2), and a scale-up to 300 mm is possible.

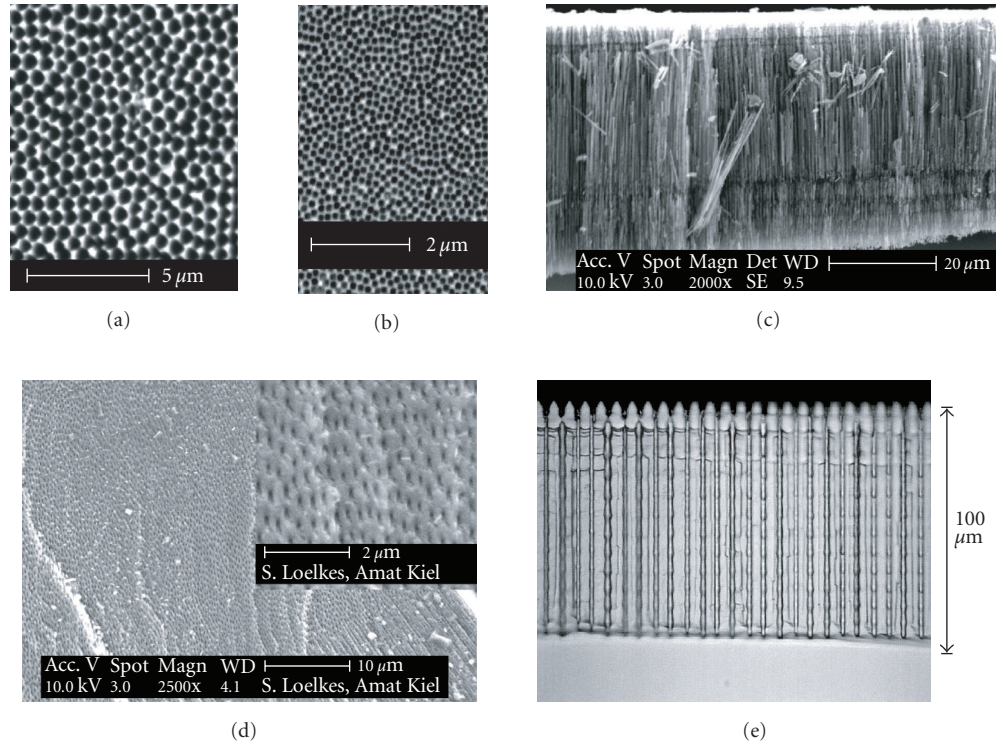


FIGURE 3: Fast pore etching in Si. (a) Plain view of pores on a (111) surface with hexagonal self-ordering. (b) On (100), a geometrically frustrated ordering of pores is evident. (c) Cross-section ((111) sample). (d) Homogeneous pore distribution of 100 nm pores in the cross-section of (111)-Si. (e) “Pulsed” fast macropore growth to a depth of 100 μm .

4. MACRO-, MESO-, AND MICROPORES IN SILICON

Macropores in Si were first discovered in 1990 [14], they are slowly growing (ca. $1 \mu\text{m}/\text{min}$) cylindrical pores with diameters between 350 nm and $10 \mu\text{m}$ which are normally proceeding in $\langle 100 \rangle$ and $\langle 113 \rangle$ directions [3]. It is nearly impossible with other techniques to obtain such extreme aspect ratios. An inherent disadvantage of the standard macropore process (n -Si under intense backside illumination) is the slow growth rate coupled to the necessarily low HF concentrations in this mode, which is a severe problem for any mass-production. However, our group has made some recent progress to boost the etching speed exploring two routes:

- (i) coupling high HF-concentrations with a pulsed etching voltage while still employing backside illumination;
- (ii) employing a less oxidizing organic electrolyte at high HF concentrations run in the breakdown mode without illumination [21].

In the first case the standard backside illumination setup is used, where a HF concentration higher than 6 wt.% normally would lead to unacceptable bad pore morphologies (heavy branching, rough walls, etc.). This effect can be suppressed if the etching bias is periodically pulsed. While the pore diameter responds somewhat to the pulsing, the generation of side pores is largely suppressed with a drastic increase of etching speed (up to $4 \mu\text{m}/\text{min}$, cf. Figure 3(e)).

In the second case it was attempted to mimic pore growth conditions as encountered in InP, where it is possible to generate beautiful pore arrays [22] with high etching rates. The hole generation in this case is confined to electrical breakdown, in contrast to standard macropore etching configuration, where breakdown is avoided because it generates small side pores which can perforate the whole pore walls (cf. Figures 3, 5, and 6). The second ingredient predicted from an analysis of the InP pores was the suppression of oxide formation by using an organic solvent (acetonitrile (MeCN) or dimethylformamide (DMF)) instead of water, supplemented by suitable salts because of the low conductivity of organic solvents. The growth speed in this case is then directly coupled to the oxide dissolution rate, as this process is by far the slowest process [18]. Therefore the HF concentration was pushed to 15–20 wt%, under conditions which normal macropore growth does not proceed properly anymore.

First results were encouraging. Figure 3 shows some examples. As in InP, some self-organization was observed: on a (111) surface, where close packing induced ordering of pores and the natural threefold crystallographic symmetry harmonize, a high degree of hexagonal self-ordering was found, albeit not as pronounced as in the InP case. While on (100) InP, pores are still forming hexagonal arrays [22]; on (100) Si a completely new self-organization feature was found: the formation of a so-called “frustrated crystal.” Since the four-fold symmetry of the crystal is competing with the hexagonal symmetry of close-packing, a geometrically frustrated

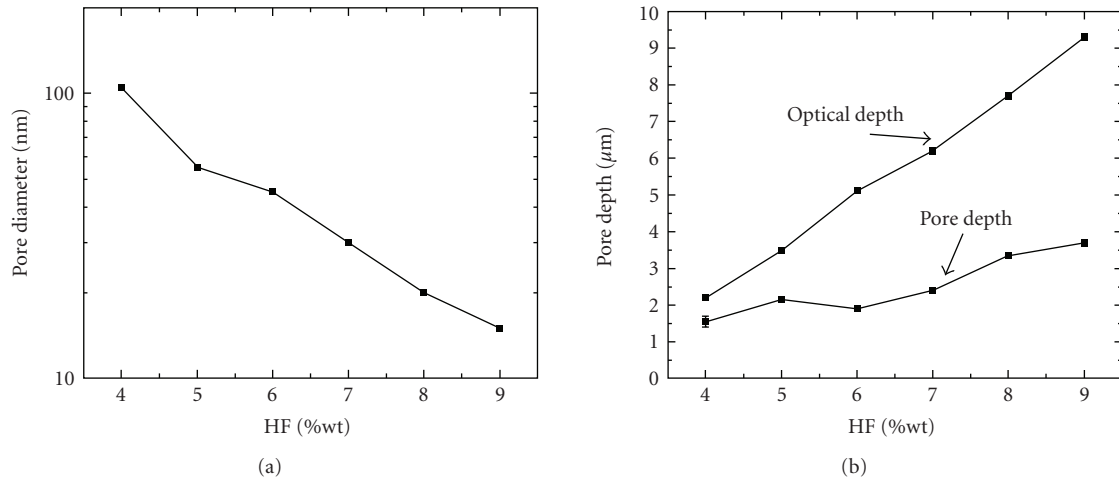


FIGURE 4: (a) Diameter and (b) depth of mesopores on *n*-Si ($100, \rho = 5\text{--}20 \Omega\text{cm}$), $j = 30 \text{ mA/cm}^2$, $t_{\text{etch}} = 100$ seconds. The “optical thickness” (ellipsometer) differs from the geometric thickness, because the pore density decreases, while the refractive index increases with increasing HF concentration.

distribution of pores results, with no angular correlation of nearest neighbor positions, but a strong correlation for second-nearest neighbors. This is a very appealing configuration for fundamental optic and magnetic investigations since it has a well-defined structure but without translational symmetry, which could, for example, cause unwanted Moiré patterns. It has to be stressed that these “macro” pores are not subject to the standard restrictions for macropores (i.e., growth speed $1 \mu\text{m}/\text{min}$, and diameter $> 200 \text{ nm}$) as can be seen from Figure 3, where several examples are shown with 100 nm pores; hence the regime of mesopores (following the strict IUPAC convention) is within reach.

Standard mesopores in Si are always grown on heavily doped samples and at relatively high HF concentrations, which necessitates only a few volts to drive large etching currents. The growth rates can reach several $10 \mu\text{m}/\text{min}$, which indicates that direct dissolution of silicon is the major process. The resulting morphology is a network of needle-like and heavily branched pores (cf. Figure 1(a)). Figure 4 shows the dependence of pore diameter and pore depth on fluoride concentration for *n*-type Si (cf. also [23] for a detailed analysis of parameters and resulting morphology).

To reach a narrow distribution of pore sizes, it is necessary to induce uniform nucleation and to suppress branching. This either necessitates pre patterning by $< 100 \text{ nm}$ lithography, “luck,” or some degree of self-organization as shown for the (macro)pores in Figure 3.

This brings us to the smallest pores, the micropores (following IUPAC). Generally, micropores grow on low-doped *p*-type material with ca. $1 \mu\text{m}/\text{min}$; crack-free growth beyond a thickness of some μm may pose a serious problem. The resulting morphology is a chaotic network of nm sized Si—branches with porosities up to 80 % (meaning that almost any atom left is a surface atom), but we skip further details of this by far most investigated pore type and refer to two recent books [24, 25].

While microporous Si triggered the immense research dedicated to light-emitting Si, real devices will most likely be based on quantum structures realized with different technologies. Nevertheless, microporous layers still provide ample ground for research and may be seen as test vehicles for structures produced with more advanced technologies which are unaffordable in most laboratories. As a somewhat unwelcome feature it must be added that so far attempts to produce micropores in semiconductors other than Si by anodic etching were not successful, with the exception of 6H-SiC [11]. This is not only frustrating, but also surprising, because the generally accepted formation mechanism for micropores (resting heavily on quantum wire effects) is not Si specific but should occur in any semiconductor.

5. PORES IN OTHER SEMICONDUCTORS

The variety of pores in III–V compounds (and to a smaller extent in SiC [10]) has been discussed elsewhere [8], here only some results from InP will be highlighted. InP most prominently features two different types of pores: crystallographically oriented (“crysto”) and current-line-oriented (“curro”) pores; which by now also have been found in GaP and Si. The former are growing at low current densities along that set of crystallographically defined $\langle 111 \rangle$ directions where one “looks” from the group V to the group III atom (the so-called $\langle 111 \rangle$ B direction) and usually has a triangular cross section. High current densities applied to a fresh surface also first yield crysto pores, which then heavily branch (including upwards) during their growth into depth. As soon as the pore density becomes so large that further branching is impeded, the pore morphology switches synchronized into the curro mode, that is, pores are now growing along the current path (same as along electrical field lines). These pores are round and try to self-organize in a hexagonal close-packing. Several self-organizational features are encountered, most

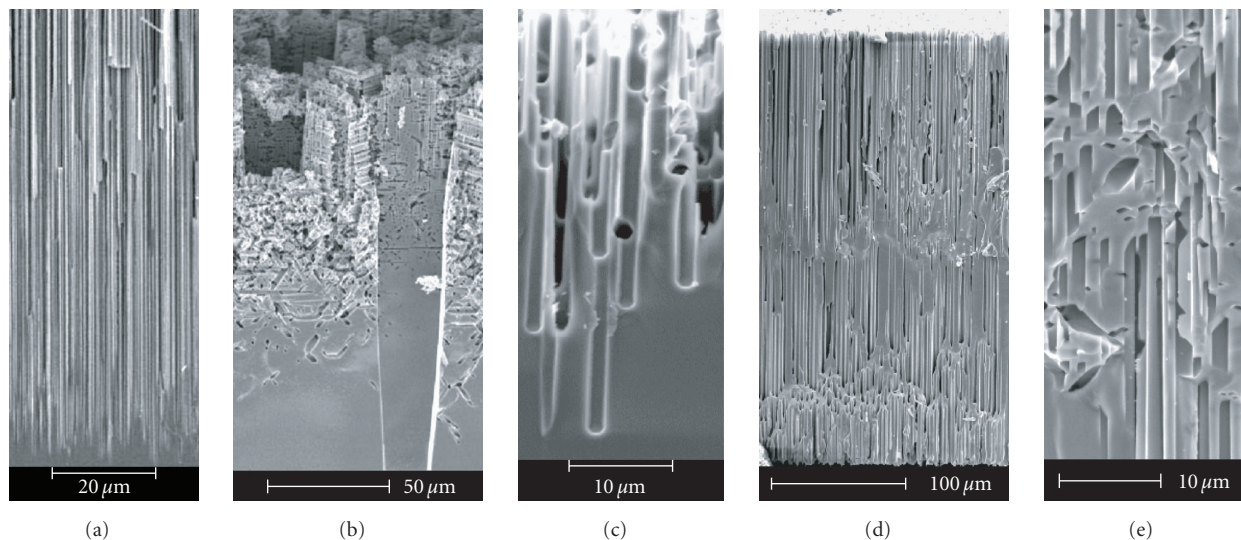
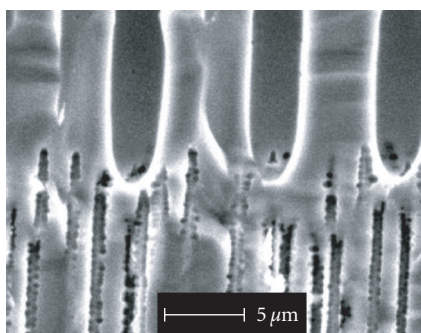
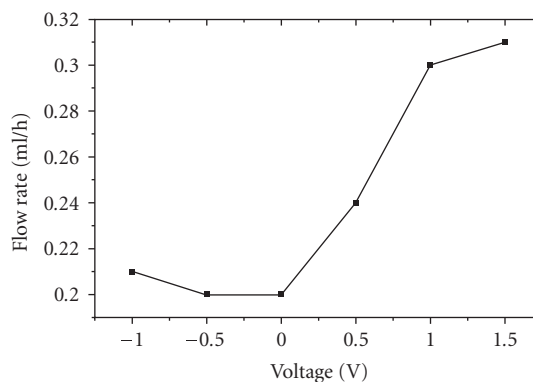


FIGURE 5: Pores in Ge. (a) Good sub- μm macropores, (b) mix of several pore types, (c) macropores in p -type Ge, (d) Ge membrane, and (e) overlap part of membrane.



(a)



(b)

FIGURE 6: (a) Meso-macro membrane; for example, for fuel cells applications, (b) flow rate through a porous Ge membrane as a function of applied potential.

prominent the formation of hexagonal single pore crystal on (111) and—amazingly—(100) substrates (cf. [22]). Induced switching between cristo and curro pores may have novel uses, as will be pointed out below.

Investigations of porous Ge began more recently [7]. While first it appeared that it was difficult to obtain pores at all [5], however by now a bewildering variety of pores has been found and some results will be reported here for the first time. Figure 5 gives a flavor of what is possible. A list of “firsts” in Ge includes (i) only other material besides Si where backside illumination can be used, however with new effects; (ii) only semiconductor besides Si where “good” pores can be produced in p -type material; (iii) first example for pore growth in $\langle 111 \rangle$ direction for nonpolar cubic semiconductor; (iv) the only material so far with $\{110\}$ “stopping” planes. While there are many more unusual features which move Ge in the focus of efforts to arrive at a better understanding of pore formation mechanisms in general. There is one feature

of porous Ge that is of considerable interest for potential uses: Ge exhibits the effect electrocapillarity or electrowetting, that is, its surface can be switched from hydrophobic to hydrophilic by just changing the applied potential; a feature that has been demonstrated in [7] and illustrated for our Ge membranes in Figure 6(b).

6. MEMBRANE FABRICATION

For many applications (especially chemical, but also optical), a porous membrane would be preferable to a layer, or is even necessary. Membrane fabrication, however, is not trivial after the electrochemical porosification step has been done. Grinding off the solid backside would be the first approach, but this process only works for rather thick and stable pore walls, that is, “big” pores. For small pores the grinding process tends to destroy the porous layer and to clog the pores with debris.

A better method uses a wet etch-back procedure from the backside. The pore surface in this case must first be protected by an oxide and/or a nitride coating, after that the backside is exposed to a chemical etching solution (in the case of Si: KOH or HF/HNO₃ mixtures). Without any protection, the pore walls would be quickly destroyed as soon as the etching front reaches them. Especially the coating with nitride, which is for reliable protection almost unavoidable, makes this process expensive, in particular when pores with a very large aspect ratio call for very low pressure CVD.

Alternatively, a membrane can be “blasted off” the substrate by simply employing a current pulse, driving the system into the electropolishing regime after the electrochemical pore etching is concluded. Especially for mesopore membranes, this process works pretty well and has been demonstrated for 100 μm thick layers on whole 100 mm wafers for an industrial application.

Another possibility is a changing in the electrolyte after the pore etching to a nonfluoride containing electrolyte that only anodically oxidizes the pore tips. Under favorable circumstances the anodic oxide grows laterally until the oxide layer around pore tips connects. Afterwards the wafer is placed in a HF solution, which dissolves the oxide and disattaches the porous region. Unlike the lift-off process, this can be done outside the electrochemical cell in an optimized process to ensure that the fragile membrane remains undamaged. Both processes mentioned produce a free-standing membrane without a solid rim which is only desirable in some cases. A certain advantage is that the wafer can be reused for further membrane production.

The growth of pores from both sides of the wafer can also be used to produce membranes. Most pores do not easily intersect (i.e., Si macro + macro, micro in any combination), because they have a carrier depleted space charge region around themselves, but mesopores in Si and macropores in Ge, for example, can overcome this obstacle (cf. Figures 5(d) and 6(a)). First a deep macroporous layer is grown. Afterwards the wafer is turned around and with a second porous layer, for example, mesopores are driven in from the backside.

Depending on the planned application, the mesoporous layer can then be chemically etched-off, as mesopores are much more prone to chemical etches than macropores, or—alternatively—a dual pore size membrane results. In the latter case, the mesoporous layer defines the critical dimensions for filtering applications, while the macropores help to stabilize the membrane and to controllably support the filter with the to-be-filtered solution.

7. SOME PROPERTIES AND APPLICATIONS OF POROUS SEMICONDUCTORS

Properties

The properties of porous semiconductor can be radically different from those of the bulk material, in particular if nanoporous materials are considered. Not only prime semiconductor parameters like conductivity, band gap, and

absorption/emission of light might be quite different, but also internal symmetries/anisotropies, high-order effects and even basic chemistry. Of course, the large surface to volume ratio also plays a major role. A few examples of new properties form a long (and not yet fully established) list.

- (a) More than 100-fold increase of second harmonic generation in porous GaP, if the pore cross-section is triangular [26].
- (b) Strongly increased or decreased cathodoluminescence in porous GaP or InP, respectively [27].
- (c) Optical anisotropy (e.g., birefringence) [28] and new types of anisotropy not encountered in natural materials, if two or more sets of pores are present simultaneously [29].
- (d) Novel absorption characteristic (e.g., transparent for UV while blocking larger wavelength [25, 30]).
- (e) Fast chemical reactions practically not observed with bulk materials; including violent explosions due to large surface to volume ratio and optimal diffusion conditions [31].
- (f) Strongly decreased thermal conductivity (and concomitantly changed phonon spectra) [32].
- (g) Strongly changed modes of plasmon, exciton, polariton, and so forth [25].
- (h) Extreme aspect ratios (up to 10 000 for InP [8]).
- (i) Strongly changed conductivity, sensitive to the presence of gases or humidity [33].

Applications

The spectrum of possible applications, which exploit the special properties given above, is large; it will be grouped into several subgroups here. From each topic, one or two examples indicated in *bold* letters are discussed more extensively.

Optics

- (i) Novel optical elements with already demonstrated capabilities are photonic crystals [34], optical short-pass filters [25, 30], as well as Bragg and Rugate mirrors obtained by modulating porosity with depth [35].
- (ii) Emerging applications only partially demonstrated include nonlinear elements (e.g., strong frequency doubling in porous GaP [26] and Si [36]) including phase matching, *integrated waveguides* [37], and novel *anisotropic* (e.g., birefringent) *materials* [29].

Structures with the potential of being used as integrated waveguides in InP rely on the possibility to abruptly switch from crystal to porous; Figure 7 shows an example. The easily induced porosity changes are coupled to a change in the refractive index suitable for waveguiding. These structures are easy to make (in contrast to conventional techniques), if all their properties (including, e.g., damping) are suitable for optoelectronic devices remains to be seen, but their usefulness for optical gas sensing is obvious. Optical gas and fluid sensing rely on sending light through a space filled with the gas or fluid and detecting changes of the spectrum at

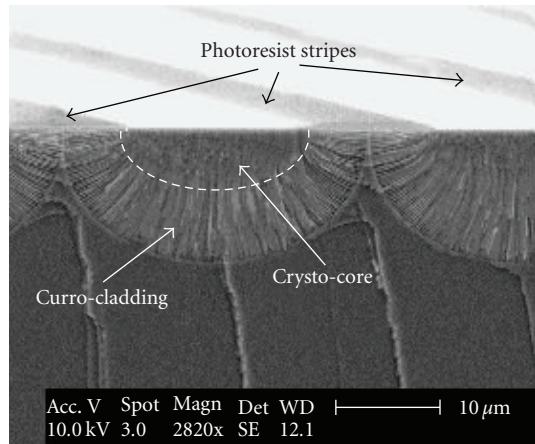


FIGURE 7: SEM cross-section of porous InP waveguides suitable for, for example, optical gas analysis: the wafer was coated with stripes of photo resist prior to electrochemical etching leading to semicylindrical pore structures. First cristo pores (low porosity) form a high index core surrounded by a low index curro cladding [37].

the end. One major problem is to confine the light on small cross section so that small quantities of substances can be analyzed. Also the signal-to-noise rises if the light is focused. Normal light waveguides are solid, that is, the analyzed substance cannot enter. A porous waveguide circumvents this problem without abandoning the waveguide properties.

A cubic crystal full of pores extending in several equivalent crystallographic directions no longer has a cubic symmetry from the viewpoint of light with a wavelength larger than the pore geometry. Indeed, (110)-oriented Si, with two sets of mesopores extending along the $\langle 100 \rangle$ directions, shows a pronounced birefringence [28] that can be much stronger than in natural crystals. Recently, this effect has been recalculated with considerable accuracy; in addition the theory has been extended to cover other pore geometries. Completely new anisotropic behavior was predicted for certain pore geometries that might be producible in GaAs or InP [29] (cf. Figure 8). Filling of the pores with a metal exhibiting strong plasmonic resonances (e.g., for Ag) is expected to further enhance these optical anisotropies [38].

Mechanics

- (i) Porous layers are generally useful for MEMS applications, most simply as sacrificial layers, but also as a kind of dielectric layer or as thermal insulation. A large-scale effort intends to use macroporous Si electrodes as well as microporous Si electrodes for micro-fuel cells [39–41].
- (ii) The extremely low thermal conductivity has been employed for ultrasonic generation [42].
- (iii) In one of the so far very few large-scale applications, canon uses porous layers as a kind of “zipper” during the fabrication of silicon on insulator (SOI) wafers [43].

- (iv) Porous layers are as buffer layers for demanding epitaxial processes, for example, GaN on SiC [44].
- (v) Porous layers serve as templates for nanorods or nanotubes of many different kinds [45].
- (vi) Microporous Si is a key ingredient for a high-power explosive [31].

If the pores of microporous Si are filled with an oxidizer, owing to the huge surface area, an amazingly potent explosive results. Research is under way to explore this (accidentally discovered) property for applications like an airbag firing device. Exotic as it appears, this application might be closer to a product than many sensor developments.

Chemical sensing

Generally, several basic effects can be used for chemical sensing (i) functionalized pore surfaces are sensitive to certain substances only, binding the analyte changes directly measurable properties like photo luminescence, (spectral) reflectivity, or conductivity/impedance. (ii) Special optical elements made from porous materials, most notably *Bragg reflectors* and resonators, change their key property (e.g., the wavelength of reflections/diffraction under a certain angle) in easily measurable ways. (iii) Specific properties of a photonic crystal made from porous materials can be used, for example, a very small effective light propagation speed which allows to miniaturize conventional optical gas spectrometers [46].

Smart dust from the Sailor group in San Diego [47] carries the Bragg reflector principle to the extreme. Several sets of mesoporous silicon rugate filters are functionalized for different protein groups (i.e., one mirror color equals one specific protein) and then ground to dust which can be blown into the atmosphere or buildings. The dust particles, if exposed to the test substance or gas, will bind the protein to be detected and then change their reflective behavior to something that can be remotely detected with a LASER.

Biotech uses

- (i) *Filters for proteins and other particles.* Due to the low dispersion in pore size, electrochemically etched meso- and macropores represent optimal candidates for filtering application with a high-size selectivity, for example, filtering of protein mixtures. As discussed in the “Membrane fabrication” section of this article, a combination of large macropores and smaller mesopores (cf. Figure 6(a)) offers a unique combination of mechanical stability, production ease, and filtering capabilities.
- (ii) Very regular arrays of macropores in Si are already used for biochip applications (DNA); and the technology is easily scaled to much smaller sizes if needed [25].
- (iii) Bio MEMS applications are emerging, for example, utilizing porous structures as templates for living cells on porous substrates [48].
- (iv) *Microrefinery and reactors.* While some work has been done along this direction [49], this is still more a vision

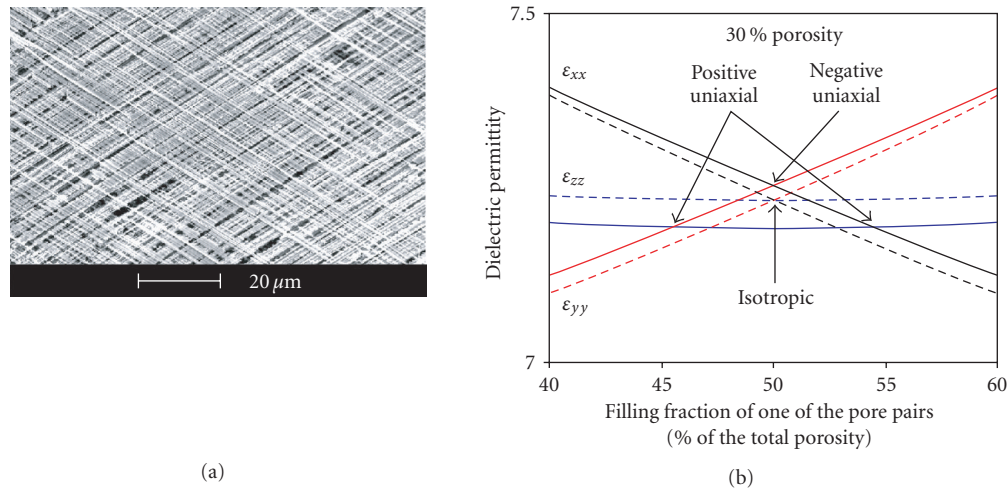


FIGURE 8: (a) Two $\langle 111 \rangle$ sets of pores in (100) GaAs. (b) Numerically calculated dielectric tensor elements of the porous GaAs layer shown in (a) as a function of the relative filling fraction of one of the pore lattices; the overall porosity of the sample is 30%. Dashed lines: pores with circular cross-section, solid lines: triangular cross-sections of crystallographic pores in GaAs. If the relative porosities of the two sets of pores are changed, novel properties result.

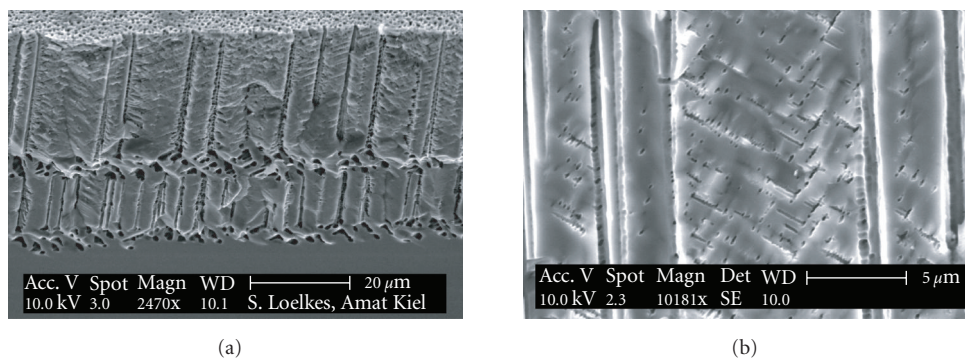


FIGURE 9: Sequential combination of different pore directions and densities. (a) Si pores switching between $\langle 111 \rangle$ directions and $\langle 113 \rangle$ directions. (b) Combination of meso- and macropores.

than a fact. With certain techniques it is possible to interconnect straight pores, while still exercising some control over the pore geometry; Figure 9 shows examples. In Figure 9(a) the pores grow along $\langle 111 \rangle$, but change to $\langle 113 \rangle$ (with three equivalent directions) and back if the voltages are cycled in a suitable way. The “fast etching” modes for Si (cf. Figure 3) and also for InP (cf. Figure 1(c)) offer similar morphologies superimposing cristo and curro pores. Figure 9(b) shows macropores interconnected by mesopores (usually considered a nuisance). All these structures resemble biological tissue optimized for processing of complex liquids, and it is tempting to speculate about applications as indicated above.

ACKNOWLEDGMENTS

M. Kemell, M. Christophersen, E. Ossei-Wusu, C. Fang, S. Langa supplied data, and AMD, MEMC; Siltronic and

Infineon supplied wafers or processes; this is gratefully acknowledged. Parts of this work were supported by the DFG.

REFERENCES

- [1] L. T. Canham, “Silicon quantum wire array fabrication by electrochemical and chemical dissolution of wafers,” *Applied Physics Letters*, vol. 57, no. 10, pp. 1046–1048, 1990.
- [2] V. Lehmann and U. Gösele, “Porous silicon formation: a quantum wire effect,” *Applied Physics Letters*, vol. 58, no. 8, pp. 856–858, 1991.
- [3] H. Föll, M. Christophersen, J. Carstensen, and G. Hasse, “Formation and application of porous silicon,” *Materials Science and Engineering: R: Reports*, vol. 39, no. 4, pp. 93–141, 2002.
- [4] A. Uhlir, “Electrolytic shaping of germanium and silicon,” *Bell System Technical Journal*, vol. 35, pp. 333–347, 1956.
- [5] K. Choi and J. M. Buriak, “Hydrogermylation of alkenes and alkynes on hydride-terminated Ge(100) surfaces,” *Langmuir*, vol. 16, no. 20, pp. 7737–7741, 2000.
- [6] S. Langa, M. Christophersen, J. Carstensen, I. M. Tiginyanu, and H. Föll, “Electrochemical pore etching in Ge,” *Physica Status Solidi (A)*, vol. 195, no. 3, pp. R4–R6, 2003.

- [7] C. Fang, H. Föll, and J. Carstensen, "Electrochemical pore etching in germanium," *Journal of Electroanalytical Chemistry*, vol. 589, no. 2, pp. 259–288, 2006.
- [8] H. Föll, S. Langa, J. Carstensen, M. Christophersen, and I. M. Tiginyanu, "Pores in III-V semiconductors," *Advanced Materials*, vol. 15, no. 3, pp. 183–198, 2003.
- [9] M. Mynbaeva, A. Titkov, A. Kryzhanovski, et al., "Strain relaxation in GaN layers grown on porous GaN sublayers," *MRS Internet Journal of Nitride Semiconductor Research*, vol. 4, p. 14, 1999.
- [10] S. Zangoie, J. A. Woollam, and H. Arwin, "Self-organization in porous 6H-SiC," *Journal of Materials Research*, vol. 15, no. 9, pp. 1860–1863, 2000.
- [11] J. S. Shor, L. Bemis, A. D. Kurtz, et al., "Characterization of nanocrystallites in porous p-type 6H-SiC," *Journal of Applied Physics*, vol. 76, no. 7, pp. 4045–4049, 1994.
- [12] E. Monaico, V. V. Ursaki, A. Urbietta, et al., "Porosity-induced gain of luminescence in CdSe," *Semiconductor Science and Technology*, vol. 19, no. 12, pp. L121–L123, 2004.
- [13] L. T. Canham, A. Nassiopoulou, and V. Parkhutik, "Proceedings of the 3rd international conference porous semiconductors—science and technology," *Physica Status Solidi (A)*, vol. 197, no. 1, 2003.
- [14] V. Lehmann and H. Föll, "Formation mechanism and properties of electrochemically etched trenches in n-type silicon," *Journal of the Electrochemical Society*, vol. 137, no. 2, pp. 653–659, 1990.
- [15] Y. Shishkin, Y. Ke, R. P. Devaty, and W. J. Choyke, to appear in *Physica Status Solidi (A)*.
- [16] C. Fang, S. Langa, L. Jiang, J. Carstensen, E. Foca, and H. Föll, "Electrochemical pore etching in Germanium, 3.8 (2005)." *Journal of the Electrochemical Society*, vol. 146, no. 8, pp. 2968–2975, 1999.
- [17] V. Lehmann and S. Rönnebeck, "The physics of macropore formation in low-doped p-type silicon," *Journal of the Electrochemical Society*, vol. 146, no. 8, pp. 2968–2975, 1999.
- [18] J. Carstensen, R. Prange, and H. Föll, "A model for current-voltage oscillations at the silicon electrode and comparison with experimental results," *Journal of the Electrochemical Society*, vol. 146, no. 3, pp. 1134–1140, 1999.
- [19] ET&TE Etch and Technology GmbH, <http://www.et-te.com>.
- [20] J. E. A. M. van den Meerakker, R. J. G. Elfrink, F. Roozeboom, and J. F. C. M. Verhoeven, "Etching of deep macropores in 6 in. Si wafers," *Journal of The Electrochemical Society*, vol. 147, no. 7, pp. 2757–2761, 2000.
- [21] S. Frey, M. Kemell, J. Carstensen, S. Langa, and H. Föll, "Fast pore etching," *Physica Status Solidi (A)*, vol. 202, no. 8, pp. 1369–1373, 2005.
- [22] S. Langa, I. M. Tiginyanu, J. Carstensen, M. Christophersen, and H. Föll, "Self-organized growth of single crystals of nanopores," *Applied Physics Letters*, vol. 82, no. 2, pp. 278–280, 2003.
- [23] V. Lehmann, R. Stengl, and A. Luigart, "On the morphology and the electrochemical formation mechanism of mesoporous silicon," *Materials Science and Engineering B*, vol. 69–70, pp. 11–22, 2000.
- [24] X. G. Zhang, *Electrochemistry of Silicon and Its Oxide*, Kluwer Academic/Plenum, New York, NY, USA, 2001.
- [25] V. Lehmann, *Electrochemistry of Silicon*, Wiley-VCH, Weinheim, Germany, 2002.
- [26] I. M. Tiginyanu, I. V. Kravetsky, S. Langa, G. Marowsky, J. Monnecke, and H. Föll, "Porous III-V compounds as nonlinear optical materials," *Physica Status Solidi (A)*, vol. 197, no. 2, pp. 549–555, 2003.
- [27] I. M. Tiginyanu, S. Langa, L. Sirbu, E. Monaico, M. A. Stevens-Kalceff, and H. Föll, "Cathodoluminescence microanalysis of porous GaP and InP structures," *The European Physical Journal: Applied Physics*, vol. 27, no. 1–3, pp. 81–84, 2004.
- [28] D. Kovalev, G. Polisski, J. Diener, et al., "Strong in-plane birefringence of spatially nanostructured silicon," *Applied Physics Letters*, vol. 78, no. 7, pp. 916–918, 2001.
- [29] V. Kochergin, M. Christophersen, and P. R. Swinehart, "Macroporous silicon UV filters for space and terrestrial environments," in *Photonics for Space Environments IX*, vol. 5554 of *Proceedings of SPIE*, pp. 223–234, Denver, Colo, USA, August 2004.
- [30] V. Kochergin, *Omnidirectional Optical Filters*, Kluwer Academic, Boston, Mass, USA, 2003.
- [31] D. Kovalev, V. Yu. Timoshenko, N. Künzner, E. Gross, and F. Koch, "Strong explosive interaction of hydrogenated porous silicon with oxygen at cryogenic temperatures," *Physical Review Letters*, vol. 87, no. 6, Article ID 068301, 4 pages, 2001.
- [32] G. Kaltsas and A. G. Nassiopoulou, "Novel C-MOS compatible monolithic silicon gas flow sensor with porous silicon thermal isolation," *Sensors and Actuators A: Physical*, vol. 76, no. 1–3, pp. 133–138, 1999.
- [33] C. J. Oton, L. Pancheri, Z. Gaburro, et al., "Multiparametric porous silicon gas sensors with improved quality and sensitivity," *Physica Status Solidi (A)*, vol. 197, no. 2, pp. 523–527, 2003.
- [34] K. Busch, S. Lölkes, R. B. Wehrspohn, and H. Föll, Eds., *Photonic Crystals: Advances in Design, Fabrication, and Characterization*, Wiley-VCH, Weinheim, Germany, 2004.
- [35] C. Mazzoleni and L. Pavesi, "Application to optical components of dielectric porous silicon multilayers," *Applied Physics Letters*, vol. 67, no. 20, pp. 2983–2985, 1995.
- [36] T. V. Dolgova, A. I. Maidikovski, M. G. Martemyanov, et al., "Giant optical second-harmonic generation in single and coupled microcavities formed from one-dimensional photonic crystals," *Journal of the Optical Society of America B: Optical Physics*, vol. 19, no. 9, pp. 2129–2140, 2002.
- [37] S. Langa, S. Frey, J. Carstensen, et al., "Waveguide structures based on porous indium phosphide," *Electrochemical and Solid-State Letters*, vol. 8, no. 2, pp. C30–C32, 2005.
- [38] V. Kochergin, M. Christophersen, and P. R. Swinehart, "Macroporous silicon-based polarization components," in *Nanoengineering: Fabrication, Properties, Optics, and Devices*, vol. 5515 of *Proceedings of SPIE*, pp. 132–141, Denver, Colo, USA, August 2004.
- [39] L. Ohlsen, to appear in *Physica Status Solidi (A)*.
- [40] S. Gold, K.-L. Chu, C. Lu, M. A. Shannon, and R. I. Masel, "Acid loaded porous silicon as a proton exchange membrane for micro-fuel cells," *Journal of Power Sources*, vol. 135, no. 1–2, pp. 198–203, 2004.
- [41] T. Pichonat and B. Gauthier-Manuel, "Development of porous silicon-based miniature fuel cells," *Journal of Micromechanics and Microengineering*, vol. 15, no. 9, pp. S179–S184, 2005.
- [42] H. Shinoda, T. Nakajima, K. Ueno, and N. Koshida, "Thermally induced ultrasonic emission from porous silicon," *Nature*, vol. 400, no. 6747, pp. 853–855, 1999.
- [43] T. Yonehara, "BESOI with porous silicon: ELTRAN," in *Properties of Porous Silicon*, L. T. Canham, Ed., IEE-Books, London, UK, 1997.
- [44] C. K. Inoki, T. S. Kuan, C. D. Lee, et al., "Growth of GaN on porous SiC and GaN substrates," *Journal of Electronic Materials*, vol. 32, no. 8, pp. 855–860, 2003.
- [45] M. Steinhart, Z. Jia, A. K. Schaper, R. B. Wehrspohn, U. Gösele, and J. H. Wendorff, "Palladium nanotubes with tailored wall morphologies," *Advanced Materials*, vol. 15, no. 9, pp. 706–709, 2003.

-
- [46] R. B. Wehrspohn, S. L. Schweizer, J. Schilling, T. Geppert, C. Jamois, and R. Glatthaar, "Application of photonic crystals for gas detection and sensing," in *Photonic Crystals: Advances in Design, Fabrication, and Characterization*, K. Busch, S. Lölkes, R. Wehrspohn, and H. Föll, Eds., Wiley-VCH, Weinheim, Germany, 2004.
- [47] F. Cunin, T. A. Schmedake, J. R. Link, et al., "Biomolecular screening with encoded porous-silicon photonic crystals," *Nature Materials*, vol. 1, no. 1, pp. 39–41, 2002.
- [48] S. C. Bayliss, P. J. Harris, L. D. Buckberry, and C. Rousseau, "Phosphate and cell growth on nanostructured semiconductors," *Journal of Materials Science Letters*, vol. 16, no. 9, pp. 737–740, 1997.
- [49] T. Laurell, J. Drott, L. Rosengren, and K. Lindström, "Enhanced enzyme activity in silicon integrated enzyme reactors utilizing porous silicon as the coupling matrix," *Sensors and Actuators B: Chemical*, vol. 31, no. 3, pp. 161–166, 1996.

Atomic Layer Deposition for the Conformal Coating of Nanoporous Materials

Jeffrey W. Elam,¹ Guang Xiong,² Catherine Y. Han,² H. Hau Wang,² James P. Birrell,² Ulrich Welp,² John N. Hryn,¹ Michael J. Pellin,² Theodore F. Baumann,³ John F. Poco,³ and Joe H. Satcher Jr.³

¹Energy Systems Division, Argonne National Laboratory, Argonne, IL 60439, USA

²Materials Science Division, Argonne National Laboratory, Argonne, IL 60439, USA

³Chemistry and Materials Science Directorate, Lawrence Livermore National Laboratory, Livermore, CA 94550, USA

Received 15 March 2006; Revised 9 May 2006; Accepted 10 May 2006

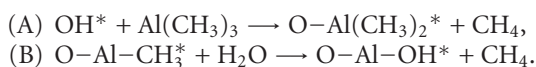
Atomic layer deposition (ALD) is ideal for applying precise and conformal coatings over nanoporous materials. We have recently used ALD to coat two nanoporous solids: anodic aluminum oxide (AAO) and silica aerogels. AAO possesses hexagonally ordered pores with diameters $d \sim 40$ nm and pore length $L \sim 70$ microns. The AAO membranes were coated by ALD to fabricate catalytic membranes that demonstrate remarkable selectivity in the oxidative dehydrogenation of cyclohexane. Additional AAO membranes coated with ALD Pd films show promise as hydrogen sensors. Silica aerogels have the lowest density and highest surface area of any solid material. Consequently, these materials serve as an excellent substrate to fabricate novel catalytic materials and gas sensors by ALD.

Copyright © 2006 Jeffrey W. Elam et al. This is an open access article distributed under the Creative Commons Attribution License, which permits unrestricted use, distribution, and reproduction in any medium, provided the original work is properly cited.

1. INTRODUCTION

Atomic layer deposition (ALD) is a thin film growth technique that uses alternating and saturating reactions between gaseous precursor molecules and a substrate to deposit films in a layer-by-layer fashion [1, 2]. By repeating this reaction sequence in an ABAB... fashion, films of virtually any thickness (atomic monolayers to microns) can be deposited with atomic layer precision. This alternating reaction strategy eliminates the “line of site” or “constant exposure” requirements that limit conventional methods such as physical- or chemical-vapor deposition, and offers the unique capability to coat complex, 3-dimensional objects with precise, conformal layers. These attributes make ALD an ideal method for applying precise and conformal coatings over nanoporous materials [3, 4].

As an example of the ALD process, consider the following binary reaction sequence for Al_2O_3 in which the surface species are designated by asterisks [5]:



In reaction (A), the substrate surface is initially covered with hydroxyl (OH) groups. The hydroxyl groups react with

trimethyl aluminum ($\text{Al}(\text{CH}_3)_3$, TMA) to deposit a monolayer of aluminum-methyl groups and give off methane (CH_4) as a byproduct. Because TMA is inert to the methyl-terminated surface, further exposure to TMA yields no additional growth beyond one monolayer. In reaction (B), this new surface is exposed to water regenerating the initial hydroxyl-terminated surface and again releasing methane. The net effect of one (A)-(B) cycle is to deposit one monolayer of Al_2O_3 on the surface. ALD can deposit a wide variety of materials including oxides, nitrides, sulfides, and metals.

In this manuscript, we describe recent work exploring the ALD coating of two nanoporous solids: anodic aluminum oxide (AAO) and silica aerogels. AAO membranes are synthesized by the anodization of aluminum metal [6], and consist of well-ordered hexagonal arrays of open pores with diameters $d \sim 40$ nm and pore length $L \sim 70$ microns. Silica aerogels are fabricated by the supercritical drying of a silica sol-gel [7] and consist of a randomly interconnected network of fine filaments and particles. The AAO and silica aerogels have been successfully coated using ALD methods with a variety of oxide films including Al_2O_3 , TiO_2 , V_2O_5 , and ZnO as well as metallic Pd films. The ALD coated AAO and aerogel materials were characterized by scanning

TABLE 1: Precursors and deposition temperatures for ALD film growth.

ALD film	Metal source	Oxidant/reductant	Deposition temperature ($^{\circ}\text{C}$)	Reference
Al_2O_3	Trimethyl aluminum (TMA)	H_2O	177	[8]
TiO_2	Titanium tetrachloride (TiCl_4)	H_2O	100	[9]
V_2O_5	Vanadyl oxytriisopropoxide (VOTP)	H_2O_2	100	[10]
ZnO	Diethyl zinc (DEZ)	H_2O	177	[11]
Pd	Pd hexafluoroacetylacetonate ($\text{Pd}(\text{hfac})_2$)	HCOH	200	[12]

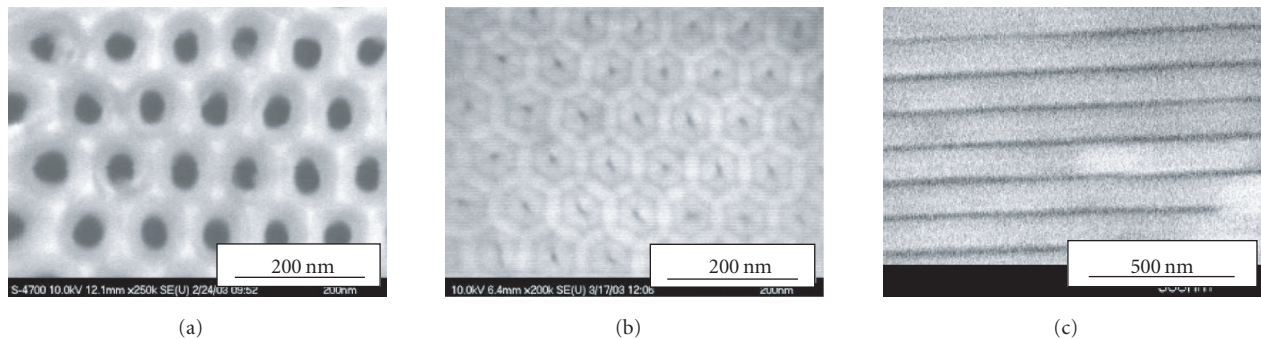


FIGURE 1: Plan view SEM images of AAO membrane before (a) and after (b) 15 nm ALD Al_2O_3 coating. (c) Cross-sectional SEM image after coating recorded from middle of membrane. Conformal Al_2O_3 coating extends to middle of AAO.

electron microscopy (SEM), energy dispersive analysis of x-rays (EDAX), transmission electron microscopy (TEM), x-ray diffraction (XRD), optical absorption, and four-point probe conductivity measurements.

The ALD/AAO materials are being employed as mesoporous catalytic membranes [13] and gas sensors. The catalytic membranes were fabricated by applying successive coatings of Al_2O_3 , TiO_2 , and V_2O_5 onto AAO membrane supports. Additional AAO membranes coated with ALD Pd exhibit fast response and high sensitivity for hydrogen detection. Silica aerogels have the lowest density and highest surface area of any solid material. Therefore, these materials are excellent templates for preparing novel catalytic materials and sensors by ALD [4]. In these initial studies, monolithic (bulk) and thin film silica aerogels were coated by ZnO ALD, and the physical properties of the resulting ZnO/SiO₂ materials were investigated as a function of the ZnO coating thickness.

2. EXPERIMENTAL

Anodic aluminum oxide (AAO) membranes consisting of hexagonally ordered arrays of nanopores with diameter $d = 40$ nm and pore length $L = 70$ micron were prepared by a two-step anodization procedure [6]. Aluminum sheets were electropolished in a solution of perchloric acid and ethanol and anodized in 0.3 M oxalic acid at 3°C for 24 h. Freestanding AAO membranes were obtained by selectively etching away the unreacted Al in saturated HgCl_2 solution and then immersing in 5.00 wt% phosphoric acid at 30.0°C for 65 min to remove the barrier layer. Bulk aerogels with a density of 10 mg/cm^3 and a surface area of $350 \text{ m}^2/\text{g}$ were prepared by

supercritical drying of a silica sol-gel using the procedure described in reference [7]. Thin film aerogels were prepared using the same procedure by first applying the sol-gel between two flat SiO_2 surfaces.

The ALD was performed in a viscous flow reactor [14] using the reactants and temperatures given in Table 1. The reactant pressures, exposure times, and purge times were increased relative to the values necessary to coat flat surfaces to allow diffusion of the gaseous reactants into the high aspect ratio pores of the AAO and aerogel materials [3]. Following the ALD coating, AAO membranes and aerogel materials were analyzed using SEM, TEM, EDAX, XRD, optical absorption, and four-point probe resistivity.

3. RESULTS AND DISCUSSION

AAO membranes were modified by ALD to fabricate nanoporous catalytic membranes for the selective oxidation of hydrocarbons. First, the AAO pore diameter was reduced to enhance the catalytic activity using Al_2O_3 ALD. AAO membranes having an initial pore diameter $d = 40$ nm and pore length $L = 70$ micron were coated by 15 nm ALD Al_2O_3 to achieve a final pore diameter of $d = 10$ nm. By tuning the AAO pore diameter, we can control the contact time between the reactants and the catalyst. An additional function of the Al_2O_3 coating is to cover up the aluminum oxalate and other impurities in the AAO that are introduced during the anodization step [15]. These impurities may cause a different initial reactivity of the AAO surface towards the Al_2O_3 ALD precursors. Plan view and cross sectional SEM images (Figure 1) demonstrate that the very high aspect ratio ($L/d \sim 10^4$) pores are conformally coated using ALD. TEM

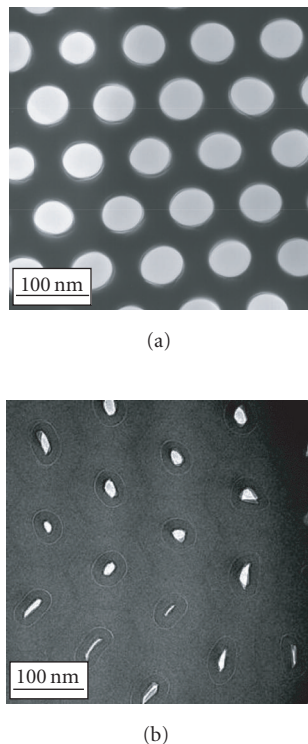


FIGURE 2: TEM images of AAO membrane before (a) and after (b) 18 nm ALD Al_2O_3 coating. Conformal ALD coating maintains initial AAO pore asymmetry.

images of the AAO samples before and after coating with an 18 nm ALD Al_2O_3 layer (Figure 2) illustrate how the conformal ALD coatings preserve the initial asymmetry present in some of the AAO pores. Oval-shaped openings in some of the pores become more exaggerated as the pores become narrower.

After depositing the ALD Al_2O_3 coating on the AAO membrane, ALD TiO_2 and V_2O_5 coatings were deposited to serve as the catalytic support layer and active catalyst layer, respectively. The TiO_2 layer has a thickness of ~ 1 nm and serves to enhance the activity of the V_2O_5 catalyst. It is possible that Cl residue from the TiCl_4 used to deposit this ALD TiO_2 layer may influence the subsequent catalytic activity of the AAO membranes. The catalyst layer is a submonolayer coating of V_2O_5 with a thickness of ~ 0.1 nm. In situ quartz crystal microbalance (QCM) measurements demonstrated that the ALD TiO_2 and V_2O_5 layers nucleate readily on the ALD Al_2O_3 layer as expected for hydroxyl-based growth [1]. It was necessary to coat the AAO membranes with ALD TiO_2 at 100°C to obtain uniform and amorphous TiO_2 coatings. At higher deposition temperatures of 250°C , the TiO_2 deposited nonuniformly as 10–50 nm anatase crystals inside of the AAO pores. Cross sectional SEM and EDAX measurements reveal that the ALD TiO_2 and V_2O_5 coatings deposited at 100°C are uniform throughout the AAO nanopores. Catalytic testing showed that the ALD/AAO membranes were highly selective in the oxidation of cyclohexane to cyclohexene. When compared with conventional powder catalysts, the

ALD/AAO membranes formed much less of the higher oxidation products benzene, CO and CO_2 . We believe that the reduced contact time in the flow-through-pore structure accounts for the enhanced selectivity [13].

AAO membranes were also coated with metal films to form prototype gas sensors. Conformal Pd coatings with a thickness of 2 nm were deposited onto AAO membranes using alternating exposures to $\text{Pd}(\text{hfac})_2$ and formaldehyde (HCOH). Prior to the ALD Pd coating, a 1 nm coating of ALD Al_2O_3 was applied to the AAO to promote rapid nucleation of the Pd. Cross-sectional EDAX measurements confirmed that the Pd films extended to the middle of the high aspect ratio pores, and plan view SEM revealed a nanocrystalline Pd morphology as shown in Figure 3. The Pd/AAO samples exhibited rapid and reversible conductivity changes upon hydrogen exposure and showed great promise as hydrogen gas sensors with fast response and high sensitivity.

The ability to coat ultralow density silica aerogels with conformal layers of different metal and metal oxide materials using ALD will enable the fabrication of novel gas sensors and catalysts. In this study, monolithic and thin film silica aerogels were coated by ZnO ALD [4]. Prior to the ZnO coatings, a 3\AA ALD Al_2O_3 coating was applied as a nucleation layer. SEM images of the silica aerogel versus number of ZnO ALD cycles (successive exposures to DEZ and H_2O) are shown in Figure 4. The silica aerogels have an open filamentous structure and the conformal ZnO coating increases the filament diameter with increasing ZnO cycles. After 80 ALD cycles, ZnO nanocrystals are visible on the surface of the coated aerogel. XRD measurements of this sample reveal hexagonal zincite. The weight change of the monolithic silica aerogels versus number of ALD ZnO cycles is shown in Figure 5. Also shown is the Zn EDAX signal obtained from thin film aerogels versus number of ZnO cycles. The weight gain and Zn content vary quadratically with the number of cycles. This finding is surprising given the highly linear growth observed on flat substrates for ALD ZnO films. This discrepancy is explained by the increase in filament diameter demonstrated in Figure 3. The amount of ZnO deposited per cycle varies with the square of the filament radius. Because the filament radius increases linearly with the number of ZnO cycles, the sample weight and Zn content increase quadratically.

The optical absorption and four-point probe electrical conductivity of the thin film silica aerogels were monitored versus number of ALD ZnO cycles. ALD ZnO is electrically conducting and absorbs blue light, while SiO_2 is electrically insulating and optically transparent. As the aerogel becomes progressively coated by the ZnO, both the electrical conductivity and optical absorption increase.

4. CONCLUSIONS

We have used atomic layer deposition (ALD) to apply precise and conformal coatings over nanoporous anodic aluminum oxide (AAO) membranes and silica aerogels. The ALD layers uniformly coat all exposed surfaces of the substrates including the inner walls of the extremely high aspect ratio

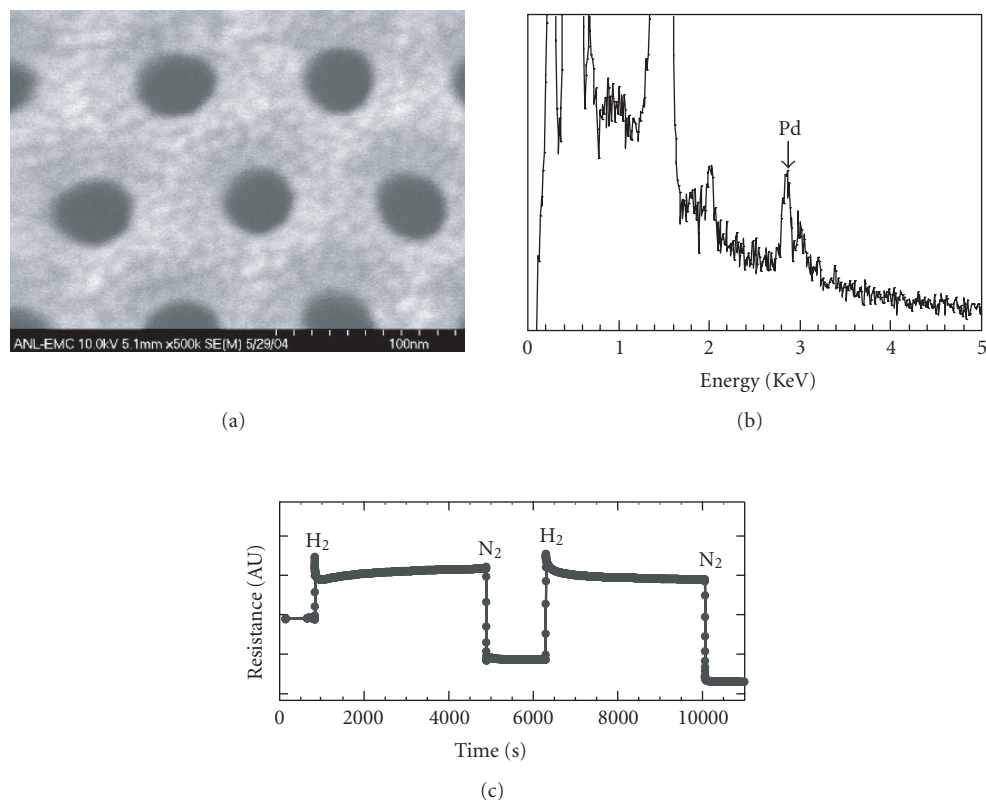


FIGURE 3: (a) SEM image of AAO membrane following 2 nm ALD Pd coating. (b) EDAX elemental analysis from middle of cleaved portion of AAO membrane demonstrating that Pd coating extends to the middle of pores. (c) Resistance changes of Pd/AAO membrane to alternating H₂ and N₂ gas streams demonstrating high H₂ sensitivity and rapid time response.

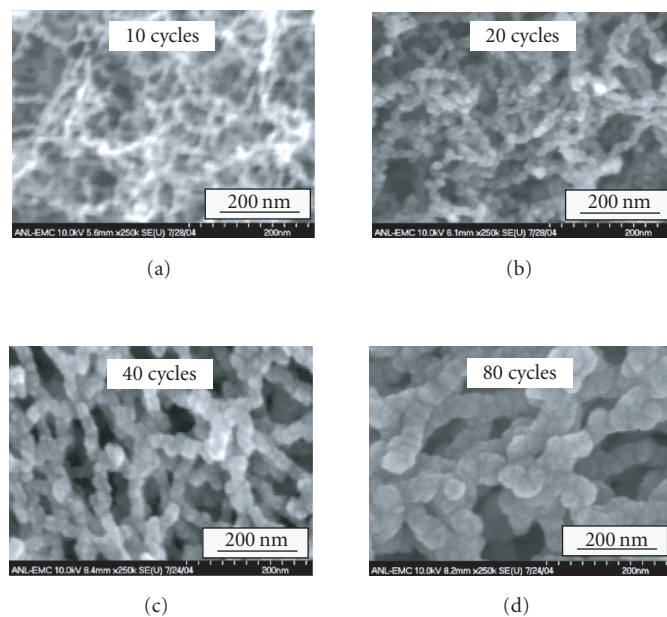


FIGURE 4: SEM images of silica aerogel versus ZnO ALD cycles illustrating progressive thickening of aerogel filaments.

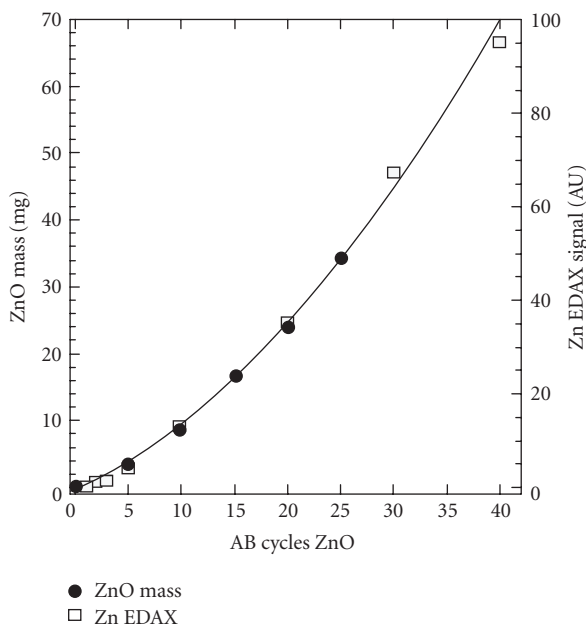


FIGURE 5: Mass gain and Zn EDAX signal versus ZnO ALD cycles on silica aerogel. Quadratic behavior results from linear increase in aerogel filament diameter with number of ZnO cycles.

($L/d \sim 10^4$) AAO pores. We have deposited successive layers of Al_2O_3 , TiO_2 , and V_2O_5 onto AAO to fabricate catalytic membranes for the selective oxidation of hydrocarbons. AAO membranes coated with ALD Pd show great promise as hydrogen sensors. Very low-density silica aerogels can be coated with ALD ZnO layers to alter the aerogel properties.

ACKNOWLEDGMENTS

Work at LLNL was performed under the auspices of the US DOE by the University of California, LLNL under Contract W-7405-Eng-48. Work at Argonne is supported by the US Department of Energy, BES-Materials Sciences under Contract W-31-109-ENG-38.

REFERENCES

- [1] S. M. George, A. W. Ott, and J. W. Klaus, "Surface chemistry for atomic layer growth," *Journal of Physical Chemistry*, vol. 100, no. 31, pp. 13121–13131, 1996.
- [2] M. Ritala and M. Leskelä, "Atomic layer deposition," in *Handbook of Thin Films Materials*, H. S. Nalwa, Ed., vol. 1, chapter 2, pp. 103–156, Academic Press, San Diego, Calif, USA, 2001.
- [3] J. W. Elam, D. Routkevitch, P. P. Mardilovich, and S. M. George, "Conformal coating on ultrahigh-aspect-ratio nanopores of anodic alumina by atomic layer deposition," *Chemistry of Materials*, vol. 15, no. 18, pp. 3507–3517, 2003.
- [4] S. O. Kucheyev, J. Biener, Y. M. Wang, et al., "Atomic layer deposition of ZnO on ultralow-density nanoporous silica aerogel monoliths," *Applied Physics Letters*, vol. 86, no. 8, Article ID 083108, pp. 1–3, 2005.
- [5] A. C. Dillon, A. W. Ott, J. D. Way, and S. M. George, "Surface chemistry of Al_2O_3 deposition using $\text{Al}(\text{CH}_3)_3$ and H_2O in a binary reaction sequence," *Surface Science*, vol. 322, no. 1–3, pp. 230–242, 1995.
- [6] H. H. Wang, C. Y. Han, G. A. Willing, and Z. Xiao, "Nanowire and nanotube syntheses through self-assembled nanoporous AAO templates," *Materials Research Society Symposium Proceedings*, vol. 775, pp. 107–112, 2003.
- [7] L. Hrubesh, T. Tillotson, and J. F. Poco, *Chemical Processing of Advanced Materials*, John Wiley & Sons, New York, NY, USA, 1992.
- [8] A. W. Ott, J. W. Klaus, J. M. Johnson, and S. M. George, " Al_3O_3 thin film growth on Si(100) using binary reaction sequence chemistry," *Thin Solid Films*, vol. 292, no. 1-2, pp. 135–144, 1997.
- [9] M. Ritala, M. Leskelä, E. Nykänen, P. Soininen, and L. Niinistö, "Growth of titanium dioxide thin films by atomic layer epitaxy," *Thin Solid Films*, vol. 225, no. 1-2, pp. 288–295, 1993.
- [10] J. C. Badot, S. Ribes, E. B. Yousfi, et al., "Atomic layer epitaxy of vanadium oxide thin films and electrochemical behavior in presence of lithium ions," *Electrochemical and Solid-State Letters*, vol. 3, no. 10, pp. 485–488, 2000.
- [11] E. B. Yousfi, J. Fouache, and D. Lincot, "Study of atomic layer epitaxy of zinc oxide by in-situ quartz crystal microgravimetry," *Applied Surface Science*, vol. 153, no. 4, pp. 223–234, 2000.
- [12] J. J. Senkevich, F. Tang, D. Rogers, et al., "Substrate-independent palladium atomic layer deposition," *Chemical Vapor Deposition*, vol. 9, no. 5, pp. 258–264, 2003.
- [13] M. J. Pellin, P. C. Stair, G. Xiong, et al., "Mesoporous catalytic membranes: synthetic control of pore size and wall composition," *Catalysis Letters*, vol. 102, no. 3-4, pp. 127–130, 2005.
- [14] J. W. Elam, M. D. Groner, and S. M. George, "Viscous flow reactor with quartz crystal microbalance for thin film growth by atomic layer deposition," *Review of Scientific Instruments*, vol. 73, no. 8, pp. 2981–2987, 2002.
- [15] G. Xiong, J. W. Elam, H. Feng, et al., "Effect of atomic layer deposition coatings on the surface structure of anodic aluminum oxide membranes," *Journal of Physical Chemistry B*, vol. 109, no. 29, pp. 14059–14063, 2005.

Size-Dependent Specific Surface Area of Nanoporous Film Assembled by Core-Shell Iron Nanoclusters

Jiji Antony,¹ Joseph Nutting,¹ Donald R. Baer,² Daniel Meyer,¹ Amit Sharma,¹ and You Qiang¹

¹Department of Physics, University of Idaho, Moscow, ID 83844, USA

²EMSL, Pacific Northwest National Laboratory, Richland, WA 99352, USA

Received 31 January 2006; Revised 22 August 2006; Accepted 28 August 2006

Nanoporous films of core-shell iron nanoclusters have improved possibilities for remediation, chemical reactivity rate, and environmentally favorable reaction pathways. Conventional methods often have difficulties to yield stable monodispersed core-shell nanoparticles. We produced core-shell nanoclusters by a cluster source that utilizes combination of Fe target sputtering along with gas aggregations in an inert atmosphere at 7°C. Sizes of core-shell iron-iron oxide nanoclusters are observed with transmission electron microscopy (TEM). The specific surface areas of the porous films obtained from Brunauer-Emmett-Teller (BET) process are size-dependent and compared with the calculated data.

Copyright © 2006 Jiji Antony et al. This is an open access article distributed under the Creative Commons Attribution License, which permits unrestricted use, distribution, and reproduction in any medium, provided the original work is properly cited.

1. INTRODUCTION

Iron nanoparticles are interesting due to their smaller size and higher reaction efficiency. Nanoporous structures are a branch of nanomaterials that have significant importance due to their ability to absorb and react, as they possess large surface area. Nanoporous materials have applications as catalysts, sensors, electrodes for batteries and fuel cells [1, 2]. Zero-valent iron [Fe(0)] nanoparticles react more quickly than their oxides and are of great importance due to their high oxidation capability and rapid kinetics in addition to their ability to reach the deep sites of contamination [3]. The iron-iron oxide core-shell nanoparticles can dechlorinate chlorinated hydrocarbons, a major source of environmental contaminant. The oxide shell provides a passivating layer that imparts stability to the particles in aqueous suspension [3] by preventing further oxidation, so that the particles react slowly for extended period. The iron nanoparticles can react with contaminants in the environment up to 8 weeks and can flow along with groundwater for a distance of 20 m [4]. Rapid *in situ* reduction of trichloroethylene is observed using nano-iron. Up to 99% of the trichloroethylene is reduced within a few days [4]. Potentially important aspect of nanoparticle structure, including protective shell or impurities, is to alter the final products formed during the oxidation of chlorinated hydrocarbons to form environmental friendly products [5]. Understanding the chemical properties of nanoparticles can be achieved by controlling the cluster

structure and their shells. Control over the iron nanoparticles by conventional methods is difficult. The knowledge of the cluster components and their interaction mechanisms with gaseous or solution environments is an important requirement to understand the cluster.

Here we report the synthesis and characterization of nanoporous, nanostructured cluster film of iron along with the study of size-dependent enhancement of specific surface area (SSA).

2. EXPERIMENTAL DETAILS

Core-shell iron nanoclusters were synthesized from a 75 mm diameter iron target [6–8] of 3 mm thickness. Target acts as the cathode of the sputtering gun inside the third generation nanocluster source. The schematic representation is given in Figure 1.

Aggregation tube cooled by chilly water promotes the cluster synthesis at low temperatures ranging from 3°C to room temperature. In this experiment, the clusters were prepared at 7°C. Inert gases are present inside the aggregation chamber, which acts as carrier gases, and Ar causes the sputtering. DC power when applied to the sputtering gun causes the gaseous Ar near the target to ionize and this generates Ar⁺ ions. Ar⁺ ions sputter the iron atoms from the surface of the target into the aggregation chamber where they aggregate due to low temperature and form clusters. Clusters move from one chamber to the other due to the gas flow and

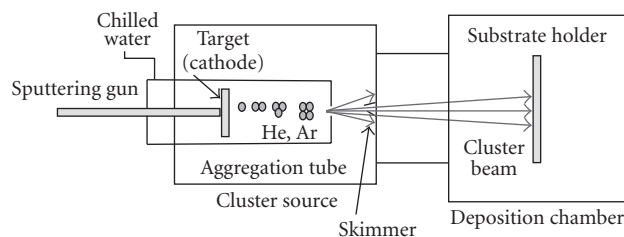


FIGURE 1: Schematic representation of the third generation nanocluster source.

pressure differences between the chambers and reach deposition chamber. Here the nanoclusters are deposited on substrates like TEM grids or Si wafers placed on the substrate holder. Size of the iron-iron oxide core-shell nanoclusters is varied using inert gas ratio, pressure, growth distance, and power supplied to the gun. Detailed information about the preparation technique can be found in [6–12]. To confirm our understanding of the properties of these particles, a comparison is made between the microscopic measurements of particle structures using transmission electron microscopy (TEM) and atomic force microscopy (AFM) and the surface area (SA) analysis using BET. Formation of well-defined particles provides useful materials for the study of chemical properties of nanoparticles.

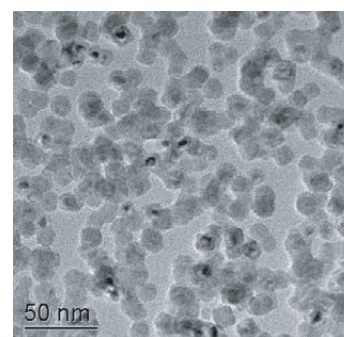
3. RESULTS AND DISCUSSION

Low-resolution TEM image of monodispersed iron-iron oxide core-shell nanoclusters of ~ 21 nm size exposed to atmosphere is shown in Figure 2(a). Figure 2(b) is a high-resolution TEM image of a core-shell nanocluster. Thickness of the pure Fe(0) core and the iron oxide shell of this core-shell structure can be clearly seen from the high-resolution TEM image. The oxide shell measured with high-resolution TEM shows a thickness of 2–3 nm, and is very stable. The characterizations of Fe(0) core and oxide shells are reported elsewhere [7]. TEM images show core-shell structure for particles exposed to the air for several months, which reveals the stability of iron-iron oxide core-shell nanoclusters.

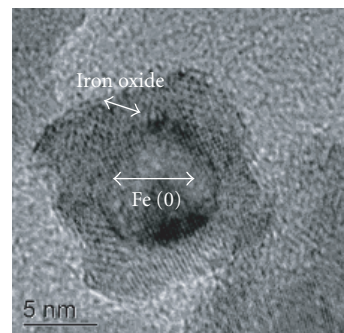
The porous nature of the cluster film, observed from the tapping mode AFM data is given in Figure 3. Here we see the cluster film deposited on Si substrate. The image below is in $2 \mu\text{m}$ range along x - y direction and 20 nm in z -direction. The image RMS value is 1.98 nm. As the deposition takes place in low energy range, the clusters retain their original shapes. The randomly deposited nanoclusters give porous nature to the film.

SSA is the SA per mass. Mathematically, SSA can be calculated using the formula: $SSA = SA_{\text{part}} / (V_{\text{part}} * \text{density})$. Here V_{part} is particle volume and SA_{part} is particle SA.

The calculated SSA uses the concept of maximally random jammed (MRJ) state [13], which is the most disordered state among all strictly jammed packing [14]. If the particles are in an MRJ state, then they cannot move or rattle around. The packing fraction for MRJ states ranges from 0.52 to



(a)



(b)

FIGURE 2: (a) Low-resolution TEM image of iron-iron oxide core-shell nanoclusters. (b) High-resolution TEM image of an iron-iron oxide core-shell nanocluster.

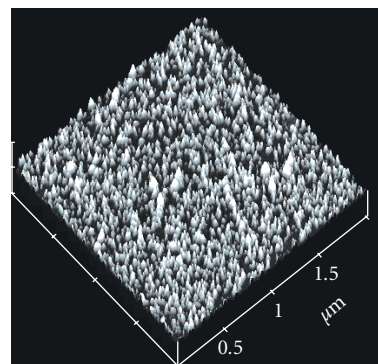


FIGURE 3: AFM image of iron-iron oxide core-shell nanoclusters (x - y : $2 \mu\text{m}$ scale, z : 20 nm, RMS = 1.98 nm).

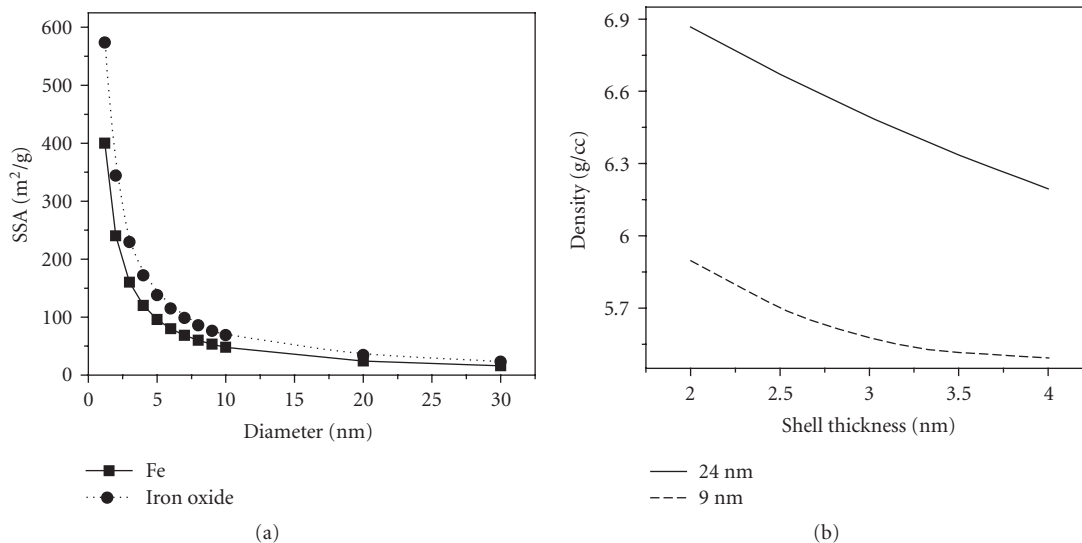


FIGURE 4: (a) Specific surface area (calculated) versus diameter curves for an iron and iron oxide particle film. (b) Density (bulk) versus iron oxide shell thickness of 9 nm and 24 nm core-shell iron-iron oxide samples.

0.74, but a packing fraction (PF) around 0.63 is much more common than others. PF increases with increasing order of configuration and lowers with the decrease in order [13].

Figure 4(a) shows the calculated SSA versus cluster diameter curves for iron and iron oxide porous cluster films. The particles are assumed spherical with bulk densities. Contact areas between particles are considered negligible. It is seen from Figure 4(a) that the SSA increases with the decrease in cluster diameter, and the increase is prominent below 10 nm. From Figure 4(a), it is seen that iron and iron oxide nanoclusters show only a small change in SSA above 10 nm sizes. Below 5 nm diameter, the discrepancy between SSA of metallic iron and iron oxide increases.

Clusters < 7 nm in size, when observed under TEM, are found to be fully oxidized, while the clusters > 7 nm have an oxide shell of thickness range 2 nm to 3 nm [7]. For a cluster of size 21 nm, the shell thickness can range from 2 nm to 3.5 nm. If we consider a nanocluster to have the density of bulk Fe or/and iron oxide, then as the thickness of the shell of a nanocluster increases, its density tends towards the iron oxide density from the iron density. Figure 4(b) gives a plot of density versus shell thickness for 9 nm and 24 nm iron-iron oxide nanoclusters. Density decreases faster in the case of 24 nm core-shell clusters with the increase in shell thickness, whereas the density decrease takes place at a slower pace for 9 nm core-shell clusters.

BET measures adsorption of nitrogen on the surface of a sample to determine the SSA of the particles. Here, BET is used to determine the SSA of core-shell iron-iron oxide nanoclusters of different sizes between 7 nm and 21 nm deposited on Si wafer substrates. Figure 5 shows BET results from the nanocluster film composed of spherical nanoclusters deposited on Si wafers, results calculated using the density of 24 nm clusters with 3 nm thick oxide shell as solid curve, and the BET results from plane Si wafers. Experimental results

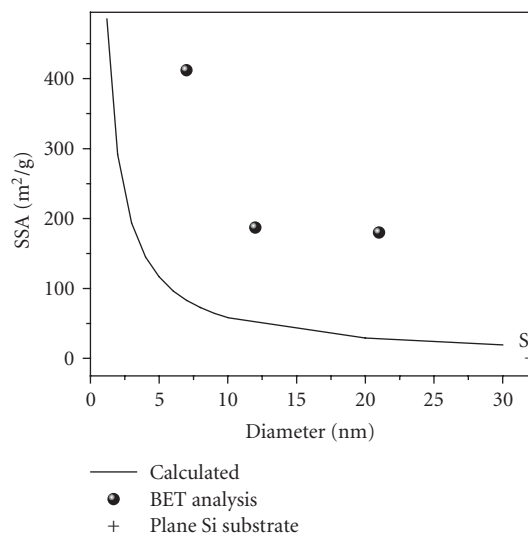


FIGURE 5: SSA (calculated) versus diameter curves for iron-iron oxide core-shell structured nanocluster with 3 nm shell thicknesses is denoted by the solid curve, SSA of nanoclusters deposited on Si wafers are given by spheres, and the SSA of plane Si wafers measured by BET is represented by plus sign.

have significantly large SSA than that expected from calculation, which can be due to lower nanocluster density and high porosity of the cluster film. Additionally, in the case of MRJ packing, particles are considered to be tightly packed, which is not strictly true for the soft landed nanoclusters deposited on Si wafer to form a thin film of clusters. This is because the nanoclusters that are deposited randomly leave lots of space in between each other and hence increases the amount of nitrogen absorbed into the sample.

4. CONCLUSIONS

In conclusion, stable monodispersed iron-iron oxide core-shell nanoporous films are synthesized using nanoclusters as building blocks. TEM, AFM, and BET measurements are done to characterize this nanoporous sample. TEM image shows the monodispersed nanocluster sample. BET measurements show that the surface areas of cluster films are significantly enhanced with decrease in particle size.

ACKNOWLEDGMENTS

Research work performed in this paper is supported by the grant from US Department of Energy (DOE) Office of Science, Offices of Basic Energy Sciences, Biological, and Environmental Research. TEM, AFM, and BET measurements were done at Environmental Molecular Sciences Laboratory, a national scientific user facility sponsored by the DOE's Office of Biological and Environmental Research at PNNL. Idaho NSF-EPSCoR Grant provided funding and support for the synthesis capabilities for this work.

REFERENCES

- [1] Y. Ding, M. Chen, and J. Erlebacher, "Metallic mesoporous nanocomposites for electrocatalysis," *Journal of the American Chemical Society*, vol. 126, no. 22, pp. 6876–6877, 2004.
- [2] E. Schofield, "Reviews in modern surface finishing no.1: anodic routes to nanoporous materials," *Transactions of the Institute of Metal Finishing*, vol. 83, no. 1, pp. 35–42, 2005.
- [3] J. T. Nurmi, P. G. Tratnyek, V. Sarathi, et al., "Characterization and properties of metallic iron nanoparticles: spectroscopy, electrochemistry, and kinetics," *Environmental Science & Technology*, vol. 39, no. 5, pp. 1221–1230, 2005.
- [4] W.-X. Zhang, "Nanoscale iron particles for environmental remediation: an overview," *Journal of Nanoparticle Research*, vol. 5, no. 3-4, pp. 323–332, 2003.
- [5] Y. Q. Liu, S. A. Majetich, R. D. Tilton, D. S. Sholl, and G. V. Lowry, "TCE dechlorination rates, pathways, and efficiency of nanoscale iron particles with different properties," *Environmental Science & Technology*, vol. 39, no. 5, pp. 1338–1345, 2005.
- [6] Y. Qiang, J. Antony, M. G. Marino, and S. Pendyala, "Synthesis of core-shell nanoclusters with high magnetic moment for biomedical applications," *IEEE Transactions on Magnetics*, vol. 40, no. 6, pp. 3538–3540, 2004.
- [7] J. Antony, Y. Qiang, D. R. Baer, and C. Wang, "Synthesis and characterization of stable iron-iron oxide core-shell nanoclusters for environmental applications," *Journal of Nanoscience and Nanotechnology*, vol. 6, no. 2, pp. 568–572, 2006.
- [8] J. Antony, J. Nutting, D. R. Baer, and Y. Qiang, "Nanoporous and nanostructured materials made out of clusters for environmental applications," in *Proceedings of the Materials Research Society Symposium (MRS '05)*, vol. 876E, p. R10.4, San Francisco, Calif, USA, 2005.
- [9] J. Antony, S. Pendyala, A. Sharma, et al., "Room temperature ferromagnetic and ultraviolet optical properties of Co-doped ZnO nanocluster films," *Journal of Applied Physics*, vol. 97, no. 10, Article ID 10D307, 3 pages, 2005.
- [10] Y. Qiang, R. F. Sabiryanov, S. S. Jaswal, Y. Liu, H. Haberland, and D. J. Sellmyer, "Magnetism of Co nanocluster films," *Physical Review B*, vol. 66, no. 6, Article ID 064404, 4 pages, 2002.
- [11] Y. Qiang, Y. Thurner, T. Reiners, O. Rattunde, and H. Haberland, "Hard coatings (TiN, Ti_xAl_{1-x}N) deposited at room temperature by energetic cluster impact," *Surface and Coatings Technology*, vol. 100-101, pp. 27–32, 1998.
- [12] D. J. Sellmyer, C. P. Luo, Y. Qiang, and J. P. Liu, "Magnetism of nanophase composite films," in *Handbook of Thin Films Materials: Nanomaterials and Magnetic Thin Films*, vol. 5, chapter 7, pp. 337–374, Academy press, New York, NY, USA, 2002.
- [13] A. R. Kansal, S. Torquato, and F. H. Stillinger, "Diversity of order and densities in jammed hard-particle packings," *Physical Review E*, vol. 66, no. 4, Article ID 041109, 8 pages, 2002.
- [14] A. Donev, F. H. Stillinger, and S. Torquato, "Unexpected density fluctuations in jammed disordered sphere packings," *Physical Review Letters*, vol. 95, no. 9, Article ID 090604, 2005.

New Development in Nanoporous Composites: Novel Functional Materials for Capturing Nitrosamines in Airstreams

Ting Ting Zhuang,¹ Jia Hui Xu,¹ Jia Rong Xia,² Yi Cao,¹ Shi Lu Zhou,² Ying Wang,² Yuan Chun,¹ and Jian Hua Zhu¹

¹Laboratory of Mesoscopic Chemistry, School of Chemistry and Chemical Engineering, Nanjing University, Nanjing 210093, China

²Department of Chemistry, School of Chemistry and Chemical Engineering, Nanjing University, Nanjing 210093, China

Received 13 March 2006; Revised 25 July 2006; Accepted 2 August 2006

The latest progresses of the series of research on the trapper of nitrosamines are reported in this paper, involving the attempts to elevate the selective adsorption of zeolites through enhancing adsorbent-adsorbate interaction, in order to prepare the new functional nanoporous materials with high efficiency to eliminate the carcinogenic pollutants in environment and to protect public health. Incorporation of metal oxide such as copper oxide in NaY accelerated adsorption of volatile nitrosamines and anthracene, and moreover, coating zirconia onto the zeolite could dramatically suppress the release of nitrogen oxides in the decomposition of *N*-nitrosopyrrolidine (NPYR) during temperature-programmed surface reaction (TPSR) process.

Copyright © 2006 Ting Ting Zhuang et al. This is an open access article distributed under the Creative Commons Attribution License, which permits unrestricted use, distribution, and reproduction in any medium, provided the original work is properly cited.

1. INTRODUCTION

Developing new processes for chemical production and controlling the environment pollution are two main challenges faced by the chemists of the 21st century, and these are also the new applications of nanoporous functional materials. Apart from a number of novel catalysts and adsorbents designed and synthesized for chemical industry, many efforts have been done for the protection of environment that connects the life of people much closer. Among these extensive efforts to be undertaken, one of the new developing areas of study is the application of nanoporous functional materials such as zeolites, because zeolite has excellent thermal and chemical stability along with the unique shape selectivity and sieving effect. These inherent features enable the nanoporous materials to recognize, discriminate, and organize molecules with precisions that can be less than 0.1 nm [1], and a noteworthy example is the zeolite additive in cigarette to remove carcinogenic agents like nitrosamines because smoking is a global problem causing health hazard [2–5]. Nitrosamines are known to be toxicant chemical not only to cause poisoning some times, but also to induce cancer and tumor in almost all organs of experimental animals [6]. They are important contributors to the total burden of carcinogens resulting from tobacco, especially the tobacco smoke, since

the nitrosamines in tobacco products and tobacco smoke can be directly deposited into the blood following inhalation through smoking. Moreover, environmental tobacco smoke is one of the major contaminants of indoor air leading to considerable exposure for the nonsmoker through passive smoking. Thus, removal of carcinogenic compounds from environment is important for environment protection. Zeolites are the potential trapper of nitrosamines owing to their unique function of selective adsorption, and about 50–70% of nitrosamines in smoke can be eliminated [2, 4]. In early literature this function of zeolite was attributed to its catalysis, but detailed researches reveal the crucial role played by the selective adsorption of zeolite [7–12]. The extraordinary interaction for the N–NO functional group of nitrosamines enables zeolite to capture the carcinogenic compounds in the smoke that contains more than 4000 components; even the zeolite A is able to adsorb the volatile nitrosamines through an especial inserting model of adsorption [13, 14], in which the carcinogens adsorb in zeolite by inserting the N–NO functional group into the narrow channel.

To meet the requirement of reducing the nitrosamines level in the aeration system of tower where the flow rate of airstreams is very large and the concentration of nitrosamines relatively lower [15], however, new functional nanoporous materials with higher efficiency are sought. These novel

candidates should have stronger capability to selectively adsorb nitrosamines and, if possible, other carcinogenic compounds in airstreams. Recently our group tried to incorporate copper oxide on NaY zeolite through impregnation method, and successfully enhanced its ability of trapping volatile nitrosamines, say, about one time higher, in the smoke of Chinese Virginia-type cigarette [16–19]. Nonetheless, suspicions still exist on the modified zeolites concerning whether they can adsorb the bulky polycyclic aromatic hydrocarbons (PAHs), that is, another carcinogens, in airstreams. Besides, further study is required to explore the possibility of replacing copper oxide by other metal oxides for lower cost and higher environmental benignity of the nanoporous functional materials.

In most cases, the degradation of nitrosamines, catalyzed by the modified zeolites or mesoporous silica, releases gaseous nitrogen oxides NO_x due to the rupture of N–NO band in the carcinogenic molecule, which, however, is not environmental benign anyway. Therefore, seeking another modifier to replace copper oxide for these porous adsorbents is another aim of the present paper, and the candidate should be able to obviously reduce the release of NO_x during the catalytic decomposition of nitrosamines. Based on our foregoing investigation [20, 21], zirconia is chosen because of its weak acidity and weak basicity. Nitrosamines possess both weak acidity and weak basicity, too; therefore establishing a suitable chemical environment in the nanoporous adsorbent should be beneficial to promote the decomposition of the worst carcinogenic compounds. Nonetheless the reason why the zirconia-coated zeolites can reduce the release of NO_x in the catalytic degradation of nitrosamines is still not understood, which spurs us to critically examine the property-function relations of zirconia embedded in zeolite, not only for deep understanding of the selective removal of nitrosamines, but also for seeking the new concept for creating novel functional nanoporous materials.

2. EXPERIMENTAL

Three volatile nitrosamines, the *N*-nitrosodimethylamine (NDMA), the *N*-nitrosopyrrolidine (NPYR), and the *N*-nitrosohexamethyleneimine (NHMI), were purchased from Sigma and dissolved in dichloromethane with volume ratio of 1 : 19, and stored at 273 K. Anthracene (Ant) was also obtained from Sigma and dissolved in cyclohexane with weight ratio of 0.18. Zeolite NaY, with Si/Al of 2.86 and a surface area of 766 m²·g⁻¹, was purchased from Wenzhou catalyst factory (China). NaZSM-5 zeolite, with Si/Al ratio of 23, was provided by the catalysts factory of Nankai University (China). It possesses the surface area of 354 m²·g⁻¹ and the mean crystal size of 7 μm.

Copper was incorporated in the porous support using “drying impregnation”: 0.456 g Cu(NO₃)₂ · 3H₂O was dissolved in 40 ml H₂O and 5 g NaY added; the mixture was stirred strongly and heated up to half dryness; then dried at 373 K overnight; finally the product was ground to

100 mesh and calcined at 773 K for 6 h in order to convert Cu(NO₃)₂ to copper oxide. The resulting sample contained 3% (w/w) CuO and to be denoted as 3%CuO/NaY. Other samples were prepared in the same way and the concentration of aqueous solution was controlled to get different loadings of copper cations. Through similar process ZnO or Fe₂O₃ was loaded on zeolites. The purity of carrier gases N₂ and H₂ was 99.99%, and all agents used were of AR grade. For the preparation of zirconia-modified zeolite, the guest oxide ZrO₂ (Toray Ltd., SA = 120 m²·g⁻¹) was first ground along with NaY zeolite at a given weight ratio, then radiated in a microwave oven (2450 MHz, 850 W) for 20 minutes. The resulting materials were characterized by XRD, that carried out on an ARL XTRA diffractometer with Cu Kα radiation, and the XRD peak intensity ratio of ZrO₂ (111) to that of NaY (111) represented the proportion of the residual bulk zirconia in the sample. The static adsorption of *n*-hexane at 303 K was employed to characterize the pore volume of the nanoporous samples, in which the sample was evacuated at 673 K for 2 h then cooled to 303 K to contact with the adsorbate at the given pressure. XPS measurements on the VG ESCALab MK II instrument were performed using a 1253.6 eV Kα magnesium X-ray source, the energy scale of spectrometer was calibrated by setting the measured C1S binding energy to 284.6 eV. The concentration of each element was then calculated from the area of the corresponding peak, calibrated by using the relative sensitivity factor of Wagner.

Instantaneous adsorption of volatile nitrosamines is performed in a stainless steel microreactor whose one end inserts deeply into the injector port of Varian 3380 gas chromatograph (GC), while another end connects with the separation column in the GC. five mg samples, in 20–40 meshes, were filled in the reactor and sealed by glass wool to fix the position where the temperature could be accurately controlled by the injector port of GC. The sample was directly heated to the given temperature, without activation, in the flow of H₂ with a rate of 30 ml·min⁻¹, and the nitrosamine solution was pulse injected with amounts of 2 μl each time. After being gasified in the injector, the nitrosamines were pushed by the carrier gas with a speed of 25 cm·s⁻¹ to pass through the zeolite bed layer then to the packed column, and the response at the column outlet was recorded by the GC with thermal conductivity detector. The rejection was repeated for several times over several hours to examine the capability of zeolite to capture the nitrosamines in gas stream. To avoid environment contamination, exhaust gas was treated by acid solution to destroy nitrosamines.

In the experiment of temperature-programmed surface reaction (TPSR), 20 mg sample was activated in N₂ at 773 K for 2 h. NPYR solution was injected in the sample at 423 K followed by purge of N₂ for 0.2 h, then the temperature of the sample was increased from 423 K to 773 K at the rate of 8 K·min⁻¹ and kept at 773 K for 0.5 h; the cracking products of nitrosamines were detected every 20 K by spectrophotometric method [5].

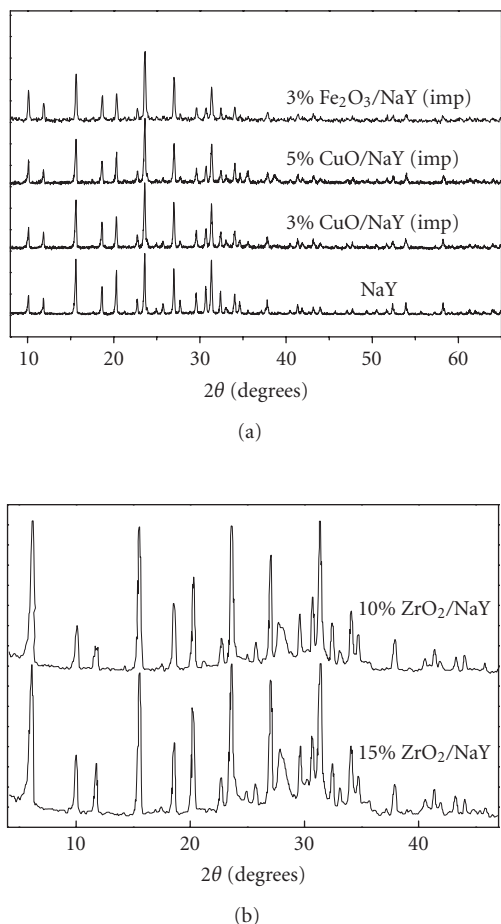


FIGURE 1: XRD patterns of transitional metal oxide-modified NaY samples.

3. RESULTS AND DISCUSSION

3.1. Characterization of the zeolite modified with metal oxide

Figure 1(a) depicts the dispersion of metal oxides on zeolite NaY, and all of three samples incorporated copper oxide or ferric oxide show the identical XRD patterns to that of parent zeolite NaY. No extra phase is observed in the case of loading 3 wt.-% of copper oxide or ferric oxide on NaY, and increasing the loading amount of copper oxide to 5 wt.-% cannot create the crystal phase of the guest on the patterns of the composite, either. It appears that the impregnation process can well disperse the metal oxide-like copper oxide or ferric oxide in zeolite NaY provided the loading amount is about 3 wt.-%.

Well-dispersion of zirconia in zeolite NaY was also observed. Microwave radiation did not damage the pore structure of NaY zeolite under the experimental conditions we used here [22, 23]. After the mixture of NaY and zirconia was microwave-radiated, no characteristic XRD peak of zirconia emerged in the patterns with the 2θ value of 28.1° , and the composite exhibited the same XRD pat-

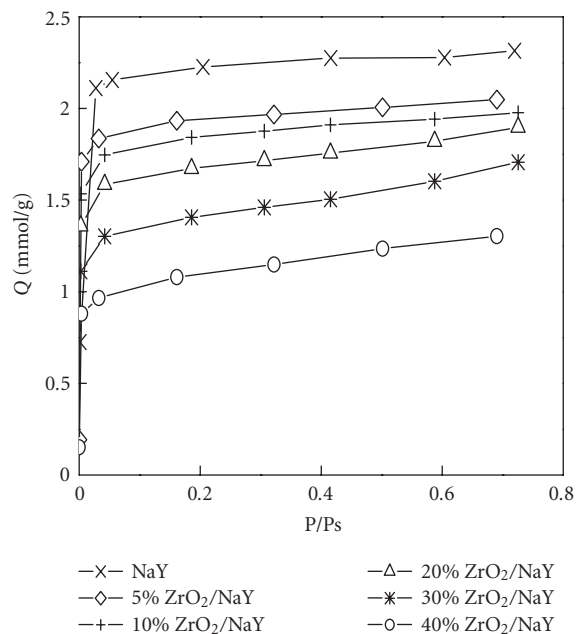


FIGURE 2: The isotherm of *n*-hexane adsorbed in zirconia-modified zeolite NaY at 303 K.

TABLE 1: Impact of loading zirconia on the adsorption of *n*-hexane in zeolite NaY ($P/P_s = 0.7$, at 303 K).

Loading amount (wt.-%)	0	5	10	20	30	40
Adsorption (mmol/g)	2.3	2.1	2.0	1.9	1.7	1.3
Decrease (%)	—	8.9	13.0	17.4	26.1	43.5

terns as that of zeolite NaY, even the loading amount reached 15 wt.-% (Figure 1(b)), since the spontaneous dispersion threshold of zirconia in the zeolite was 15 wt.-% [21]. However, adsorptive isotherm of *n*-hexane revealed the variation of the pore volume of the resulting composites. As is evident from Figure 2 and Table 1, the pore volume of zeolite NaY host, represented by the adsorption amount of *n*-hexane at 303 K, is gradually lowered owing to the occupation of the channel of zeolite by the guest oxide. Besides, the isotherm of 20%ZrO₂/NaY sample became turned up as the P/P_s exceeded 0.4, and such trend was observed on the sample of 30%ZrO₂/NaY and 40%ZrO₂/NaY. Nonetheless, the adsorption isotherm of *n*-hexane on ZrO₂/NaY sample still kept its original Langmuir type as that on zeolite NaY (Figure 2). This phenomenon demonstrates the existence of the uniform channel in the ZrO₂/NaY composites, that is, the characteristic of zeolite and very important for selective adsorption or catalysis. In general the reduced pore volume of zeolites goes against their adsorption of nitrosamines [12, 14], consequently the sample loaded with the zirconia of more than 20 wt.-% will not be used for further experiments.

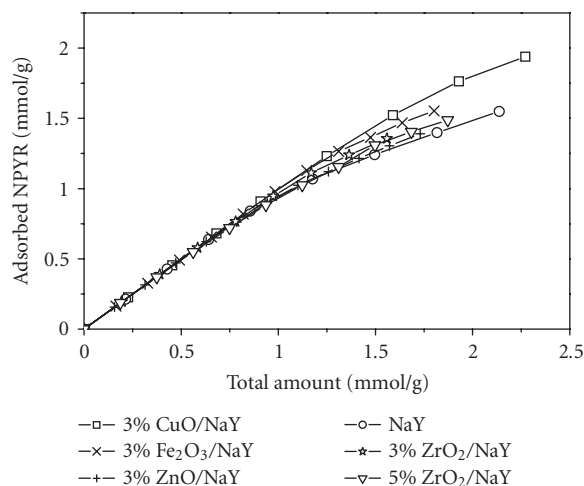


FIGURE 3: Adsorption of NPYR in zeolite NaY and metal oxide-modified NaY at 453 K.

3.2. The promoted adsorption capacity of zeolite for trapping nitrosamines in stream

Figure 3 illustrates the impact of loading 3 wt.-% transitional metal oxide on the capacity of zeolite NaY for instantaneous adsorbing NPYR at 453 K. It should be pointed out that the contact time between the adsorbent and the nitrosamines is very short in these tests, say, less than 0.1 second, which is similar to that in actual application of zeolites in aeration system. Both copper oxide and ferric oxide show an obvious promotion on zeolite NaY while a faint effect is found in the modification with zinc oxide. When the accumulated amount of NPYR reached $1.00 \text{ mmol}\cdot\text{g}^{-1}$, CuO/NaY or Fe₂O₃/NaY could adsorb 99.2% of the carcinogenic compound while ZnO/NaY or NaY adsorbed 93.8%. As the accumulated amount of NPYR increased to $1.70 \text{ mmol}\cdot\text{g}^{-1}$, ZnO/NaY exhibited a little larger adsorption capacity (81.0%) than the parent zeolite (78.5%). Promoted adsorption of nitrosamines in stream by zeolite is also observed on the samples of 3%ZrO₂/NaY and 5%ZrO₂/NaY, and they exhibit an enhanced adsorptive capacity slightly higher than both parent zeolite and zinc-modified NaY as demonstrated in Figure 3. Nitrosamines adsorbed in zeolite through the manner of inserting the N–NO group into the channel [9, 10, 12], which is accelerated by the strong interaction with the metal ions in the zeolite. Among the metal oxides used here, CuO appears to be the best one, however ferric oxide-modified sample possesses an excellent promotion function on the adsorptive ability of zeolite NaY, much close to that of copper-modified sample (Figure 3), which implies the possibility of replacing copper modifier by ferric oxide to promote the adsorptive capability of zeolite.

Figure 4 shows the promotion of CuO on the adsorption of NPYR in different zeolites. As the accumulated amount of NPYR rose from 0.5 to $1.5 \text{ mmol}\cdot\text{g}^{-1}$, CuO/NaY ad-

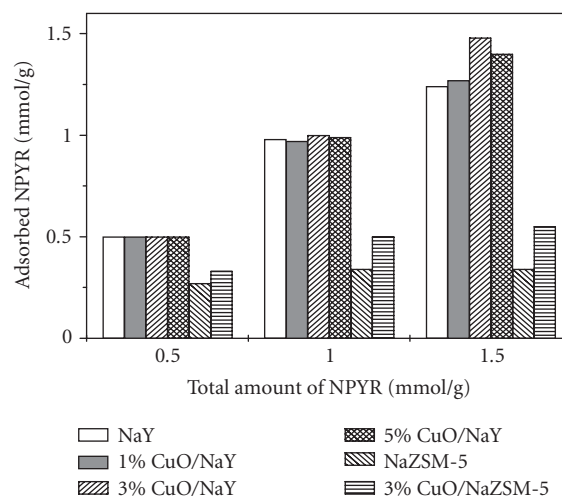
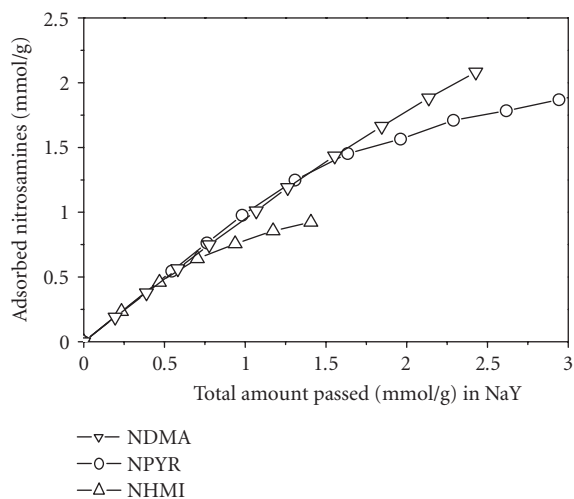


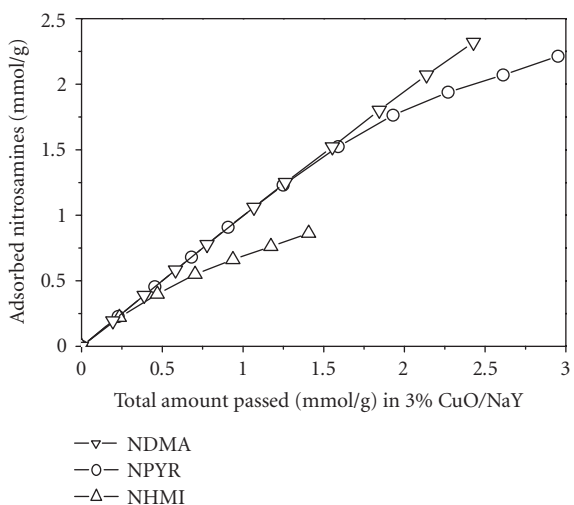
FIGURE 4: Amount of NPYR adsorbed on zeolites Y and ZSM-5 before and after loading copper oxide at 453 K.

sorbed more NPYR than NaY ($1.24 \text{ mmol}\cdot\text{g}^{-1}$), and the highest capacity was observed on 3%CuO/NaY sample ($1.48 \text{ mmol}\cdot\text{g}^{-1}$). Promotion of CuO became more obvious on NaZSM-5 zeolite, and the 3%CuO/NaZSM-5 adsorbed more NPYR ($0.33 \text{ mmol}\cdot\text{g}^{-1}$) than the parent zeolite ($0.27 \text{ mmol}\cdot\text{g}^{-1}$) even at the low accumulated amount of NPYR ($0.5 \text{ mmol}\cdot\text{g}^{-1}$). This difference became larger when the accumulated amount of NPYR reached $1.5 \text{ mmol}\cdot\text{g}^{-1}$: the former adsorbed $0.55 \text{ mmol}\cdot\text{g}^{-1}$ while the latter adsorbed $0.34 \text{ mmol}\cdot\text{g}^{-1}$. The adsorptive capability of NaZSM-5 is elevated about 60%.

Figure 5 depicts the impact of the molecular size on the adsorption of nitrosamines in the copper modification NaY zeolite. NDMA, NPYR, and NHMI have the molecular diameter of 0.45, 0.56, and 0.59 nm, respectively [12, 24], so that the adsorbed amount of three nitrosamines is diverse. For NaY when the accumulated amount of nitrosamines arrived $1.25 \text{ mmol}\cdot\text{g}^{-1}$, 70.5% of NHMI, 94.6% of NDMA, or NPYR could be adsorbed. In case $2.40 \text{ mmol}\cdot\text{g}^{-1}$ of nitrosamines passed through the adsorbents, about 85.7% of NDMA and 72.0% of NPYR were adsorbed. No doubt the NDMA with the smallest molecular volume can be adsorbed in zeolite much more easily due to its fast diffusion inside the channel of adsorbent [7]. Same tendency was found on 3%CuO/NaY. When the accumulated amount reached $1.25 \text{ mmol}\cdot\text{g}^{-1}$, 64.1% of NHMI, 97.9% of NDMA, or NPYR could be adsorbed; while the amount rose to $2.40 \text{ mmol}\cdot\text{g}^{-1}$, 95.1% of NDMA and 82.9% of NPYR were adsorbed. It is conclusive that the difference between the adsorption of three volatile nitrosamines is magnified on the copper-modified zeolite: more NDMA or NPYR but less NHMI adsorbed on the sample of 3%CuO/NaY. That is to say, incorporation of copper oxide delicately modifies the channel of zeolite and made the shape selectivity increased which may be beneficial for the separation in environment protection.



(a)



(b)

FIGURE 5: Different nitrosamines adsorbed on (a) NaY and (b) 3%CuO/NaY at 453 K.

Figure 6 shows the adsorption of anthracene (Ant), one of polycyclic aromatic hydrocarbons that exists widely in environment such as smoke [25], on zeolite NaY. In case that the accumulated amount of Ant was $30.0 \text{ mg}\cdot\text{g}^{-1}$, 70.4% of the adsorbate could be trapped by NaY. For 3%CuO/NaY, the corresponding value was 94%, one third higher than that of the parent zeolite. As is evidenced from Figure 6, the sample of 3%CuO/NaY can capture more anthracene molecules than NaY zeolite in the instantaneous adsorption in which the contact time is less than 0.1 second. This result replies a new application of the copper-modified nanoporous adsorbent in protection of environment, and this functional material may be used to trap the polycyclic aromatic hydrocarbons (PAH) in aeration system of tower. It is the first time to find the promotion of CuO modification on the instantaneous adsorption of both nitrosamines and PAH in zeolite

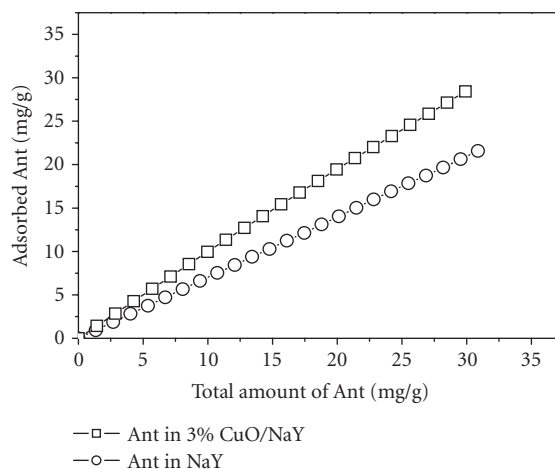


FIGURE 6: Anthracene (Ant) adsorbed on NaY and 3%CuO/NaY at 503 K.

NaY, but the mechanisms of the promotion may be different. Copper oxide attracts the N–NO group, through the interaction similar to that with NO_x [26], to accelerate adsorption of nitrosamines in NaY. Anthracene consists of only C and H without N and O as well as N–NO group, so the copper nanoparticles embedded in NaY cannot induce it into the channel as that happens in the case of nitrosamines. Decoration of channel of the adsorbent may result in this promotion, since the copper oxide dispersed into the channel of NaY should reduce the actual pore size, even a little. Anthracene has a molecular size of 0.49 nm, smaller than the pore size of NaY (0.76 nm), so the delicately reducing of the pore size and/or the curvature of channel in the adsorbent will be helpful for anthracene because the confinement of channel is elevated and thus forms a stronger adsorbate-adsorbent interaction with the adsorbate. Judged on these results, it seems feasible to promote adsorption of both nitrosamines and PAH in airstreams by nanoporous materials like zeolite, through tailoring the pore structure and surface state by coating metal oxide on the porous host.

3.3. Suppressing the release of nitric oxygen in decomposition of nitrosamines on zeolite NaY

Figure 7 depicts the degradation of NPYR on zeolite NaY in the temperature-programmed surface reaction (TPSR) process. NPYR is a volatile nitrosamines consisting of five-membered ring and its degradation starts from the rupture of N–NO bond to release nitric oxygen product [27, 28]. Consequently, the detected nitric oxide and other nitrogen oxides, that result from the further reactions of the primary nitric oxide, represent the amount of nitrosamines to be degraded [5, 8]. The NPYR adsorbed in ZrO₂/NaY began to degrade and liberate NO_x at 473 K when nitrogen was used as the carrier gas, giving rise to a maximum concentration of NO_x near 593 K on the sample of 5%ZrO₂/NaY

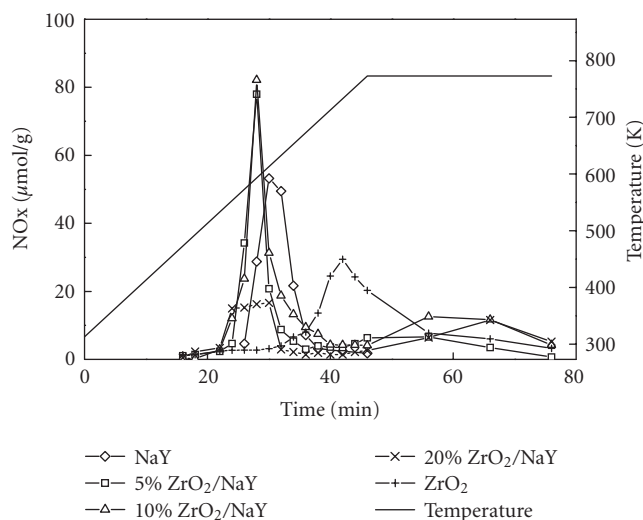


FIGURE 7: Impact of loading zirconia in zeolite NaY on the decomposition of NPYR.

and 10%ZrO₂/NaY with the amount of 78 and 82 $\mu\text{mol}\cdot\text{g}^{-1}$, respectively. When the reaction temperature was held at 773 K for 0.5 h, another unobvious desorption of nitrogen oxides appeared on 5%ZrO₂/NaY with a relative low concentration of about 6.6 $\mu\text{mol}\cdot\text{g}^{-1}$. This phenomenon became obvious in the sample of 10%ZrO₂/NaY and the corresponding value increased to 11.8 $\mu\text{mol}\cdot\text{g}^{-1}$. As a comparison, the maximum value of 53 $\mu\text{mol}\cdot\text{g}^{-1}$ emerged on parent zeolite NaY at 613 K, and no further desorption of NO_x was detected during which the sample was held at 773 K (Figure 7). The unsupported zirconia itself could adsorb a considerable amount of nitrosamines and most of them seemed to be decomposed at around 733 K, giving rise to a maximum concentration of 29 $\mu\text{mol}\cdot\text{g}^{-1}$. These nitrogen oxides continuously desorbed when the sample was held at 773 K, similar to that observed on those ZrO₂/NaY composites. On the basis of these results, it is very likely that desorption of NO_x from the zirconia-modified zeolite NaY at 773 K in the TPSR process of NPYR originates from the inherent feature of zirconia. The unsupported zirconia is a porous material with a pore volume of 0.23 $\text{ml}\cdot\text{g}^{-1}$ and an average pore size of 6.66 nm [29]. Under the test conditions used here, the detected total amount of NO_x in the decomposition of NPYR over zirconia (0.164 $\text{mmol}\cdot\text{g}^{-1}$) is smaller than that over zeolite NaY (0.179 $\text{mmol}\cdot\text{g}^{-1}$). However, the surface area of zirconia (120 $\text{m}^2\cdot\text{g}^{-1}$) is one sixth of that of NaY (766 $\text{m}^2\cdot\text{g}^{-1}$), so that the oxide probably possesses a comparable capability to NaY for trapping the volatile nitrosamine if judged on the efficiency per square meter surface area of the sample. Thus, coating zirconia on zeolite NaY through microwave-radiation considerably enhanced the efficiency for catalytic degradation of NPYR, and more NPYR were degraded at lower temperature than that on the parent zeolite. Moreover, desorption of NO_x at high temperature in TPSR process appeared on these nanoporous composites as the characteristic

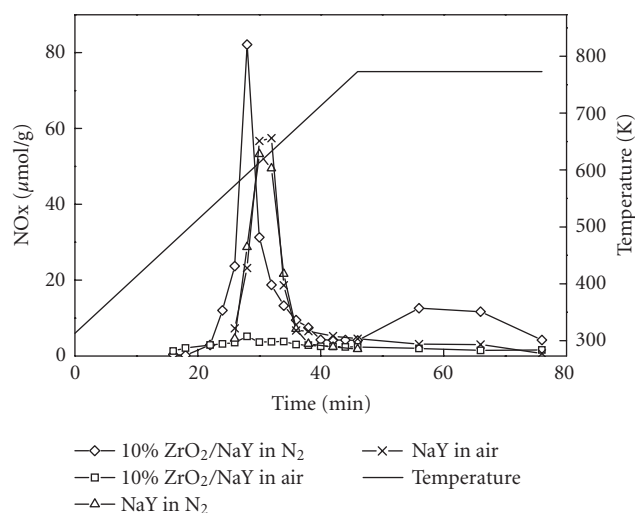


FIGURE 8: TPSR of NPYR over zeolite NaY in different carrier gases.

of zirconia. Incorporation of more zirconia in NaY did not cause further promotion on the catalytic activity of the composite, the detected amount of NO_x from the sample of 20%ZrO₂/NaY dramatically declined, as demonstrated in Figure 7, at the same time the desorption of NO_x at 773 K was still obvious.

When the carrier gas in TPSR process was changed from nitrogen to air, however, the maximum concentration of NO_x released from the sample of 10%ZrO₂/NaY was abruptly decreased to below 10 $\mu\text{mol}/\text{g}$ under the same conditions (Figure 8). Similar phenomenon was also observed on 5%ZrO₂/NaY sample, and these results were confirmed by several repeated experiments. In contrary, only slightly variation was found on the desorption of NO_x on NaY zeolite alone, and the concentration of NO_x at 633 K increased from 49.4 to 54.5 $\mu\text{mol}\cdot\text{g}^{-1}$ instead, as demonstrated in Figure 8. One may argue that these differences result from the different amounts of NPYR adsorbed on 10%ZrO₂/NaY in the different carrier gases, this argument however, is not justified by experiments. Two samples adsorbed NPYR in nitrogen or air prior to the TG-DTA tests, and the similar weight loss (about 8%) emerged accompanied by the same exothermic peak of NPYR decomposition that appeared around 473 K and continued to 873 K [21], indicating the similar amount of NPYR adsorbed on ZrO₂/NaY regardless of the kind of carrier gas. To check if the most of adsorbed NPYR escaped from the nanoporous material, the nitrosamine content of the exhaust gas was analyzed. However, only less than 1% of the adsorbed NPYR was found to desorb from 10%ZrO₂/NaY sample during the TPSR process, which confirms that most of the nitrosamines are degraded. This is rationalized by proposing that the products distribution of NPYR degradation is changed in the sample of 10%ZrO₂/NaY when the carrier gas becomes air. That is to say, the release of nitrogen oxides is suppressed though the reason is not known yet.

TABLE 2: XPS analysis of 10%ZrO₂/NaY sample.

Sample	Before activation		After activation in nitrogen	
	Atom %	Binding energy (eV)	Atom %	Binding energy (eV)
O1s	66.74	531.61	63.0	531.72
Zr3d	3.20	181.65	3.66	181.54
Na1s	7.65	1072.15	8.68	1072.15
Si2p	16.80	102.35	18.68	102.45
Al2p	5.59	73.95	5.97	74.25

Figure 9 shows the degradation of NPYR on the unsupported zirconia in different carrier gases. Unlike the sample activated and tested in nitrogen on which a lot of nitrogen oxides formed as aforementioned, only a few the gaseous NO_x products were detected on the bare oxide when the sample was activated and tested in air, and the total amount of NO_x lowered to 0.009 mmol·g⁻¹, about 5% of that on the former (0.164 mmol·g⁻¹). If the zirconia was directly used in the TPSR test in air without activation, the analyzed amount of nitrogen oxides (0.133 mmol·g⁻¹) was still smaller than that in nitrogen (0.164 mmol·g⁻¹), however dramatically higher than that activated in air (0.009 mmol·g⁻¹). Accordingly, activation of zirconia in nitrogen seems to elevate its ability to catalyze the formation of nitrogen oxides in decomposition of NPYR. Table 2 lists the XPS analysis results of the zirconia-modified zeolite NaY before and after activation in nitrogen, and both samples possess the same value of binding energy within the experimental error. This excludes the possibility that activation changes the electrovalent state of zirconium in the composite. Although the surface composition of the sample is slightly changed, say, the concentration of sodium cation increases from 7.65% to 8.68%, which cannot be used to account for the different catalytic properties of the composite activated in different carrier gases.

Figure 10 illustrates the XRD patterns of bare zirconia activated in air or nitrogen. Two crystal phases monoclinic baddeleyite and tetragonal form exist in the zirconia, and the former has intensity weaker than the latter. The peaks at 2θ of 30.2°, 50.2°, and 60.2° in the XRD patterns are the characteristic of tetragonal form [30]. After the sample was activated at 773 K in air, the XRD peak of monoclinic baddeleyite with 2θ value of 28.3° [29] became stronger but the tetragonal form was still the main phase. By contrary, activation at 773 K in nitrogen made the monoclinic baddeleyite to be the primary phase while the peak with 2θ value of 31.3° grew dramatically along with that of 28.3°. Drawing on these results, the impact of carrier gas in activation is further proposed. Tetragonal crystal in zirconia is metastable phase [29, 31], and activation in nitrogen seems to promote its conversion. Nonetheless, the available data do not allow a discussion of the possible mechanism involved, and further study is thus required to explore the relationship between the phase conversion extent of zirconia and the suppression of nitrogen oxides in TPSR test.

Although the reason why the zirconia-modified zeolite NaY can strangely suppress the release of NO_x during the decomposition of nitrosamines is still enigmatic; discovery

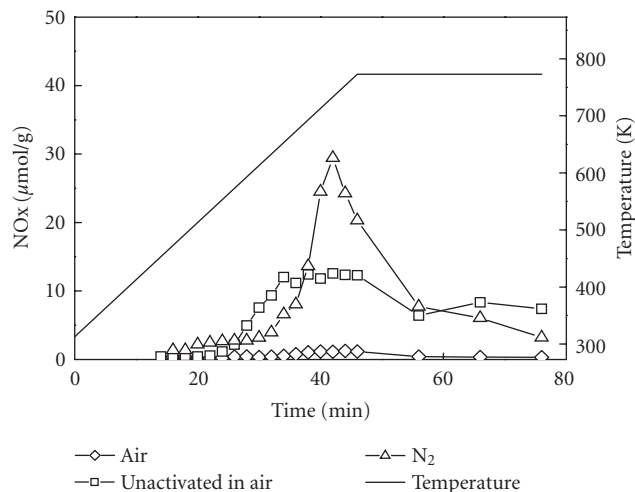


FIGURE 9: Decomposition of NPYR on the unsupported zirconia in different carrier gases.

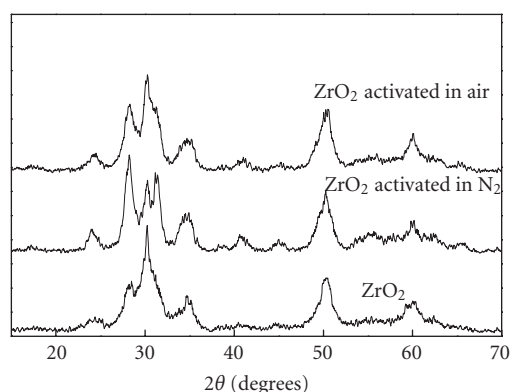


FIGURE 10: XRD patterns of zirconia activated in different atmospheres.

of this unwanted feature of the nanoporous adsorbent gives a clue for design and synthesis of novel functional materials that can act as killer traps for the carcinogenic pollutants in environment, for which choosing suitable guest components and incorporating them inside the pore of nanoporous host will be crucial.

4. CONCLUSION

Incorporation of transitional metal oxide such as copper oxide in zeolite can efficiently elevate the capability of the host to selectively trap the volatile nitrosamines in airstreams, opening the new application of the nanoporous materials into the aeration system of tower.

Ferric oxide-modified zeolite NaY exhibits a high ability of adsorbing volatile nitrosamines in stream, too, proving the possibility to replace copper oxide for modification of zeolites.

Coating zirconia on NaY through microwave-radiation can enhance the capability of the zeolite to capture nitrosamines in stream, too, and more importantly it dramatically suppress the release of nitrogen oxides when the decomposition of nitrosamine is performed in air, which may relate with the crystal phase of the guest but further investigation is needed.

ACKNOWLEDGMENTS

NSF of China (20273031 and 20373024), Ningbo Cigarette Factory, and Analysis Center of Nanjing University financially supported this work.

REFERENCES

- [1] M. E. Davis and R. F. Lobo, "Zeolite and molecular sieve synthesis," *Chemistry of Materials*, vol. 4, no. 4, pp. 756–768, 1992.
- [2] W. M. Meier and K. Siegmann, "Significant reduction of carcinogenic compounds in tobacco smoke by the use of zeolite catalysts," *Microporous and Mesoporous Materials*, vol. 33, no. 1–3, pp. 307–310, 1999.
- [3] Y. Wang, B. Shen, J. H. Zhu, L. Ji, L. L. Ma, and Q. H. Xu, "Investigation on the selective removing *N*-nitrosamines from the smoke of cigarette," *Chinese Environment. Chemistry*, vol. 19, pp. 280–286, 2000.
- [4] Y. Xu, Y. Wang, J. H. Zhu, L. L. Ma, and L. Liu, "Application of zeolite in the health science: novel additive for cigarette to remove," *Studies in Surface Science and Catalysis*, vol. 142, pp. 1489–1496, 2002.
- [5] Y. Xu, J. H. Zhu, L. L. Ma, A. Ji, Y. L. Wei, and X. Y. Shang, "Removing nitrosamines from mainstream smoke of cigarettes by zeolites," *Microporous and Mesoporous Materials*, vol. 60, no. 1–3, pp. 125–138, 2003.
- [6] S. S. Hecht, "DNA adduct formation from tobacco-specific *N*-nitrosamines," *Mutation Research/Fundamental and Molecular Mechanisms of Mutagenesis*, vol. 424, no. 1–2, pp. 127–142, 1999.
- [7] J. H. Zhu, D. Yan, J. R. Xia, L. L. Ma, and B. Shen, "Attempt to adsorb *N*-nitrosamines in solution by use of zeolites," *Chemosphere*, vol. 44, no. 5, pp. 949–956, 2001.
- [8] J. H. Zhu, S. L. Zhou, Y. Xu, Y. Cao, and Y.-L. Wei, "Ordered mesoporous materials. Novel catalyst for degradation of *N*-nitrosanornicotine," *Chemistry Letters*, vol. 32, no. 4, pp. 338–339, 2003.
- [9] C. F. Zhou, Z. Y. Yun, Y. Xu, Y. Wang, J. Chen, and J. H. Zhu, "Adsorption and room temperature degradation of *N*-nitrosodiphenylamine on zeolites," *New Journal of Chemistry*, vol. 28, no. 7, pp. 807–814, 2004.
- [10] Z.-Y. Yun, Y. Xu, J. H. Xu, et al., "In situ FTIR investigation on the adsorption of nitrosamines in zeolites," *Microporous and Mesoporous Materials*, vol. 72, no. 1–3, pp. 127–135, 2004.
- [11] C. F. Zhou and J. H. Zhu, "Adsorption of nitrosamines in acidic solution by zeolites," *Chemosphere*, vol. 58, no. 1, pp. 109–114, 2005.
- [12] C. F. Zhou, Y. Cao, T. T. Zhuang, et al., "Investigation on the adsorption of nitrosamines in zeolites," *Studies in Surface Science and Catalysis*, vol. 158, pp. 1003–1011, 2005.
- [13] J. H. Zhu, B. Shen, Y. Wang, and D. Yan, "Strong selective adsorption of *N*-nitrosamines on zeolites," *Chinese Science Bulletin*, vol. 46, pp. 705–707, 2001.
- [14] Y. Xu, Z. Y. Yun, C. F. Zhou, S. L. Zhou, J. H. Xu, and J. H. Zhu, "Adsorption of bulky nitrosamines on zeolite with small pore size," *Studies in Surface Science and Catalysis*, vol. 154, pp. 1858–1865, 2004.
- [15] K.-S. Liu, L. E. Alevantis, and F. J. Offermann, "A survey of environmental tobacco smoke controls in California office building," *Indoor Air*, vol. 11, pp. 25–34, 2001.
- [16] Y. Xu, Z.-Y. Yun, J. H. Zhu, et al., "Trapping volatile nitrosamines with copper incorporated zeolites," *Chemical Communications*, no. 15, pp. 1894–1895, 2003.
- [17] Y. Xu, H.-D. Liu, J. H. Zhu, et al., "Removal of volatile nitrosamines with copper modified zeolites," *New Journal of Chemistry*, vol. 28, no. 2, pp. 244–252, 2004.
- [18] H. D. Liu, S. L. Zhou, Y. Wang, Y. Xu, Y. Cao, and J. H. Zhu, "CuO modified NaY zeolite: efficient catalyst for degrading nitrosamines," *Studies in Surface Science and Catalysis*, vol. 154, pp. 2527–2535, 2004.
- [19] L. L. Ma, B. Shen, J. H. Zhu, J. R. Xia, and Q. H. Xu, "Modifying NaY zeolite with metal oxide by microwave irradiation: Influence on the adsorption and decomposition of *N*-nitrosamines," *Chinese Chemical Letters*, vol. 11, pp. 649–652, 2000.
- [20] J. H. Zhu, J. R. Xia, Y. Wang, G. Xie, J. Xue, and Y. Chun, "ZrO₂/NaY: new composite for removal of *N*-nitrosamines pollution," *Studies in Surface Science and Catalysis*, vol. 135, p. 320, 2001, (30-P-08).
- [21] J. R. Xia, J. H. Zhu, Y. Chun, Y. Wang, and R. K. Jia, "Preparing ZrO₂/NaY zeolite-based materials for catalytic degradation of *N*-nitrosamines by use of microwave irradiation," *Acta Chimica Sinica*, vol. 59, no. 8, pp. 1196–1200, 2001.
- [22] Y. Wang, J. H. Zhu, J. M. Cao, Y. Chun, and Q. H. Xu, "Basic catalytic behavior of MgO directly dispersed on zeolites by microwave irradiation," *Microporous and Mesoporous Materials*, vol. 26, no. 1–3, pp. 175–184, 1998.
- [23] L. L. Ma, B. Shen, J. H. Zhu, J. R. Xia, and Q. H. Xu, "Modifying NaY zeolite with metal oxide by microwave irradiation: influence on the adsorption and decomposition of *N*-nitrosamines," *Chinese Chemical Letters*, vol. 11, no. 7, pp. 649–652, 2000.
- [24] Y. Wang, S. L. Zhou, J. R. Xia, J. Xue, J. H. Xu, and J. H. Zhu, "Trapping and degradation of volatile nitrosamines on cyclodextrin and zeolites," *Microporous and Mesoporous Materials*, vol. 75, no. 3, pp. 247–254, 2004.
- [25] R. R. Baker, "Smoke chemistry," in *Tobacco Production, Chemistry and Technology*, D. L. Davis and M. T. Nielsen, Eds., pp. 419–426, Blackwell Science, London, UK, 1999.
- [26] J. Szanyi and M. T. Paffett, "The adsorption of NO and reaction of NO with O₂ on H-, NaH-, CuH-, and Cu-ZSM-5: an in situ FTIR investigation," *Journal of Catalysis*, vol. 164, no. 1, pp. 232–245, 1996.

-
- [27] J.-P. Cheng, M. Xian, K. Wang, X. Zhu, Z. Yin, and P. G. Wang, "Heterolytic and homolytic Y-NO bond energy scales of nitroso-containing compounds: chemical origin of NO release and NO capture," *Journal of the American Chemical Society*, vol. 120, no. 39, pp. 10266–10267, 1998.
- [28] K. Hiramoto, Y. Ryuno, and K. Kikugawa, "Decomposition of *N*-nitrosamines, and concomitant release of nitric oxide by Fenton reagent under physiological conditions," *Mutation Research/Genetic Toxicology and Environmental Mutagenesis*, vol. 520, no. 1, pp. 103–111, 2002.
- [29] Y. Wang, W. Y. Huang, Y. Chun, J. R. Xia, and J. H. Zhu, "Dispersion of potassium nitrate and the resulting strong basicity on zirconia," *Chemistry of Materials*, vol. 13, no. 2, pp. 670–677, 2001.
- [30] JCPDS file number 17-0932.
- [31] P. Duwez, F. Odell, and F. H. Brown Jr., "Stabilization of zirconia with calcia and magnesia," *Journal of the American Ceramic Society*, vol. 35, no. 5, pp. 107–113, 1952.

Synthesis and Characterization of Strontium Titanate Nanoparticles as Potential High Temperature Oxygen Sensor Material

Florian Voigts,¹ Tanja Damjanović,² Günter Borchardt,² Christos Argiris,²
and Wolfgang Maus-Friedrichs¹

¹*Institut für Physik und Physikalische Technologien, Technische Universität Clausthal, Leibnizstraße 4,
38678 Clausthal-Zellerfeld, Germany*

²*Institut für Metallurgie, Technische Universität Clausthal, Robert-Koch-Straße 42,
38678 Clausthal-Zellerfeld, Germany*

Received 13 March 2006; Revised 18 May 2006; Accepted 6 June 2006

We present a simple and highly reproducible method for the preparation of thin films consisting of strontium titanate nanoparticles. The films are produced by spin coating of a sol on silicon targets and subsequent annealing under ambient conditions. Analysis by atomic force microscopy shows particles with typical sizes between 10 nm and 50 nm. X-ray photoelectron spectroscopy displays a stoichiometry of the films as anticipated from preliminary experiments with strontium titanate single crystals. Metastable-induced electron spectroscopy and ultraviolet photoelectron spectroscopy are used as tools to give evidence to the similar electronic properties of nanoparticle film and single crystal. These results support the prospect for an application of the nanoparticle films as high temperature oxygen sensor with superior properties.

Copyright © 2006 Florian Voigts et al. This is an open access article distributed under the Creative Commons Attribution License, which permits unrestricted use, distribution, and reproduction in any medium, provided the original work is properly cited.

1. INTRODUCTION

Donor doped SrTiO₃ (STO) is well known for its capability as resistive high temperature oxygen sensor [1–4]. STO is stable without recrystallization over a wide temperature range between 104 K and about 2300 K [5]. Furthermore, STO accepts very high donor dopant concentrations up to 30% without any phase transition thus allowing to vary the sensor capacity over a wide range [6, 7]. Especially very porous donor doped STO was found to be of interest, because it provides quick response times in contrast to STO crystals. 0.5 at.-% Nb-doped STO layers, for example, show response times around 30–40 ms at 1130 K [1]. These response times can be improved even further if the particle size is decreased. Meyer and Waser found, that STO crystalline material with grain sizes of about 1 μm provides response times of about 10 ms [2].

Response times in the range of ms are necessary for most applications, for example, for oxygen sensors in car exhaust management. Therefore, the donor doped STO nanocrystalline particles may be of relevance in future high temperature oxygen sensor applications.

Sol-gel is a powerful method for preparation of nano-scaled oxide powders and nanoscale thin films for a variety of applications. It enables processing of refractory oxide layers at temperatures as low as 370 K in some special cases [8]. Materials with different compositions can be easily obtained in the form of glasses, fibers, ceramic powders, and thin films [9]. Multilayers are also easily made by means of sol-gel methods [10].

In this study we report a sol-gel route for the production of undoped and donor doped STO nanostructured thin films for sensor applications. We characterized these films by microscopic and electron spectroscopic methods.

2. EXPERIMENTAL

2.1. STO-sol and STO coatings preparations

STO sols were synthesized by means of a sol-gel method starting from alkoxides of the corresponding metals. The reagent grade chemicals used were Sr(C₂H₃O₂)₂ (99.995% Sr—Sigma-Aldrich) and Ti(OC₄H₉)₄ (97% Ti—Sigma-Aldrich). First, Sr-acetate was dissolved in concentrated

acetic acid under addition of small amounts of acetyl acetone which acts as a complexing agent. The dissolution of Sr-acetate was performed on a magnetic stirrer under continuous heating. After a clear solution of Sr-acetate was obtained Ti-butoxide was added dropwise to the solution.

For the preparation of Nb-doped STO, sol $\text{Nb}(\text{C}_2\text{H}_3\text{O}_2)_5$ (99.9% Nb—Strem Chemicals) was weighed and added with a syringe to an aliquot of the aforementioned undoped STO sol. In order to achieve the optimal viscosity of the final sol to be spin coated, we continued heating of the Nb-doped STO sol under stirring. The final sol was clear and stable on storage.

STO layers were applied on Si-wafers by means of spin coating upon addition of 20, 50, and $60\ \mu\text{l}$ of the STO sol, followed by spinning at $12000\ \text{s}^{-1}$ for 15 seconds. After deposition, the layers were left in ambient air for 1 hour and then thermally treated in air according to the following program: 2 K/min up to 570 K with a dwell of 30 minutes, and further with 3 K/min up to 1000 K with a 1-hour dwell. The samples were cooled down to room temperature at a cooling rate of 3 K/min.

2.2. STO particle characterization

The spectroscopic measurements were carried out using an ultrahigh vacuum (UHV) apparatus with a base pressure of 5×10^{-9} Pa, which has been described in detail previously [11].

Electron spectroscopy is performed with a hemispherical analyzer (VSW HA100) in combination with a source for metastable helium atoms (He^*) and ultraviolet photons (HeI line) for metastable induced electron spectroscopy (MIES) and ultraviolet photoelectron spectroscopy (UPS) as well as with a commercial non-monochromatic X-ray source (Specs RQ20/38C) for X-ray photoelectron spectroscopy (XPS).

During XPS, X-ray photons hit the surface under an angle of 80° to the surface normal, illuminating a spot with a diameter of a few millimeters. For the measurements shown here we used the Mg K_α and Al K_α lines with photon energies of 1253.7 eV and 1486.7 eV. Emitted electrons were analyzed by the hemispherical analyzer under 10° to the surface normal with a resolution of 1.1 eV. All XPS spectra are displayed as a function of the electron binding energy with respect to the Fermi level. Therefore, an apparent shift of all Auger lines by 233.0 eV occurs when switching between excitation sources.

For quantitative XPS analysis, the photoelectron peak area is calculated by mathematical fitting with Gauss-type profiles using OriginPro 7 G including the PFM fitting module. Photoelectric cross sections as calculated by Scofield [12] and inelastic mean free paths from the NIST database [13] are taken into account when calculating stoichiometry. Furthermore, the transmission function of our hemispherical analyzer is included into the calculation.

MIES and UPS are performed applying a cold cathode gas discharge via a two-stage pumping system. Here, metastable He^* atoms and HeI photons are produced. The

ratio between He^*2^3S and He^*2^1S amounts to 7 : 1 [14] at least. Therefore, no contribution of the He^*2^1S -surface interaction can be detected. A time-of-flight technique is used to separate electrons emitted by He^* (MIES) and HeI (UPS) interaction with the surface. The mixed He^*/HeI beam strikes the surface under an angle of 45° and illuminates an area of about 2 mm diameter on the sample surface. MIES and UPS spectra are simultaneously recorded by the hemispherical analyzer with a resolution of 220 meV under normal emission within 130 second.

Metastable He^* atoms may interact with the sample via different mechanisms depending on surface electronic structure and work function [15, 16]. In this work, we will only discuss the relevant processes.

During Auger deexcitation (AD), an electron from the sample surface fills the 1s orbital of the impinging He^* . Simultaneously, the He 2s electron is emitted carrying the excess energy. The resulting spectra directly display the surface density of states (SDOS). The excitation potential of the He^* amounts to 19.8 eV [15–18]. Because the He^* atoms interact with the surface in distances typically between 0.3 and 0.5 nm in front of it, MIES is extremely surface sensitive and displays the SDOS of the uppermost layer of the sample only. To distinguish surface from bulk effects, AD-MIES and UPS can be compared directly.

For STO, a different interaction takes place: the 2s electron of the impinging He^* is resonantly transferred into the surface of the sample and localizes at near surface Ti 3d states. Subsequently, a Ti 3d electron fills the hole in $\text{He}^+ 1\text{s}$ in an interatomic Auger neutralization (AN) process, followed by the emission of an O(2p) surface electron carrying the excess energy. The energy of the resulting MIES peak is shifted by 1.2 eV toward higher binding energies compared to AD due to a diminished local ionization potential. A detailed discussion of this process is given in [19].

Oxygen incorporation into STO most strongly depends on the dissociation probability in the vicinity of the surfaces. This probability depends on the very outermost surface wave functions which are most sensitively probed by MIES.

All MIES and UPS spectra are displayed as a function of the electron binding energy with respect to the Fermi level. The surface work function can be determined from the left onset of the MIES or the UPS spectra with an accuracy of 0.1 eV.

The silicon samples bearing the STO nanoparticles are mounted in a molybdenum sample holder and transferred into the UHV via a transfer system. Afterwards, the sample is cleaned from surface contamination by heating to about 850 K before measuring.

Atomic force microscopy (AFM) measurements are performed with a digital instruments dimension 3100 AFM in tapping mode using a silicon cantilever. The AFM is operated under ambient conditions. AFM images are analyzed concerning particle size distribution and surface roughness with SPIP 3.2 from image metrology.

Auger depth profiles were used to measure the thickness of the STO layers on the silicon by sputtering with argon under control of a PHI Auger microprobe system. These

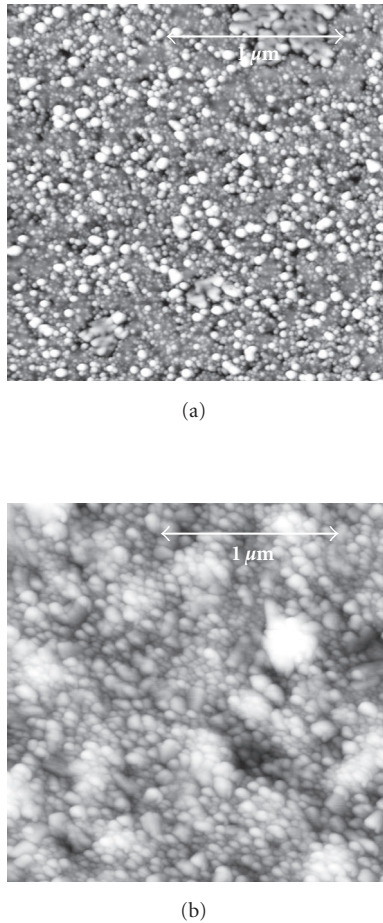


FIGURE 1: AFM images ($2 \times 2 \mu\text{m}^2$) of an (a) undoped and (b) Nb-doped SrTiO_3 nanoparticle film on a $\text{Si}(100)$ substrate.

measurements were carried out in a separate vacuum chamber.

3. RESULTS

Figure 1 shows the AFM images of a STO undoped (Figure 1(a)) and Nb-doped (Figure 1(b)) nanoparticle film, which was produced via the sol-gel route described in Section 2. After deposition the samples were transferred to the microscope immediately. We evaluate an average size of 25 nm with a full width at half maximum (FWHM) of 20 nm for the undoped particles and an average size of 50 nm with a FWHM of 30 nm for the donor doped particles. The films are thinner than 100 nm in both cases, which was evaluated by Auger depth profile analysis. The particle sizes and their distributions can be reproduced with high accuracy applying the synthesis parameters described in Section 2. The surfaces possess roughnesses of about 3.8 nm for the undoped and 6.3 nm for the doped films (root mean square corresponding to ISO 4287/1). Heating to temperatures substantially higher than described in Section 2.1 does not change neither the size nor the distribution of the nanoparticles.

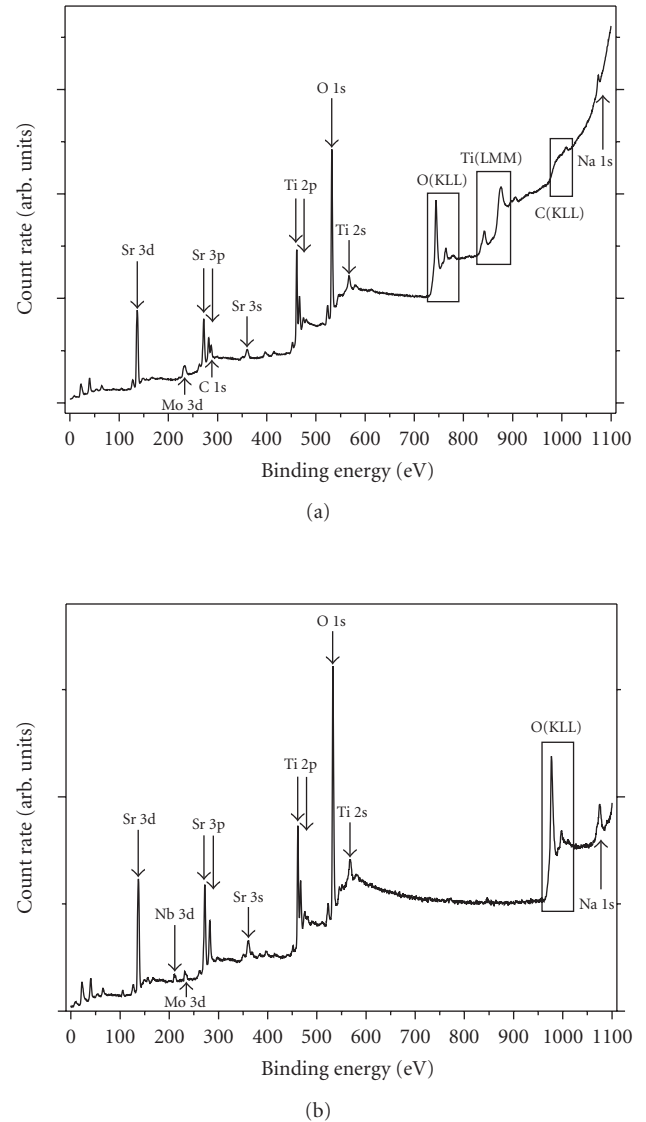


FIGURE 2: (a) XPS spectrum using $\text{Mg K}\alpha$ excitation of an undoped SrTiO_3 nanoparticle film on a $\text{Si}(100)$ substrate, (b) XPS spectrum using $\text{Al K}\alpha$ excitation of a Nb-doped SrTiO_3 nanoparticle film on a $\text{Si}(100)$ substrate. O(KLL) , Ti(LMM) , and C(KLL) are shifted by 233.0 eV towards higher binding energies compared to Figure 2(a).

Figure 2 shows the XPS spectra of the undoped (Figure 2(a)) and Nb-doped (Figure 2(b)) STO nanoparticle films shown in Figure 1. The samples were immediately inserted into the UHV after the microscopy. The peak areas are analyzed as described in Section 2 and are compared with the corresponding ones for stoichiometric STO. For the undoped particles we find a composition near to STO but with a Sr concentration about 5% lower than the Ti concentration. Comparable values are found for the doped particles with a Nb concentration of about 1 at.-%. This corresponds well to the value expected from preparation.

Besides the peaks corresponding to STO we observe Mo, C, and Na signals. Mo is due to the sample holder and is not

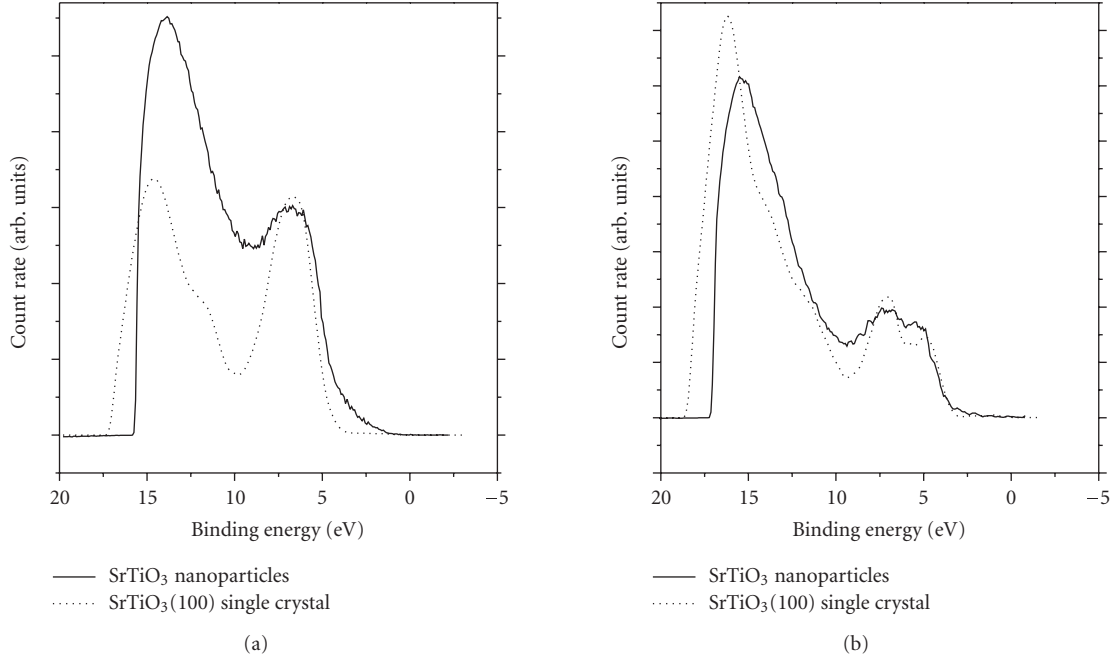


FIGURE 3: (a) MIES and (b) UPS spectra of an SrTiO₃ nanoparticle film on an Si(100) substrate (solid line) compared to the corresponding spectra of SrTiO₃(100) single crystals (dotted line).

found on the sample surface. C is typically due to a surface contamination with carbon containing species like CO₂ or CO₃²⁻. The Na contamination is mostly due to NaCl residues from the deposition process.

It is well known from literature that donor doped STO crystals heated under ambient conditions loose Sr [20, 21]. We assume that the annealing during the synthesisation process induces similar processes on the nanoparticle surfaces, thus reducing the Sr concentration.

Figure 3 shows MIES (Figure 3(a)) and UPS spectra (Figure 3(b)) of the undoped nanoparticle film discussed above compared with corresponding spectra for SrTiO₃(100) single crystals [19, 22, 23]. Nb-doped nanoparticles show similar spectra which are therefore not shown here. The spectra are displayed as a function of the binding energy E_B with the Fermi level at $E_B = 0$ eV. The contributions beyond $E_B \approx 10$ eV are induced by secondary electrons and will not be discussed here. The MIES spectra show one peak at $E_B = 6.5$ eV being induced by the localized AN process described in Section 2 [19]. This peak is well known and corresponds to the ionization of non-hybridized O(2p) of the SrTiO₃(100) surface, which is terminated by a TiO₂ layer [24]. The valence band maximum (VBM) of SrTiO₃(100) single crystals is found around $E_B = 3.2$ eV while the VBM on the STO particle film reaches to $E_B \approx 1.9$ eV.

UPS shows a double peak structure at $E_B = 7.0$ eV and $E_B = 4.9$ eV. The peak at higher binding energy corresponds to the ionization of O(2p) orbitals being hybridized with Ti 3d, while the peak at lower binding energy is due to non-hybridized O(2p). The VBM is found around $E_B \approx 3.2$ eV for the single crystal and the film.

4. DISCUSSION

Applying the simple synthesis procedure described in Section 2, films containing nanoscale particles are produced easily. These particles consist of Sr, Ti, and O with near STO stoichiometry. The reduced Sr concentration is most probably due to the applied heating procedure described in Section 2. It is well known that an Sr loss occurs during heating STO single crystals in oxygen containing atmospheres. UPS and MIES show a quite good similarity between the particle film and well-defined SrTiO₃(100) surfaces. The latter one is known to show good high temperature oxygen sensor capabilities. The (110) and (111) surfaces are known to show the same electronic structures.

The similarity between the UPS spectra proves that the surface density of states of the nanoparticles is very similar to the one for STO single crystals. It is known that the electronic and geometric structure of STO does not change even for large amount of Sr vacancies inside the crystal [6, 7].

The interaction of the impinging He* atoms approaching the surface with thermal velocity probes only the very outermost surface wave functions. These wave functions are also responsible for the interaction of sensor surfaces with impinging oxygen or ambient atmospheres molecules. In this sense MIES is a very reasonable and powerful tool to investigate the heterogenous reactivity of the sensor surface. The observed similarity between the MIES spectra for single crystal and the film is of great relevance for future sensor applications. It suggests that the nanocrystalline film can be expected to behave similarly to STO single crystals. Furthermore, in MIES contributions within the STO band gap are

observed. These are likely due to surface defects, which will enhance the surface reactivity further.

It was shown previously that typical oxygen diffusion lengths in STO amount to several 10 nm in a diffusion time of 10 ms [25]. The oxygen diffusion on the nanoparticles surfaces may be expected to be much faster than inside the crystals. For ZrO_2 it was found that the surface diffusion is about 10^4 times faster than the diffusion into the bulk [26]. This means that nanoparticles with a diameter of several 10 nm can be expected to provide a very high signal, because all particles contribute to the oxygen sensor signal with their complete volume.

5. SUMMARY

Undoped and 1 at.-% Nb-doped nanoparticle containing films with near STO stoichiometry were produced applying a simple sol-gel procedure. The undoped particles show a mean diameter of 25 nm with a FWHM of 20 nm while the doped particles show a mean diameter of 50 nm with a FWHM of 30 nm. The films are electronically very similar to STO single crystals. Their surface provides a reactivity which is expected to be even higher than the ones for single crystal surfaces. On the one hand, the particle size of several 10 nm is sufficiently high to provide stable electronic conditions of the particles. On the other hand, the size is low enough to allow complete oxygen diffusion into the particles within 10 ms. It can be expected that oxygen diffusion on the particles surface is very fast. Therefore, the produced nanocrystalline STO is a highly promising candidate for a very fast and very sensitive high temperature oxygen sensor.

ACKNOWLEDGMENTS

The authors gratefully acknowledge support from the Deutsche Forschungsgemeinschaft (DFG) under contract numbers. Ma 1893/9-1 and Ar 248/3-1. We wish to express our gratitude to Dipl.-Ing. Peter Cyris for the accomplishment of the AFM and Auger depth profile measurements.

REFERENCES

- [1] W. Menesklou, H.-J. Schreiner, K. H. Härdtl, and E. Ivers-Tiffée, "High temperature oxygen sensors based on doped SrTiO_3 ," *Sensors and Actuators B: Chemical*, vol. 59, no. 2, pp. 184–189, 1999.
- [2] R. Meyer and R. Waser, "Resistive donor-doped SrTiO_3 sensors: I, basic model for a fast sensor response," *Sensors and Actuators B: Chemical*, vol. 101, no. 3, pp. 335–345, 2004.
- [3] A. Gunhold, L. Beuermann, K. Gömann, et al., "Study of the electronic and atomic structure of thermally treated $\text{SrTiO}_3(110)$ surfaces," *Surface and Interface Analysis*, vol. 35, no. 12, pp. 998–1003, 2003.
- [4] A. Gunhold, K. Gömann, L. Beuermann, V. Kempter, G. Borchart, and W. Maus-Friedrichs, "Changes in the surface topography and electronic structure of $\text{SrTiO}_3(110)$ single crystals heated under oxidizing and reducing conditions," *Surface Science*, vol. 566–568, no. 1–3, part 1, pp. 105–110, 2004.
- [5] J. Padilla and D. Vanderbilt, "Ab initio study of SrTiO_3 surfaces," *Surface Science*, vol. 418, no. 1, pp. 64–70, 1998.
- [6] R. Moos, T. Bischoff, W. Menesklou, and K. H. Härdtl, "Solubility of lanthanum in strontium titanate in oxygen-rich atmospheres," *Journal of Materials Science*, vol. 32, no. 16, pp. 4247–4252, 1997.
- [7] S. Steinsvik, R. Bugge, J. Gjønnnes, J. Taftø, and T. Norby, "The defect structure of $\text{SrTi}_{1-x}\text{Fe}_x\text{O}_{3-y}$ ($x = 0 - 0.8$) investigated by electrical conductivity measurements and electron energy loss spectroscopy (EELS)," *Journal of Physics and Chemistry of Solids*, vol. 58, no. 6, pp. 969–976, 1997.
- [8] S. Sakka, "Current sol-gel activities in Japan," *Journal of Sol-Gel Science and Technology*, vol. 37, no. 2, pp. 135–140, 2006.
- [9] M. L. Zheludkevich, I. Miranda Salvado, and M. G. S. Ferreira, "Sol-gel coatings for corrosion protection of metals," *Journal of Materials Chemistry*, vol. 15, no. 48, pp. 5099–5111, 2005.
- [10] W. Hu, C. Yang, W. Zhang, and Y. Qiu, "Dielectric characteristics of sol-gel-derived BST/BST/BST multilayer," *Journal of Sol-Gel Science and Technology*, vol. 36, no. 3, pp. 249–255, 2005.
- [11] M. Frerichs, F. Voigts, and W. Maus-Friedrichs, "Fundamental processes of aluminium corrosion studied under ultra high vacuum conditions," to appear in *Applied Surface Science*.
- [12] J. H. Scofield, "Hartree-Slater subshell photoionization cross-sections at 1254 and 1487 eV," *Journal of Electron Spectroscopy and Related Phenomena*, vol. 8, no. 2, pp. 129–137, 1976.
- [13] "NIST Electron Inelastic-Mean-Free-Path Database 1.1," <http://www.nist.gov/srd/nist71.htm>.
- [14] J. Günster, *Elektronenspektroskopische Untersuchungen an Isolierenden Schichten auf W (110), Al (111) und Si (100)*, Ph.D. thesis, Technische Universität Clausthal, Clausthal, Germany, 1996.
- [15] Y. Harada, S. Masuda, and H. Ozaki, "Electron spectroscopy using metastable atoms as probes for solid surfaces," *Chemical Reviews*, vol. 97, no. 6, pp. 1897–1952, 1997.
- [16] H. Morgner, "The characterization of liquid and solid surfaces with metastable helium atoms," *Advances in Atomic, Molecular, and Optical Physics*, vol. 42, pp. 387–488, 2000.
- [17] G. Ertl and J. Küppers, *Low Energy Electrons and Surface Chemistry*, VCH, Weinheim, Germany, 1985.
- [18] V. Kempter, "Study of insulator surfaces with the Metastable Impact Electron Spectroscopy (MIES)," *Materials Science Forum*, vol. 239–241, pp. 621–628, 1997.
- [19] W. Maus-Friedrichs, M. Frerichs, A. Gunhold, S. Krischok, V. Kempter, and G. Bihlmayer, "The characterization of $\text{SrTiO}_3(001)$ with MIES, UPS(HeI) and first-principles calculations," *Surface Science*, vol. 515, no. 2-3, pp. 499–506, 2002.
- [20] K. Szot, W. Speier, J. Herion, and Ch. Freiburg, "Restructuring of the surface region in SrTiO_3 ," *Applied Physics A: Materials Science & Processing*, vol. 64, no. 1, pp. 55–59, 1997.
- [21] K. Szot and W. Speier, "Surfaces of reduced and oxidized SrTiO_3 from atomic force microscopy," *Physical Review B: Condensed Matter and Materials Physics*, vol. 60, no. 8, pp. 5909–5926, 1999.
- [22] A. Gunhold, L. Beuermann, M. Frerichs, et al., "Island formation on 0.1 at.% La-doped $\text{SrTiO}_3(100)$ at elevated temperatures under reducing conditions," *Surface Science*, vol. 523, no. 1-2, pp. 80–88, 2003.
- [23] V. E. Henrich and P. A. Cox, *The Surface Science of Metal Oxides*, Cambridge University Press, Cambridge, UK, 1994.

-
- [24] P. A. W. van der Heide, Q. D. Jiang, Y. S. Kim, and J. W. Rabalais, "X-ray photoelectron spectroscopic and ion scattering study of the SrTiO₃(0 0 1) surface," *Surface Science*, vol. 473, no. 1-2, pp. 59–70, 2001.
- [25] K. Gömann, G. Borchardt, M. Schulz, et al., "Sr diffusion in undoped and La-doped SrTiO₃ single crystals under oxidizing conditions," *Physical Chemistry Chemical Physics*, vol. 7, no. 9, pp. 2053–2060, 2005.
- [26] H. L. Tuller, "Ionic conduction in nanocrystalline materials," *Solid State Ionics*, vol. 131, no. 1, pp. 143–157, 2000.

Ferromagnetic Nanostructures Incorporated in Quasi-One-Dimensional Porous Silicon Channels Suitable for Magnetic Sensor Applications

P. Granitzer, K. Rumpf, and H. Krenn

Institute of Physics, University of Graz, Universitätsplatz 5, 8010 Graz, Austria

Received 15 March 2006; Revised 18 July 2006; Accepted 19 September 2006

Mesoporous silicon structures are fabricated during an anodization process of highly doped n-type silicon in hydrofluoric acid solution. The resulting pores are oriented perpendicular to the surface and exhibit a diameter of about 50 nm and a length up to 50 μm , controlled by the etching time. The growth of the pores is self-organized and depends on the crystal orientation of the used silicon wafer. The achieved channels, highly oriented along the (100) direction, are filled with nickel in a second electrochemical step. The deposition process leads to a distribution between high aspect ratio Ni-wires and Ni-particles of the incorporated metal. This achieved (porous silicon/Ni)-nanocomposite system exhibits a twofold switching behavior of the magnetization curve at two different field ranges. This property gives rise to high-magnetic field sensor applications based on a silicon technology.

Copyright © 2006 P. Granitzer et al. This is an open access article distributed under the Creative Commons Attribution License, which permits unrestricted use, distribution, and reproduction in any medium, provided the original work is properly cited.

1. INTRODUCTION

There is a great demand of nanostructures, especially nanowires in a nonmagnetic matrix [1] for a lot of promising applications in today's data storage technology, spintronic as well as sensor applications. The most popular are porous alumina templates, growing in a hexagonal honeycomb-like structure which is intensively investigated [2, 3]. These structures are filled with a ferromagnetic material like Ni and the achieved magnetic properties are examined [4–6] up to now in the low-field regime below 1 T only. The introduced nanocomposite system, consisting of Ni-structures embedded in a porous silicon skeleton with high-aspect ratio channels (> 300), exhibits a feature at high-magnetic fields between 3 T and 6 T, which leads to a possible application of a high-magnetic field sensor of high sensitivity. This magnetic high-field behavior depends on the temperature as well as the electrochemical loading conditions. Furthermore this deposition technique of metallic Ni in silicon is inexpensive and requires only two electrochemical steps in comparison to the multistep process of anodic oxidation of aluminium with subsequent metallization. The structure of this nanocomposite system is visualized by SEM. The verification of nickel within the pores is carried out by AES [7] and EDX

spectroscopy. Magnetic measurements are performed by a SQUID magnetometer in the field range ± 7 T.

2. EXPERIMENTAL DETAILS

Porous silicon (PS) generally shows an irregular growth of a sponge-like structure with interconnected channels in the diameter regime between 2 nm and 4 nm. Mesopores with pores between 5 nm and 50 nm grow in a dendritic manner with a star-like cross-section of the pores. In this work we present a mesoporous silicon structure with highly oriented pores and dendrites smaller than the porediameter, indicating that the channels are really separated from each other. A further remarkable feature is the sharp termination between porous layer and bulk silicon (see Figure 1) which is sufficient for light reflection in the mid-infrared range and gives rise to optical and magneto-optical applications after the channels are filled with a ferromagnetic material. Despite a whole pore length of about 30 μm , the corrugation of the pore tips at this border lies in the range of about 10 nm.

The mesoporous silicon layer is fabricated during anodization in a hydrofluoric acid solution. The essential parameters to achieve oriented channels with a diameter of a few tens of nanometers are the current density (100 mA/cm²),

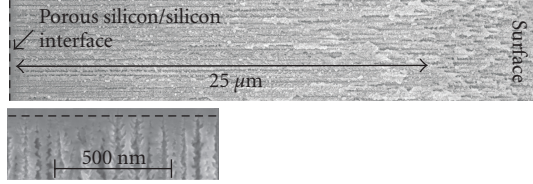


FIGURE 1: Scanning electron micrograph—with a magnification of 30000—of a cleaved edge of a sample show the pores in full length as well as the sharp termination between porous layer and bulk silicon. The pores are oriented strictly perpendicular to the surface. The small image below indicates that the roughness of the porous silicon/bulk silicon interface lies in the range of 10 nm.

electrolyte concentration (10 wt% HF), as well as the doping concentration of the used wafer (10^{18} cm^{-3}). These parameters have to match accurately to obtain straight mesopores oriented perpendicular to the surface. Furthermore the bath temperature is kept at 20°C and the etching time is varied within the range of a few minutes to achieve a porous layer between $10 \mu\text{m}$ and $50 \mu\text{m}$ since the etching rate is about $5 \mu\text{m}/\text{min}$. To obtain a flat surface without cracks, a post treatment of the sample is necessary, like supercritical drying [8] or replacing of water by a liquid of lower surface tension.

The filling procedure of the channels with Ni is carried out in a galvanic process using nickel chloride (NiCl_2) and boric acid (H_3BO_3) as electrolyte. The deposition is performed in a pulsed way to get a homogeneous exchange of the electrolyte along the entire pore length (after [9] with modified electrolyte and deposition conditions). Otherwise, if there is a gradient of electrolyte concentration along the pores, they are blocked and not completely filled with nickel. However, the parameters of the electrochemical filling procedure can be varied to achieve different Ni-distributions within the samples. Typical used electrolyte concentrations are $150\text{--}160 \text{ g/l NiCl}_2$ and $50\text{--}55 \text{ g/l H}_3\text{BO}_3$. The current density (j) is varied between 20 and $50 \text{ mA}/\text{cm}^2$, the pulse duration (t_p) ranges within a few tens of seconds. Ni is either concentrated near the surface region of the sample or at the pore tips or it is homogeneously spread over the whole pore length, as demonstrated in the EDX images in Figure 2. The EDX images are performed at 3 keV showing qualitative elemental maps to get a rough survey of the Ni-distribution at the cleaved edge of the specimens. In these pictures the brightness of each pixel is controlled by the intensity of the chosen X-ray line at the spot, and higher brightness corresponds to a higher element concentration.

3. STRUCTURAL AND MAGNETIC CHARACTERIZATIONS

Considering the top view of the surface of the fabricated mesoporous template, the pores show a self-organization in a quadratic-like way with a quite homogeneous distribution of the pore diameter (Figure 4) which is mainly influenced by the (100) crystal orientation of the used silicon wafer. Scanning electron microscopy (SEM) with subsequent image

processing demonstrates the square-like arrangement of the etched channels in Figure 3.

The electrodeposited Ni-structures within the pores consist of high-aspect ratio Ni-wires as well as Ni-particles, indicated by structural as well as magnetic characterizations. Magnetic measurements are performed by a SQUID magnetometer (MPMS XL, Quantum Design) in the field range between $\pm 7 \text{ T}$ and a temperature range from 4.2 K up to 300 K . The magnetization curve shows two switching fields at different magnetic field ranges: one at low-magnetic fields around 500 Oe (HSW1) and the other at higher fields (HSW2) in the range of a few tesla. Ferromagnetic particles contributing to the magnetization signals which are below 200 nm in size are single domain [10]. An example of two Ni-particles of about 150 nm and 50 nm is shown in Figure 5 by EDX images.

The hysteresis loops in this low-field regime correlate with the size and amount of ferromagnetic particles. The coercivity for a magnetic field perpendicular to the sample surface ranges between 200 Oe and 600 Oe , depending on the Ni-loading of the sample. If the magnetic field is applied in-plane, the coercivity decreases and shows values between 90 Oe and 150 Oe . The squareness M_R/M_S varies between 20% and 70% , depending on the magnetic field if applied out-of-plane or in-plane, respectively. Note that the coercivity shows a 30-fold increase with respect to bulk Ni, having a coercivity of 20 Oe , mainly caused by domain wall motion. With increasing temperature, the coercivity decreases as listed in Table 1. The presented system shows an analogous magnetic behavior in this low-field region as porous anodic alumina templates are filled with a ferromagnetic metal [11–13].

In using the following relation [14]:

$$r_c = \frac{36 \cdot \sqrt{AK_1}}{\mu_0 M_s^2}, \quad (1)$$

the critical radius of Ni single-domain particles results in $r_c \approx 50 \text{ nm}$. Most of the particles found in the sample are below 50 nm in diameter and can therefore be assumed as single domain. Due to the spheroidal-like shape, the easy axis is isotropic without any preferential direction, except for the small crystalline anisotropy of Ni which is negligible due to the polycrystalline structure of the wires. In this low-field range, the saturation magnetization is nearly equal for magnetic field direction parallel or perpendicular to the surface, respectively. For particles with a radius greater than the coherence radius R_{coh} ($\sim 20 \text{ nm}$ for Ni [15]), magnetization reversal occurs favourably in the curling mode [16–18]. Calculating the coercive field of a particle with a diameter of 60 nm by using the following relation, [17, equation (2)], for the curling mode, we achieve a coercivity of about 450 Oe for a sphere, which is in good agreement with the measurements

$$H_C = \frac{2K_1}{\mu_0 M_s} + \frac{c(N)A}{\mu_0 M_s r^2} \quad (2)$$

K_1 magnetocrystalline anisotropy, M_s saturation magnetization, N demagnetizing factor, A exchange stiffness constant, c geometrical factor depending on the aspect ratio.

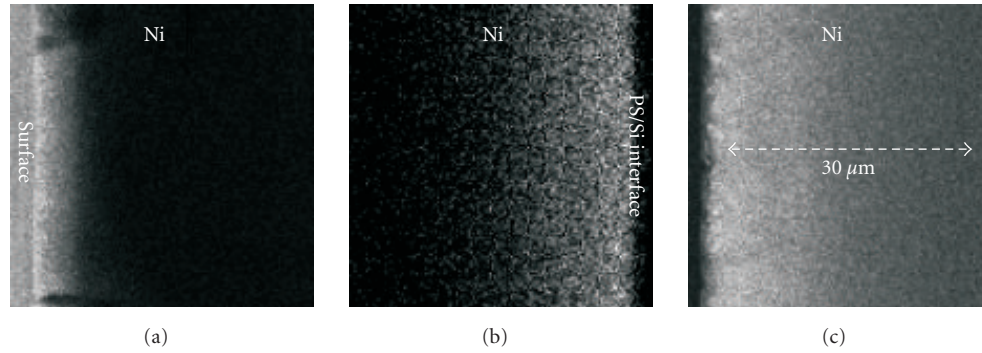


FIGURE 2: EDX scans at 3 keV show different Ni-distributions controlled by changed loading conditions. Areas of higher brightness mean higher Ni-concentration. (a) Shows an accumulation of Ni near the surface ($j = 10 \text{ mA/cm}^2$, $t_p = 20$ seconds), (b) indicates that the nucleation of Ni starts at the pore bottom ($j = 50 \text{ mA/cm}^2$, $t_p = 10$ seconds) and (c) shows a nearly homogeneous Ni-distribution ($j = 20 \text{ mA/cm}^2$, $t_p = 20$ seconds) within the porous layer.

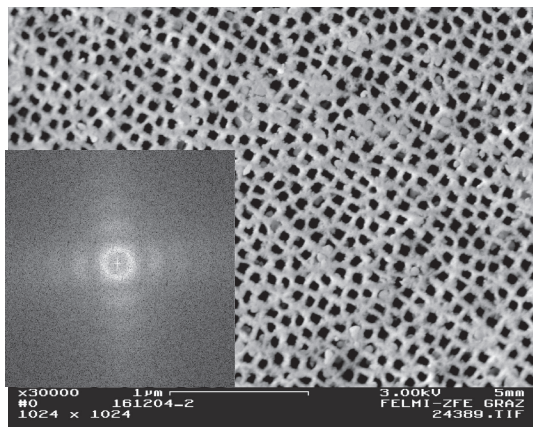


FIGURE 3: Scanning electron micrograph (SEM) of the top view of the surface of a porous silicon sample demonstrates the quadratic-like arrangement of the pore growth. In the inset, a corresponding 2D-Fourier transformed reciprocal image demonstrating the pattern of a square grid with a certain degree of disorder can be seen.

The nanocomposite system consists also of nanowires with a maximum diameter corresponding to the pore diameter of the porous silicon template. The magnetization reversal of Ni-nanowires depends strongly on the wire diameter and magnetostatic interaction between the wires also influences the reversal mechanism [19–21]. Considering diameters greater than the coherence radius, the curling mode is dominant. Therefore the coercivity of such wires can be estimated by using (2) and is in the range of about 300 Oe, which is also in agreement with experimental data of the low-field hysteresis loop.

This bimodal nanocomposite system shows a further characteristic switching field at higher magnetic fields of a few tesla presented in Figure 6. The mechanisms leading to this depression in the magnetization curve are not fully understood yet, but there are some remarkable points in considering the magnetization curve of Figure 6. First it can be

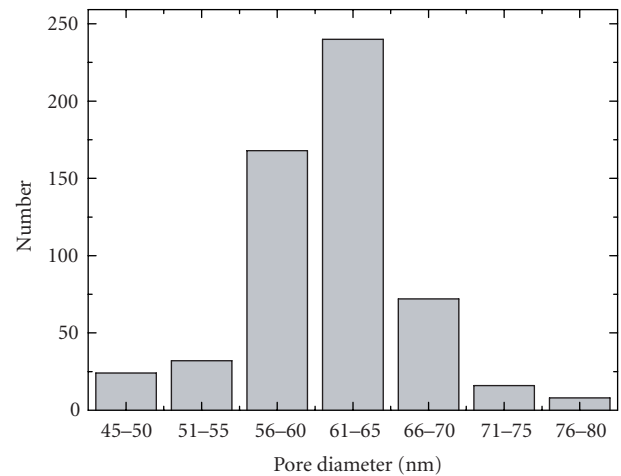


FIGURE 4: Histogram of a typical rather homogeneous distribution of the pore diameter within one porous silicon sample. The main pore diameter ranges between 56 nm and 70 nm, considering a sample area of about $3 \mu\text{m} \times 3 \mu\text{m}$.

seen that the negative magnetization peak occurs at rather high fields between 4 T and 6 T (Figures 6 and 7) which is much higher than interwire dipolar coupling fields. A second point is the slight increase of the magnetization signal for fields greater than HSW1 up to field strengths at the beginning negative slope of the magnetization curve. Furthermore no hysteresis can be observed in the high-field range above HSW1. At last it can be seen that the described magnetic behavior at high fields can only be observed in an external magnetic field perpendicular to the sample surface (parallel to the nanowires) but does not occur if the magnetic field is applied parallel to the sample surface. Taking into account all these facts, we suggest the following as a first starting point for further investigations of the mentioned magnetic behavior. In order to comply all these experimental results, it is justified to assume transitions between antiparallel and parallel alignments of Ni-nanowires. The strong depression,

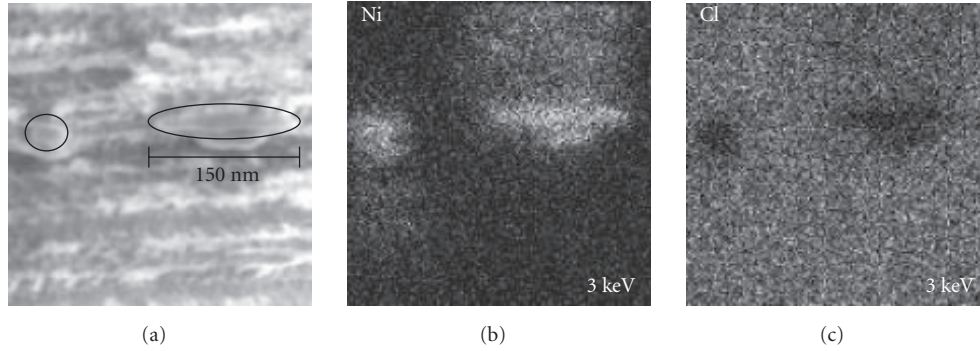


FIGURE 5: EDX scans showing a zoomed sample area containing two Ni-particles indicated by ellipses in picture (a) which is obtained from the backscattered electrons. (b) shows the Ni-distribution being confined to these two regions and (c) demonstrates the absence of chlorine in these two areas.

TABLE 1: Coercivity of a Ni-nanowire sample (pitch: ~ 120 nm) in dependence on the temperature when the magnetic field is applied parallel to the long wire axis. The coercive field decreases with increasing temperature.

T	4.2	25	50	100	250
H_C	330	320	260	200	140

which can be observed as descending magnetization in the hysteresis loop for an increasing magnetic field ($H > 4$ T), could be understood by this increase of antiparallel alignment of single-domain wires ($H_{ex} = HSW2$). If the external field is further increased ($H_{ex} > HSW2$), finally all the wires order into the same direction and are aligned with the magnetic field. Hence, the system gets saturated above 6.5 T (Figure 6).

The main problem of this explanation is the interaction between the Ni-wires leading to an antiparallel alignment at rather high fields of a few tesla which is still under investigation and not completely understood yet. As mentioned before, the interaction mechanism cannot be of dipolar character because it is too weak to obtain switching fields at high fields of a few tesla. In order to elucidate the behavior with respect to all experimental results, an assumed exchange interaction has to fulfill some requirements. First, it has to take place at high-magnetic fields and as a second point it has to act across the distance between the wires. The latter point is critical due to the pitch of the porous silicon template in the range of tens of nanometers. This can be eased taking into account that the pores are not ideal cylindrical, exhibiting not completely smooth pore walls but dendritic growth. This affects an effective distance between the wires which is considerably smaller in the real system than in an array of ideal cylindrical wires. On behalf of this consideration, the effective distance is in the range of only a few nanometers and this is not too large for an exchange interaction to take place.

A further interesting behavior is the temperature dependence of the second switching field. HSW2 decreases with increasing temperature (Figure 7). Beneath 30 K, the available magnetic field of ± 7 T in our SQUID magnetometer does not suffice to monitor a measurable depression of the

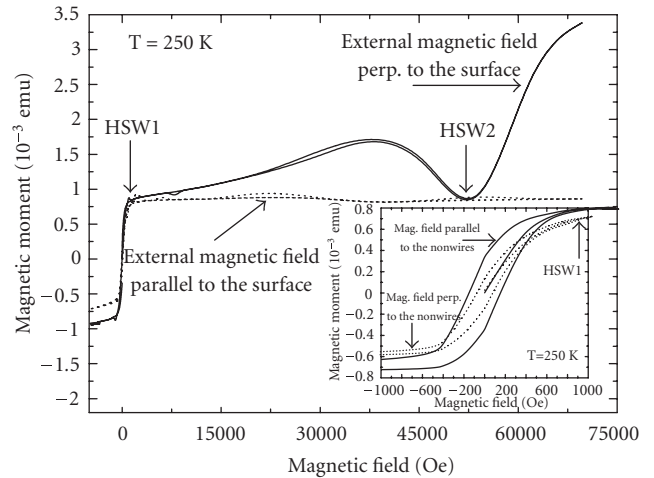


FIGURE 6: Magnetization curve showing the first switching field HSW1 at 500 Oe (inset) as well as the second switching field HSW2 at 5.1 T which is suggested to be due to the mutual antiferromagnetic alignment of the Ni-wires. The diamagnetic contribution of the substrate is subtracted. If the applied magnetic field is parallel to the sample surface, no negative magnetization peak is observed.

magnetization signal. The temperature dependence of the second switching field is assumed to be due to the strong temperature dependence of the anisotropy constant K_1 of nickel, which generally decreases with increasing temperature [22].

The shape anisotropy constant is independent of the temperature and thus the uniaxial anisotropy constant K_1 remains as the only temperature-dependent entity. These observations correspond to experiments reported in the literature [20] where the nucleation fields also increase with decreasing temperature. Note, however, the one order of magnitude has smaller nucleation field than in our Ni/porous silicon samples. Usually the magnetocrystalline contributions tend to average out due to random distributions of the Ni-structures incorporated into the pores [23]. A further contribution is the magnetoelastic anisotropy caused

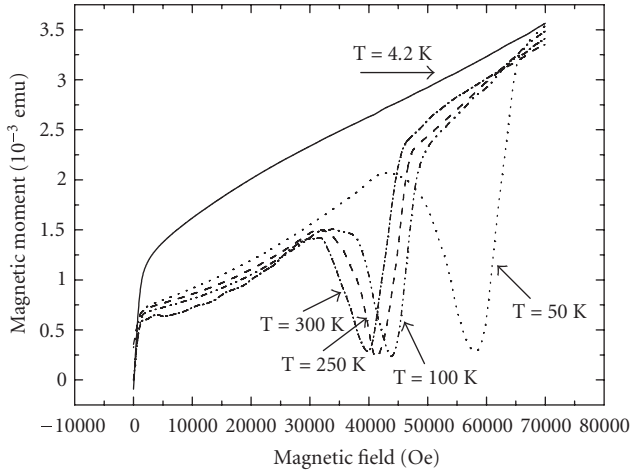


FIGURE 7: Temperature variation between 300 K and 4.2 K shifts the second switching field HSW2 from 3.9 T up to 5.7 T.

by stress due to the lattice mismatch between the incorporated metallic Ni and PS. These effects are mainly caused by the deposition conditions due to the bridging of the Ni-PS [24]. Furthermore the temperature-dependent behavior is also caused by the strain, due to the mismatch of the thermal expansion coefficients between nickel ($\alpha_{th,Ni} = 13.4 \cdot 10^{-6} \text{ K}^{-1}$) and porous silicon ($\alpha_{th,PS} = 1.2 \cdot 10^{-6} \text{ K}^{-1}$). The magnetoelastic anisotropy K_{el} [25] decreases with increasing temperature from $K_{el} = -0.5 \cdot 10^6 \text{ Jm}^{-3}$ to $K_{el} = -3.39 \cdot 10^6 \text{ Jm}^{-3}$ taking into account that the strain of Ni has a value of $\epsilon \sim -3.5 \cdot 10^{-3}$ at 4.2 K and $\epsilon \sim -5.246 \cdot 10^{-4}$ at 250 K. A further correlation is found between the second switching field and the loading condition of the Ni-filling process of the channels. Varying the electrochemical parameters like current density and pulse duration leads to a different distribution of particles and wires and therefore to various coercivities as well as negative magnetization peaks. The Ni-content varies with the loading conditions. For $H_C = 350 \text{ Oe}$, a Ni-content of $3.813 \cdot 10^{-6} \text{ cm}^3$ is estimated and it decreases with decreasing $H_C = 220 \text{ Oe}$, Ni-content = $1.9 \cdot 10^{-6} \text{ cm}^3$. Figure 8 demonstrates that also the depression in the high-field region can be influenced by different deposition conditions.

The switching in the range of a few tesla works in a broad temperature range even up to room temperature, which is of great interest for technical applications. A shift of the depression of the magnetization curve to higher magnetic fields is observable if the temperature decreases (see Figure 7). The steep decrease of the $M(H)$ curves around the second switching field followed by a steep increase gives rise to applications in magnetic sensor technology. Furthermore, the high-field switching feature can be controlled by different Ni-loading conditions. Changing the parameters of the electrochemical deposition alters the distribution of Ni-particles and Ni-wires, leading to different slopes of the declining and inclining branches of the magnetization curve (see Figure 8). Higher steepness of the magnetization curve around

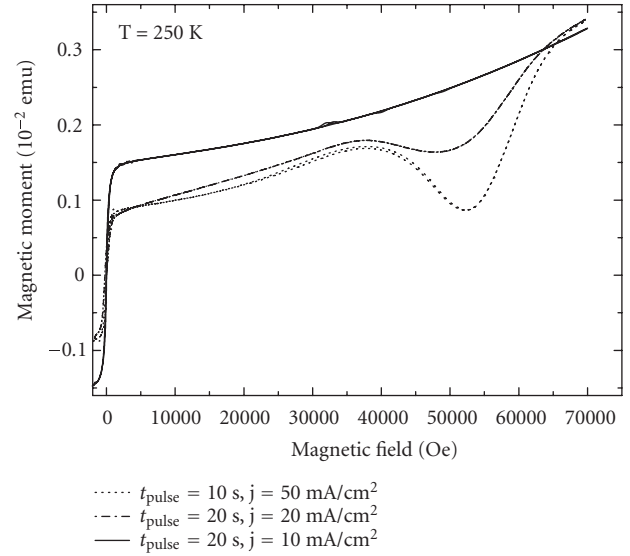


FIGURE 8: Onset of a negative magnetization at the second switching field for different Ni-loading conditions, of a (Ni/porous silicon)-nanocomposite. The corresponding EDX images of the Ni-distributions are shown in Figure 2.

the second switching field means higher sensitivity for a magnetic field sensor. The width of the switching peak is responsible for the field range within the sensor working. However, the strong correlation of the incorporated nanostructures and of the temperature with the switching field has been demonstrated in this work.

Because of the temperature-dependent shift of the switching field, a magnetic field sensor is possible to be realized with both, high sensitivity as well as a wide working range between 3 T and 6 T. For applications at fixed temperatures (i.e., room temperature), the sensor specification can only be influenced by the amount of electrochemical Ni-deposition. In this case, the sensitivity and the working range are competing features. In consideration of this fact, special nanocomposite systems can be tailored, to customize a favored magnetization curve. For example, a sharp and narrow peak of the $M(H)$ curve is realizable. A specimen of such a behavior is a very promising candidate for a high-magnetic field sensor with a small working range but with a rather high sensitivity, and can be used to stabilize a magnetic field at a fixed temperature.

4. CONCLUSIONS

The proposed method to fabricate Ni-nanowires embedded in a porous silicon matrix is a two-step electrochemical process. This procedure, managed by less steps, is inexpensive and opens a lot of opportunities for technical applications in silicon technology. In the first step, the porous silicon template is fabricated during an anodization process, using aqueous hydrofluoric acid as solution. The achieved porous structure consists of highly oriented channels with an extremely

high-aspect ratio up to 1 : 1000. In a second step, this template is filled with Ni during pulsed electrodeposition. The obtained nanocomposite system consists of a distribution of particles and wires dependent on the electrochemical parameters of the deposition process like current density and pulse duration. The electrolyte concentration is also an important Ni-loading parameter. The structural characterization of this nanoscopic arrangement is carried out by scanning electron microscopy (SEM) and energy dispersive X-ray spectroscopy (EDXS). SEM investigations demonstrate that the pores are highly oriented perpendicular to the sample surface and that the pores are arranged in a square-like manner, shown by image processing of top view SEM images. EDXS indicates that the pores are filled with Ni down to the pore tips. With EDXS the distribution of different elements within one sample is shown as well as the Ni-distribution of differently processed samples.

The bimodal ferromagnetic nanocomposite consisting of Ni-particles and Ni-wires shows an interesting twofold magnetic switching behavior at different external magnetic fields. The first switching in the low-field regime shows a clear anisotropic behavior of the hysteresis loops between in-plane and out-of-plane magnetizations. This behavior is similar to that one known from other nanowire arrays like in porous anodic alumina templates. Due to the geometry of the system, the magnetization reversal process occurs mainly by curling. The mechanisms of the second switching at high fields cannot be explained completely up to now but are still under investigation.

This (porous silicon/Ni)-nanocomposite exhibiting the described novel bimodal magnetic behavior is a promising candidate for applications in magnetic high-field sensor devices. An advantage of this system is the use of silicon as basic material which can be integrated in today's semiconductor microtechnology.

ACKNOWLEDGMENTS

The authors thank Dr. P. Pölt and Dr. A. Reichmann from the Institute for Electron Microscopy (FELMI) at the University of Technology in Graz for SEM and EDX and the Austrian FWF-fund for its Grant under Project P15397.

REFERENCES

- [1] T. M. Whitney, J. S. Jiang, P. C. Searson, and C. L. Chien, "Fabrication and magnetic properties of arrays of metallic nanowires," *Science*, vol. 261, no. 5126, pp. 1316–1319, 1993.
- [2] O. Jessensky, F. Müller, and U. Gösele, "Self-organized formation of hexagonal pore arrays in anodic alumina," *Applied Physics Letters*, vol. 72, no. 10, pp. 1173–1175, 1998.
- [3] H. Masuda and K. Fukuda, "Ordered metal nanohole arrays made by a two-step replication of honeycomb structures of anodic alumina," *Science*, vol. 268, no. 5216, pp. 1466–1468, 1995.
- [4] K. Nielsch, R. B. Wehrspohn, J. Barthel, et al., "Hexagonally ordered 100 nm period nickel nanowire arrays," *Applied Physics Letters*, vol. 79, no. 9, pp. 1360–1362, 2001.
- [5] R. Skomski, H. Zeng, and D. J. Sellmyer, "Incoherent magnetization reversal in nanowires," *Journal of Magnetism and Magnetic Materials*, vol. 249, no. 1–2, pp. 175–180, 2002.
- [6] L. Clime, P. Ciureanu, and A. Yelon, "Magnetostatic interactions in dense nanowire arrays," *Journal of Magnetism and Magnetic Materials*, vol. 297, no. 1, pp. 60–70, 2006.
- [7] P. Granitzer, K. Rumpf, S. Surnev, and H. Krenn, "Squid-magnetometry on ferromagnetic Ni-nanowires embedded in oriented porous silicon channels," *Journal of Magnetism and Magnetic Materials*, vol. 290–291, part 1, pp. 735–737, 2005.
- [8] L. T. Canham, A. G. Cullis, C. Pickering, O. D. Dosser, T. I. Cox, and T. P. Lynch, "Luminescent anodized silicon aerocrystal networks prepared by supercritical drying," *Nature*, vol. 368, no. 6467, pp. 133–135, 1994.
- [9] K. Nielsch, F. Müller, A.-P. Li, and U. Gösele, "Uniform nickel deposition into ordered alumina pores by pulsed electrodeposition," *Advanced Materials*, vol. 12, no. 8, pp. 582–586, 2000.
- [10] J. I. Martín, J. Nogués, K. Liu, J. L. Vicent, and I. K. Schuller, "Ordered magnetic nanostructures: fabrication and properties," *Journal of Magnetism and Magnetic Materials*, vol. 256, no. 1–3, pp. 449–501, 2003.
- [11] D.-H. Qin, H.-L. Zhang, C.-L. Xu, T. Xu, and H.-L. Li, "Magnetic domain structure in small diameter magnetic nanowire arrays," *Applied Surface Science*, vol. 239, no. 3–4, pp. 279–284, 2005.
- [12] M. Vázquez, K. Pirota, J. Torrejón, D. Navas, and M. Hernández-Vélez, "Magnetic behaviour of densely packed hexagonal arrays of Ni nanowires: influence of geometric characteristics," *Journal of Magnetism and Magnetic Materials*, vol. 294, no. 2, pp. 174–181, 2005.
- [13] M. Knobel, L. C. Sampaio, E. H. C. P. Sinnecker, P. Vargas, and D. Altbir, "Dipolar magnetic interactions among magnetic microwires," *Journal of Magnetism and Magnetic Materials*, vol. 249, no. 1–2, pp. 60–72, 2002.
- [14] D. J. Sellmyer, M. Zheng, and R. Skomski, "Magnetism of Fe, CO and Ni nanowires in self-assembled arrays," *Journal of Physics: Condensed Matter*, vol. 13, no. 25, pp. R433–R460, 2001.
- [15] A. Aharoni, "Incoherent magnetization reversals in elongated particles," *Journal of Magnetism and Magnetic Materials*, vol. 196–197, pp. 786–790, 1999.
- [16] C. A. Ross, R. Chantrell, M. Hwang, et al., "Incoherent magnetization reversal in 30-nm Ni particles," *Physical Review B: Condensed Matter and Materials Physics*, vol. 62, no. 21, pp. 14252–14258, 2000.
- [17] R. Skomski, "Nanomagnetics," *Journal of Physics: Condensed Matter*, vol. 15, no. 20, pp. R841–R896, 2003.
- [18] R. Hertel and J. Kirschner, "Magnetization reversal dynamics in nickel nanowires," *Physica B: Condensed Matter*, vol. 343, no. 1–4, pp. 206–210, 2004.
- [19] R. Wieser, U. Nowak, and K. D. Usadel, "Domain wall mobility in nanowires: transverse versus vortex walls," *Physical Review B: Condensed Matter and Materials Physics*, vol. 69, no. 6, Article ID 064401, 5 pages, 2004.
- [20] S. Pignard, G. Goglio, A. Radulescu, et al., "Study of the magnetization reversal in individual nickel nanowires," *Journal of Applied Physics*, vol. 87, no. 2, pp. 824–829, 2000.
- [21] R. Hertel, "Computational micromagnetism of magnetization processes in nickel nanowires," *Journal of Magnetism and Magnetic Materials*, vol. 249, no. 1–2, pp. 251–256, 2002.
- [22] B. D. Cullity, *Introduction to Magnetic Materials*, Addison Wesley, Reading, Mass, USA, 1972.

-
- [23] H. Zeng, S. Michalski, R. D. Kirby, D. J. Sellmyer, L. Menon, and S. Bandyopadhyay, “Effects of surface morphology on magnetic properties of Ni nanowire arrays in self-ordered porous alumina,” *Journal of Physics: Condensed Matter*, vol. 14, no. 4, pp. 715–721, 2002.
- [24] H. Zeng, R. Skomski, L. Menon, Y. Liu, S. Bandyopadhyay, and D. J. Sellmyer, “Structure and magnetic properties of ferromagnetic nanowires in self-assembled arrays,” *Physical Review B: Condensed Matter and Materials Physics*, vol. 65, no. 13, Article ID 134426, 8 pages, 2002.
- [25] G. Bertotti, *Hysteresis in Magnetism*, Academic Press, New York, NY, USA, 1998.

Gas Sensors Based on Tin Oxide Nanoparticles Synthesized from a Mini-Arc Plasma Source

Ganhua Lu,¹ Kyle L. Huebner,² Leonidas E. Ocola,³ Marija Gajdardziska-Josifovska,⁴ and Junhong Chen¹

¹ Department of Mechanical Engineering and Laboratory for Surface Studies, University of Wisconsin-Milwaukee, Milwaukee, WI 53211, USA

² Department of Mechanical Engineering, University of Wisconsin-Milwaukee, Milwaukee, WI 53211, USA

³ Center for Nanoscale Materials, Argonne National Laboratory, Argonne, IL 60439, USA

⁴ Department of Physics and Laboratory for Surface Studies, University of Wisconsin-Milwaukee, Milwaukee, WI 53211, USA

Received 15 March 2006; Revised 20 July 2006; Accepted 1 August 2006

Miniaturized gas sensors or electronic noses to rapidly detect and differentiate trace amount of chemical agents are extremely attractive. In this paper, we report on the fabrication and characterization of a functional tin oxide nanoparticle gas sensor. Tin oxide nanoparticles are first synthesized using a convenient and low-cost mini-arc plasma source. The nanoparticle size distribution is measured online using a scanning electrical mobility spectrometer (SEMS). The product nanoparticles are analyzed ex-situ by high resolution transmission electron microscopy (HRTEM) for morphology and defects, energy dispersive X-ray (EDX) spectroscopy for elemental composition, electron diffraction for crystal structure, and X-ray photoelectron spectroscopy (XPS) for surface composition. Nonagglomerated rutile tin oxide (SnO₂) nanoparticles as small as a few nm have been produced. Larger particles bear a core-shell structure with a metallic core and an oxide shell. The nanoparticles are then assembled onto an e-beam lithographically patterned interdigitated electrode using electrostatic force to fabricate the gas sensor. The nanoparticle sensor exhibits a fast response and a good sensitivity when exposed to 100 ppm ethanol vapor in air.

Copyright © 2006 Ganhua Lu et al. This is an open access article distributed under the Creative Commons Attribution License, which permits unrestricted use, distribution, and reproduction in any medium, provided the original work is properly cited.

1. INTRODUCTION

Rutile tin oxide (SnO₂), a wide band gap (3.6 eV at 300 K [1]) *n*-type semiconductor material, is widely used as sensing elements in gas sensors [2]. The sensing mechanism is based on the fact that the adsorption of oxygen on the semiconductor surface can cause a significant change in the electrical resistance of the material [3]. The formation of oxygen adsorbates (O₂⁻ or O⁻) results in an electron-depletion surface layer due to electron transfer from the oxide surface to oxygen [4]. Recent studies [5, 6] have shown that the use of tin oxide nanocrystals as sensing elements significantly improves the response and the sensitivity of sensors since the space charge region may develop in the whole crystallite.

Tin oxide nanoparticles have been produced by both colloidal and aerosol routes. The colloidal synthesis route affords considerable control over particle size and structure since the surface chemistry can be manipulated through adjustment of the solution properties [7–9]. Nanoparticles produced in the gas phase can be subsequently deposited onto solid substrates for immediate device applications. Aerosol routes hence provide more flexibility in process control

[10, 11] and improve the compatibility of the nanoparticle sensor fabrication process with existing microelectronics fabrication facilities. In addition, the higher processing temperature employed in aerosol synthesis facilitates production of stable phases that are difficult to achieve in colloidal synthesis [12].

This paper introduces a simple, convenient, and low-cost mini-arc plasma source to synthesize tin oxide nanoparticles at atmospheric pressure. Because of the small crystallite size, high resolution transmission electron microscopy (HRTEM) becomes a powerful technique to analyze the product nanoparticles. The new source shows great potential in producing high-quality tin oxide nanoparticles for gas sensing applications. A miniaturized gas sensor has been fabricated using the as-produced tin oxide nanoparticles. The microfabricated nanoparticle sensor exhibits good sensitivity and dynamic response to low concentration ethanol gas.

2. EXPERIMENTAL DETAILS

A schematic diagram of the nanoparticle synthesis system, including the mini-arc plasma reactor and devices for

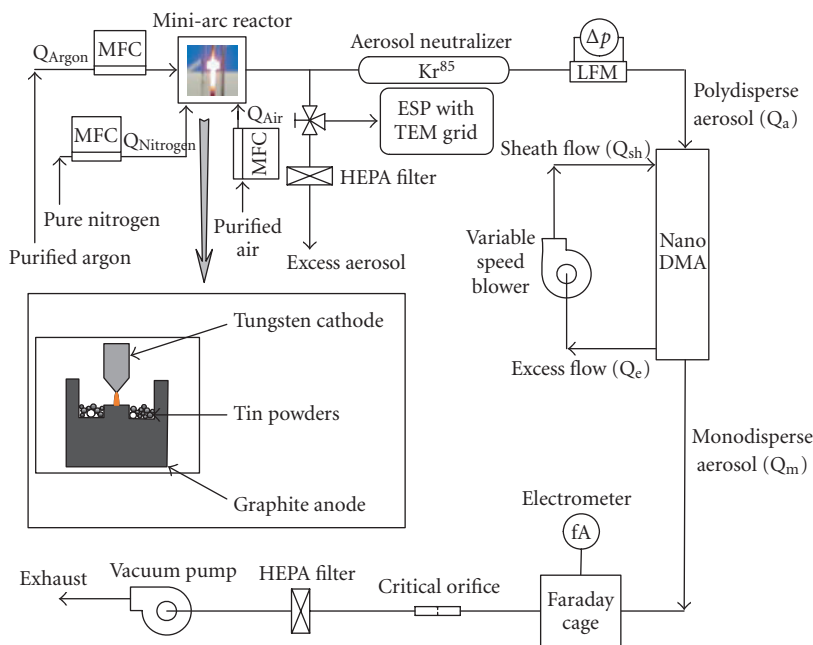


FIGURE 1: Schematic diagram of the experimental setup for nanoparticle synthesis using a mini-arc plasma source. The inset shows the magnified cathode and anode loaded with tin powders.

collection and characterization of nanoparticles, is shown in Figure 1. The atmospheric mini-arc reactor consists of a 1/16" tungsten rod cathode and a 1/4" graphite rod anode housed in a chamber constructed with Swagelok fittings and quartz tube. The cathode tip was sharpened to facilitate the arc initiation. The anode was designed to maximize the utilization of thermal energy from the arc discharge. To facilitate the arc stability, the anode surface was machined to form an annulus groove so that the dc arc only burns between the cathode tip and the central island on the anode surface. The typical discharge gap was on the order of 0.1 mm, and it may be adjusted using a translation stage on which the anode was mounted. Coarse tin powders or small pieces (~ 1 mm) of solid tin cut from commercially available pure tin wires were placed in the groove between the central island and the outside wall of the graphite anode. A commercial tungsten inert gas (TIG) arc welder (Miller Maxstar 150 STL) was used to drive the dc arc. Purified argon was used as the plasma and carrier gas. The high temperature in the arc discharge melts and vaporizes the solid tin from the graphite crucible. A pure and cold nitrogen flow was injected to quench the tin vapor and nucleate tin nanoparticles, which were then oxidized to form tin oxide nanoparticles by introducing purified air immediately at the exit of the mini-arc reactor.

The product tin oxide nanoparticles were monitored online to obtain the particle size distribution using a scanning electrical mobility spectrometer (SEMS) [13]. The SEMS consists of an aerosol neutralizer (Kr⁸⁵ charger) to impart a known charge distribution to nanoparticles, a differential mobility analyzer (DMA, TSI 3081) to size charged nanoparticles, and a very sensitive electrometer (Keithley 6514A) to count nanoparticles size-selected by the DMA. Nanoparticles

exiting the neutralizer, if charged, typically carry a single elementary charge due to their small sizes [14]. The DMA sizes charged particles according to their electrical mobilities [15]. For a given flow residence time, only particles having mobilities within a narrow range are transmitted through the DMA. The voltage applied to the DMA was scanned to probe the expected range of the particle size. A Faraday cage based on the design of Yun et al. [16] continuously collected all the singly charged particles selected by the DMA on a filter and the resulting current was measured by the Keithley electrometer. The particle concentration is then calculated by the ratio of the charge flow rate to the gas flow rate, taking into account the known charge distribution from the neutralizer and the transfer function of the DMA [13]. All devices and instruments were continuously monitored and controlled by a dedicated data acquisition (DAQ) computer running LabView, which displays the nanoparticle size distribution in a three-minute time interval.

A fraction of nanoparticles exiting the mini-arc plasma reactor was electrically charged by the plasma or thermionic emission of electrons from the nanoparticle surface. The charged nanoparticles were periodically collected for ex-situ analyses by electrostatic precipitation [17, 18] onto carbon-coated TEM grids installed immediately downstream of the reactor. The TEM sample collection was initiated using a three-way valve. The collected particles were analyzed using a Hitachi H 9000 NAR TEM, which has a point resolution of 0.18 nm at 300 kV in the phase contrast HRTEM imaging mode and is equipped with an energy-dispersive X-ray (EDX) spectrometer. Selected area diffraction (SAD) and amplitude contrast bright field (BF) imaging were also employed. The surface composition of as-produced

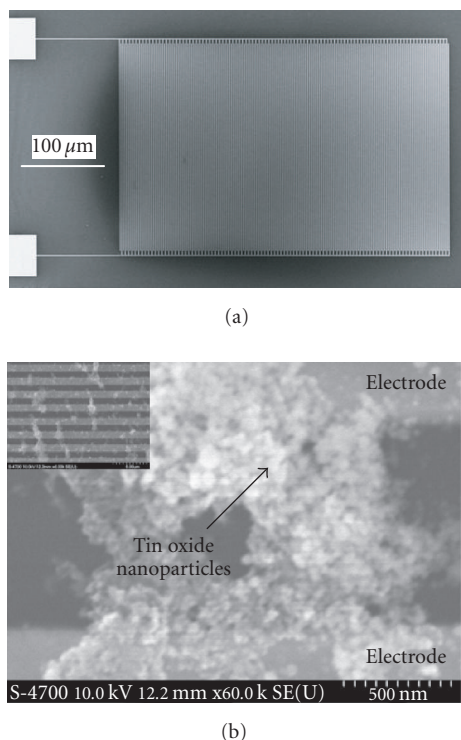


FIGURE 2: (a) SEM image of Au interdigitated electrodes used for sensor fabrication. The width and the separation of the electrodes are both $1\ \mu\text{m}$. (b) High resolution SEM image of a gas sensor fabricated by electrostatic assembly of tin oxide nanoparticles. The inset shows a larger area of the interdigitated electrode.

nanoparticles was analyzed using an HP5950 ESCA spectrometer with monochromatic Al $K\alpha$ radiation as X-ray source.

The charged tin oxide nanoparticles from the mini-arc nanoparticle generation system were assembled onto a prefabricated substrate with electrostatic force to build gas sensors. An interdigitated electrode based on the design of Kennedy et al. [5] was used to enable the electrostatic assembly of nanoparticles as well as the subsequent sensor characterization. The mechanism for functioning is simple; nanoparticles deposited between any two fingers close the electrical circuit to form a sensor, with the impedance of which changing in response to the exposed analyte molecules. For this purpose, an embedded gold interdigitated electrode in silicon substrate has been fabricated using e-beam lithography (30 KV Raith 150 e-beam tool) at Argonne National Laboratory (ANL). A scanning electron microscopy (SEM) image of the embedded electrode is shown in Figure 2(a). The line width of the gold electrode is $1\ \mu\text{m}$ and the spacing between the interdigitated fingers is also $1\ \mu\text{m}$. Figure 2(b) shows a high resolution SEM image of the final tin oxide nanoparticle sensor acquired on a Hitachi S4700 SEM at ANL. The inset shows a larger area of the interdigitated electrode bridged by tin oxide nanoparticles. The sensing performance of the nanoparticle sensor was evaluated at an operating temperature of 250°C with 100 ppm

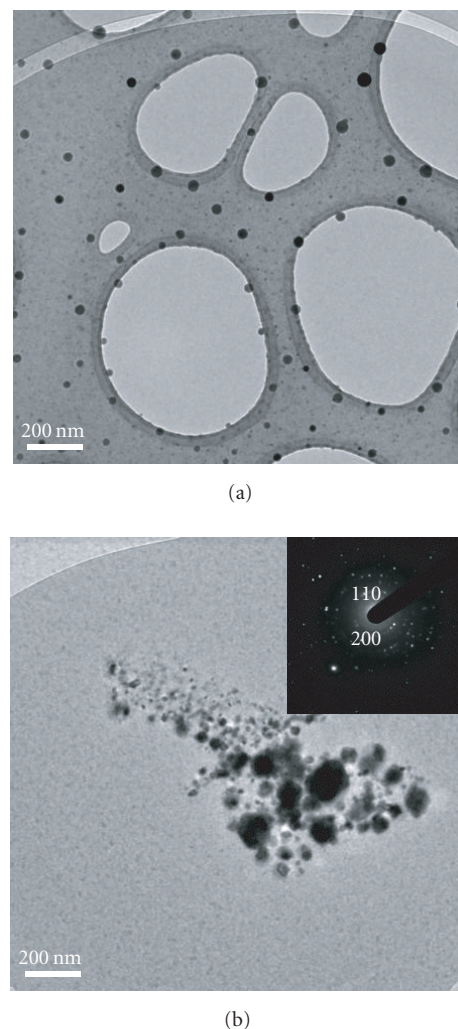


FIGURE 3: Bright field (BF) TEM images of tin oxide nanoparticles as produced from the mini-arc reactor. (a) Typical nonagglomerated nanoparticles are approximately spherical with diameter in the 20 to 40 nm range. (b) Agglomerated nanoparticles and nonspherical particles are seldom observed; the inset shows the selected area diffraction (SAD) pattern of the particles.

ethanol vapor diluted in air. Resistance measurements were performed by applying a constant dc voltage (10 V) to the interdigitated circuit and monitoring the variation of the current passing through tin oxide nanoparticles when the sensor was exposed to either air or 100 ppm ethanol.

3. RESULTS AND DISCUSSION

Figure 3 shows two low-magnification bright field (BF) TEM images of the as-produced nanoparticles. Figure 3(a) is representative of the prevalent images with uniformly distributed and nonagglomerated nanoparticles that are preferred for gas sensor applications. The nonagglomerated entity of nanoparticles may be attributed to the fast coalescence of these particles in the high temperature environment. The larger particles shown in Figure 3(a) are approximately

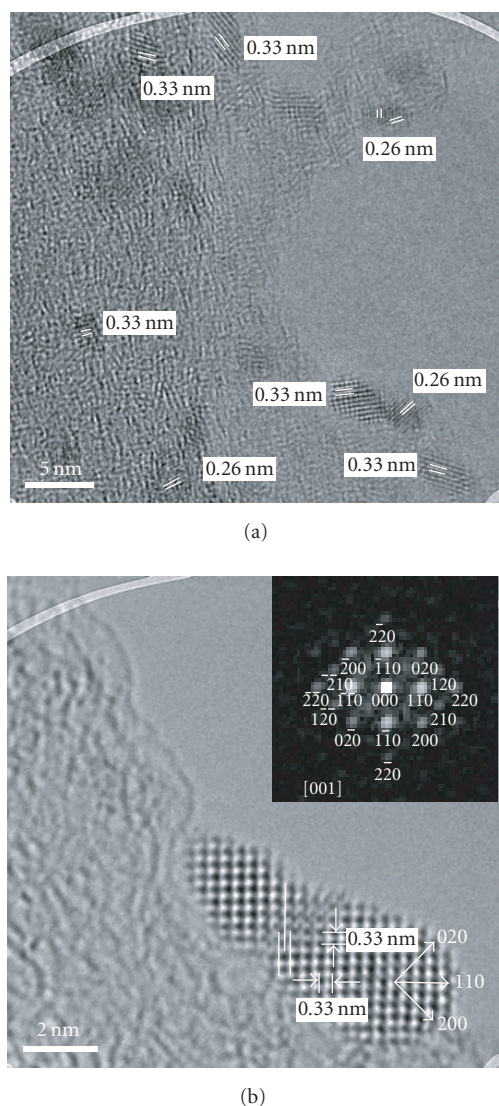


FIGURE 4: HRTEM images of (a) small nanoparticles showing lattice fringes corresponding to rutile SnO_2 and (b) SnO_2 agglomerate composed of two primary nanoparticles with denoted $\{110\}$ lattice fringes and $\{110\}$ and $\{200\}$ facet planes; the inset is the diffractogram of the agglomerate in the $[001]$ projection and defect is observed at the joining neck where fringes misfit by $1/2$ $\{110\}$.

spherical with diameters in the 20 to 40 nm range and slight ellipticity and/or small flat facets observed in some projections. This is a unique advantage of the mini-arc process since the high temperature in the arc reactor induces particle melting which leads to relatively large and at the same time quasi-spherical particles. Nanoparticles produced by many other vapor-phase processes, such as the flame spray synthesis [19], most often exhibit agglomerated structure if no special care is taken [20]. The smaller particles shown in Figure 3(a) can also be discerned, and are clearly shown in the HRTEM images of Figure 4. Although nonagglomerated nanoparticles are dominant, some agglomerated

nanoparticles or agglomerates are also observed as shown in Figure 3(b). These agglomerates are likely formed due to the nonuniform residence time in the reactor. Although agglomerates are not preferred, their selected area diffraction (SAD) pattern shows that they are crystalline. With further examination, the unique reflections of (110) and (200) lattice planes of rutile SnO_2 ($a = 4.74 \text{ \AA}$ and $c = 3.19 \text{ \AA}$) are identified.

HRTEM images of smaller SnO_2 nanoparticles with sizes below 5 nm are shown in Figure 4(a). Lattice spacing analysis by numerical diffractograms gives recurrent values of 0.33 and 0.26 nm, which correspond to the lattice spacings of rutile SnO_2 from (110) and (101) reflections, respectively. Some agglomerates are also observed for these smaller particles. Figure 4(b) shows an agglomerate composed of two rutile SnO_2 nanoparticles. The diffractogram shows that the zone axis of the diffraction pattern is $[001]$. Based on the indices of the diffraction pattern, three termination surfaces of the agglomerate are identified as (110) , (020) , and (200) , with the (110) surface being reported as the lowest energy surface of rutile SnO_2 [21]. This faceting may also explain the small flat regions seen at some of the edges of the larger round nanocrystals in Figure 3. Although both of the primary particles in Figure 4(b) are free of defects, fringes misfit by about 0.16 nm at the neck where the two particles join as a result of agglomeration. The defects present in the semiconductor SnO_2 may adversely affect the density and transport of charge carriers, and consequently degrade the sensor performance [22]. As a result, agglomerated nanoparticles should be minimized to achieve the best sensor performance.

Elemental analysis from EDX (Figure 5(a)) clearly shows the presence of both Sn and O in the as-produced nanoparticle sample. However, the atomic ratio O : Sn is below 2, which implies that not all as-produced nanoparticles are completely oxidized to stoichiometric SnO_2 . HRTEM images of smaller particles with a diameter of a few nm shown in Figure 4 already indicate that they are fully oxidized to SnO_2 . It is inferred that larger particles are not fully oxidized. The surface composition of the as-produced nanoparticles determined by XPS is shown in Figure 5(b). The binding energy for Sn $3d_{5/2}$ peak at 486.9 eV indicates the presence of SnO or SnO_2 [23, 24]. No metallic Sn peak (around 484.6 eV [25]) was observed from the surface, which implies that the surface of larger nanoparticles is covered with an oxidation layer. Therefore, larger particles bear a core-shell structure, with a metallic core and an oxide shell. Since the binding energy peak Sn $3d_{5/2}$ of SnO_2 is very close to that of SnO [23, 24], it is difficult to know the exact valence state of Sn in the surface oxidation layer. However, the binding energy of 486.9 eV is relatively high compared to that of Sn, suggesting a larger fraction of higher valence state of Sn (IV) at the nanoparticle surface. The O $1s$ peak shown in the XPS spectrum consists of two components, one at 530.5 eV corresponding to oxygen bound to tin and the other at 532.1 eV corresponding to adsorbed oxygen. The strong peak from adsorbed oxygen is attributed to the larger surface to volume ratio of smaller particles and suggests the enhanced sensing

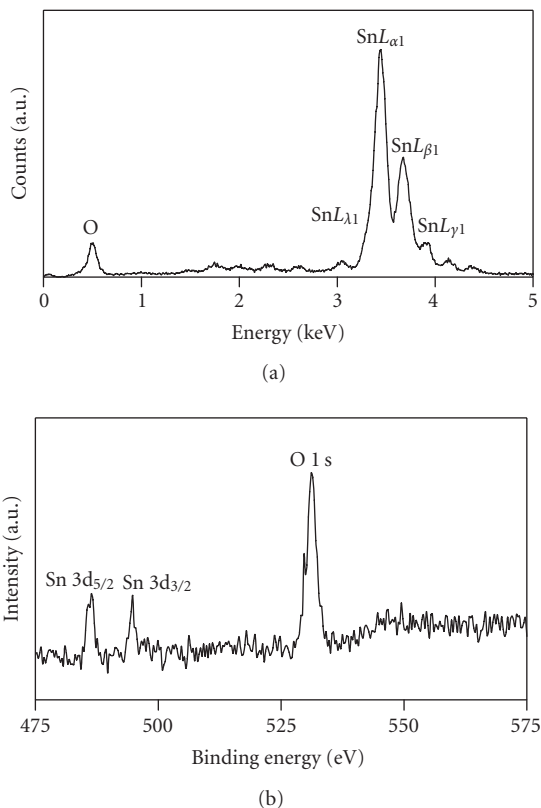


FIGURE 5: (a) EDX spectrum. (b) XPS spectrum of as-produced nanoparticles.

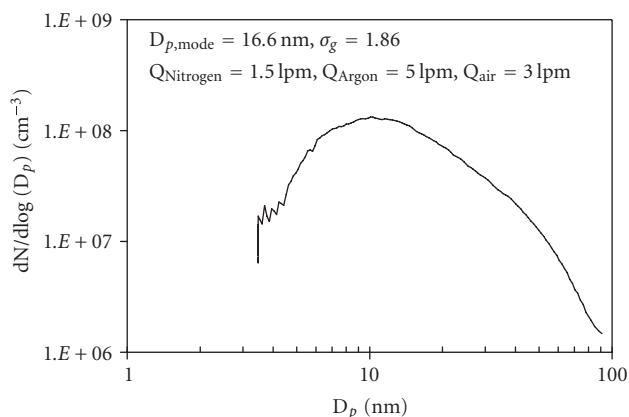


FIGURE 6: Tin oxide nanoparticle size distribution measured by SEMS for an arc current of 37.5 A.

performance of these nanoparticles. After being heated in air for several hours before the sensor test, the particles are further oxidized. The sensing experiment presented later clearly shows that the surface SnO_x layer on larger nanoparticles and the smaller SnO_2 nanoparticles contribute to the rapid sensing reactions.

SEMS measurement of the size distribution of tin oxide nanoparticles used for gas sensor fabrication is shown in Figure 6 for an arc current of 37.5 A, an argon flow rate

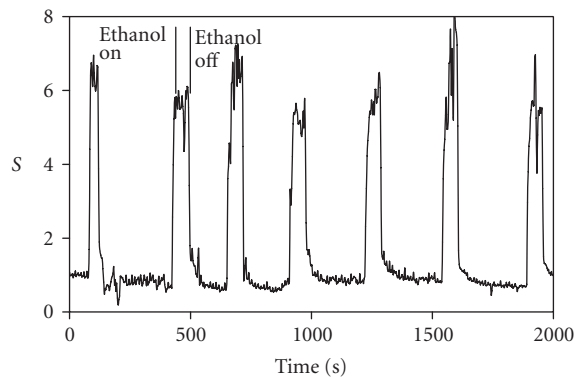


FIGURE 7: Dynamic response of tin oxide nanoparticle sensor to 100 ppm ethanol at an operating temperature of 250°C.

(Q_{Argon}) of 5 lpm, a nitrogen flow rate (Q_{Nitrogen}) of 1.5 lpm, and an air flow rate (Q_{Air}) of 3 lpm. The mode diameter ($D_{p,\text{mode}}$) of as-produced tin oxide nanoparticles is 16.6 nm and the geometrical standard deviation (σ_g) is 1.86. The size distribution of nanoparticles from the mini-arc plasma source may be adjusted by varying the quenching flow rate and other operating conditions. The quenching flow suppresses the coagulation of nanoparticles and slows down the particle growth. As a result, both $D_{p,\text{mode}}$ and σ_g of as-produced nanoparticle size distribution become smaller with the increase of quenching flow rate. Based on the SEMS measurements, the mass production rate of nanoparticles from the reactor was on the order of a few mg/hr. The evaporation rate of precursor tin was found to be on the same order of magnitude as the production rate by comparing the weight of precursor tin before and after the experiment. The reactor can potentially be scaled up by enabling a continuous supply of solid precursors and running many mini-arc sources in parallel. For fabrication of the gas sensor shown in Figure 2, the nanoparticle deposition time was about 30 minutes with a single reactor.

The small size and well-defined crystalline structure of as-produced tin oxide nanoparticles are expected to lead to improved gas sensing performance. Both the sensitivity and the dynamic response of the tin oxide nanoparticle sensor have been evaluated. The sensor sensitivity ($S = R_a/R_g$) is defined as the ratio of the resistance of the sensor in air (R_a) to the resistance in the sensing environment (R_g). The dynamic response of the nanoparticle sensor is measured by recording the change in the resistance of the tin oxide nanoparticle sensor as a function of time when switching on or off the sensing gas. The time constant (τ) of the sensor is then determined by the time it takes for the sensor to attain 63.2% of the initial difference in electrical resistance before and after changing the gas environment.

Figure 7 shows the dynamic behavior of the tin oxide nanoparticle-based gas sensor at an operating temperature of 250°C. The “ethanol on” represents the introduction of 100 ppm ethanol and the “ethanol off” represents the introduction of clean air. Upon the introduction of ethanol, the

resistance of the nanoparticle sensor decreases and a sensitivity greater than 1 is observed. Upon the introduction of clean air, the resistance of the nanoparticle sensor returns to a base value and a sensitivity around 1 is registered. The increased electrical conductivity of the tin oxide nanoparticle sensor is attributed to the reactions between ethanol and oxygen adsorbates on the surface of tin oxide nanoparticles that lead to the backflow of free electrons to tin oxide nanoparticles [26]. The sensor response is quite reproducible with an average sensitivity of about 6. The fluctuation in sensitivity is most likely due to slight variations in the operating temperature and the gas flow rates during the experiment. The sensing time constant of the nanoparticle sensor is about 8 seconds while the recovery time constant is about 15 seconds. This sensing performance represents a significant improvement over that published in the literature. For example, Kennedy et al. [27] reported a tin oxide nanoparticle sensor with a sensitivity of 1.3, a sensing time constant of 110 seconds, and a recovery time constant of 403 seconds for the same operating conditions (100 ppm ethanol and 250°C). The higher sensitivity and faster response of the new sensor may be attributed to the smaller nonagglomerated tin oxide nanoparticles and smaller spacing between interdigitated fingers.

4. CONCLUSION

Tin oxide nanoparticles with sizes as small as a few nm have been successfully produced using a mini-arc plasma source to fabricate a functional gas sensor. Most of the larger nanoparticles greater than 20 nm are approximately spherical, while smaller nanoparticles below 5 nm are mostly faceted. Although some agglomerated nanoparticles are observed, nonagglomerated nanoparticles are dominant in the product. Based on the SAD and HRTEM analyses, both nonagglomerated and agglomerated nanoparticles bear a crystalline structure. However, agglomerated nanoparticles should be minimized for gas sensor applications since defects are induced at the joining neck as a result of agglomeration. Good response and sensitivity of the gas sensor fabricated from the as-produced tin oxide nanoparticles suggest that the mini-arc plasma source is capable of producing high-quality nanoparticles for gas sensing applications.

ACKNOWLEDGMENTS

The authors would like to thank Donald Roberson for technical support with TEM analyses, Liying Zhu and Steven Hardcastle for XPS analysis, and Nikolai Kouklin for assisting the initial sensor test. TEM analyses were performed in the HRTEM Laboratory at University of Wisconsin-Milwaukee (UWM) and XPS analyses were done at the Advanced Analysis Facility of UWM. The e-beam lithography was carried out in the Center for Nanoscale Materials at ANL and the high resolution SEM imaging was carried out in the Electron Microscopy Center at ANL, both of which are supported by the DOE Office of Science under contract #W-31-109-Eng-38. This work was financially supported by National Science Foundation (DMI-0609059) and UWM.

REFERENCES

- [1] R. Summitt, J. A. Marley, and N. F. Borrelli, "The ultraviolet absorption edge of stannic oxide (SnO₂)," *Journal of Physics and Chemistry of Solids*, vol. 25, no. 12, pp. 1465–1469, 1964.
- [2] Y. Shimizu and M. Egashira, "Basic aspects and challenges of semiconductor gas sensors," *MRS Bulletin*, vol. 24, no. 6, pp. 18–24, 1999.
- [3] D. E. Williams, "Conduction and gas response of semiconductor gas sensors," in *Solid State Gas Sensors*, P. T. Moseley and B. C. Tofield, Eds., p. 71, Adam Hilger, Bristol, UK, 1987.
- [4] S. C. Chang, "Oxygen chemisorption on tin oxide: correlation between electrical conductivity and EPR measurements," *Journal of Vacuum Science & Technology*, vol. 17, no. 1, pp. 366–369, 1980.
- [5] M. K. Kennedy, F. E. Kruijs, H. Fissan, B. R. Mehta, S. Stappert, and G. Dumpich, "Tailored nanoparticle films from monosized tin oxide nanocrystals: particle synthesis, film formation, and size-dependent gas-sensing properties," *Journal of Applied Physics*, vol. 93, no. 1, pp. 551–560, 2003.
- [6] M. Su, S. Li, and V. P. Dravid, "Miniaturized chemical multiplexed sensor array," *Journal of the American Chemical Society*, vol. 125, no. 33, pp. 9930–9931, 2003.
- [7] E. R. Leite, I. T. Weber, E. Longo, and J. A. Varela, "A new method to control particle size and particle size distribution of SnO₂ nanoparticles for gas sensor applications," *Advanced Materials*, vol. 12, no. 13, pp. 965–968, 2000.
- [8] F. Gu, S. F. Wang, M. K. Lū, G. J. Zhou, D. Xu, and D. R. Yuan, "Photoluminescence properties of SnO₂ nanoparticles synthesized by sol-gel method," *Journal of Physical Chemistry B*, vol. 108, no. 24, pp. 8119–8123, 2004.
- [9] L. H. Jiang, G. Q. Sun, Z. H. Zhou, et al., "Size-controllable synthesis of monodispersed SnO₂ nanoparticles and application in electrocatalysts," *Journal of Physical Chemistry B*, vol. 109, no. 18, pp. 8774–8778, 2005.
- [10] F. E. Kruijs, H. Fissan, and A. Peled, "Synthesis of nanoparticles in the gas phase for electronic, optical and magnetic applications - a review," *Journal of Aerosol Science*, vol. 29, no. 5-6, pp. 511–535, 1998.
- [11] R. W. Siegel, "Synthesis and properties of nanophase materials," *Materials Science and Engineering A-Structural Materials Properties Microstructure and Processing*, vol. 168, no. 2, pp. 189–197, 1993.
- [12] R. C. Flagan and M. M. Lunden, "Particle structure control in nanoparticle synthesis from the vapor phase," *Materials Science and Engineering A-Structural Materials Properties Microstructure and Processing*, vol. 204, no. 1-2, pp. 113–124, 1995.
- [13] S. C. Wang and R. C. Flagan, "Scanning electrical mobility spectrometer," *Aerosol Science and Technology*, vol. 13, no. 2, pp. 230–240, 1990.
- [14] A. Wiedensohler, "An approximation of the bipolar charge distribution for particles in the submicron size range," *Journal of Aerosol Science*, vol. 19, no. 3, pp. 387–389, 1988.
- [15] D.-R. Chen, D. Y. H. Pui, D. Hummes, H. Fissan, F. R. Quant, and G. J. Sem, "Design and evaluation of a nanometer aerosol differential mobility analyzer (Nano-DMA)," *Journal of Aerosol Science*, vol. 29, no. 5-6, pp. 497–509, 1998.
- [16] C.-M. Yun, Y. Otani, and H. Emi, "Development of unipolar ion generator-separation of ions in axial direction of flow," *Aerosol Science and Technology*, vol. 26, no. 5, pp. 389–397, 1997.

- [17] T. J. Krinke, K. Deppert, M. H. Magnusson, F. Schmidt, and H. Fissan, "Microscopic aspects of the deposition of nanoparticles from the gas phase," *Journal of Aerosol Science*, vol. 33, no. 10, pp. 1341–1359, 2002.
- [18] J. Dixkens and H. Fissan, "Development of an electrostatic precipitator for off-line particle analysis," *Aerosol Science and Technology*, vol. 30, no. 5, pp. 438–453, 1999.
- [19] T. Sahm, L. Madler, A. Gurlo, N. Barsan, S. E. Pratsinis, and U. Weimar, "Flame spray synthesis of tin dioxide nanoparticles for gas sensing," *Sensors and Actuators, B: Chemical*, vol. 98, no. 2-3, pp. 148–153, 2004.
- [20] M. T. Swihart, "Vapor-phase synthesis of nanoparticles," *Current Opinion in Colloid & Interface Science*, vol. 8, no. 1, pp. 127–133, 2003.
- [21] E. R. Leite, T. R. Giraldo, F. M. Pontes, E. Longo, A. Beltrán, and J. Andrés, "Crystal growth in colloidal tin oxide nanocrystals induced by coalescence at room temperature," *Applied Physics Letters*, vol. 83, no. 8, pp. 1566–1568, 2003.
- [22] X. Pan and J. G. Zheng, "Microstructure of and crystal defects in nanocrystalline tin dioxide thin films," in *Proceedings of Materials Research Society Symposium (MRS '97)*, vol. 472, pp. 87–92, Boston, Mass, USA, December 1997.
- [23] P. A. Grutsch, M. V. Zeller, and T. P. Fehlner, "Photoelectron spectroscopy of tin compounds," *Inorganic Chemistry*, vol. 12, no. 6, pp. 1431–1433, 1973.
- [24] H. Willemen, D. F. Van De Vondel, and G. P. Van Der Kelen, "An ESCA study of tin compounds," *Inorganica Chimica Acta*, vol. 34, pp. 175–180, 1979.
- [25] R. I. Hegde, "Preparation of metal-polymer dispersions by plasma techniques: an ESCA investigation," *Surface and Interface Analysis*, vol. 4, no. 5, pp. 204–207, 1982.
- [26] H. Fissan, M. K. Kennedy, T. J. Krinke, and F. E. Kruis, "Nanoparticles from the gas phase as building blocks for electrical devices," *Journal of Nanoparticle Research*, vol. 5, no. 3-4, pp. 299–310, 2003.
- [27] M. K. Kennedy, F. E. Kruis, H. Fissan, and B. R. Mehta, "Fully automated, gas sensing, and electronic parameter measurement setup for miniaturized nanoparticle gas sensors," *Review of Scientific Instruments*, vol. 74, no. 11, pp. 4908–4915, 2003.

Effect of Pressure on Synthesis of Pr-Doped Zirconia Powders Produced by Microwave-Driven Hydrothermal Reaction

A. Opalinska,^{1,2} C. Leonelli,³ W. Lojkowski,¹ R. Pielaszek,¹ E. Grzanka,¹ T. Chudoba,¹
H. Matysiak,² T. Wejrzanowski,² and K. J. Kurzydowski²

¹Laboratory of Nanomaterials, Institute of High Pressure Physics, Polish Academy of Science, Sokolowska 29, 01-142 Warsaw, Poland

²Faculty of Materials Science and Engineering, Warsaw University of Technology, Woloska 141, 02-507 Warsaw, Poland

³Department of Materials and Environmental Engineering, University of Modena and Reggio Emilia, Via Vignolese 905/A, 41100 Modena, Italy

Received 15 March 2006; Revised 19 December 2006; Accepted 20 December 2006

A high-pressure microwave reactor was used to study the hydrothermal synthesis of zirconia powders doped with 1 mol % Pr. The synthesis was performed in the pressure range from 2 to 8 MPa corresponding to a temperature range from 215°C to 305°C. This technology permits a synthesis of nanopowders in short time not limited by thermal inertia of the vessel. Microwave heating permits to avoid contact of the reactants with heating elements, and is thus particularly well suited for synthesis of doped nanopowders in high purity conditions. A mixture of ZrO₂ particles with tetragonal and monoclinic crystalline phases, about 15 nm in size, was obtained. The p/T threshold of about 5-6 MPa/265–280°C was necessary to obtain good quality of zirconia powder. A new method for quantitative description of grain-size distribution was applied, which is based on analysis of the fine structure of the X-ray diffraction line profiles. It permitted to follow separately the effect of synthesis conditions on the grain-size distribution of the monoclinic and tetragonal phases.

Copyright © 2006 A. Opalinska et al. This is an open access article distributed under the Creative Commons Attribution License, which permits unrestricted use, distribution, and reproduction in any medium, provided the original work is properly cited.

1. INTRODUCTION

Several papers report microwave- (MW-) driven hydrothermal synthesis of nano-sized powders at elevated pressure [1–5] stimulated by some reports on acceleration of chemical reaction rates when microwaves are used to heat the reactants [4], which however can be rationalized in terms of local superheating of the fluids during microwave heating [6–8]. Most commercial microwave hydrothermal apparatuses used for the production of nanocrystalline powders work at maximum pressure/temperature in range of 2-3 MPa/200°C [9–11]. Very few commercial apparatuses have been built in order to reach extreme reaction conditions: 260°C and 10 MPa [12], in practice pressure exceeding 5 MPa has been applied rarely.

In the present paper, we report the results of the effect of pressure on the synthesis of nanosized ZrO₂ powders doped with 1 mol% of Pr, in a microwave-driven hydrothermal reaction in a range of pressures 2–8 MPa. The investigation of the evolution of grain phase distribution and phase composition of zirconia nanopowders aroused from its widespread applications [13–16]. In particular, Pr-doped zirconia is used

as pigment [17, 18], and as luminescent material [19, 20]. Both the tetragonal and monoclinic phases or their mixtures are usually present in the powders synthesized hydrothermally [21–24] and it is also well known that a decrease in grain size leads to an increase in the content of tetragonal phase, which for larger than 10 nm grained material is metastable at room temperature [25, 26]. Since for a range of applications, like ceramics with superior mechanical properties or luminescent material, the phase composition of the powders plays an important role, the stability of the tetragonal phase in nano-sized powders and methods to control it were extensively discussed.

Garvie et al. [26] explained the stability of tetragonal 1–9 nm diameter nanopowders assuming a lower surface energy of the tetragonal phase compared to the monoclinic one, so that at low grain sizes, where the surface energy is a considerable fraction of the total energy of the system, it is favorable to form the tetragonal phase. The threshold value for the stability of the tetragonal phase was also explained in terms of internal strain energy [27] or internal pressures resulting from surface stress terms [27, 28]. The above threshold value is close to that calculated by Simeone et al. [23] who

obtained a value of 13.7 nm. However, some authors report observations of 6 nm diameter monoclinic zirconia nanoparticles [29].

The mechanisms of crystallization of the tetragonal and monoclinic phases and their mutual transformation under hydrothermal conditions were extensively investigated by Yoshimura et al. [30–32]. Their experimental results can be explained in terms of dissolution/precipitation, structural rearrangement of the tetragonal phase, or simultaneous nucleation of the two phases of ZrO_2 . Mineralogical, morphological, and physical characterizations were combined to get additional insight in the nucleation and growth mechanism which are then discussed in the context of the above presented concepts on the synthesis and grain-growth process. The kinetics and conditions for zirconia precipitation were recently reviewed by Piticescu et al. [33].

It should be noted that the presence of 1% of Pr in the zirconia ceramics does not influence significantly phase equilibrium, as it is seen from phase diagrams of zirconia doped with rare earth ions [34, 35]. The effect on the synthesis conditions on luminescence properties of Pr in nanosized ZrO_2 is the subject of separate papers [19]. The high-pressure microwave reactor used for this investigation provided shorter reaction times than those reported in literature, so that the properties of the product depended solely on the process parameters, and the kind of powder produced can be rapidly changed by changing the teflon vessel [1, 19, 20, 36–38]. Particularly interesting is the possibility of doping nanopowders with rare earth ions in very high purity conditions ensured in the reactor heated by means of microwaves, in a pure teflon vessel, without any contamination sources. The present study is one of the first in a series of planned works on application of microwave-driven hydrothermal reactors for the synthesis of doped nanopowders.

2. EXPERIMENTAL METHODS

2.1. Sample preparation

ZrO_2 powders containing 1 mol% praseodymium were obtained through the addition of praseodymium (III) nitrate $Pr(NO_3)_3 \cdot 6H_2O$ to 0.5 M $ZrOCl_2$ aqueous solutions. The solutions were neutralized with 1 M NaOH to $pH = 10$ and were poured in a PTFE reaction vessel of the MW reactor. The MW reactor (produced by “ERTEC,” Wroclaw, Poland) working at 2.45 GHz delivers a maximum unpulsed power of 270 W to a fluid volume of 70 mL, hence the delivered power density reaches 4 W/mL. The system can be operated at a maximum autogenous pressure of 12 MPa closed vessel. The design of the reactor is schematically shown in Figure 1. The time, pressure, and power, are computer-controlled and a typical run is given in Figure 2. In the present experiments, the feedback signal was delivered to the control system by the pressure gauge. A thermocouple is situated outside the reaction vessel and displays the temperature change with a delay of about 100 seconds, and for this reason is of limited use as a feedback signal for short processes. The reaction temperature was calculated from p/T diagram of water so only pressure was controlled during the process and kept constant at

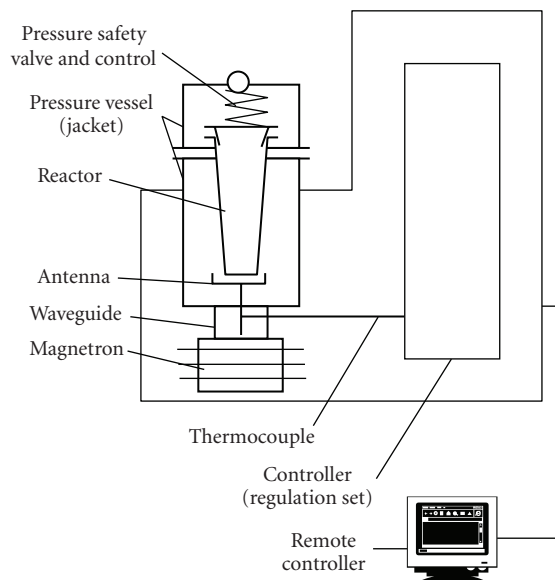


FIGURE 1: Scheme of the MW reactor.

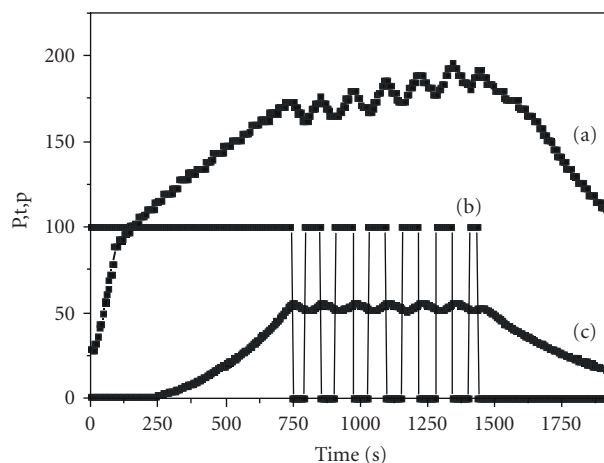


FIGURE 2: The chart of typical reaction with pressure kept as the control parameter. Curves are for (a) temperature, (b) power, (c) pressure.

seven different pressures from 2 to 8 MPa with an accuracy of 0.5 MPa, which corresponds to temperature range 215–305 °C. The overall reaction time was 40 minutes, heating for 30 minutes and cooling time was 10 minutes. The reproducibility of the process was tested by repeating the synthesis at 5 MPa six times and simultaneous measurements of grain size and phase composition of the powders by XRD method.

After syntheses, the powders were centrifuged, washed, and dried prior to their characterization.

2.2. Characterization of samples

For all the powders, thermogravimetric analysis (TGA) was performed (using a Netzsch STA 402, Selbs, Germany). The

sample weight was approximately 100 mg and the sample was dried in the air at room temperature before analyses. The density of the powders was measured using helium pycnometry (Model AccuPyc 1330, Micromeritics Instruments, Norcross, Ga, USA). The density measurement procedure was as follows: the powders were flushed in a helium atmosphere for 120 minutes at a temperature of 200°C, weighted, and transferred to the helium pycnometer. The results of density measurements could be influenced by air absorbed at the surface of the nanopowders. Therefore, the measurements were repeated up to 100 times, and the density as a function of number of cycles was determined. The process was interrupted when the results reached an asymptotic value which was considered as the result of the measurement.

The X-ray diffraction (XRD) patterns were collected in 2Θ range of 20° – 90° at room temperature, with a step of 0.05° using an X-ray ($\text{CuK}\alpha$) diffractometer (Model D5000, Siemens, Germany). The grain-size distributions (GSDs) were determined using a newly developed method of XRD peak fine structure analysis of polydispersed powders (XRD-GSD) [39, 40]. This method permits to fit the peaks using an analytical function with fitting parameters: average particle diameter $\langle R \rangle$ and dispersion of particle sizes σ as fitting parameters. The ratio of the volume fraction of the monoclinic and tetragonal phases was determined by measuring the peaks area belonging to the respective phases. In order to compare phase-specific (T/M) GSD measurements to the grain-size readings from other methods (e.g., BET), joint T and M grain size was calculated as weighted average of T and M phases. For comparison, the well-known Scherrer method for average crystallite diameter evaluation was applied [41].

The specific surface area analysis was conducted by means of the multipoint BET method (Gemini 2360, Micromeritics Instruments, Norcross, Ga, USA), using nitrogen as an adsorbate. Based on BET data, the particle size was calculated, assuming that the particles are spherical, using the equation

$$\phi = \frac{6}{S\rho}, \quad (1)$$

where ϕ (m) is the average diameter of a spherical particle, S (m^2/g) is specific surface area of powder, and ρ (g/m^3) the density value of crystalline zirconia ($5.6 \times 10^6 \text{ g}/\text{m}^3$).

In addition to the grain size calculated assuming spherical particles, (2) permits to calculate the average chord crossing the particles without any assumption on their shape [42]:

$$\langle l \rangle = \frac{2}{S_v}, \quad (2)$$

where $\langle l \rangle$ is the average chord and S_v is the relative surface [1]. Finally, for comparison, the well-known Scherrer method for average crystallite diameter evaluation was applied [41].

3. RESULTS

The weight-loss curve can be divided into two stages. (1) From room temperature up to 200°C, the weight loss is at-

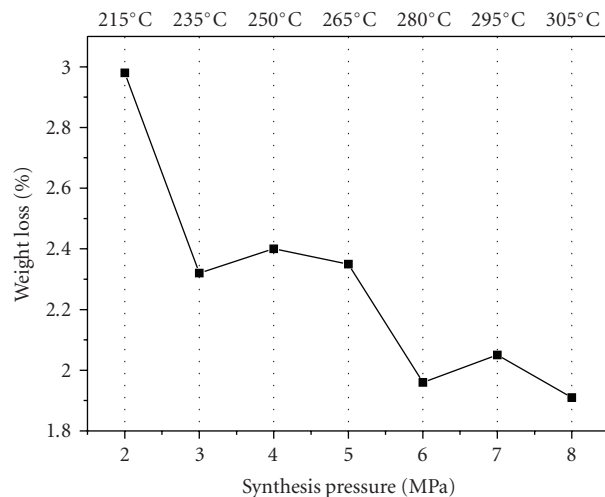


FIGURE 3: Weight loss of the powders in the temperature range 200–700°C as a function of synthesis pressure.

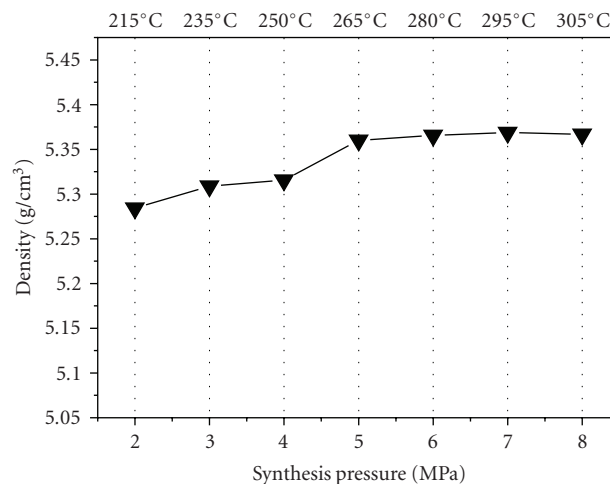


FIGURE 4: Density of nanopowders as a function of synthesis pressure.

tributed to evaporation of water absorbed on the powders surface. (2) In the range 200–700°C, the loss is attributed to transformation of hydroxide that remained after synthesis into oxide [43]. It is important to notice how the overall weight loss in the range 200–700°C decreases when the synthesis pressure increases (Figure 3). The weight loss in the range 2.3–3.0% above 200°C for powders synthesized under pressure up to 5 MPa indicated a high content of hydroxides. The decrease in weight loss correlates well with the increase of density of the nanopowders as the synthesis pressure is increased (Figure 4), and again a threshold pressure of 5 MPa is observed above which the density reaches 95% of the density of a single crystal.

Figure 5(a) shows X-ray diffraction patterns of ZrO_2 doped with 1% of Pr synthesized at seven different pressures. No peaks belonging to phases other than ZrO_2 phases have

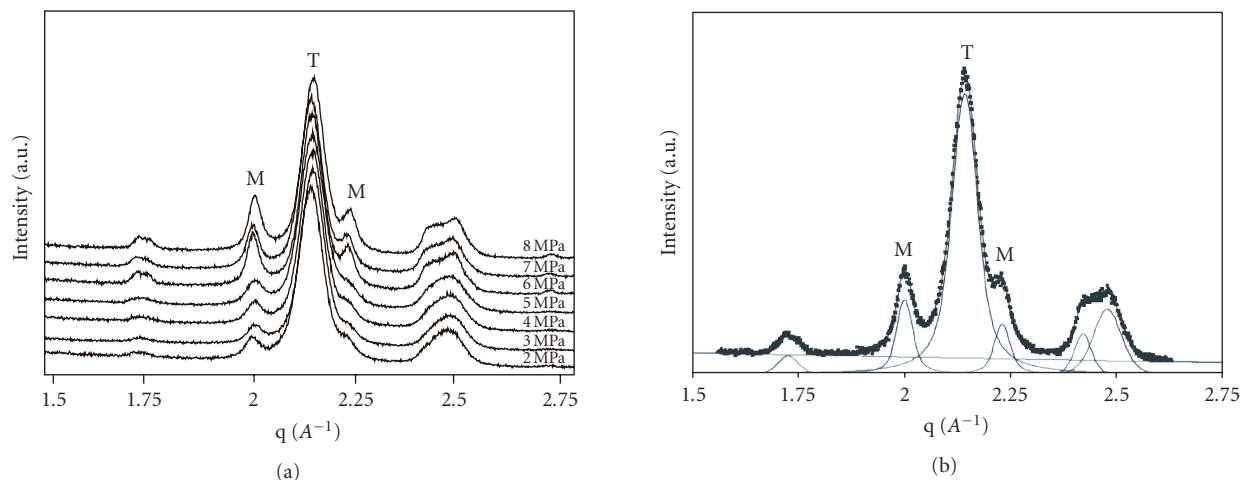


FIGURE 5: (a) X-ray diffraction patterns of Pr-doped ZrO_2 powders synthesized at pressures in the range 2–8 MPa. The diffraction peak from the tetragonal phase is indicated by “T” and from the monoclinic phase by “M,” respectively. (b) Example of simultaneous evaluation of phase composition and grain-size distribution (GSD) by analysis of the peak profiles.

been recognized. Figure 5(b) shows an example of evaluation of the GSD by analysis of the fine structure of the X-ray peak profile.

The average grain size $\langle R \rangle$, dispersions of sizes σ , and contents of monoclinic/tetragonal phases derived by analysis of the peak profile are given in Tables 1 and 2. In particular, Figure 6(a) shows the average grain size as a function of synthesis pressure obtained by means of Scherrer’s method, specific surface measurements, and XRD-GSD data. Figure 6(b) shows the average size estimated from XRD line profile analysis, for monoclinic and tetragonal crystalline phases separately.

The error in grain size measured based on XRD investigations has been estimated as a result of 6 subsequent synthesis at 5 MPa. The standard deviations were 1.0 nm for monoclinic and 0.3 nm, respectively, for tetragonal phase. The volume fraction of the tetragonal phase decreases from 89% for 2 MPa to 77% for 8 MPa (Figure 6(d) and Table 2).

Table 3 shows specific surface areas and derived particle-size parameters as well as the density of the powders.

4. DISCUSSION

The present results confirmed the advantages of microwave heating during hydrothermal synthesis of nanocrystalline powders. Microwaves transmit the energy directly to the reaction media, thus shortening both the heating and cooling times, which saves energy on heating the thick walls used usually for a pressurized reaction vessel. For such reactors, thermal inertia forces to carry out the reaction for much longer time than it is needed for the reaction to be completed. In addition, the temperature control is more difficult than in low thermal inertia systems. Application of microwaves to heat the reagents during hydrothermal reac-

TABLE 1: Grain-size distribution parameters for ZrO_2 1 mol% Pr nanopowders synthesized at pressures ranging from 2 to 8 MPa as measured by means of XRD. The values provided are the average ones from the given fraction of tetragonal and monoclinic phases, where the XRD-GSD parameters were obtained for each phase separately.

Synthesis pressure/ temperature (MPa/°C)	XRD (both phases)	
	$\langle R \rangle$ (nm)	σ (nm)
2/215	13.7 ± 1.2	2.5 ± 0.6
3/235	14.2 ± 1.0	1.9 ± 0.3
4/250	14.2 ± 1.0	1.4 ± 0.3
5/265	13.6 ± 1.0	1.1 ± 0.3
6/280	16.6 ± 1.3	3.0 ± 0.6
7/295	16.2 ± 1.2	2.2 ± 0.4
8/305	16.7 ± 1.2	3.2 ± 0.6

tion permitted to precisely control the process parameters: time and pressure, and ensure high purity of reaction conditions, since the substrates of the reaction were enclosed in a teflon vessel and had no contact with heating elements. The precise control of the synthesis pressure and time enabled to study the effects of the synthesis pressure on the phase composition and grains-size distribution of the nanopowders. In particular, it can be shown that there is a threshold pressure above which the quality of the powders (measured indirectly, by assessing their density and weight loss during thermogravimetric tests) may be significantly improved.

The TGA results indicate a low content of volatile phases for samples obtained at pressure above 5 MPa (Figure 3). The first stage of heating, from room temperature up to 200°C, is connected most likely with evaporation of water absorbed at the surface of the powders. Further weight loss in the temperature range 200–700°C (Figure 3) is most

TABLE 2: Grain-size distribution parameters for ZrO₂ 1 mol% Pr nanopowders synthesized at pressures ranging from 2 to 8 MPa as measured by means of XRD-GSD method applied separately to the monoclinic phase and tetragonal phase. Column “%” shows the volume fraction of the tetragonal or monoclinic phases.

Synthesis pressure/temperature (MPa/°C)	Monoclinic				Tetragonal			
	$\langle R \rangle$ (nm)	σ (nm)	$\sigma/\langle R \rangle$	%	$\langle R \rangle$ (nm)	σ (nm)	$\sigma/\langle R \rangle$	%
2/215	19 ± 5	9 ± 4	0.49	11	13.1 ± 0.6	1.8 ± 0.2	0.14	89
3/235	22 ± 5	4 ± 1	0.16	8	13.5 ± 0.6	1.8 ± 0.2	0.13	92
4/250	21 ± 5	4 ± 1	0.17	10	13.4 ± 0.6	1.2 ± 0.1	0.09	90
5/265	16 ± 3	6 ± 2	0.40	15	13.2 ± 0.6	0.2 ± 0.02	0.01	85
6/280	25 ± 3	7 ± 2	0.29	21	14.3 ± 0.7	1.8 ± 0.2	0.13	79
7/295	24 ± 3	6 ± 1	0.24	19	14.4 ± 0.7	1.4 ± 0.2	0.10	81
8/305	24 ± 3	7 ± 1	0.27	23	14.5 ± 0.7	2.3 ± 0.3	0.16	77

likely connected with decomposition of hydroxides that remained bound to the particles after the synthesis process [43]. The pressure of 5 MPa is a threshold, above which there are no much changes in weight loss of the powders. Therefore above this pressure of synthesis, a minimum of hydroxides content in the reaction product was achieved.

Also the powder density increases with synthesis pressure from 5.28 g/cm³ for powder produced at pressure of 2 MPa to 5.37 g/cm³ for powder produced at a pressure of 8 MPa (Figure 4), that is, 95.3% of that of microcrystalline ZrO₂, which is 5.6 g/cm³. An additional result of the present study is that measurements of density of nanopowders using helium pycnometry are a simple tool for characterizing their quality, provided that proper measurement procedures are applied.

The average grain size increases when synthesis pressure is increased (Figure 6(a)). For sake of comparison, the results of particle-size evaluation using three different methods (BET, Scherrer’s, and XRD-GSD) are reported in a single plot (Figure 6(a)). Using Scherrer’s formula or specific surface measurements give values on the average 5 and 3 nm smaller for the average grain size than the XRD-GSD method. This result indicates that application of Scherrer’s formula or BET method to powders with a wide or bimodal gain size distribution may lead to considerable errors.

The XRD-GSD analysis permitted us to get insight in the grain growth of the tetragonal and monoclinic phases separately (Figure 6(b)). The average grain size of the monoclinic phase drops from about 20 nm to 16 nm at 5 MPa, and then increases to 24–26 nm for synthesis pressures above 6 MPa. The average grain size of the tetragonal phase remains below 14 nm for all the pressures of synthesis applied.

The volume fraction of the monoclinic phase increases with synthesis pressure from 11% for 2 MPa to 23% for 8 MPa (Figure 6(d)).

The GSD of the tetragonal phase is relatively independent of the time and pressure of synthesis. On the other hand, the GSD for the monoclinic phase and its coefficient of variation C_v ($\sigma/\langle R \rangle$) are very sensitive for the conditions of synthesis. In our previous work [40, 44], we have found that the coefficient of variation is a fingerprint of the synthesis mechanism. Therefore the synthesis or growth mechanism of the two phases must be different, and for the monoclinic phase it depends on synthesis pressure. Figure 6 shows an apparent drop of grain size of zirconia grain with the monoclinic phase, but this drop is within the experimental error (see error bars).

The average grain size and grain-size dispersion of the tetragonal phase are relatively independent of synthesis pressure (the variations are in the range of 2 nm), while that of the monoclinic phase is affected by the synthesis pressure (variations in the range 10 nm). The observed behavior of the GSD functions of the two phases can be interpreted as follows (Figure 7). The two phases nucleate in parallel at pressures about 2 MPa (temperature about 215°C). With further increase of pressure of synthesis, the average grain size of the monoclinic phase as well as its dispersion increase more rapidly, while there is an upper limit for the grain size of the tetragonal phase at about 20 nm. This evolution of GSD leads to a bimodal grain-size distribution.

The synthesis pressure range 5-6 MPa is crucial for the quality of the powders. Above 6 GPa, the density of the powders reaches 95% of the density of ZrO₂ and stabilizes. At the same time, the results of the thermogravimetric studies show a low weight loss of powders produced above 5 MPa pressure, that is, above 265°C. These results indicate that for hydrothermal synthesis of zirconia nanopowders below these pressures or temperatures, a high fraction of hydroxide phase is expected to be present. Such a third phase may influence phase equilibria, stabilizes the monoclinic phase below grain sizes of 10 nm, and leads to deviations between experimental

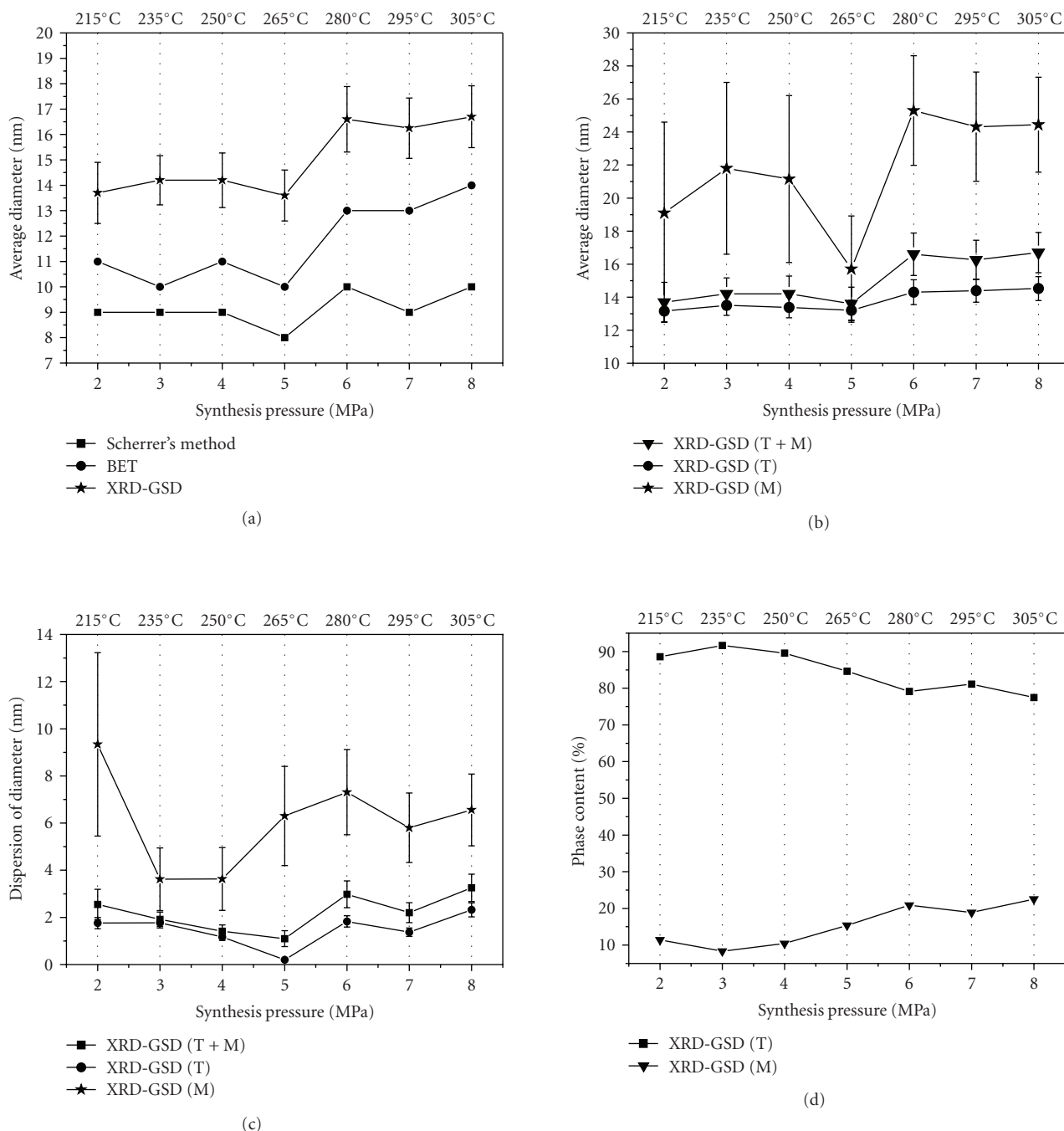


FIGURE 6: (a) Average size of nanopowders (both phases) as a function of pressure as measured using three methods indicated in the figure. (b) Average size of monoclinic (M) and tetragonal (T) phases evaluated from XRD line profile analysis. (c) Dispersion of the GSD as a function of synthesis pressure for M and T phases. (d) Phase content of the powders synthesized.

results and theoretical predictions on the stability of the two phases.

5. CONCLUSIONS

Microwave-driven hydrothermal synthesis permits to precisely control the time, pressure, and temperature during the

synthesis of zirconia nanopowders and to perform the reactions in high purity conditions. The high power density achieved during synthesis, which reaches 4 W/mL, permits to shorten synthesis time to 15 minutes.

The pressure/temperature of 5 MPa/265°C is a threshold where the zirconia powders reached a high density indicating a fairly perfect crystalline structure.

TABLE 3: Density and specific surface area measured by BET method and evaluation of the average particle diameter $\langle\phi\rangle$ and chord $\langle l\rangle$.

Synthesis pressure/ temperature (MPa/°C)	Density (g/cm ³)	Specific surface area by BET method (m ² /g)	Grain size calculated from specific surface area	
			Average diameter $\langle\phi\rangle$ (nm)	Average chord $\langle l\rangle$ (nm)
2/215	5.284	101	11	1.9
3/235	5.309	102	10	1.9
4/250	5.315	101	11	2.0
5/265	5.360	103	10	1.9
6/280	5.366	83	13	2.4
7/295	5.369	85	13	2.3
8/305	5.367	78	14	2.5

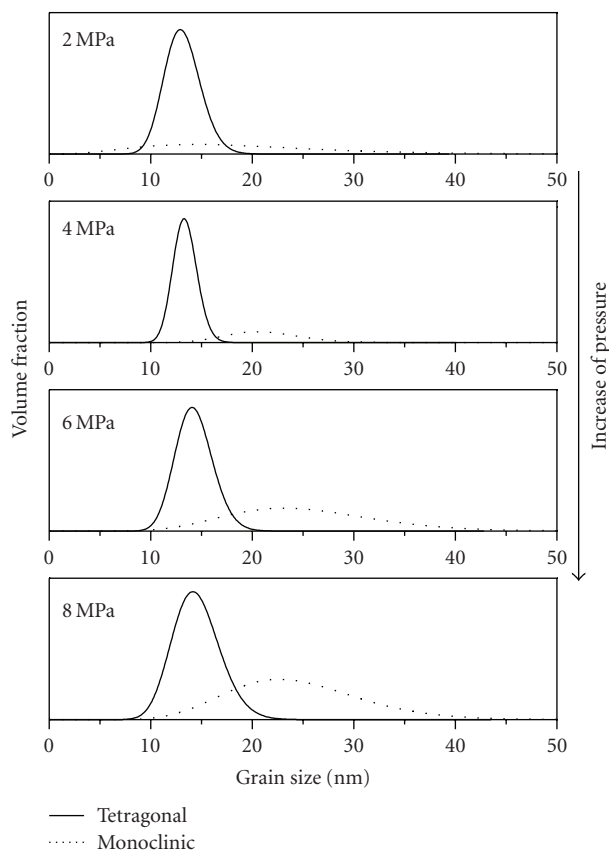


FIGURE 7: Model of the grain-size distribution changes for the monoclinic and tetragonal phases with increasing pressure.

Measurements of density of nanopowders using helium pycnometry is a convenient method for determination of the quality of the powders.

The XRD-GSD analysis permitted us to get insight into the grain growth of the tetragonal and monoclinic phases separately. The two phases are nucleated in parallel at less than 2 MPa synthesis pressure. Presence of hydroxides should be taken into account when discussing phase equilibria, grain-growth mechanisms, and properties of zirconia produced hydrothermally at pressures below 5 MPa.

ACKNOWLEDGMENTS

This work was supported by COST Action D30 “High Pressure Synthesis and Processing of Nano-Powders” and D32 “Chemistry in High-Energy Microenvironments (CHEM),” as well as Polish Ministry for Science and Information technology Grant 3T08A 029 27.

REFERENCES

- [1] F. Bondioli, A. M. Ferrari, S. Braccini, et al., “Microwave-hydrothermal synthesis of nanocrystalline Pr-doped zirconia powders at pressures up to 8 MPa,” *Diffusion and Defect Data. Part B: Solid State Phenomena*, vol. 94, pp. 193–196, 2003.
- [2] S. Somiya and T. Akiba, “Hydrothermal zirconia powders: a bibliography,” *Journal of the European Ceramic Society*, vol. 19, no. 1, pp. 81–87, 1999.
- [3] F. Bondioli, C. Leonelli, C. Siligardi, G. C. Pellacani, and S. Komarneni, “Microwave and conventional hydrothermal synthesis of zirconia doped powders,” in *Report from the 8th International Symposium on Microwave and High Frequency Processing*, Springer, New York, NY, USA, 2002.
- [4] S. Komarneni, R. Pidugu, Q. H. Li, and R. Roy, “Microwave-hydrothermal processing of metal powders,” *Journal of Materials Research*, vol. 10, no. 7, pp. 1687–1692, 1995.
- [5] J. R. Huang, Z. X. Xiong, C. Fang, and B. L. Feng, “Hydrothermal synthesis of Ba₂Ti₉O₂₀ nano-powder for microwave ceramics,” *Materials Science and Engineering B*, vol. 99, no. 1–3, pp. 226–229, 2003.
- [6] D. M. P. Mingos and D. R. Baghurst, “Applications of microwave dielectric heating effects to synthetic problems in chemistry,” *Chemical Society Reviews*, vol. 20, no. 1, pp. 1–47, 1991.
- [7] D. M. P. Mingos, “The applications of microwaves in chemical syntheses,” *Research on Chemical Intermediates*, vol. 20, no. 1, pp. 85–91, 1994.
- [8] A. G. Whittaker and D. M. P. Mingos, “Application of microwave heating to chemical syntheses,” *Journal of Microwave Power and Electromagnetic Energy*, vol. 29, no. 4, pp. 195–219, 1994.
- [9] F. Bondioli, A. M. Ferrari, C. Leonelli, C. Siligardi, and G. C. Pellacani, “Microwave-hydrothermal synthesis of nanocrystalline zirconia powders,” *Journal of the American Ceramic Society*, vol. 84, no. 11, pp. 2728–2730, 2001.
- [10] S. Verma, P. A. Joy, Y. B. Kholam, H. S. Potdar, and S. B. Deshpande, “Synthesis of nanosized MgFe₂O₄ powders by

- microwave-hydrothermal method,” *Materials Letters*, vol. 58, no. 6, pp. 1092–1095, 2004.
- [11] D. Stuerger and M. Delmotte, “Wave-materials interactions, microwave technology and equipment,” in *Microwaves in Organic Chemistry*, A. Loupy, Ed., Wiley-VCH, Weinheim, Germany, 2002.
- [12] K. D. Raner, C. R. Strauss, R. W. Trainor, and J. S. Thorn, “A new microwave reactor for batchwise organic synthesis,” *Journal of Organic Chemistry*, vol. 60, no. 8, pp. 2456–2460, 1995.
- [13] M. E. S. Hegarty, A. M. O’Connor, and J. R. H. Ross, “Syngas production from natural gas using ZrO₂-supported metals,” *Catalysis Today*, vol. 42, no. 3, pp. 225–232, 1998.
- [14] S. P. S. Badwal and K. Foger, “Solid oxide electrolyte fuel cell review,” *Ceramics International*, vol. 22, no. 3, pp. 257–265, 1996.
- [15] G. Xin and Y. Run-Zhang, “On the grain boundaries of ZrO₂-based solid electrolyte,” *Solid State Ionics*, vol. 80, no. 1–2, pp. 159–166, 1995.
- [16] M. H. Tavakkoli and H. Wilke, “Numerical study of induction heating and heat transfer in a real Czochralski system,” *Journal of Crystal Growth*, vol. 275, no. 1–2, pp. e85–e89, 2005.
- [17] Y. Masahiro and S. Shiegeyuki, “Hydrothermal synthesis of crystallized nano-particles of rare earth-doped zirconia and hafnia,” *Materials Chemistry and Physics*, vol. 61, no. 1, pp. 1–8, 1999.
- [18] J. Karch, R. Birringer, and H. Gleiter, “Ceramics ductile at low temperature,” *Nature*, vol. 330, no. 6148, pp. 556–558, 1987.
- [19] A. Opalińska, D. Hreniak, W. Lojkowski, W. Strek, A. Presz, and E. Grzanka, “Structure, morphology and luminescence properties of Pr-doped nanocrystalline ZrO₂ obtained by hydrothermal method,” *Diffusion and Defect Data. Part B: Solid State Phenomena*, vol. 94, pp. 141–144, 2003.
- [20] D. Millers, L. Grigorjeva, A. Opalińska, and W. Lojkowski, “Luminescence of nanosized ZrO₂ and ZrO₂: Pr powders,” *Diffusion and Defect Data. Part B: Solid State Phenomena*, vol. 94, pp. 135–140, 2003.
- [21] M. M. Bućko, K. Haberko, and M. Faryna, “Crystallization of zirconia under hydrothermal conditions,” *Journal of the American Ceramic Society*, vol. 78, no. 12, pp. 3397–3400, 1995.
- [22] W. Pyda, K. Haberko, and M. M. Bućko, “Hydrothermal crystallization of zirconia and zirconia solid solutions,” *Journal of the American Ceramic Society*, vol. 74, no. 10, pp. 2622–2629, 1991.
- [23] D. Simeone, G. Baldinozzi, D. Gosset, M. Dutheil, A. Bulou, and T. Hansen, “Monoclinic to tetragonal semireconstructive phase transition of zirconia,” *Physical Review B*, vol. 67, no. 6, Article ID 064111, 8 pages, 2003.
- [24] V. Lanteri, T. E. Mitchell, and A. H. Heuer, “Morphology of tetragonal precipitates in partially stabilized ZrO₂,” *Journal of the American Ceramic Society*, vol. 69, no. 7, pp. 564–569, 1986.
- [25] R. C. Garvie, “The occurrence of metastable tetragonal zirconia as a crystallite size effect,” *Journal of Physical Chemistry*, vol. 69, no. 4, pp. 1238–1243, 1965.
- [26] R. C. Garvie and M. F. Goss, “Intrinsic size dependence of the phase transformation temperature in zirconia microcrystals,” *Journal of Materials Science*, vol. 21, no. 4, pp. 1253–1257, 1986.
- [27] M. Mitsuhashi, M. Ichihara, and T. Tatsuke, “Characterization and stabilization of metastable tetragonal ZrO₂,” *Journal of the American Ceramic Society*, vol. 57, no. 2, pp. 97–101, 1974.
- [28] R. Nitsche, M. Winterer, and H. Hahn, “Structure of nanocrystalline zirconia and yttria,” *Nanostructured Materials*, vol. 6, no. 5–8, pp. 679–682, 1995.
- [29] G. Baldinozzi, D. Simeone, D. Gosset, and M. Dutheil, “Neutron diffraction study of the size-induced tetragonal to monoclinic phase transition in zirconia nanocrystals,” *Physical Review Letters*, vol. 90, no. 21, 2003.
- [30] E. Tani, M. Yoshimura, and S. Somiya, “Formation of ultrafine tetragonal ZrO₂ powder under hydrothermal conditions,” *Journal of the American Ceramic Society*, vol. 66, no. 1, pp. 11–14, 1983.
- [31] M. Yashima, M. Kakihana, and M. Yoshimura, “Metastable phase diagrams in the zirconia-containing systems utilized in solid-oxide fuel cell application,” *Solid State Ionics*, vol. 86–88, part 2, pp. 1131–1149, 1996.
- [32] M. Yoshimura, T. Hiuga, and S. Somiya, “Dissolution and reaction of yttria-stabilized zirconia single crystals in hydrothermal solutions,” *Journal of the American Ceramic Society*, vol. 69, no. 7, pp. 583–584, 1986.
- [33] R. Piticescu, C. Monty, and D. Millers, “Hydrothermal synthesis of nanostructured zirconia materials: present state and future prospects,” *Sensors and Actuators B: Chemical*, vol. 109, no. 1, pp. 102–106, 2005.
- [34] Y. Li, Y. Liu, L. Huang, and X. G. Li, “Phase transition of nanostructure zirconias doped with rare earth elements,” *Journal of Nanoscience and Nanotechnology*, vol. 5, no. 9, pp. 1546–1551, 2005.
- [35] F. Boulc’h and E. Djurado, “Structural changes of rare-earth-doped, nanostructured zirconia solid solution,” *Solid State Ionics*, vol. 157, no. 1–4, pp. 335–340, 2003.
- [36] COST D30 Mid Term Evaluation Meeting, <http://www.uni-press.waw.pl/COST/>.
- [37] T. Strachowski, E. Grzanka, B. Palosz, A. Presz, L. Slusarski, and W. Lojkowski, “Microwave driven hydrothermal synthesis of zinc oxide nanopowders,” *Diffusion and Defect Data. Part B: Solid State Phenomena*, vol. 94, pp. 189–192, 2003.
- [38] R. Fedyk, T. Chudoba, A. Presz, W. Lojkowski, and K. J. Kurzydowski, “Study of grain size distribution in nanocrystalline iron oxides synthesized by hydrothermal method,” *Diffusion and Defect Data. Part B: Solid State Phenomena*, vol. 94, pp. 239–242, 2003.
- [39] R. Pielaszek, “Analytical expression for diffraction line profile for polydispersive powders,” in *Proceedings of the 19th Conference on Applied Crystallography*, Kraków, Poland, September 2003.
- [40] R. Pielaszek, *Dyfrakcyjne badania mikrostruktury polikrystalow nanometrowych poddawanych dzialaniu wysokiego cisnienia*, Ph.D. thesis, Department of Physics, Warsaw University, Warsaw, Poland, 2003.
- [41] W. H. Zachariasen, *Theory of X-Ray Diffraction in Crystals*, John Wiley & Sons, New York, NY, USA, 1945.
- [42] T. Wejrzanowski and K. J. Kurzydowski, “Stereology of grains in nano-crystals,” *Diffusion and Defect Data. Part B: Solid State Phenomena*, vol. 94, pp. 221–228, 2003.
- [43] R. C. Mackenzie, *Differential Thermal Analysis, Vol. 1*, Academic Press, London, UK, 1970.
- [44] W. Lojkowski, A. Daniszewska, M. Chmielecka, et al., Nanometrology Report, <http://www.nanoforum.org/>.

Epoxy-Carbazole Polymeric Network Nanolayers for Organic Light-Emitting Devices

Jin-Woo Park,¹ Eung-Kyoo Lee,¹ Myon Cheon Choi,¹ Hwajeong Kim,^{1,2} Jihwan Keum,^{1,3} Chang-Sik Ha,¹ and Youngkyoo Kim⁴

¹ Department of Polymer Science and Engineering, Pusan National University, Busan 609-735, South Korea

² Institute of Biomedical Engineering, Imperial College London, Exhibition Road, London SW7 2AZ, UK

³ Samsung SDI Co. Ltd., 818 Gacheon-Ri, Samnam-Myeon, Ulju-Gu, Ulsan 689-701, South Korea

⁴ Experimental Solid State Physics Group, Blackett Laboratory, Department of Physics, Imperial College London, Prince Consort Road, London SW7 2BW, UK

Received 24 March 2006; Revised 5 August 2006; Accepted 24 October 2006

We report the study of epoxy-carbazole polymeric network (ECzPN) nanolayers as a hole injection/transport layer in organic light-emitting devices. The ECzPN nanolayers were prepared by the thermal curing reaction of epoxidized cresol novolak and 3,6-diaminocarbazole in the presence of catalytic amount of triphenyl phosphine. The curing reaction was examined with Fourier transformed infrared spectroscopy, whilst the thermal stability was studied with thermogravimetric analysis. Optical absorption and emission spectroscopy were employed to investigate the optical properties of ECzPN nanolayers, whilst atomic force microscopy was used to examine the surface nanomorphology of ECzPN nanolayers. The result showed that the device performance was greatly influenced by the weight ratio of monomers, because the highest occupied molecular orbital level of ECzPN was significantly changed with the ratio. This is attributed to the ground-state complexes induced by the specific interaction (hydrogen bonding) between the lone pair electrons in amines of carbazole moieties and the hydroxyl group of ring-opened epoxide moieties.

Copyright © 2006 Jin-Woo Park et al. This is an open access article distributed under the Creative Commons Attribution License, which permits unrestricted use, distribution, and reproduction in any medium, provided the original work is properly cited.

1. INTRODUCTION

Organic light-emitting devices (OLED) have attracted great attention for flat-panel-display (FPD) applications due to their sophisticated device structure that is simpler than liquid crystal displays (LCDs) as well as their fast response time and wide viewing angle which are similar to typical cathode ray tube (CRT) [1]. These features still lure FPD manufacturers to consider OLED as one of the next generation's digital television candidates, even though some obstacles including unsatisfied lifetime and lower device efficiency have been recently issued by the concentrated research and development for a couple of decades [2]. Of these obstacles the short device lifetime can be mainly attributed to the inherent instability of organic nanolayers in devices, which is much prominent for small molecule-based OLEDs. Although one of the factors leading to the instability could be sorted out by applying the accelerated preoxidation method [2], all the factors could not be overcome at the moment when it comes to the fundamental aspect of organic nanolayers, particularly based on small molecules.

This problem has motivated the development of molecularly doped polymer films based on thermally stable polymers as well as functional polymer films for hole injection and/or transport layer, since each monomer in polymers, whether they are linked via covalent bonds or strongly bound in stable polymer host, could be more stabilized in polymers than in individual small molecules [3–11]. For instance, we have introduced a semiconducting polyimide (SPI) nanolayer as a hole injection/transport layer for OLEDs, which resulted in a remarkably extended device lifetime [12]. This improved reliability is undoubtedly ascribed to the excellent thermal stability of SPI nanolayers due to the high glass transition temperature ($T_g = 220^\circ\text{C}$) of SPI [13, 14].

With similar concept, we made a chemically cross-linked epoxy network nanolayer doped with hole-transporting molecules as a hole injection/transport layer for durable OLEDs [15]. This pioneering work shed a light on a possibility of using epoxy network nanolayers for OLEDs, because cross-linked epoxy networks are insoluble in common organic solvents and show very excellent thermal stability due

to their three-dimensional network structure [15]. Because in the previous work the hole-transporting molecules were dispersed in the chemically cross-linked epoxy network made of epoxidized cresol novolak (ECN) and phenolic novolak in which both are electronically/electrically insulating, however, heavy loading of hole-transporting molecules to obtain a good hole-transporting property resulted in large-scale phase segregation.

In this work, we have attempted to make chemically cross-linked epoxy networks using ECN and functionalized carbazole moiety, without any inclusion of hole-transporting components, because the carbazole moiety is electronically active so that it is expected to play a hole-transporting role, considering previous uses of several carbazole moieties in organic photorefractive devices, OLEDs, and solar cells [16–18]. The result showed that controlling the monomer ratio between ECN and carbazole moiety led to a uniform epoxy-carbazole polymer network (ECzPN) nanolayer that exhibits no phase segregation at all. At this monomer ratio, the improved device performance has been achieved, which is similar to the performance of well-known standard OLED based on *N,N'*-diphenyl-*N,N'*-bis(3-methylphenyl)-1,1-biphenyl-4,4'-diamine (TPD).

2. EXPERIMENTAL

2.1. Materials

Epoxidized cresol novolak (ECN, molecular weight = 17 523) was supplied from Kukdo Chemical Co. and was further purified by recrystallization from *n*-hexane/ethanol [90 : 10 (v/v)] followed by drying in a vacuum at 80°C for 24 hours. 3,6-diaminocarbazole (DACz), tris(8-hydroxyquinolino)aluminum (Alq₃), and TPD were purchased from Tokyo Kasei Kogyo Co., Ltd. and used without further purification. Triphenyl phosphine (TPP), a catalyst for epoxy cross-linking reaction, was used as received from Junsei Chemical Co., Ltd. *N,N'*-dimethylacetamide (DMAc) was purchased from Aldrich Chemical Co. Figure 1 shows the chemical structure of ECN, DACz, and TPP.

2.2. Preparation of epoxy-carbazole polymeric network nanolayers and devices

For preparing epoxy-carbazole polymeric network (ECzPN), a mixture solution of ECN, DACz, and TPP was made using DMAc (solvent) at the solid concentration of 10 wt% and was vigorously stirred to well mixing. Three different weight ratios (1.5 : 1, 2 : 1, and 3 : 1) of ECN to DACz were employed to investigate the influence of composition. Then these solutions were refluxed at 170°C for 1 hour to make a partially reacted (precured) ECzPN for securing a viscous solution suitable for spin-coating. These viscous solutions were spin coated onto various substrates for further characterization, and then finally postcured at the same condition in a vacuum oven.

For the fabrication of OLEDs, indium-tin oxide (ITO) coated glass substrates were patterned in a strip (ITO) size

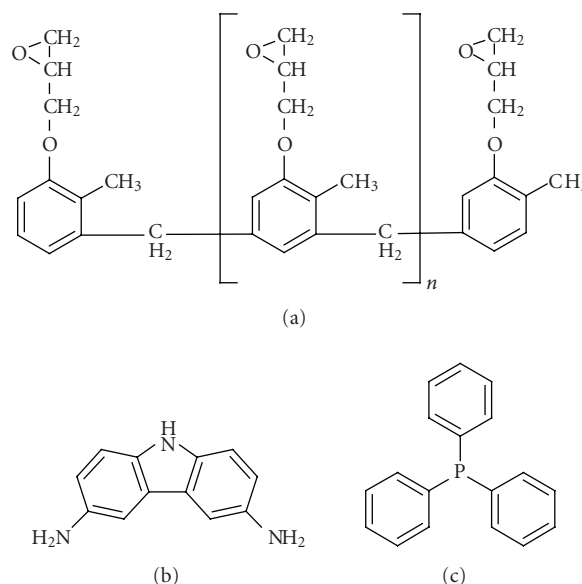


FIGURE 1: Chemical structure of materials used for the preparation of epoxy-carbazole polymeric networks (ECzPN): (a) ECN, (b) DACz, and (c) TPP.

of 2 mm × 30 mm and then were precleaned ultrasonically in deionized water using a nonphosphorus detergent followed by washing in ethanol before drying. The viscous ECzPN solution was spin-coated onto the precleaned ITO coated glass at 4000 rpm for 60 seconds and then soft-baked at 100°C for 5 hours in a vacuum oven. Finally, the ECzPN nanolayers (thickness = 60 nm) were made by further thermal curing at 170°C for 1 hour in a vacuum oven, which were insoluble in DMAc. On top of these ECzPN nanolayers, a 60 nm thick Alq₃ layer was deposited as an emission layer (EML) followed by evaporating the aluminum (Al) cathode in a vacuum of $\sim 5 \times 10^{-6}$ Torr, defining the active emission area of 4 mm². The control device was also prepared by replacing the ECzPN nanolayer with the 60 nm thick TPD layer (see Figure 2) which was directly deposited onto the ITO substrate as a deposition rate of 0.5 ~ 1 nm/s.

2.3. Measurements of films and devices

The chemical cross-linking reaction of nanolayers (films) was monitored using an attenuated total reflection (ZnSe crystal) Fourier transform infrared spectrophotometer (ATR FT-IR 460 plus, JASCO Inc.), whilst the thermal degradation was examined using a thermogravimetric analyzer (TGA Q50, TA Instruments Inc.) under a nitrogen environment at a heating rate of 10°C/min. The optical absorption spectra of ECzPN nanolayers were measured using a UV-visible spectrophotometer (UV 2010, HITACH), while corresponding photoluminescence (PL) spectra were measured using a fluorescence spectrophotometer (F4500, HITACH). Cyclic voltammetry (CV) measurements were performed using an electrochemical instrument (WPG100, WonATech Co.): Pt and Ag/Ag⁺ were used as counter and reference electrodes,

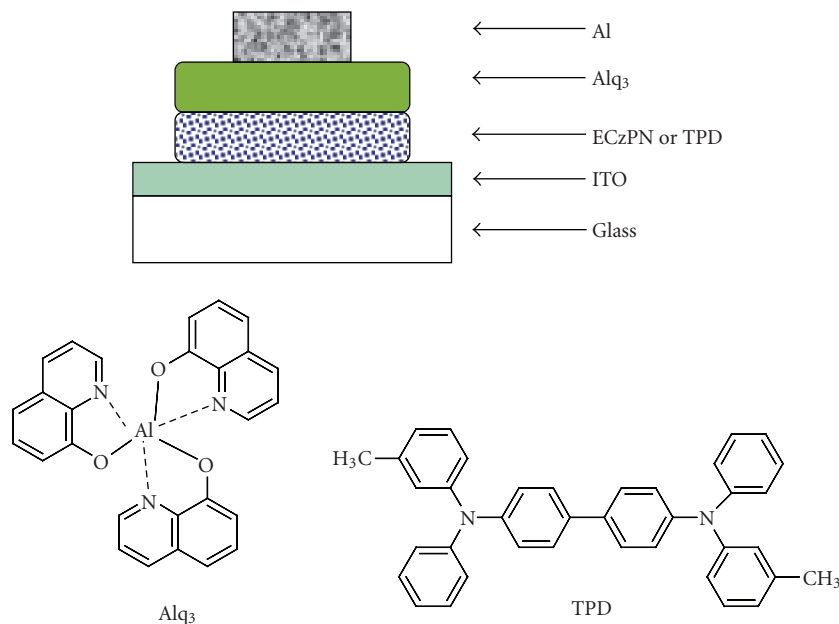


FIGURE 2: Schematic cross-sectional structure of OLED used in this study and chemical structure of Alq₃ and TPD.

respectively, whilst 0.1 M TBAP (Tetra-*n*-butylammonium perchlorate)/CH₃CN was employed as a supporting electrolyte solution. The highest occupied molecular orbital (HOMO) of films was calculated using the oxidation onset potential and the work function (4.8 eV) of Ag electrode (calibrated to the standard Fc/Fc⁺ redox system) [19]. The surface nanomorphology of TPD and ECzPN nanolayers was measured in air using an atomic force microscope (Nanoscope IIIa, Digital Instrument Co.). The scan area was 5 μm × 5 μm and a tapping mode (scan rate = 1.969 Hz; set point = 1.447–1.46 V) was applied to avoid any damage of nanolayer surface upon scanning. We note that the surface images could be slightly deformed because of the possible exposure to moist air during measurements.

The current density-voltage-luminance (J-V-L) characteristics of OLEDs were measured using a customized device measurement system equipped with a photomultiplier tube (PMT, Hamamatsu Photonics Co.) and an electrometer (Keithley 6517). All devices were mounted in a dark sample chamber for the J-V-L measurements in order to get rid of any influence of ambient light.

3. RESULTS AND DISCUSSION

3.1. Characterization for curing reaction and thermal stability

The curing reaction between ECN and DACz (e.g., weight ratio = 3 : 1) was characterized with FT-IR spectroscopy. As shown in Figure 3, ECN shows no characteristic peaks in the high wavenumber region over 3000 cm⁻¹ (see Figure 3(a)), whereas DACz exhibits strong secondary amine (NH, 3390 cm⁻¹) and primary amine (NH₂, 3280 cm⁻¹ and 3180 cm⁻¹) peaks at this range (see Figure 3(b)). In addition,

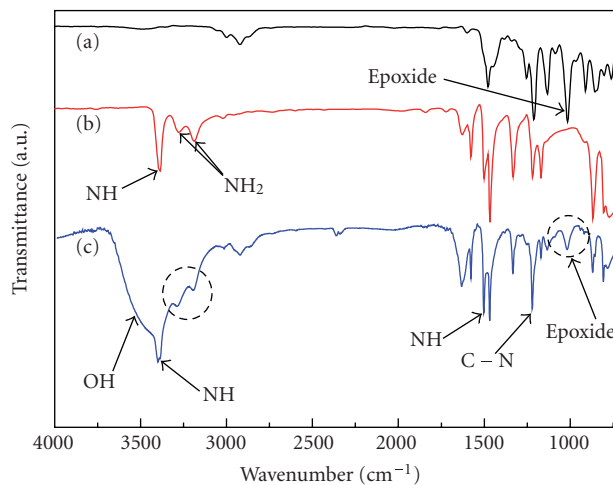


FIGURE 3: FT-IR spectra of (a) ECN, (b) DACz, and (c) ECzPN (3 : 1). The dotted circles point out the remaining monomer materials.

the epoxide peak of ECN is found at 1015 cm⁻¹ which is not observed for DACz. After curing reaction, the broad and huge shoulder at around 3700–3430 cm⁻¹ was measured for ECzPN (see Figure 3(c)), which is attributed to the formation of hydroxyl groups by the ring opening reaction of epoxide ring in ECN (see Figure 4(a) for the reaction mechanism). In the same sense, the peak intensity of epoxide rings at 1015 cm⁻¹ was remarkably reduced for the ECzPN film. Therefore, this basically evidences the occurrence of reaction between ECN and DACz to make a three dimensional polymeric network, namely ECzPN here. In addition, the C-N single covalent bond formation between the aliphatic carbon

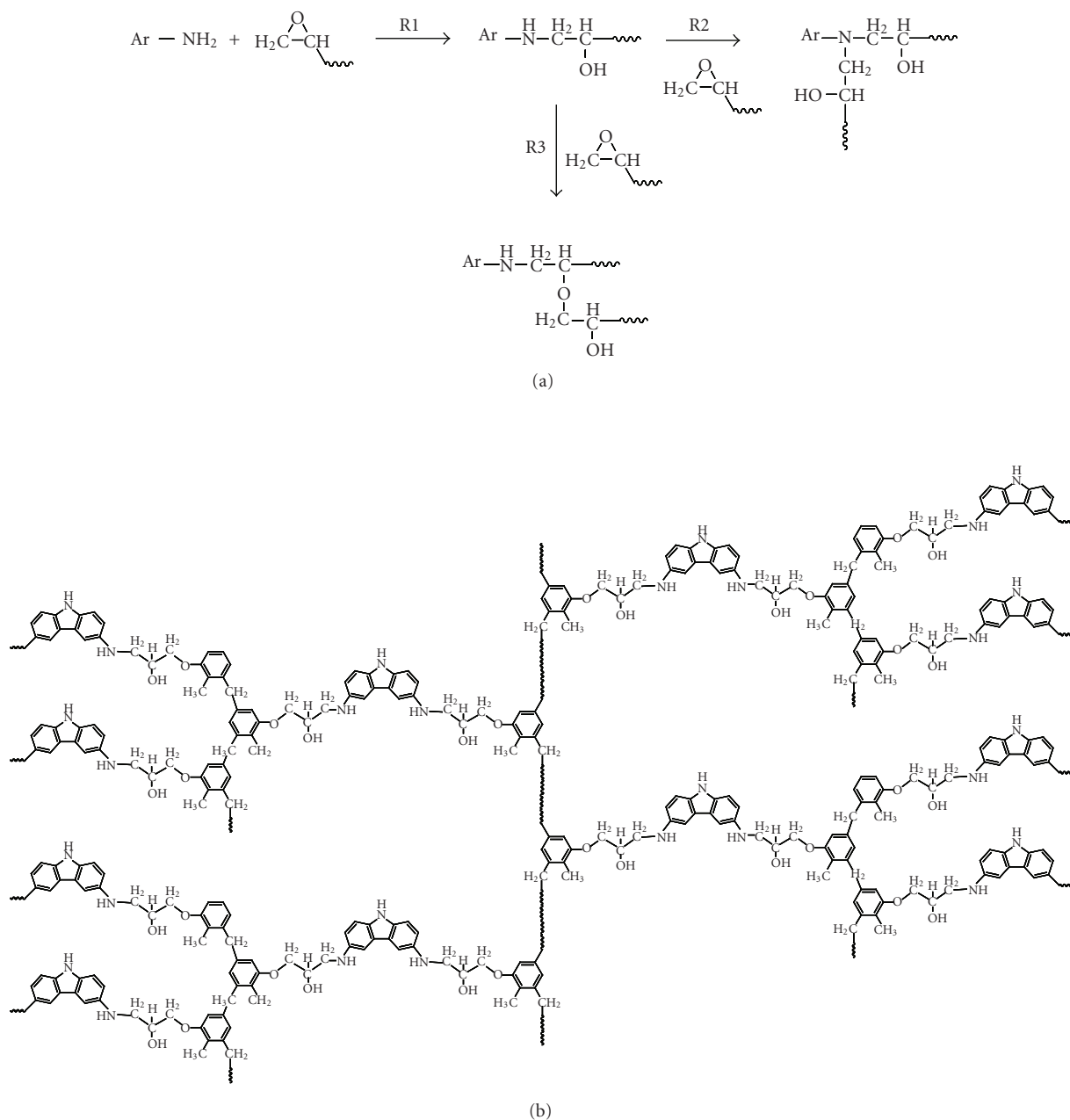


FIGURE 4: (a) Reaction steps between ECN and DACz to make the epoxy-carbazole polymeric networks: R1 denotes the epoxy ring opening reaction step, whilst R2 and R3 represent the successive curing steps; (b) expected three-dimensional cross-linking structure for ECzPN made in this work.

(CH₂) of ECN and the secondary amine (NH₂) of DACz is identified from the increased intensity of C-N stretching and secondary (out-of-plane) NH peaks at 1220 cm⁻¹ and 1503 cm⁻¹, respectively.

However, considering still existence of NH₂ (3280 cm⁻¹ and 3180 cm⁻¹) and epoxide (1015 cm⁻¹) peaks (see dotted circles in Figure 3(c)), the reaction is considered to be incomplete due to the saturation of three-dimensional geometry which hinders moving of two chemicals (ECN and DACz) for further physical contact leading to chemical reaction between

two functional groups (epoxide and NH₂). In addition, because no clear clues were found for the further reactions (R2 and R3 steps in Figure 4(a)), we assume that the dominant reaction here is limited to the R1 step in Figure 4(a). Based on this stage of reaction, the three-dimensional polymeric network (ECzPN) is considered to be made like the schematic drawing as shown in Figure 4(b).

Figure 5 shows the weight loss (thermal degradation) as a function of temperature for ECzPN and starting materials (ECN and DACz). Obviously, DACz exhibits very quick

weight loss between 250°C and 330°C and at last only 5 wt% remain above this temperature. This indicates the thermally unstable nature of functional (hole-transporting) materials like DACz. In contrast, ECN shows relatively quite stable trend. In particular, further improvement in thermal stability is observed for the ECzPN film (3 : 1 weight ratio), which is mainly ascribed to the formation of covalent bond to bind the thermally unstable component (DACz) in the three-dimensional network structure. In this context of improved thermal stability against degradation and three-dimensional network formation, we expect the ECzPN film to have a high glass transition temperature though this still needs to be verified by actual measurements.

3.2. Optical properties

As shown in Figure 6, the unreacted mixture of ECN and DACz (3 : 1) shows an onset absorption wavelength of ~ 430 nm (2.9 eV), which is mainly assigned to the lowest unoccupied molecular orbital (LUMO) of DACz in the mixture film. Surprisingly, new absorption peaks are observed in the wavelengths of 430–600 nm for the reacted (cured) ECzPN nanolayers (films) (also note the increased intensity at around 350 nm and 400–425 nm). This is considered as a ground-state complex made by the specific interaction (hydrogen bonding) between the lone pair electrons of nitrogen atoms in DACz and the hydroxyl groups of ring-opened epoxide unit of ECN upon the curing reaction (see inset to Figure 6). Here two different resonance states of nitrogen atoms in DACz could result in different complexes (**a** and **b**) peaking at 470 nm (**a**) and 520 nm (**b**). As a consequence, the ECzPN nanolayers have two LUMO bands: major LUMO band from original DACz singlet (onset = 430 nm, 2.9 eV), sub-LUMO band from these complexes (onset = 600 nm, 2.1 eV). In particular, it is noted that these complexes are pronounced as the ECN content increases. This indicates that the hydroxyl group concentration plays a critical role in forming the ground-state complexes.

Due to these ground-state complexes made in the ECzPN nanolayers, the photoluminescence spectra also show two major emission peaks at around 450 nm and 610 nm: the former is assigned to the singlet transition of DACz, the latter is considered to be a transition for the two complexes (see Figure 7). The intensity of complex peaks increases with the ECN contents, which is in consistent with the absorption spectral trend. Here we note that the very small peak at around 600 nm was also measured for the unreacted mixture film, which is considered as the marginal formation of complexes even in the unreacted mixture though it is unclear at the moment whether owing to the hydrogen bonding or not. In particular, the width of major peak at 450 nm is wider for the ECzPN nanolayers than the unreacted mixture film (also note additional peaks below 400 nm and shoulders at around 500 nm). This result may infer the increased delocalization of electrons in the carbazole ring of DACz owing to the specific interaction leading to the ground-state complex formation.

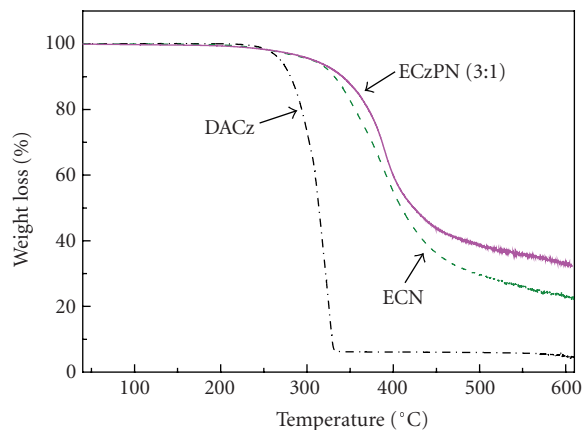


FIGURE 5: TGA thermograms for ECN, DACz, and ECzPN. The scan rate was 10°C/min.

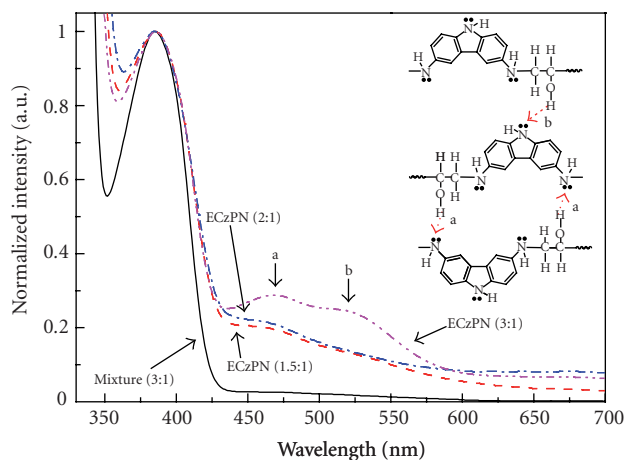


FIGURE 6: Optical absorption spectra of unreacted mixture (3 : 1), ECzPN (1.5 : 1), ECzPN (2 : 1), and ECzPN (3 : 1). “a” and “b” denote the absorption peaks of complexes formed in the ECzPN nanolayers (see inset for the specific interaction by hydrogen bonding). Here we note that the unreacted mixture showed nearly solid-state film after spin coating but we expect that the internal phase might be gel-like because this film was not fully cross-linked.

3.3. Characteristics of OLEDs and nanomorphology

As shown in Figure 8(a), the device made with the ECzPN (2 : 1) nanolayer exhibits almost similar J-V shape to the TPD device below the current density of 100 mA/cm². However, the devices made with the ECzPN nanolayers at the (1.5 : 1) and (3 : 1) weight ratios of ECN to DACz showed much higher charge injection/transport voltages. The result for the (3 : 1) ratio is acceptable because of the low hole-transporting DACz contents, but that for the (1.5 : 1) ratio is not a normal case because the hole-transporting characteristics should be improved by increasing the content of hole-transporting moiety (DACz). To understand this, we have measured the HOMO level (or ionization potential) of films

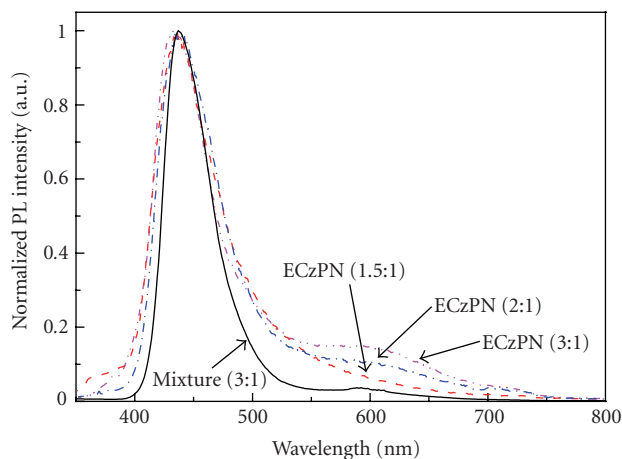


FIGURE 7: Photoluminescence spectra of unreacted mixture (3 : 1), ECzPN (1.5 : 1), ECzPN (2 : 1), and ECzPN (3 : 1).

using a cyclic voltammetry (see Figure 9(a)–9(d)), which resulted in 6.0 eV, 5.3 eV, and 4.6 eV for (1.5 : 1), (2 : 1), and (3 : 1) weight ratios, respectively (see Figure 9(e)–9(h) for the flat-energy-band diagrams built by taking into account the complex states as well). This very huge change in HOMO level might be attributed to the role of the specific interaction leading to the formation of complexes. In other words, the measured HOMO level is not solely originated from the pristine DACz or ECN components but is significantly affected by the lone pair electrons in the complexes which are expected to be more easily extracted as we have previously proposed the similar activation effect between lone pair electrons in nitrogen atoms and carbonyl dipoles in imide groups [12]. In more detail, although for the ECN film with TPP (1 wt%) without DACz the oxidation onset is observed at 1.3 V leading to the HOMO level of 6.1 eV (see Figure 9(d)), the (3 : 1) ECzPN film shows a very different oxidation onset at -0.2 V in the presence of the onset peak at around 1.1 V which might be related to the oxidation of ECN components (see Figure 9(c)). This evidences the presence of specific interaction leading to making the ground-state complexes as discussed in Figures 6 and 7. Therefore, this HOMO level trend clearly indicates that the hole injection from ITO to the ECzPN layer limits the performance of the (1.5 : 1) device owing to the large barrier height, even though the high loading (content) of DACz could just help to improve the hole transport inside the ECzPN nanolayer.

In particular, the (1.5 : 1) device shows much slower increase in the luminance than the current density as the applied voltage increases, whereas other devices show similar increasing trend for luminance and current density (see Figures 8(b) and 8(c)). This huge imbalance (high current but low luminance) of the (1.5 : 1) device is attributed to the large electron leakage through the sub-LUMO level (gap) of complexes (3.9 eV) as seen in Figure 9(f). It is worthy to note that the band structure of the ECzPN (2 : 1) nanolayer, which resulted in the best device performance amongst the devices with ECzPN nanolayers, is very similar to that of TPD.

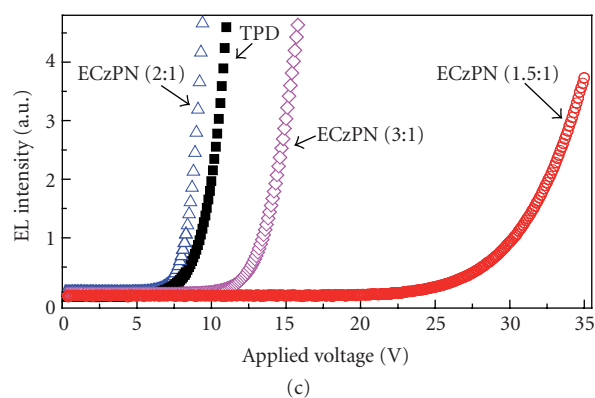
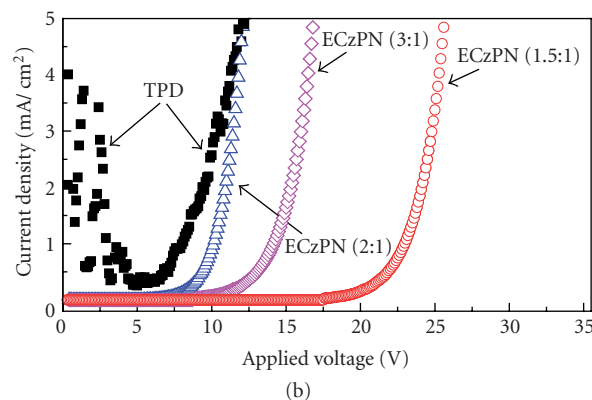
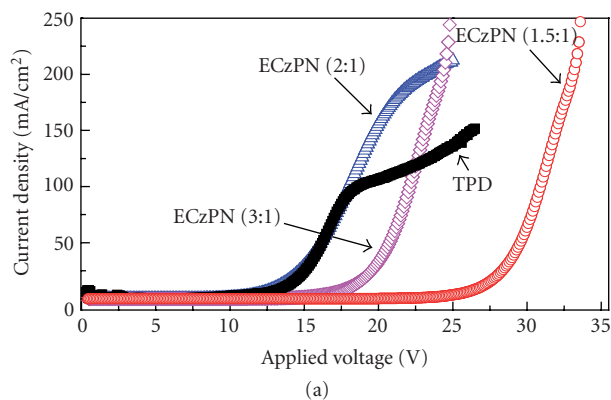


FIGURE 8: Current density—voltage ((a) full scale; (b) enlarged scale adjusted for the comparison with luminance) and luminance—voltage (c) characteristics of OLEDs made with the ECzPN nanolayers or TPD as a hole injection/transport layer.

Finally, we have tried to correlate the device characteristics with the nanomorphology of ECzPN nanolayers. As shown in Figure 10, the TPD film shows very coarse morphology that features large TPD crystals aggregated each other, indicating a poor film quality which might be responsible for the early degradation of corresponding device at relatively lower current density though the low T_g (63°C) of TPD is normally understood as the cause for the poor device

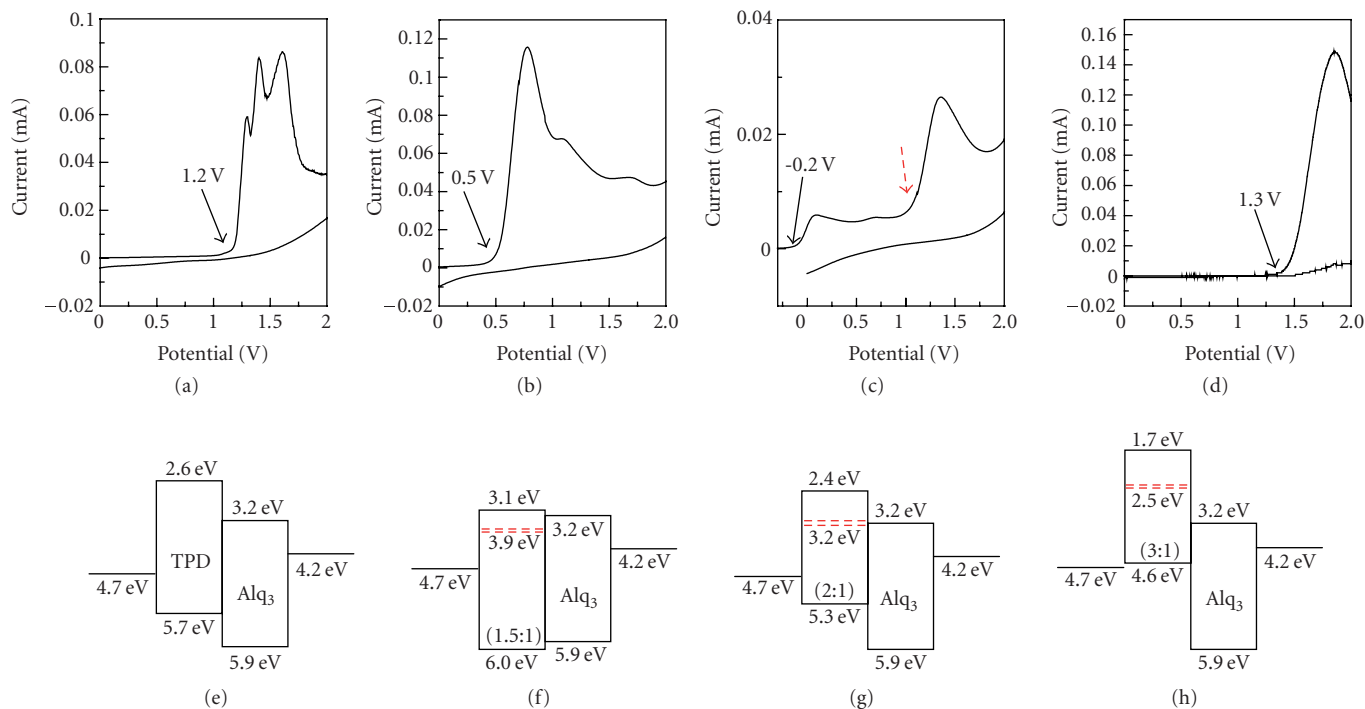


FIGURE 9: Cyclic voltammograms for (a) ECzPN (1.5 : 1), (b) ECzPN (2 : 1), (c) ECzPN (3 : 1), and (d) ECN with TPP (1 wt%); the potential is against Ag/Ag⁺. Flat energy band diagrams of OLEDs fabricated in Figure 8, where the hole injection/transport layer is (e) TPD, (f) ECzPN (1.5 : 1), (g) ECzPN (2 : 1), and (h) ECzPN (3 : 1). The sub-LUMO band (see dashed red lines) in the middle of HOMO-LUMO levels of each ECzPN nanolayers was calculated on the basis of the ground-state complex band gap (2.1 eV) as shown in Figure 6.

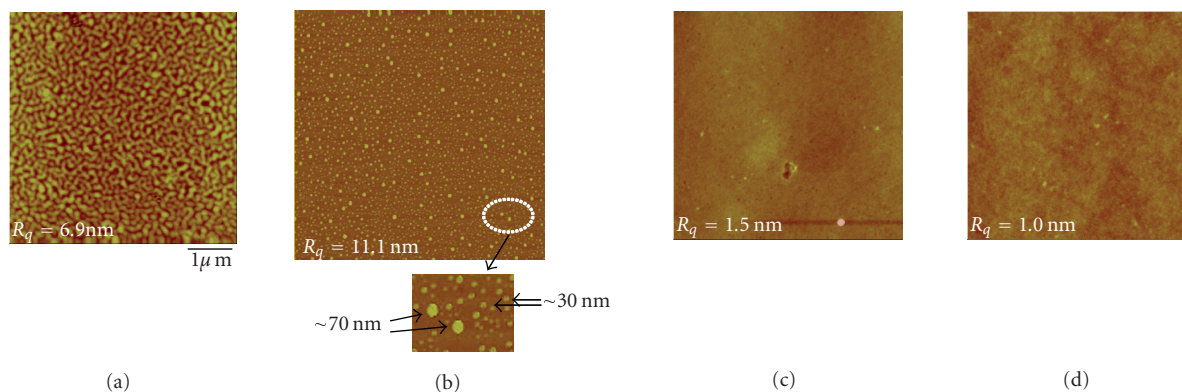


FIGURE 10: AFM images (scan size = 5 μm \times 5 μm) of (a) TPD, (b) ECzPN (1.5 : 1), (c) ECzPN (2 : 1), and (d) ECzPN (3 : 1). “ R_q ” denotes the root-mean-squared roughness of nanolayer surfaces. Note that the enlarged image of (b) shows two kinds of nanoparticles in a size of about 70 nm and 30 nm.

stability [3]. In contrast, the ECzPN (1.5 : 1) nanolayer shows a phase-segregated coarse nanomorphology in which two kinds of nanoparticles (70 nm and 30 nm) are evenly dispersed over the entire surface of nanolayers: these nanoparticles are considered as the unreacted DACz molecules remained after the curing reaction and contributed the worst surface roughness (11.1 nm) amongst all films investigated here. This coarse nanomorphology might be more or less re-

sponsible for the poor device performance (poor correlation between luminance and current density), even though the major reason is ascribed to the large hole-injection barrier and electron-leakage pathways (sub-LUMO band) due to the ground-state complex formation as discussed in Figure 9. However, no detectable phase segregation was observed for the (2 : 1) and (3 : 1) nanolayers, indicating almost perfect participation of DACz molecules in the curing reaction.

4. CONCLUSION

The epoxy-carbazole polymeric network (ECzPN) nanolayers were prepared and applied as a hole injection/transport layer for OLEDs. These nanolayers showed fairly good stability against thermal degradation. In particular, a ground-state complex was observed for the cross-linked (reacted) ECzPN nanolayers by optical measurements, which is considered to affect the significant shift in the HOMO levels of corresponding films. The OLED with the ECzPN (2 : 1) nanolayer exhibited almost the similar performance to the TPD device, which is attributed to the shifted HOMO level by the specific interaction (hydrogen bonding) between carbazole and ring-opened epoxy moieties. However, the nanoparticle-contained nanomorphology in the ECzPN (1.5 : 1) nanolayer needs further studies to confirm whether it contributes to the device performance badly or not.

ACKNOWLEDGMENTS

This work was financially supported by the National Research Laboratory Program, Korea, the BK 21 Project, and the SRC/ERC of MOST/KOSEF Program (Grant no. R11-2000-070-080020). Youngkoo Kim personally thanks Professor Donal D. C. Bradley for financial support for research and living in London.

REFERENCES

- [1] L. S. Hung and C. H. Chen, "Recent progress of molecular organic electroluminescent materials and devices," *Materials Science and Engineering: R: Reports*, vol. 39, no. 5-6, pp. 143-222, 2002.
- [2] Y. Kim, D. K. Choi, H. Lim, and C.-S. Ha, "Accelerated pre-oxidation method for healing progressive electrical short in organic light-emitting devices," *Applied Physics Letters*, vol. 82, no. 14, pp. 2200-2202, 2003.
- [3] Y. Kim, J. Keum, J.-G. Lee, H. Lim, and C.-S. Ha, "Non-linear charge conduction and emission behaviour of OLED fabricated with Alq₃ and TPD-doped soluble polyimide," *Advanced Materials for Optics and Electronics*, vol. 10, no. 6, pp. 273-283, 2000.
- [4] C.-M. Bouche, P. Berdague, H. Facoetti, P. Robin, P. Le Barny, and M. Schott, "Side-chain electroluminescent polymers," *Synthetic Metals*, vol. 81, no. 2-3, pp. 191-195, 1996.
- [5] E. Bellmann, S. E. Shaheen, R. H. Grubbs, S. R. Marder, B. Kippelen, and N. Peyghambarian, "Organic two-layer light-emitting diodes based on high- T_g hole-transporting polymers with different redox potentials," *Chemistry of Materials*, vol. 11, no. 2, pp. 399-407, 1999.
- [6] A. Kraft, P. L. Burn, A. B. Holmes, D. D. C. Bradley, R. H. Friend, and J. H. F. Martens, "Hole-transporting compounds for multi-layer polymer light-emitting diodes," *Synthetic Metals*, vol. 57, no. 1, pp. 4163-4167, 1993.
- [7] A. Yamamori, C. Adachi, T. Koyama, and Y. Taniguchi, "Electroluminescence of organic light emitting diodes with a thick hole transport layer composed of a triphenylamine based polymer doped with an antimonium compound," *Journal of Applied Physics*, vol. 86, no. 8, pp. 4369-4376, 1999.
- [8] D. B. Roitman, H. Antoniadis, M. Hueschen, R. Moon, and J. R. Sheats, "Polymer thermosetting organic light-emitting devices," *IEEE Journal of Selected Topics in Quantum Electronics*, vol. 4, no. 1, pp. 58-66, 1998.
- [9] D. Müller, M. Gross, K. Meerholz, et al., "Novel cross-linkable hole-transport monomer for use in organic light emitting diodes," *Synthetic Metals*, vol. 111-112, pp. 31-34, 2000.
- [10] T. D. de Morais, F. Chaput, K. Lahlil, and J.-P. Boilot, "Hybrid organic-inorganic light-emitting diodes," *Advanced Materials*, vol. 11, no. 2, pp. 107-112, 1999.
- [11] H. Suzuki and S. Hoshino, "Behavior of charge carriers and excitons in multilayer organic light-emitting diodes made from a polysilane polymer as monitored with electroluminescence," *Journal of Applied Physics*, vol. 79, no. 2, pp. 858-865, 1996.
- [12] Y. Kim, K. H. Bae, Y. Y. Jeong, D. K. Choi, and C.-S. Ha, "An electronically active molecularly doped polyimide hole injection layer for an efficient hybrid organic light-emitting device," *Chemistry of Materials*, vol. 16, no. 24, pp. 5051-5057, 2004.
- [13] Y. Kim, K. Han, and C.-S. Ha, "Synthesis and characteristics of poly[N,N'-diphenyl-N,N'-bis(4-aminobiphenyl)-(1,1'-biphenyl)-4,4'-diamine pyromellitimide] as a hole injecting and transporting layer for hybrid organic light-emitting device," *Macromolecules*, vol. 35, no. 23, pp. 8759-8767, 2002.
- [14] Y. Kim and C.-S. Ha, "Semiconducting polyimide nanolayers for organic nanoelectronics: the first applications to hybrid organic light-emitting devices," in *Nanotechnology at The Leading Edge*, E. V. Dirote, Ed., Nova Science, New York, NY, USA, 2006.
- [15] J. Keum, Y. Kim, and C.-S. Ha, "Molecularly doped polymeric network nanolayers for organic light-emitting devices," *Macromolecular Research*, vol. 14, no. 4, pp. 401-403, 2006.
- [16] D. B. Romero, M. Schaer, L. Zuppiroli, M. Leclerc, D. Adès, and A. Siove, "The role of carbazole in organic light-emitting devices," *Synthetic Metals*, vol. 80, no. 3, pp. 271-277, 1996.
- [17] J. Wagner, J. Pielichowski, A. Hinsch, et al., "New carbazole-based polymers for dye solar cells with hole-conducting polymer," *Synthetic Metals*, vol. 146, no. 2, pp. 159-165, 2004.
- [18] E. Mandowska, W. Mazela, P. Czub, A. Mandowski, J. Pielichowski, and J. Swiatek, "Luminescence properties of epoxy resins modified with a carbazole derivative," *Macromolecular Symposia*, vol. 212, no. 1, pp. 269-274, 2004.
- [19] J. Pommerehne, H. Vestweber, W. Guss, et al., "Efficient two layer leds on a polymer blend basis," *Advanced Materials*, vol. 7, no. 6, pp. 551-554, 1995.

Incorporation of Vanadium Oxide in Silica Nanofiber Mats via Electrospinning and Sol-Gel Synthesis

Jeanne E. Panels and Yong Lak Joo

School of Chemical and Biomolecular Engineering, Cornell University, Ithaca, NY 14853, USA

Received 4 April 2006; Revised 8 September 2006; Accepted 19 September 2006

Submicron scale vanadia/silica hybrid nanofiber mats have been produced by electrospinning silica sol-gel precursor containing vanadium oxytriisopropoxide (VOTIP), followed by calcinations at high temperature. The properties of the resulting inorganic hybrid nanofiber mats are compared to those of electrospun pure silica nanofibers. SEM images show fibers are submicron in diameter and their morphology is maintained after calcination. Physisorption experiments reveal that silica nanofiber mats have a high specific surface area of 63 m²/g. FT-IR spectra exhibit Si–O vibrations and indicate the presence of V₂O₅ in the fibers. XPS studies reveal that the ratio of Si to O is close to 0.5 on the surface of fibers and the amount of vanadium on the surface of fibers increases with calcination. XRD diffraction patterns show that silica nanofibers are amorphous and orthorhombic V₂O₅ crystals have formed after calcination. EFTEM images demonstrate the growth of crystals on the surface of fibers containing vanadium after calcination. SEM images of fibers with high-vanadium content (50 mol% V : Si) show that vanadia crystals are mostly aligned along the fiber axis. XPS shows an increase in vanadium contents at the surface, and XRD patterns exhibit an increase in the degree of crystallinity. A coaxial electrospinning scheme has successfully been employed to selectively place V₂O₅ in the skin layer.

Copyright © 2006 J. E. Panels and Y. L. Joo. This is an open access article distributed under the Creative Commons Attribution License, which permits unrestricted use, distribution, and reproduction in any medium, provided the original work is properly cited.

1. INTRODUCTION

Electrospinning is a fiber formation process typically used to produce nonwoven polymer fiber mats with diameters one or two orders of magnitude smaller than conventional textile fibers. Electrospinning produces mats with large surface area to mass ratios, typical surface areas can be 10 m²/g for fiber diameters of 500 nm and 1000 m²/g for diameters around 50 nm [1]. During electrospinning a strong electric field is used to draw a solution from the tip of a capillary to the collector. The electrostatic field causes a pendant droplet of the solution at the capillary tip to deform into a conical shape or a Taylor cone. When the electrical force at the surface of the solution overcomes the surface tension a fine, charged jet is ejected. The jet moves toward a ground plate acting as a counter electrode. The solvent begins to evaporate immediately after the jet is formed causing the deposit of a thin fiber on the collector plate [1]. We refer the reader to recent reviews that elaborate on the versatility and promise of electrospinning processes [1–3].

One dimensional, inorganic, nanosized fibers and fibrous mats are of interest for their high thermal stability and large surface to mass ratios. Recently, silica nanofiber mats

have been produced using a sol-gel synthesis/electrospinning technique without using any polymer binder [4]. Silica nanofiber mats provide an ideal platform for the incorporation of transition metals and their oxide particles [5]. Previously, the incorporation of metal oxides into electrospun fibers has been achieved using polymer as a binder or a matrix due to its better processabilities. However, calcination at high temperature is needed to grow transition metal oxide crystals and high temperature treatment in turn weakens fibers due to the disintegration of the polymer matrix in fibers [6]. If silica is used as a matrix, however, metal precursors can be included by directly adding them to the sol-gel precursor [7], and the growth of crystalline metal oxides on silica fibers can be achieved, while the fiber morphology is preserved during calcination.

In the present study, we incorporate V₂O₅ into silica nanofibers, and the effect of the inclusion of V₂O₅ on the properties of silica nanofibers is investigated. More specifically, we developed submicron scale vanadia/silica hybrid fiber mats by electrospinning a silica sol-gel precursor containing vanadium oxytriisopropoxide (VOTIP), followed by calcinations at high temperatures. Resulting silica nanofibers containing vanadium pentoxide crystal particles can be used

to detect trace amounts of toxic or flammable gases such as ammonia and hydrocarbons. If vanadium oxide comes into contact with trace amounts of toxic or flammable gases the surface conductance changes, indicating the presence of small amounts of gases [6]. It is important to note that the sensitivity in sensing depends on grain size and smaller grain sizes lead to an increase in the sensitivity [8]. We anticipate that this simple and versatile electrospinning/sol-gel directed approach to conducting layers that combine a large surface area as well as electrical interactions will lead to more sensitive detection in sensing gases. Dispersing V_2O_5 nanoparticles onto the surface of silica nanofibers may allow outstanding specificity and selectivity in gas sensing to be gained. Currently, thin films containing V_2O_5 are used for sensing toxic or flammable gases, but this method only utilizes the limited surface layer of the film because the gas flows over the film [9, 10]. Nanofiber mats can provide a highly porous network which the gas can flow through, and thus the entire active sites on fibers are effectively utilized.

Coaxial electrospinning is a technique that uses a dual syringe system during electrospinning [11]. It allows the creation of hollow nanofibers, with the outer syringe containing an inorganic substance and the inner syringe containing an organic substance, such as mineral oil. Fibers can then be calcined at the appropriate temperature to eliminate organics inside the fiber, while the inorganic part of the fiber will remain and therefore create a hollow, tubular nanostructure. Using a coaxial spinning scheme, hollow silica fibers containing V_2O_5 particles have been produced. Coaxial electrospinning can provide a useful means to produce vanadia-silica nanofiber mats for gas sensing, because V_2O_5 crystals can be placed selectively in the skin layer of fibers such that the loading of transition metal oxides can be greatly reduced.

2. EXPERIMENTAL PROCEDURE

Tetra(ethyl) ortho silicate (TEOS) and VOTIP were supplied by Aldrich. To produce silica nanofibers, a solution that undergoes a sol-gel synthesis reaction was prepared with the molar ratio of TEOS : EtOH : H_2O : HCl being 1 : 2 : 2 : 0.01. After vigorous mixing to produce a homogeneous solution, the solution was placed in a $50^\circ C$ oven to accelerate the sol-gel transition. When vanadia/silica fibers were desired, a VOTIP/EtOH solution containing half of the overall EtOH contents was added after vigorous mixing of the TEOS/EtOH and H_2O /HCl solutions. The spinning solution contained a 23 mol% V : Si ratio, while a 50 mol% V : Si ratio was also used to obtain a higher vanadium content in silica fibers. After ripening for 3–5 h, the solution was electrospun with an applied voltage of 20 kV, a flow rate of 0.03 mL/min, and a tip to collector distance of 4.5 inches. These spinning conditions were carefully chosen to obtain a continuous production of submicron scale fibers. A sample of electrospun fibers was then heated to $150^\circ C$ for 1 h to remove residual solvents followed by calcination at $600 \sim 800^\circ C$ in a tube furnace heated at a rate of $5^\circ C/min$ for 1 ~ 6 h.

A 23 mol% V : Si sol-gel precursor containing TEOS and VOTIP was prepared in the same manner as mentioned previously for coaxial electrospinning. The coaxial electrospin-

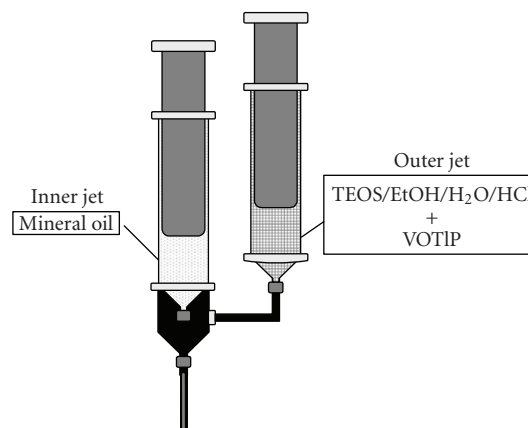


FIGURE 1: Coaxial electrospinning set-up.

ning set up used in the current study is shown in Figure 1. The sol-gel solution was used for the outer syringe with an inner nozzle diameter of 0.84 mm and mineral oil was used for the inner syringe with an inner nozzle diameter of 0.15 mm. The mineral oil had a constant flow rate of 0.01 mL/min, while the flow rate of the TEOS/VOTIP solution was controlled by gravity. The applied voltage was 20 kV and the tip-to-collector distance was 4.5 inches. The collected fibers were heated to $150^\circ C$ for 1 h to remove residual solvents. The coaxially spun fibers were heated at a rate of $5^\circ C/min$ and calcined at $1000^\circ C$ for 6 h to grow vanadium oxide crystals and remove the mineral oil to create hollow fibers.

Scanning electron microscopy (SEM) was conducted using the LEICA 440 and the samples were coated using an Au-Pd sputterer. Specific surface area and pore size distribution of electrospun fiber mats were measured using a micromeritics phys/chemi sorption analyzer and gases used for measurements were either N_2 or Kr. X-ray diffraction (XRD) was done on the Scintag, Inc. Theta-Theta Diffractometer, using a Cu target and a step size of 0.02° . Energy filtering transmission electron microscopy (EFTEM) was conducted using the FEI Tecnai G20. Thermogravimetric analysis (TGA), Fourier transform infrared spectroscopy (FT-IR), and X-ray photoelectron spectroscopy (XPS) experiments were also conducted to characterize electrospun silica-vanadia fibers before and after calcination.

3. RESULTS AND DISCUSSION

3.1. Effect of Inclusion of VOTIP on the properties of sol-gel precursor

Since the conductivity and viscosity of the solution affects both initial thinning behavior and whipping motion of the jet during electrospinning, one can easily surmise that the final fiber diameter can be influenced by the inclusion of vanadium oxide precursor in the silica-sol precursor. The effect of inclusion of vanadium particles on both conductivity and viscosity of the sol-gel precursor is presented in this section.

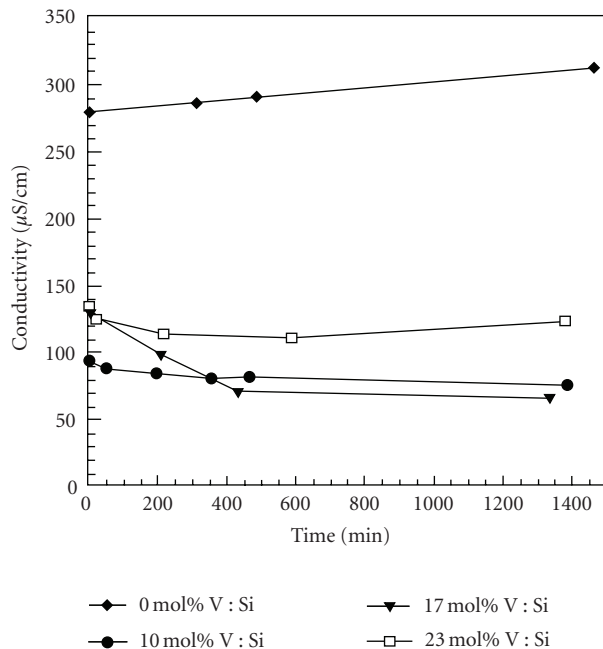


FIGURE 2: Evolution of conductivity of electrospinning solutions containing various amounts of vanadium.

First, conductivity measurements were carried out using a digital conductivity meter (VWR scientific products). The solutions used for conductivity measurements had the same composition as solutions used in electrospinning experiments and they contained various amounts of VOTIP ranging from 0 ~ 23 mol% V to Si ratio. The change in conductivity during the sol-gel transition was measured over time. Figure 2 indicates that the presence of vanadium particles in the sol-gel solution substantially decreases its conductivity from 300 $\mu\text{S}/\text{cm}$ to 100 $\mu\text{S}/\text{cm}$. Since the conductivity of VOTIP solution is very low ($\sim 0.001 \mu\text{S}/\text{cm}$), the addition of VOTIP to the silica precursor resulted in a decrease in conductivity. However, there is no simple trend observed between the conductivity and the amount of vanadium in the solution. We note that a decrease in the solution conductivity, in general, leads to larger fiber diameters [12]. SEM images confirm that the vanadia/silica fibers have a larger average diameter than pure silica fibers under similar spinning conditions possibly due to the change in conductivity and viscosity.

Viscosity measurements of sol-gel precursor solutions containing various concentrations of vanadium have also been carried out on electrospinning solutions during the sol-gel transition. As shown in Figure 3, it is observed that the rate of gelation increases with increasing vanadium concentration. This suggests that as the vanadium concentration increases, solutions will be spinnable at an earlier time and the time period in which they remain spinnable will be shorter. It should be noted that for conventional spinning, silica precursors are spinnable in the range of 10–1000 Poise [7], while silica nanofibers were able to be obtained even at a lower initial solution viscosity (0.5 to 10 Poise) possibly due to the

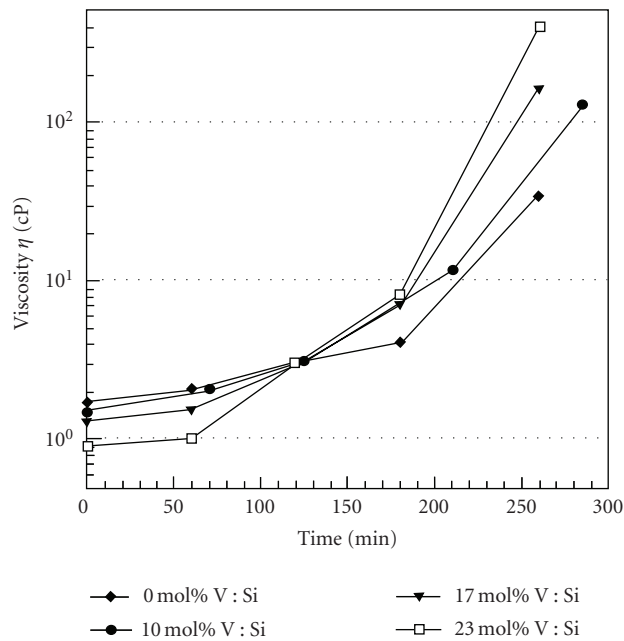


FIGURE 3: Evolution of viscosity of electrospinning solutions with various concentrations of vanadium.

faster evaporation of solvent and thus rapid sol-gel transition during electrospinning.

3.2. Fiber morphology of electrospun nanofibers

Silica sol-gel precursors with and without VOTIP were electrospun and the morphology of the electrospun fibers are presented in this section. First, the SEM images of silica fibers before and after calcination are shown in Figures 4(a) and 4(b), respectively. It is observed that pure silica fibers are sub-micron in diameter and they exhibit a relatively uniform size distribution. For an inner needle diameter of 0.18 mm, as-spun fibers and fibers after calcination range mostly from 100 to 400 nm. As shown in Table 1, the average diameter of silica fibers before and after calcination is $270 \pm 100 \text{ nm}$ and $260 \pm 70 \text{ nm}$, respectively. It should be noted that even after heating at 600°C for 2 h, the morphology of fibers is preserved. However, fibers after calcinations at 600°C for 2 h appear to exhibit a slightly rougher surface, which is most likely due to the evaporation of solvents and water upon heating.

The SEM images of electrospun silica fibers containing 23 mol% V : Si before and after calcination are shown in Figures 4(c) and 4(d). The image after calcination again shows slightly rougher fiber surfaces. In addition, calcined fibers clearly show some crystal growth on the fiber surface. As listed in Table 1, the average diameter of silica fibers containing vanadium is $510 \pm 220 \text{ nm}$ after calcination at 800°C , when using a nozzle with an inner diameter of 0.29 mm, while the average diameter before calcination is $540 \pm 230 \text{ nm}$. Although it appears that the average diameter decreases after calcination, the very large standard deviations put the average diameters within the range of one another. Table 1

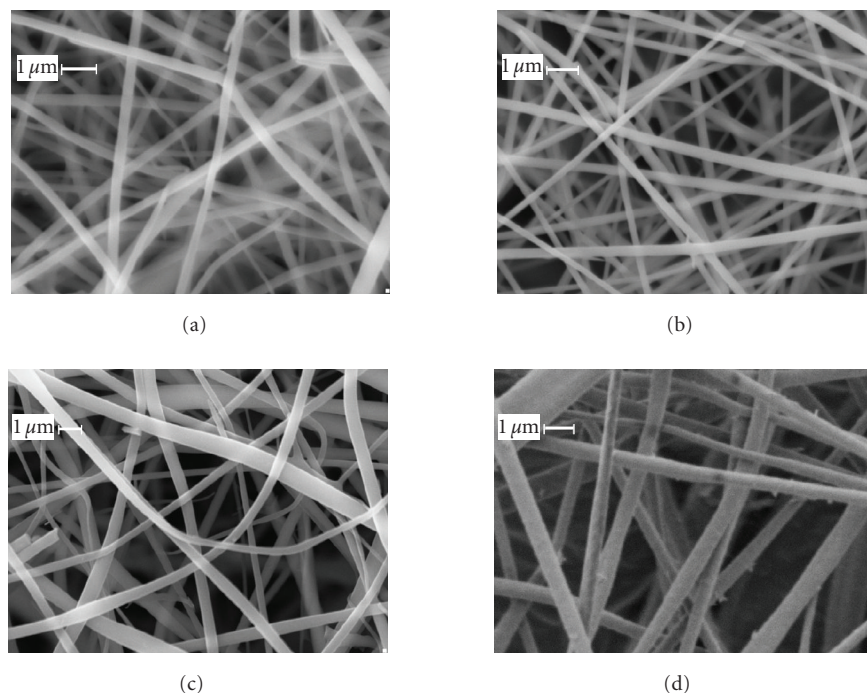


FIGURE 4: SEM images of (a) as-spun silica fibers (b) silica fibers after calcination at 600°C for 2 h (c) as-spun 23 mol% V : Si fibers (d) 23 mol% V : Si fibers after calcination at 800°C for 6 h. The inner diameter of the needle used during electrospinning was 0.29 mm.

TABLE 1: Average diameters of pure silica and vanadia-silica fibers at various nozzle sizes.

Needle size (ID)	Silica fiber, as-spun	Silica fiber, 800°C	23 mol% V : Si fiber, as-spun	23 mol% V : Si fiber, 800°C
0.18 mm	270 ± 100	260 ± 70	—	—
0.29 mm	400 ± 200	370 ± 160	540 ± 230	510 ± 220
0.58 mm	—	—	800 ± 420	770 ± 430

demonstrates that as the inner diameter of the nozzle decreases, the diameter of fibers also decreases. In addition, larger nozzle sizes lead to an increased variation in fiber diameters. Table 1 also shows that the addition of vanadium increases fiber diameter when compared with pure silica fibers. This may be due to the effect that the inclusion of VOTIP has on the conductivity and viscosity of the sol-gel precursor, as discussed in the previous section.

3.3. Thermal and physical properties of electrospun nanofibers

Thermogravimetric analysis (TGA) was applied to as-spun fibers with and without VOTIP. The TGA curve in Figure 5(a) shows a weight loss of about 10 wt% at 200°C in electrospun silica fibers due to evaporation of residual solvents, while at 800°C the weight loss is about 17 wt%. The extra weight loss at high temperature is a result of the self-condensation reactions of the silanol groups [4]. This result is in agreement with the FT-IR study (Figure 7) which indicates that intra- and inter-molecular hydrogen bonds of the

silanol groups disappear after calcination at 800°C. The TGA peak shown in Figure 5(b) was obtained for a silica fiber containing 23 mol% V : Si up to 1200°C to verify the removal of residual solvents and the completion of self-condensation of silanol groups in fibers. The first steep decrease in weight loss up to 400°C shows the removal of residual solvents. A small weight loss continues to 900°C, which points to a change in the composition of fibers. This most likely indicates the completion of self-condensation of silanol group as well as the formation and sublimation of V₂O₅ in the fibers at high temperature.

Physisorption analysis was carried out on pure silica fibers before and after calcination to obtain the BET surface area and information on pore size. The average diameter of electrospun silica fibers before calcination was 520 ± 220 nm. The BET surface area of as-spun fibers was reported as 15.6 m²/g. After calcination at 600°C for 2 h the BET surface area increased to 65.3 m²/g. The pore area distribution of electrospun silica nanofibers before and after calcination is also shown in Figure 6. It is observed that the pore area for small internal pores (1 nm ~ 10 nm) is increased, while that

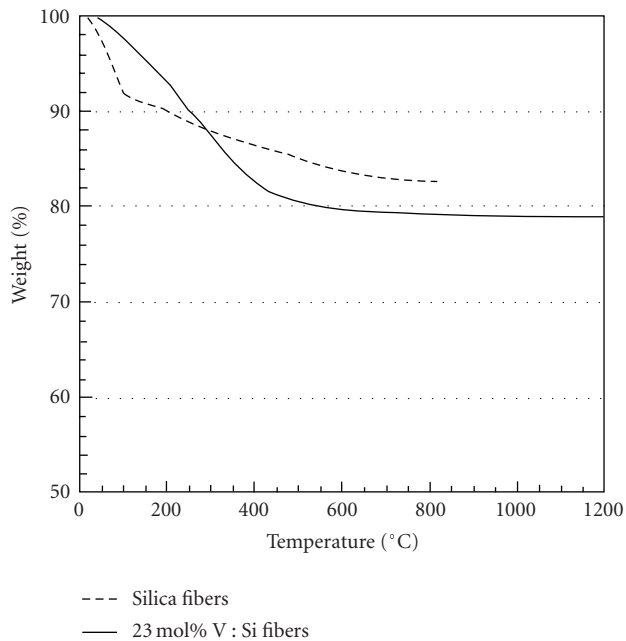


FIGURE 5: TGA curve of pure silica fibers and 23 mol% V : Si fibers.

of large pores (10 nm ~ 100 nm) is decreased after calcination at 600°C for 2 h. Hence, the observed increase in surface area is most likely due to the creation of small pores caused by the removal of residual solvents that occurs during calcination.

Physisorption analysis was also carried out on vanadia/silica fibers after calcination at 800°C for 6 h. The BET surface area of the fibers after calcination was 1.9 m²/g. This value is comparable to that for nanoparticles obtained from high-energy milling (1 ~ 10 m²/g), but is much lower than those for nanoparticles obtained by gas phase condensation (100 m²/g) [8]. We note that the surface area of vanadia/silica fibers is much lower than that of silica fibers possibly due to the higher calcination temperature and larger deviation in vanadia/silica fiber diameter. As shown in Figure 6, not only the area of small pores but also the area of large pores in the vanadia/silica fibers calcined at 800°C are considerably lower than those of as-spun silica fibers and silica fibers calcined at 600°C.

To identify the specific molecular components and structures in the electrospun silica fibers before and after calcination, FT-IR spectroscopy was carried out. Figure 7(a) shows that the FT-IR spectrum of the as-spun silica fibers has peaks at 1038, 918, and 776 cm⁻¹, which are assigned to the Si-O vibration [4]. In particular, the band near 918 cm⁻¹ indicates the Si-OH group and this peak disappears after calcination at 800°C (Figure 7(b)). Bands located between 750 and 1300 cm⁻¹ can be attributed to asymmetric stretching modes of Si-O-Si [13]. There is a broad band around 3300 cm⁻¹ that is representative of an O-H vibration. This band results from intra- and inter-molecular hydrogen bonds of the silanol groups (Si-OH), and residual water and ethanol [4].

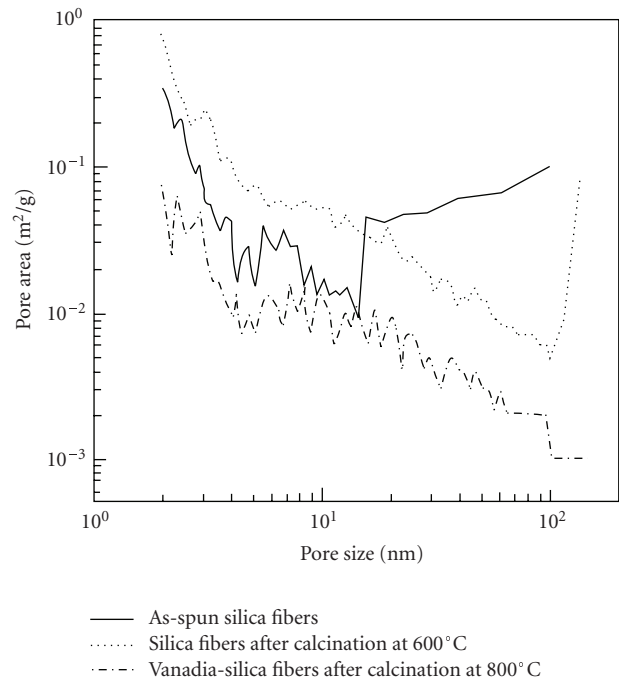


FIGURE 6: Pore area distribution of as-spun silica fibers, silica fibers after calcination at 600°C for 2 h, and vanadia/silica fibers after calcination at 800°C for 6 h.

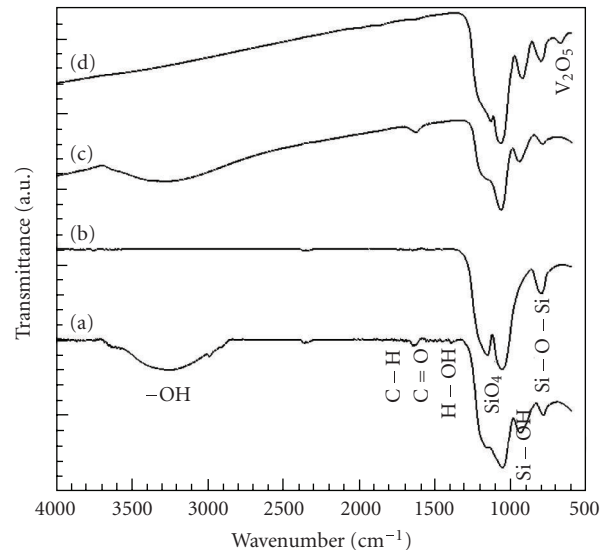


FIGURE 7: FT-IR spectrum of (a) as-spun silica fibers (b) silica fibers after calcination at 800°C for 6 h (c) as-spun 23 mol% V : Si fibers (d) 23 mol% V : Si fibers calcined at 800°C for 6 h.

After calcination at 800°C the broad band peak disappears due to evaporation of water and ethanol from the fibers while peaks are still observed representing Si-O vibrations.

FT-IR was conducted on silica fibers containing 23 mol% V : Si before calcination and after calcination at 800°C, and

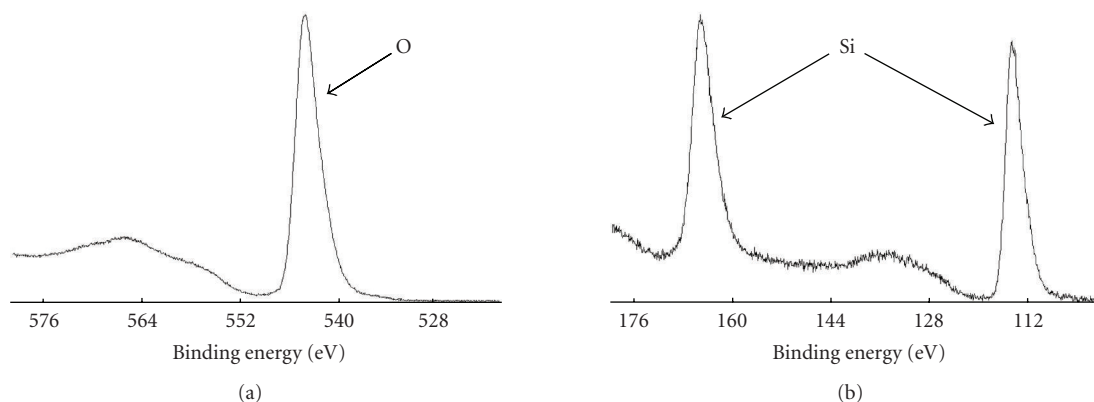


FIGURE 8: XPS of silica fibers after calcination at 400°C.

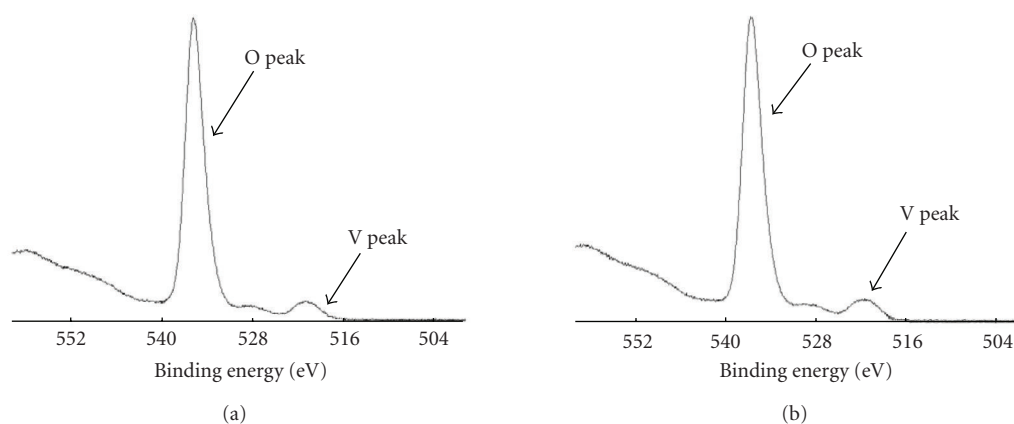


FIGURE 9: XPS spectra of (a) as-spun 23 mol% V : Si fiber (b) 23 mol% V : Si fiber after calcination at 800°C for 6 h.

the spectra are shown in Figures 7(c) and 7(d). The spectra for 23 mol% V : Si fibers before calcination bear a resemblance to those of the silica fibers before calcination (Figure 7(a)) and match. On the other hand, the spectrum for the 23 mol% V : Si fiber after calcination has one additional peak at 670 cm^{-1} when compared with the spectrum for the silica fibers after calcination. The band at 670 cm^{-1} can be attributed to the presence of V_2O_5 [14]. The other bands observed may indicate the presence of V_2O_5 , but they overlap with the Si–O vibrations that are also present in the fibers. For example, the V=O band is observed around 1000 cm^{-1} and at 750 cm^{-1} the V–O–V asymmetric stretch is observed. Bands are observed near these locations for the 23 mol% V : Si fiber after calcination, but Si–O vibrations are also observed at those points as shown in Figure 7(b) [15].

3.4. Surface characteristics of silica and vanadia/silica nanofibers

An X-ray photoelectron spectroscopy (XPS) study was carried out on pure silica fibers calcined for 6 h at 400°C and 800°C. The spectrum, shown in Figure 8, indicates the presence of silicon and oxygen on the surface of fibers. Using (1)

the atomic ratio, N_A/N_B of Si : O may be found [16],

$$\frac{N_A}{N_B} = \frac{I_A/S_A}{I_B/S_B}, \quad (1)$$

where N represents the concentration of a relevant element, i (atomic density), and I_i and S_i are the intensity of the photoelectron signal and atomic sensitivity factor of element, i , respectively. S for O and Si are 2.494 and 0.903, respectively [17]. The number of groups was 8 and the number of scans was 20. After calcination at 400°C and after calcination at 800°C the Si : O ratio is around 0.60, which is within error of 0.5, the Si : O ratio to be expected for SiO_2 .

XPS analysis was also done on silica fibers containing vanadium. As shown in Figure 9 a small vanadium peak is observed for both as-spun fibers and fibers after calcination [10, 18]. Using (1), where S for vanadium is 5.496, it was found that the amount of vanadium at the surface of the fibers increased after calcination [16]. The highest V : Si ratio achieved to date using 23 mol% V : Si fibers is 10 mol%, which indicates that a little less than one half of the total vanadium reside on the surface of the fiber as V_2O_5 .

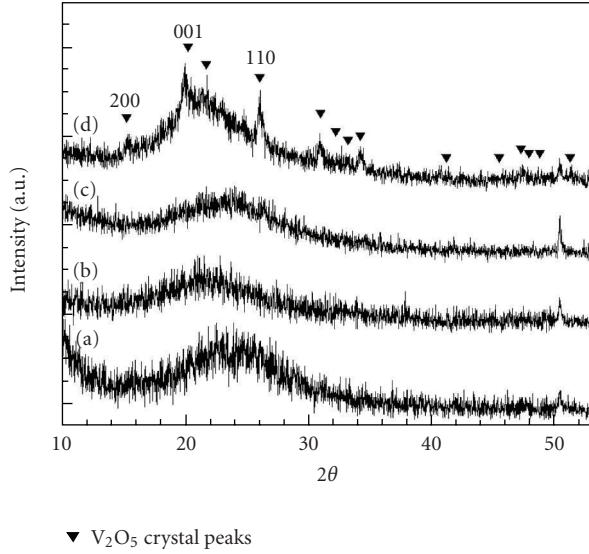


FIGURE 10: XRD patterns of (a) as-spun silica fibers (b) silica fibers calcined at 800°C for 6 h (c) as-spun 23 mol% V : Si fibers, and (d) 23 mol% V : Si fibers after calcination at 800°C for 6 h.

3.5. Vanadia crystals in silica nanofibers

XRD patterns shown in Figures 10(a) and 10(b) for both as-spun silica fibers and silica fibers heated at 800°C for 6 h have a broad peak at $2\theta = 23\text{--}27^\circ$, which represents amorphous SiO [4]. The silica fibers do not exhibit crystalline characteristics upon calcination at 800°C.

XRD patterns were obtained for silica fibers containing 23 mol% V : Si; both as-spun and calcined fibers are shown in Figures 10(c) and 10(d). Before calcination, no V_2O_5 crystal peaks are observed. The peaks that are observed after calcination indicate the formation of V_2O_5 crystals [6]. Using the Scherrer equation (2) the average crystallite domain size in each direction may be obtained [19],

$$L_{hkl} = \frac{0.9\lambda}{B_{hkl} \cos \theta_0}, \quad (2)$$

where B_{hkl} is the width at half height, in radians, for a particular hkl reflection, λ is the wavelength, and θ_0 is the Bragg angle of the reflection. As shown in Table 2, the crystallite domain dimensions are in tens of nanometers, which are similar to the crystallite sizes observed in EFTEM images.

We note that a peak at $2\theta = 50.5^\circ$ is observed in each pattern for pure silica fibers and silica fibers containing vanadium which may be attributed to the formation of hydrates and xerogels [14, 20, 21]. This peak only appears when the average diameter of as-spun fibers is below $1\ \mu\text{m}$, and thus the surface area of the fibers is possibly large. This peak at $2\theta = 50.5^\circ$ decreases after calcination.

A phase diagram obtained from XRD of silica fibers containing various amounts of vanadium is shown in Figure 11. In each case the time of calcination remained the same at 6 h, while the calcination temperature was changed. The lower limit temperature line at a given vanadium concentration

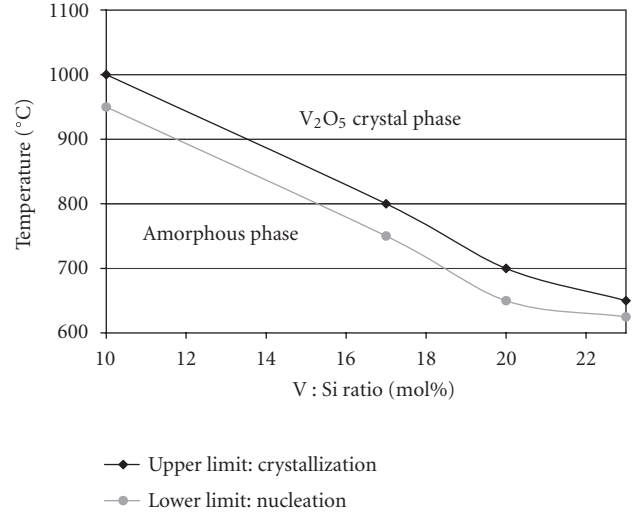


FIGURE 11: Phase diagram for silica fibers containing various concentrations of vanadium oxide.

TABLE 2: Average crystallite domain size of V_2O_5 on silica nanofibers obtained from XRD patterns and the Scherrer equation.

Direction	Average crystallite domain dimension (nm)
200	10.1
001	13.2
110	14.0

represents the first sign of nucleation of V_2O_5 crystals, while the upper-limit temperature line represents the onset of the formation of well-defined V_2O_5 crystal peaks. Therefore, calcination at or above the lower limit temperature should result in the formation of V_2O_5 crystals in the fibers, and the crystal size and degree of crystallization depends on both calcination time and temperature. It is observed that the onset temperature for the phase transition from amorphous to V_2O_5 crystals decreases with increasing vanadium content.

The vanadium crystal phases of 23 mol% V : Si fibers can also be identified with EFTEM images in Figure 12. Although EFTEM only provides the spatial distribution of elements such as V or Si (not V_2O_5 or SiO_2) and O is present in both V_2O_5 and SiO_2 phases, such elemental mappings can also offer a rough assessment on the size and distribution of V_2O_5 crystals in the fibers. Figure 12(b) shows an EFTEM image of a calcined, vanadia/silica fiber where V was filtered out, and thus distinct bright spots that are tens of nanometers in size correspond to the domains of V (and thus V_2O_5) on silica fibers. In Figure 12(c) an EFTEM image of the same fiber after Si was filtered out, and thus the dark spots represent V rich regions which are in agreement with bright spots in the V filtered image in Figure 12(b).

3.6. Higher vanadium content fibers

Vanadia/silica fibers with a higher vanadium content (50 mol% V : Si) have been electrospun to increase the amount of V_2O_5 crystals on the surface and to achieve a higher degree

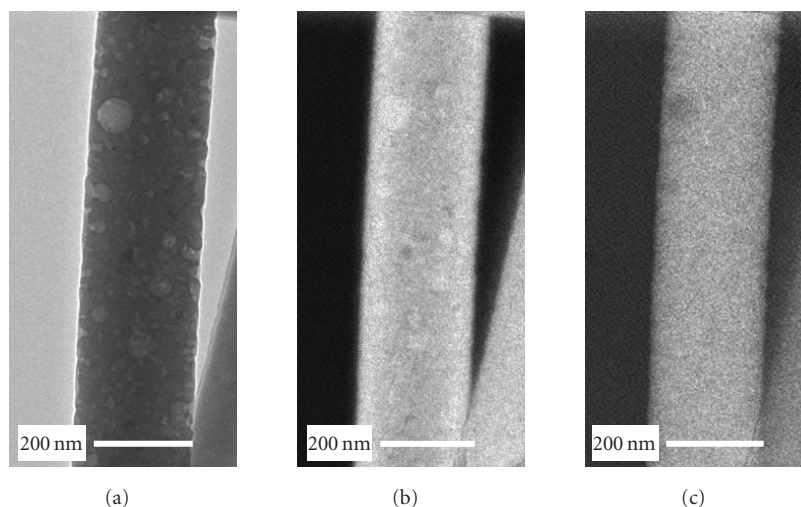


FIGURE 12: EFTEM images of 23 mol% V : Si fiber after calcination at 800°C (a) with $E_{\text{filter}} = 0$ eV, (b) with $E_{\text{filter}} = 38$ eV, (c) with $E_{\text{filter}} = 99$ eV. Fiber diameter is about 250 nm.

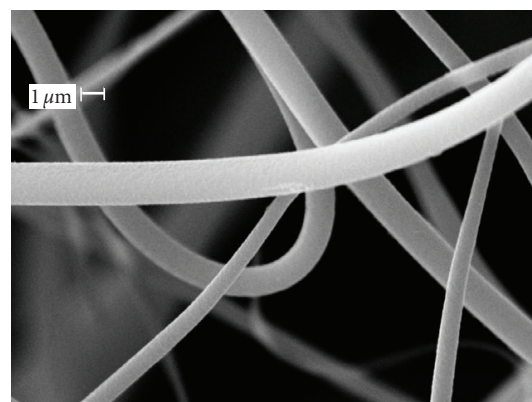
of crystallinity in the fibers. The SEM image in Figure 13(b) shows 50 mol% V : Si fibers after calcination at 650°C. A more evident crystal growth on the fiber surface is observed when compared with 23 mol% V : Si fibers after calcination (Figure 4(d)) due to the higher vanadium content in the fibers. In addition, the vanadia crystals appear to be aligned along the fiber axis.

XPS was conducted on the 50 mol% V : Si fibers after calcination at 650°C. As shown in Figure 14 the amount of vanadium on the surface increased drastically when compared with the 23 mol% V : Si fibers, which is consistent with observations made from SEM images. The V : Si ratio achieved was 27 mol%, which means that a little more than one half of the vanadium is at or near the fiber surface.

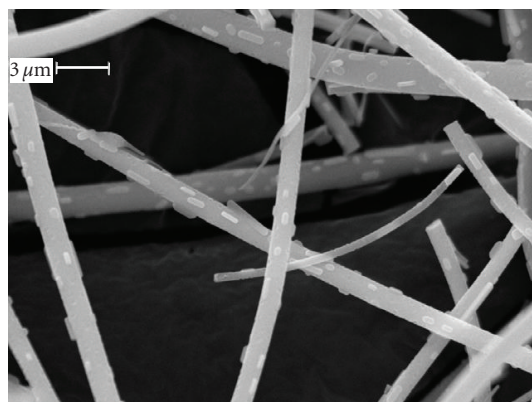
XRD patterns for 50 mol% V : Si fibers after calcination at 650°C and 800°C are shown in Figure 15. The fibers exhibit the growth of V_2O_5 crystals and they have a much higher degree of crystallinity than the 23 mol% V : Si fibers after calcination. From the Scherrer equation it was determined that the average crystal domain size after calcination at 650°C and 800°C ranges from 31 to 33 nm and from 17 to 25 nm, respectively. The observed decrease in crystal domain size is most likely due to a possible melting and sublimation of V_2O_5 above 690°C.

3.7. Hollow vanadia/silica nanofibers via coaxial electrospinning

Silica fibers containing vanadium have been made using coaxial electrospinning in order to selectively place V_2O_5 crystals on the surface of the fibers. Mineral oil and silica precursor containing VOTIP were placed as the core and skin, respectively, and thus hollow silica fibers containing V_2O_5 were produced after calcination at high temperature. Calcination at 1000°C created some hollow fibers as indicated in



(a)



(b)

FIGURE 13: SEM images of (a) as-spun 50 mol% V : Si fibers, and (b) 50 mol% V : Si fibers after calcination at 650°C for 6 h.

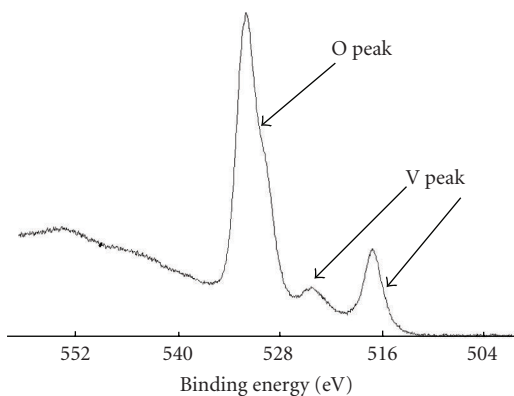


FIGURE 14: XPS spectrum of 50 mol% V : Si fibers after calcination at 650 °C for 6 h.

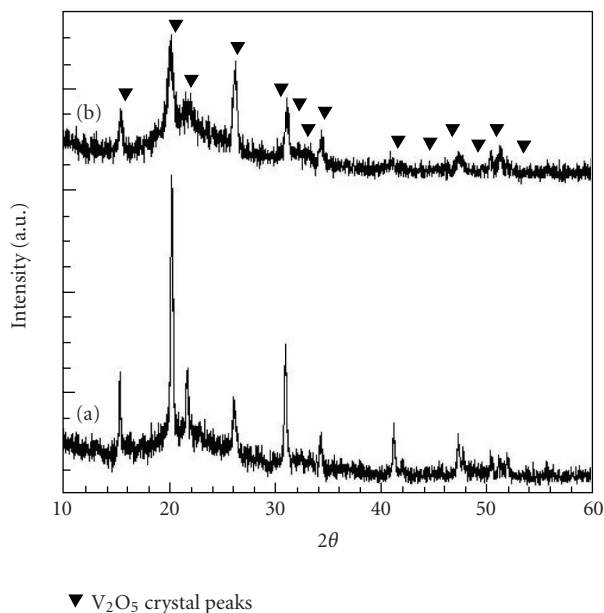
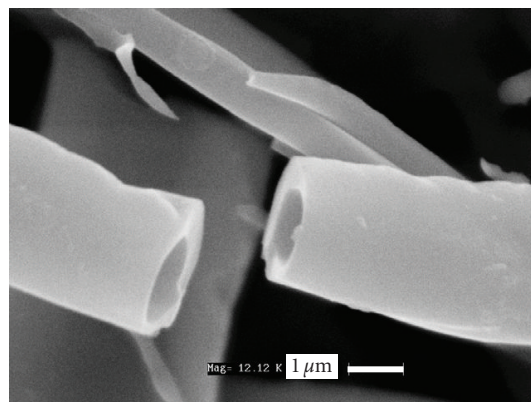


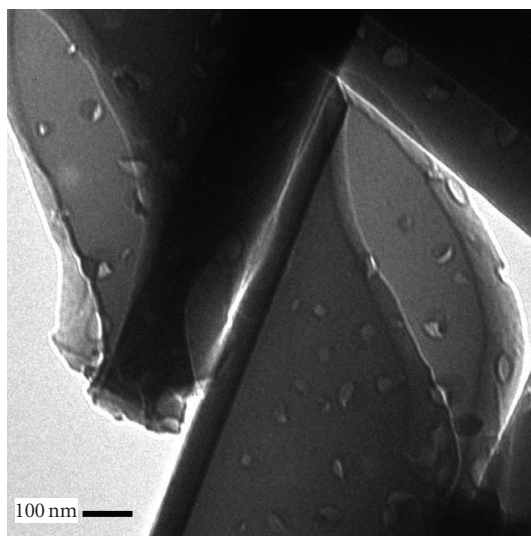
FIGURE 15: XRD patterns for (a) 50 mol% V : Si fibers after calcination at 650 °C for 6 h, and (b) 50 mol% V : Si fibers after calcination at 800 °C for 6 h.

the SEM image shown in Figure 16(a). The inner diameter of the fibers ranges from about 500 nm to 1 μm and the thickness of the core shell is about 300 nm. Hollow fibers are advantageous because the coaxial scheme can greatly reduce the loading required of metal oxides by placing the metal oxide particles exclusively in the skin layer.

TEM images of two fibers cut open in Figure 16(b) also show the hollow nature of the fibers after calcination at 1000 °C. The images demonstrate the domains of crystals (bright spots) on the surface of both the inner and outer side of the fiber, which suggests that hollow fibers can possibly increase the number of active sites of the fiber, when compared with monoaxial fibers.



(a)



(b)

FIGURE 16: Coaxially spun silica fibers containing 23 mol% V : Si after calcination at 1000 °C for 6 h (a) SEM image and (b) TEM image.

4. CONCLUSION

Silica nanofiber mats have been produced by combining sol-gel synthesis and electrospinning without using any polymer binder. SEM images show silica fibers range in diameter from 100 to 400 nm and the morphology of the silica fibers was preserved after calcination at 600 °C. TGA showed an overall weight loss of 17 wt% at 800 °C. The BET surface area of the fibers increased dramatically after calcination at 600 °C, while the fibers contain a very large number of micropores. FT-IR showed Si–O vibrations and the removal of residual solvents after calcination. XPS data after calcination indicated the presence of the correct ratio of Si to O. XRD showed the fibers remained amorphous after calcination and TEM indicates a change in morphology and the collapse of pores in the fibers after calcination at 800 °C.

This new scheme to produce inorganic nanofibers has been extended to the development of silica nanofiber mats containing vanadium pentoxide crystals by directly incorporating the vanadium oxide precursor into a sol-gel synthesis reaction. SEM images showed vanadia/silica fibers are also submicron in diameter. TGA demonstrated the composition of the fibers continued to change up to 900°C. FT-IR data confirms the formation of V₂O₅ after calcination at 800°C. XPS analysis showed an increase in vanadium contents at the fiber surface after calcination. XRD indicates V₂O₅ crystals form after calcination and the crystal sizes match those observed from TEM. EFTEM images demonstrate vanadia crystal growth on the surface of the fibers. SEM images of high vanadium content (50 mol% V : Si) fibers show more crystal growth on the fiber surface and the crystals are mostly aligned along the fiber axis. XPS shows an increase in vanadium contents at the fiber surface, while XRD shows an increase in the degree of crystallinity when compared with 23 mol% V : Si fibers. Hollow silica fibers containing vanadium oxide crystals on the surface have also been produced using coaxial electrospinning in order to selectively place V₂O₅ at the surface of the fiber.

ACKNOWLEDGMENTS

This work was supported by the United States Department of Agriculture through a National Research Initiative Competitive Grant in a Nanoscale Science and Engineering, Award no. 2005-35603-15298. The authors also thank Christina Jackson for her help in developing silica fibers with high vanadia content.

REFERENCES

- [1] H. Fong and D. H. Reneker, "Electrospinning and the formation of nanofibers," in *Structure Formation in Polymeric Fibers*, D. R. Salem, Ed., chapter 6, Hanser Gardner, Cincinnati, Ohio, USA, 2001.
- [2] Y. Dzenis, "Spinning continuous fibers for nanotechnology," *Science*, vol. 304, no. 5679, pp. 1917–1919, 2004.
- [3] D. Li and Y. Xia, "Electrospinning of nanofibers: reinventing the wheel?" *Advanced Materials*, vol. 16, no. 14, pp. 1151–1170, 2004.
- [4] S.-S. Choi, S. G. Lee, S. S. Im, S. H. Kim, and Y. L. Joo, "Silica nanofibers from electrospinning/sol-gel process," *Journal of Materials Science Letters*, vol. 22, no. 12, pp. 891–893, 2003.
- [5] Z.-M. Huang, Y.-Z. Zhang, M. Kotaki, and S. Ramakrishna, "A review on polymer nanofibers by electrospinning and their applications in nanocomposites," *Composites Science and Technology*, vol. 63, no. 15, pp. 2223–2253, 2003.
- [6] P. Viswanathamurthi, N. Bhattarai, H. Y. Kim, and D. R. Lee, "Vanadium pentoxide nanofibers by electrospinning," *Scripta Materialia*, vol. 49, no. 6, pp. 577–581, 2003.
- [7] L. C. Klein, "Part III. Continuous, discontinuous, and woven fibers," in *Sol-Gel Technology for Thin Films, Fibers, Preforms, Electronics, and Specialty Shapes*, Knovel, Binghamton, NY, USA, 1988.
- [8] D. D. Beck and R. W. Siegel, "Dissociative adsorption of hydrogen sulfide over nanophase titanium dioxide," *Journal of Materials Research*, vol. 7, no. 10, pp. 2840–2845, 1992.
- [9] M. C. Carotta, M. Ferroni, S. Gherardi, et al., "Thick-film gas sensors based on vanadium-titanium oxide powders prepared by sol-gel synthesis," *Journal of the European Ceramic Society*, vol. 24, no. 6, pp. 1409–1413, 2004.
- [10] S. Zhuiykov, W. Wlodarski, and Y. Li, "Nanocrystalline V₂O₅-TiO₂ thin-films for oxygen sensing prepared by sol-gel process," *Sensors and Actuators B: Chemical*, vol. 77, no. 1-2, pp. 484–490, 2001.
- [11] D. Li and Y. Xia, "Direct fabrication of composite and ceramic hollow nanofibers by electrospinning," *Nano Letters*, vol. 4, no. 5, pp. 933–938, 2004.
- [12] S.-H. Tan, R. Inai, M. Kotaki, and S. Ramakrishna, "Systematic parameter study for ultra-fine fiber fabrication via electrospinning process," *Polymer*, vol. 46, no. 16, pp. 6128–6134, 2005.
- [13] Q. Hu, H. Suzuki, H. Gao, H. Araki, W. Yang, and T. Noda, "High-frequency FTIR absorption of SiO₂/Si nanowires," *Chemical Physics Letters*, vol. 378, no. 3-4, pp. 299–304, 2003.
- [14] M. Gotić, S. Popović, M. Ivanda, and S. Musić, "Sol-gel synthesis and characterization of V₂O₅ powders," *Materials Letters*, vol. 57, no. 21, pp. 3186–3192, 2003.
- [15] G. P. Holland, F. Huquenin, R. M. Torresi, and D. Buttry, "Comparison of V₂O₅ xerogels prepared by the vandate and alkoxide routes using X-ray absorption and other methods," *Journal of the Electrochemical Society*, vol. 150, no. 6, pp. A721–A725, 2003.
- [16] I. Losito, L. Sabbatini, and J. A. Gardella Jr., "Electron, ion, and mass spectroscopy," in *Comprehensive Desk Reference of Polymer Characterization and Analysis*, R. F. Brady Jr., Ed., Oxford University Press, New York, NY, USA, 2003.
- [17] C. D. Wagner, et al., "Appendix 6," in *Practical Surface Analysis. Vol. 1*, John Wiley & Sons, New York, NY, USA, 2nd edition, 1990.
- [18] A. Lavacchi, B. Cortigiani, G. Rovida, U. Bardi, and A. Atrei, "Composition and structure of tin/vanadium oxide surfaces for chemical sensing applications," *Sensors and Actuators B: Chemical*, vol. 71, no. 1-2, pp. 123–126, 2000.
- [19] J. Blackwell, "Microstructure characterization," in *Structure Formation in Polymeric Fibers*, D. R. Salem, Ed., chapter 13, Hanser Gardner, Cincinnati, Ohio, USA, 2001.
- [20] O. Durupthy, N. Steunou, T. Coradin, J. Maquet, C. Bonhomme, and J. Livage, "Influence of pH and ionic strength on vanadium(v) oxides formation. From V₂O₅.nH₂O gels to crystalline NaV₂O₈.1.5H₂O," *Journal of Materials Chemistry*, vol. 15, no. 10, pp. 1090–1098, 2005.
- [21] M. J. Niederberger, "Synthesis and characterization of novel micro- and nanostructured vanadium, molybdenum, and iron oxides," Dissertation, Swiss Federal Institute of Technology, Lausanne, Switzerland, 2000.